Investigation of the deformation of in-vessel components of a nuclear fusion experiment using optical strain sensors

Christian Vorpahl

Investigation of the deformation of in-vessel components of a nuclear fusion experiment using optical strain sensors

Zur Erlangung des akademischen Grades
Doktor der Ingenieurwissenschaften
der Fakultät für Maschinenbau
Karlsruher Institut für Technologie (KIT)
genehmigte Dissertation von

Dipl.-Ing. Christian Georg Vorpahl

Tag der mündlichen Prüfung: 3.5.2013

Hauptreferent: Prof. Marc Kamlah, KIT
1. Korreferent: Prof. Hartmut Zohm, IPP
2. Korreferent: Prof. Wolfgang Seemann, KIT

"The merit of an action lies in finishing it to the end."

Temujin, Genghis Khan of Mongolia, speaking to his sons.
from GENGHIS KHAN - The Emperor of All Men
by Harold Lamb, 1927.

Acknowledgements

This thesis presents my PhD project carried out at the Max-Planck-Institute for Plasmaphysics (IPP) in Garching near Munich. I would like to express my deep gratitude to the many people who have contributed to the successful completion of this project.

First of all, I would like to thank Hartmut Zohm and Wolfgang Suttrop for their excellent supervision. Advice given by both of you has been a great help to understanding the plasma physics involved in the various types of structural forces experienced by a tokamak. I also greatly benefited from your research experience in general, your professional guidance and the fact that you granted me the independence I needed to perform this research. I am also thankful to Wolfgang for programming the drivers for the implementation of my sensing hardware in the ASDEX Upgrade data acquisition infrastructure. I am especially grateful for the assistance from Marc Kamlah, my academic supervisor from KIT, whose professional expertise and willingness to discuss the mechanical and engineering parts of this work in countless conversations provided me with essential insights. For his professional counsel and for accepting the task of supervising this work as secondary academic advisor, I would also like to thank Wolfgang Seemann from the Institute of Engineering Mechanics of KIT. I would like to express my gratitude for the important contributions provided by Irene Zammuto, who designed the original finite element model of the PSL as well as the numerical routines for extracting the eigenmodes from the simulation results. On the technical side, I would like to offer my special thanks to Michael Ebner for his invaluable support in welding tasks and issues of general mechanics. I am indebted to Gabi Fröhlich and Robert Schindler for their assistance during welding and installation of the sensors, to Wolfgang Zeidner and Stefan Eder for the 3D-measurements in the vessel, to the whole 'vessel crew' for all of their help, and to CAD mastermind Jacek Spychala for his continuous support. I thank Bernhard Streibl for various discussions and for sharing with me some of his wisdom about how ASDEX Upgade was designed and built - and why it was done this way. I must not forget to mention Andreas Burckhart, who helped me a lot with disruption statistics and EMD, and was also a great officemate whose camaraderie I appreciated very much. I owe many thanks to Stefan Kimmig, Till Höschen, Martin Balden, Gabriele Matern and the materials department for support in the context of tensile testing and for giving me the opportunity to use their facilities for electron microscopy and specimen preparation. Finally, I wish to thank my dear colleagues Rachael McDermott and Mike Dunne, who accepted the thankless job of proof-reading the manuscript, for their valuable remarks which, in my opinion, pretty much improved the readability of this whole thing.

For making my working life at the institute a worthwhile and enjoyable experience, I would like to express my appreciation to all my colleagues, many of whom have become friends.

Thank you.

Abstract

A fibre-optic measurement system to analyse the deformation of in-vessel components of the nuclear fusion experiment ASDEX Upgrade (AUG) has been successfully developed, installed and commissioned. This technology has thereby been qualified for in-vessel use at experimental fusion devices. The measured data were interpreted regarding operational safety, amongst others.

AUG is equipped with an internal conductor for plasma stabilisation called the Passive Stabilisation Loop (PSL), on which a set of 16 internal coils (B-coils) is directly mounted. The PSL structure weighs 8 t and is composed of two solid copper rings of 4 m diameter, connected by eight bridges. It is highly prone to vibrations. Resonant oscillations in response to forces induced by the recently installed B-coils are potentially hazardous. They need to be understood and possibly avoided. This made the development of the present diagnostic necessary.

The system consists of 34 fibre-optic strain sensors incorporated in two glass fibres and is completely insensitive to electromagnetic interference. The fibres are highly customised to avoid inconvenient excess fibre length in the vacuum vessel and were tested for neutron tolerance and vacuum compatibility prior to installation. The actual sensors are embedded in stainless steel carriers that were attached to the PSL by laser welding. Appropriate welding parameters were defined in view of the metallurgical dissimilarity. The weld quality was approved by tensile tests and microscopic investigations. Accurate in-vessel positioning of the sensors was assured using a 3D measurement system and coordinates from CAD.

Data acquisition is automated and allows a sampling rate of 1 kHz. The temporal and spatial resolutions of the system are sufficient to resolve the potentially dangerous natural bending modes of the PSL. The magnetic loads on it are due to plasma current disruptions, actuation of the B-coils, and actuation of the plasma position control coils in interaction with the plasma itself. These effects can clearly be distinguished.

The highest operational loads are impulse forces during disruptions which excite free oscillations of the PSL at its natural frequencies. Oscillations occur at frequencies between 10 Hz and 120 Hz. In general, the measured spectral peaks correspond to ideal ring modal shapes. Resonant excitation tests showed the n=4 (quadratic) mode to be the most dangerous configuration when using the B-coils. Disruptive oscillations are typically dominated by n=3 modes. The influences of the vertical PSL supports and the bridges on the development of particular modes were identified.

Finite element (FE) modal analyses showed good agreement with the measurements in terms of frequencies and modal shapes. A discrete PSL model was developed by modal expansion of shapes extracted from the FE modal solution. The associated modal participation factors are based on experimental strain data. For short time intervals of PSL oscillations with constant amplitude, the model thereby allows the calculation of the strain, stress and deflection for every element of the FE model. For the strongly damped vibrations following disruptions, it exhibits non-negligible deviations. For this reason, a simple conservative approach was used to calculate the stresses at critical points of the PSL structure.

By linear damage accumulation, the present fatigue damage was estimated to be negligible. Equivalent stress values and the numbers of cycles were obtained with a two-parameter counting algorithm based on a representative load collective. Experimental strain data from resonant PSL excitation experiments using the B-coils were extrapolated towards higher coil currents. Coil currents of 300 A, just 30% of the maximum design value, may lead to PSL deformations which exceed those of the hardest measured disrup-

tions. These values allowed the calculation of a second damage accumulation and to define the operational limits of the internal coils in terms of critical frequencies and maximum currents.

Kurzfassung

Ein faseroptisches Messystem zur Verformunganalyse interner Komponenten des nuklearen Fusionsexperiments ASDEX Upgrade (AUG) wurde erfolgreich entwickelt, installiert und in Betrieb genommen. Diese Technologie wurde somit erstmals für den Einsatz im Vakuumgefäß von Fusionsexperimenten qualifiziert. Die gewonnenen Messdaten wurden unter anderem im Hinblick auf die Betriebssicherheit ausgewertet.

AUG verfügt über einen internen Leiter zur Plasmastabilisierung, genannt Passiver Stabilisierungsleiter (PSL), an dem kürzlich 16 interne Sattelspulen (B-Spulen) direkt montiert wurden. Der PSL hat ein Gesamtgewicht von 8 t und besteht aus zwei massiven Kupferringen von je 4 m Durchmesser, verbunden durch 8 Brücken. Diese Struktur ist hochgradig schwingungsfähig. Resonante PSL Schwingungen, die durch die magnetischen Kräfte der B-Spulen angeregt werden, stellen eine Gefahr dar und müssen verstanden und gegebenenfalls vermieden werden. Dies erforderte die hier beschriebene Diagnostik.

Das System besteht aus 34 faseroptischen Dehnungssensoren, integriert in zwei Glasfasern, und ist gegenüber elektromagnetischen Interferenzen absolut unempfindlich. Zur Vermeidung jeglicher Überlänge im Vakuumgefäß sind beide Sensorfasern individuell angepasst. Ihre Vakuumkompatibilität und Neutronenstrahlungsresistenz wurde vor Einbau getestet. Die eigentlichen Sensoren sind in Träger aus austenitischem Stahl eingebettet, welche auf dem kupfernen PSL mittels Laserschweißen angebracht wurden. Angesichts der metallurgischen Verschiedenartigkeit wurden geeignete Schweißparameter definiert. Die Qualität der Verbindungen wurde durch Zugversuche und mikroskopische Untersuchungen geprüft. Mit einem 3D Meßsystem nebst CAD-Koordinaten wurden die Sensoren im Vakuumgefäß exakt positioniert.

Die Datenerfassung erfolgt automatisiert und erlaubt eine Abtastrate von 1 kHz. Die zeitliche und räumliche Auflösung des Systems sind ausreichend, um die potentiell festigkeitskritischen PSL Biegeeigenschwingungen zu detektieren. Auf den PSL wirken magnetische Kräfte infolge von Plasmastromabbrüchen (Disruptionen), durch Aktivität der B-Spulen oder der Spulen zur Plasmapositionsregelung im Zusammenwirken mit dem Plasma selbst. Diese Effekte können eindeutig unterschieden werden.

Die größten Lasten treten stoßartig während Disruptionen auf und regen den PSL zu freien Schwingungen bei dessen Eigenfrequenzen an. Schwingungen des PSL treten hauptsächlich im Frequenzintervall von 10 Hz bis 120 Hz auf. Die Maxima der gemessenen Frequenzspektren können in der Regel Biegeeigenformen idealer Ringe zugeordnet werden. Versuche mit resonanter Anregung identifizierten die quadratische Eigenschwingung (n=4) als kritische Konfiguration im B-Spulen Betrieb. Disruptiv erregte Schwingungen hingegen sind typischerweise n=3 dominiert. Der Einfluß der PSL Aufhängung sowie der Brücken auf die Ausbildung bestimmter Eigenmoden wurde gezeigt.

Modalanalysen mittels finiter Elemente (FE) zeigten gute Übereinstimmung mit den Messungen hinsichtlich Frequenz und Eigenform der Schwingungen. Daher wurde ein diskretisiertes Modell des PSL auf Basis von Eigenformen entwickelt, die aus der FE Modalanalyse exportiert wurden. Die zugehörigen modalen Amplituden werden mit Hilfe der Messung näherungsweise ermittelt. Für kurze Zeitintervalle von PSL Schwingungen konstanter Amplitude erlaubt das Modell die Berechnung von Spannung, Dehnung und Durchbiegung für alle Elemente des FE Modells. Im Falle der stark gedämpften Oszillationen nach Disruptionen treten nicht vernachlässigbare Abweichungen auf. Zur Berechnung

der Spannung an kritischen Punkten des PSL wurde deswegen ein einfacher, konservativer Ansatz gewählt.

Der aktuelle Ermüdungzustand des PSL wurde mittels linearer Schädigungsakkumulation als vernachlässigbar bewertet. Die Zyklenzahlen und Spannungswerte wurden mit einem zweiparametrigen Zählalgorithmus auf Basis eines repräsentativen Lastkollektivs bestimmt. Meßdaten von Experimenten mit resonanter PSL Anregung durch die internen Spulen wurden zu höheren Spulenströmen hin extrapoliert. Bereits eine Stromstärke von 300 A, also 30% der Auslegungsstromstärke, kann zu stärkeren Verformungen führen als die stärksten gemessenen Disruptionen. Mit diesen Daten wurde eine zweite Schädigungsrechnung durchgeführt und der Betriebsbereich der B-Spulen hinsichtlich maximaler Ströme und kritischer Frequenzen begrenzt.

Résumé

Un systeme de mesure à base de fibres optiques pour analyser la deformation mécanique de composants internes de l'expérience de fusion nucléaire ASDEX Upgrade (AUG) a été developpé, installé et commissioné avec succès. Ainsi, cette technologie a été qualifiée pour l'application dans l'enceinte d'appareils expérimentaux de fusion. Les données mesurées ont été analysées en vue de la sécurité de service, entre autres.

AUG dispose d'un conducteur electrique interne pour la stabilisation du plasma, appelé Passive Stabilisation Loop (PSL). Seize bobines internes (bobines-B), récemment installées, y sont attachées directement. La structure du PSL a une masse totale de 8 t et une grande capacité vibratoire. Elle est composée de deux anneaux solides en cuivre de 4 m de diamètre chacun, interconnectés par huit ponts. Des oscillations résonantes du PSL en réponse aux forces magnétiques induites par les bobines internes peuvent représenter un danger. Elles doivent être comprises et, si nécessaire, évitées. Cette investigation a nécessité le present diagnostic.

Le système consiste de 34 jauges extensiométriques optiques incorporées dans deux fibres optiques. Il est complètement insensible aux interférences électromagnétiques. Les fibres sont adaptées pour éviter l'inconvénient de surlongueurs dans l'enceinte. Leur compatibilité au vide et leur résistance au rayonnement neutronique ont été testées avant leur installation. Les capteurs sont encastrés dans des supports d'acier austénitique attachés au PSL par soudage au laser. En face de la dissimilarité métallurgique, paramètres de soudage appropriés ont été definies. La qualité des joints a été vérifiée par des essais de traction et des investigations de leur microstructure. Le positionnement exact des jauges dans l'enceinte a été réalisé avec un système de mesure 3D et des coordonnées de CAO.

L'acquisition automatisée des données permet une fréquence d'échantillonnage de 1 kHz. La resolution spatiale et temporelle du système est suffisante pour résoudre les modes propres de flexion du PSL qui sont potentiellement dangereuses. Les forces magnétiques qui agissent sur le PSL proviennent de disruptions du courant du plasma, de l'action des bobines internes ou de l'action des bobines de contrôle de la position du plasma en combinaison avec l'effet du plasma lui-même. Ces effets peuvent être distingués clairement.

En opération, les charges maximales apparaissent au cours de disruptions, et excitent par impulsion des oscillations libres du PSL à ses fréquences propres. Les fréquences des oscillations se trouvent entre 10 Hz et 120 Hz. Les maxima spectraux mesurés correspondent en général à des modes propres d'anneaux idéaux. Les tests avec une excitation resonante ont revelé que le mode quadratique (n=4) est le plus dangereux pour l'opération des bobines-B. Les oscillations post-disruptives sont typiquement dominées par les modes avec n=3. Le rôle des supports verticaux du PSL et des ses ponts dans le developpement de certains modes a été démontré.

Les analyses modales avec la méthode des éléments finis (FE) sont en bon accord avec les fréquences et les formes propres mesurées. Un modèle discrétisé du PSL a été developpé par expansion modale de modes propres exportés de la simulation (FE). Les amplitudes de ces modes sont calculés à partir de données expérimentales de déformation. Ainsi, pour de courtes périodes de temps et des oscillations du PSL à amplitude constante, le modèle permet de calculer la déformation, la contrainte et la déflexion de chaque élément du modèle FE. Pour les vibrations fortement attenuées après une disruption, des déviations non-négligeables apparaissent. Pour cette raison, une approche plus simple mais plus conservative a été utilisée afin de calculer les contraintes aux points critiques du PSL.

Par accumulation linéaire du dommage, l'état d'endommagement actuel du PSL a été estimé négligeable. Les valeurs de contraintes equivalentes et les nombres de cycles ont été determinés sur la base d'un collectif de charge représentatif en utilisant un algorithme de comptage à deux paramètres. Les déformations mesurées pendant l'excitation resonante du PSL utilisant les bobines-B ont été extrapolées vers des courants des bobines plus élevés. Il se trouve qu'un courant de 300 A, donc 30% de la valeur maximale du dimensionnement éléctrique des bobines, peut causer des déformations qui dépassent ceux des disruptions les plus fortes. Ces résultats ont permis de construire un deuxième modèle d'accumulation du dommage et de définir les limites tolérables de fonctionnement des bobines internes en termes de courant maximal et fréquences critiques.

Contents

1 Introduction

1.1 Nuclear Fusion

The term nuclear fusion generally refers to the reaction of two atomic nuclei which combine to form one product nucleus. The energy release of this reaction depends on the binding energy of the reactants. Iron has, together with nickel, the highest binding energy per nucleon of all elements, so fusion reactions of elements lighter than iron tend to release energy, and fusion reactions of heavier elements usually consume energy [1, 2]. Conversely, fission reactions of heavy nuclei release energy, which forms the basis of nuclear fission energy.

Fusion is the energy source of the stars. On earth, fusion has been practically used so far only in an uncontrolled manner as a booster in thermonuclear explosive devices, so-called hydrogen bombs. The controlled, peaceful, and safe use of nuclear fusion as an energy source has been investigated on an ever growing laboratory scale since the 1950s. These efforts are now culminating in the international project ITER[1], which is an experimental device currently being built in France. ITER will be the first fusion device large enough to deliver more thermal energy from fusion reactions than it consumes for plasma heating. Naturally, its success is of crucial importance for the future of fusion energy research.

To allow fusion reactions the repulsive force of the nuclei, resulting from their electric charge and known as the Coulomb barrier, needs to be overcome. In reality, the necessary energies are lower than expected from classical theory, owing to the effect of quantum-mechanical tunnelling. Nevertheless, the energy of the particles, i.e. their temperature, needs to be very high. Under the conditions in question, the fusion fuel and the reaction products are in the state of an ionised plasma. There are two principally different methods for confinement of this plasma: Inertial and magnetic confinement. Inertial confinement methods make use of the inertia of the fuel to generate extremely high pressures. Usually, the outer layer of a frozen fuel pellet is abruptly ablated using e.g. laser beams, and a pressure shock-wave develops which generates fusion relevant temperatures and pressures in the pellet core. The fusion reaction, generating additional heat, starts in the centre and drives a reaction wavefront outwards. The second method uses magnetic fields to confine the fusion plasma, making use of the fact that the electrically charged plasma particles are confined to magnetic field lines. In the plane normal to the field line, they gyrate around the field lines in a characteristic distance (the Larmor radius), which depends on their kinetic energy and the field strength. The particles also have a net velocity along the field line. The pressure values attained in inertial fusion devices are considerably higher than with magnetic confinement while the temperatures are lower.

Two different approaches of magnetic confinement fusion are particularly successful on the laboratory scale and appear promising for the commercial production of electricity: The stellarator and the tokamak. Both types use torus-shaped plasmas. The most noticeable difference between these two approaches is that the tokamak magnetic configuration is toroidally symmetric, which is not the case for

[1] Originally an acronym for International Thermonuclear Experimental Reactor which was abandoned due to negative connotations, also "(the) way" in latin.

a stellarator. This makes the tokamak comparatively simple to analyse and design, which is one of the reasons for its success in the past decades. ITER, as well as ASDEX Upgrade[2], the experiment on which the present work has been carried out are of the tokamak type. The disadvantage of complexity of the stellarator concept is compensated more and more by progresses in the field of supercomputing.

Compared to the development of fission power, where physical principles allow the building of small and rather inexpensive experimental reactors and plant prototypes, fusion research suffers from a fundamental handicap. The plasma confinement capabilities and the performance of e.g. a tokamak device depend on the ratio of the plasma surface, where energy is lost, to the plasma volume, where heat is generated by the fusion reactions. This means that there is a critical size below which no net energy output can be generated. ITER, being an international, multi-billion Euro effort and designed to produce a thermal power of 500 MW will be slightly bigger than this size. For comparison, EBR[3] I in Arco, Idaho supplied enough electricity for just four (conventional) light bulbs in an early test in 1951. The first reactors that actually fed electricity into the grid like the Russian AM-1[4] in Obninsk and the British power plant in Calder Hall[5] were projects realised by the research and energy authorities of single countries. ITER is the first fusion experiment design to be able to demonstrate self-sustained heating by α-particles, an important feature of a fusion power plant. The first plasma discharge is scheduled[6] for 2020. Data gathered from this test reactor will then be used to finalise plans for a demonstration power reactor, the so-called DEMO project. DEMO is anticipated to be the final step before commercialisation of fusion power.

Equation (1) presents the reaction of two particular hydrogen nuclei, deuterium and tritium, which fuse to helium and emit a highly energetic neutron.

$$ {}^{2}_{1}D + {}^{3}_{1}T \rightarrow {}^{4}_{2}He + n + 17.6\ MeV \tag{1} $$

According to momentum conservation and the masses of the particles, the produced alpha particle has an energy of 3.5 MeV (20%). This fraction of energy is available for plasma self-heating, while the neutron with 14.1 MeV energy (80%) leaves the plasma unaffected by the magnetic confinement due to its charge neutrality. Considering that chemical burning, e.g. of hydrogen and oxygen releases energy in the range of several eV per reaction only, the potential of fusion reactors to operate at low mass flows of fuel is obvious. The produced helium is a stable isotope and not radioactive. The neutron irradiation, occurring during operation of the facility must be shielded against, but it ceases as soon as the reaction ends when the plasma discharge is shut down. The structural materials of a fusion reactor are subject to this irradiation and are radioactively activated depending on their composition and the neutron flux. The design of structural materials with low-activation properties is therefore part of fusion energy research. One goal is to reduce the amount of (mostly low and medium level) nuclear waste to be disposed of after the decommissioning

[2]Axially Symmetric Divertor Experiment, AUG.
[3]Experimental Breeder Reactor, 1951: P_{th}=1.4 MW, P_{el}=200 kW.
[4]Atom Mirny (Russian for 'peaceful atom'), 1954: P_{th}=30 MW, P_{el}=5 MW.
[5]Calder Hall I, 1956: P_{el}=60 MW.
[6]As of December, 2012.

of a fusion power plant. Another is to minimise the time these components have to be stored before their radioactivity has decayed to hands-on level.

The reaction shown above is not the one which takes place in the sun. But it is presently the most favoured reaction for realising fusion energy on earth because it has a very high fusion cross-section and high energy gain at lower temperature compared to alternative reactions (like D-D or $^3_2$He-D). In a fusion reactor, it is therefore easier to bring a D-T-plasma to steady-state self-heating conditions (ignition) compared to a plasma composed of other reactants, which would require higher temperature and pressure. The requirements for ignition are described by the Lawson criterion [3]. It defines the lower limit of the product of temperature T, density n and energy confinement time τ_E:

$$nT\tau_E > 3 \cdot 10^{21} \ \frac{keV \cdot s}{m^3}. \tag{2}$$

The right-hand constant depends on the profiles of n and T, the value mentioned here assumes flat profiles for both variables. This relation allows us to define practical ignition conditions. For example, values of $n = 6.66 \cdot 10^{19}$ m^{-3}, $T = 13$ keV and $\tau_E = 3.5$ s meet the above requirements for ignition.

1.2 The Tokamak

The following description is based on the standard work "Tokamaks" by John Wesson [3] and the comprehensive lecture notes of the IPP Summer University for Plasma Physics [4]. The term tokamak is an acronym of Russian origin referring to the confinement of a hot plasma in a toroidal chamber using magnetic coils. A tokamak fusion device produces torus-shaped plasmas inside a vacuum vessel, using a solenoid in the centre of the torus for ohmic plasma heating. This central solenoid acts as the primary winding of a transformer of which the plasma is the secondary winding. When the electric current of this central solenoid is ramped up or down, i.e. when the magnetic flux in the torus centre varies, a toroidal current is induced in the plasma, thus heating it up. In the beginning of each plasma experiment, also called discharge, the vacuum vessel contains neutral gas at low pressure and density. The toroidal loop voltage due to the flux change in the transformer accelerates the few, statistically distributed ionised particles and free electrons. When the voltage is sufficiently high, the electrons collide with other gas particles and ionise them, successively increasing the toroidal current and ionising the entire gas volume inside the vessel. This method is also called ohmic heating (OH), because it relies on the resistance of the plasma. As the plasma resistance drops considerably at high temperatures, ohmic heating is less effective at high temperatures. Due to reasons of magnetohydrodynamic (MHD) stability, the plasma current cannot be increased infinitely[7], which limits the temperature attainable by ohmic heating. To reach higher temperatures, auxiliary heating is required, which uses either electromagnetic wave heating or high-energy neutral particles that are injected into the plasma.

[7]The plasma current is inversely proportional to the so-called safety factor q. For $q \to 0.5$ at the plasma edge, an MHD instability (an m=2, n=1 kink mode) occurs, leading to termination of the discharge [4].

1.2.1 Magnetic topology

In a tokamak, a torus shaped plasma is used, closing the field lines in order to reduce end losses which limit the performance of linear devices. The magnetic field configuration is toroidally symmetric. The toroidal field is usually much stronger than the other field components. Figure 1 shows a schematic view of the minimal coil configuration of a tokamak. The toroidal direction is indicated in the image. The

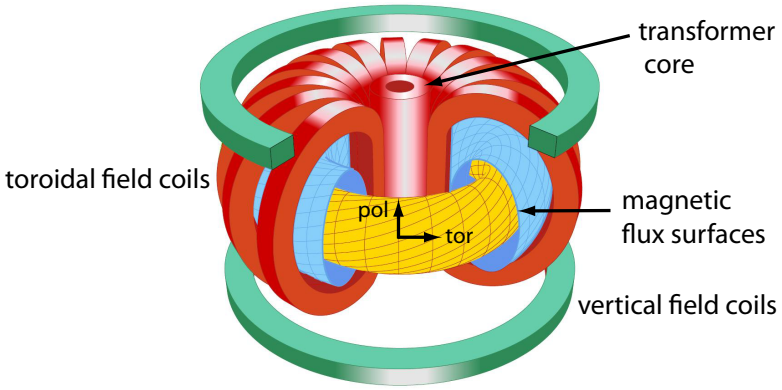

Figure 1: Schematic view of a tokamak configuration [4]

cross-sections normal to this axis are called poloidal. The (toroidal) field strength is higher at the inner side of the torus than at the outer side, approximately proportional to $1/R$. Therefore, the inboard and outboard sides are also referred to as high- and low-field side.

A simple toroidal field is insufficient for plasma confinement. The field lines around which the charged particles gyrate are bent around the central torus axis. Hence, a centripetal force acts on the particles, which is directed towards the outboard side. This results in a vertical drift of the particles perpendicular to both this force and the toroidal field, called curvature drift. Thereby, electrons and ions are separated, due to their opposite electric charge. In addition to that, the Larmor radius of a particle at the low-field side is larger than on the high-field side, which also causes a net particle movement. In analogy to the curvature drift, the associated vertical drift (∇B-drift) also separates the plasma particles of opposite charge. The resulting vertical electric field gives rise to an $E \times B$-drift producing radial particle losses.

To avoid these effects, a poloidal field can be applied, twisting the field lines, as shown in figure 1. This ensures a continuous redistribution of the plasma particles to regions of different field strength and the drifts are avoided. In a tokamak, the toroidal plasma current creates the poloidal field. The poloidal field strength is of the order of 10% of the toroidal field strength. In a stellarator, the twist of the magnetic field lines is generated without plasma current by external coils. As illustrated in figure 1, the surfaces of constant magnetic flux are nested toroids. As a result of its internal pressure, the plasma tends to expand radially. Stabilisation is provided by a vertical field created by poloidal field (PF) coils.

It has been shown [5] that plasma shapes with an elongation in the vertical direction are beneficial in terms of maximum pressure and confinement. The vertical field systems of real tokamaks are composed of several coils to enable flexible

plasma shaping. The outer boundary of the plasma is defined either by a material limiter in the vessel, or by a modification of the magnetic topology with vertical field coils which generate the so-called x-point[8] configuration. A magnetic separatrix, separating the closed, confined plasma from the open field lines is created in this configuration. There are dedicated areas where the 'first' open field lines, i.e. those next to the central, confined region reach the walls (see also figure 3b). These target plates and the surrounding volume are called the divertor, as it serves as a heat and particle exhaust of the plasma. Particles following the field lines are neutralised in the low temperatures in the divertor and are evacuated by vacuum pumps. The plasma pressure is (in most cases) constant along field lines. As the plasma density in this region is higher than at the separatrix closer to the plasma centre, the temperature in the divertor region is correspondingly lower. This is of course beneficial to limit thermal damage and erosion of the target plates. Configurations with an x-point on top and bottom of the plasma are called double-null, those with only one are called single-null configurations.

The length of a plasma discharge is practically limited by the maximum flux change of the central transformer. In the past, plasma discharges of tokamaks often were only several micro- or milliseconds long. The loud noise resembling a gunshot that accompanied each experiment led to the slang expression 'shot' for plasma discharge. Today, discharges are usually much longer and the characteristic noise has vanished, but the term shot is still widely used.

The force balance of the internal plasma pressure and the magnetic forces exerted by the coils in the toroidal reference system is described by the so-called Grad-Shafranov equation. It is used for reconstruction of the magnetic configuration of a discharge based on numerous measurements.

Apart from shaping issues, vertical field coils are also used for plasma position control. Elongated plasmas, which can be considered as being stretched by coils above and below them, are inherently unstable in the vertical direction. Their position needs to be stabilised actively, i.e. with a feed-back control system with the real-time plasma position as input variable that actuates at least one pair of vertical field coils. In AUG, this instability is damped by the so-called Passive Stabilising Loop (PSL), which produces a negative feedback on vertical plasma movements.

1.2.2 Mechanical impacts on the machine

Induced currents constantly interact with the magnetic field and generate forces on the structural components of a tokamak. A so-called major disruption is a violent event where the plasma current collapses and the plasma confinement is lost. During disruptions, the mechanical load on the machine is particularly high. Disruptions are non-equilibrium and non-linear processes and subject of on-going research. Their physical causes are only partly understood. A frequent cause for disruptions is e.g. heat loss by excessive radiation due to a sudden increase of plasma impurity concentration. Disruptions also occur when a critical density limit is reached [6], or if the plasma position control fails and the plasma comes in contact with the vessel wall. The causes of these events are not of primary concern in this work. However, it

[8] X-*point* refers to two-dimensional representations. In three dimensions, this corresponds to a toroidal x-line.

is important to notice that phenomenologically, different consecutive characteristic phases of disruptions are distinguished [7]. During disruptions, cooling of the plasma edge region often finally leads to an MHD instability and the sudden loss of thermal energy. This phase is called the thermal quench and has a typical length of the order of 1 ms. As a consequence of the temperature drop, the electrical resistance suddenly rises, and the current collapses. This final phase of the disruption, called the current quench, has a typical length of around 10 ms. In the case of elongated plasmas, the position control is often lost during the current quench, leading to a vertical displacement event (VDE). The fast displacement of the plasma (current) column induces strong electric currents in its electrically conducting surroundings. The current quench itself also induces halo currents in the structures close to the plasma. Interacting with the external magnetic field, these currents result in high mechanical loads ($j \times B$-forces) on the entire device. The vessel supports, its inner components and the magnetic coil supports in particular are highly stressed.

1.3 Motivation and structure of the present work

A set of 16 internal magnetic coils for the control of MHD instabilities, the so-called B-coils, was recently installed in ASDEX Upgrade. These are mounted on the Passive Stabilising Loop (PSL), to which they transmit forces that might lead to resonant oscillations. As shown in figure 2, the PSL is a structure that is highly prone to vibrations: It is composed of two solid, slender copper rings with a diameter of 4 m and has a total weight of 8 tons. Both the B-coils and the PSL are described in detail in the following chapter. The state of knowledge of the mechanical properties of the PSL (prior to this work) is mostly[9] based on its original, static dimensioning.

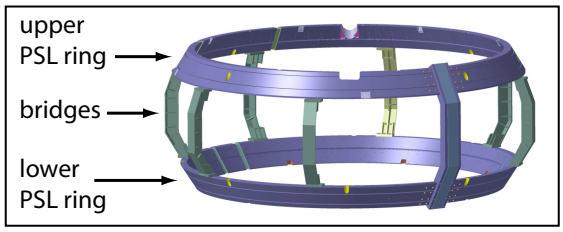

Figure 2: The Passive Stabilising Loop of ASDEX Upgrade (CAD representation)

The two principle aims of this work are to build a measurement system for the in-service deformation of the PSL and to assess its strength and fatigue limits in view of the novel loading condition applied by the B-coils as well as the loads which originate from disruptions. The second point necessitates a profound understanding of the oscillatory behaviour of the mechanical system. This understanding is acquired through an appropriate analysis of the experimental data, measured with the system to be built. For the measurement of the PSL deformation, optical strain sensing was chosen for its insensitivity to the strong electromagnetic disturbances inside AUG. If these sensors can successfully be integrated into the tokamak environment, which has not been done before, this sensing technique would be qualified for magnetic confinement fusion experiments.

The second chapter presents the experimental environment consisting of the ASDEX Upgrade tokamak and the PSL mechanical system and recalls fundamental concepts of oscillation theory. Additionally, less common calculation methods for

[9]Additionally, a finite element modal analysis was carried out with a PSL model including an internal coil design that was not realised. This model was adapted and is used in chapter 4.2.

natural frequencies of rings based on mechanical shell theory are introduced. The third chapter contains the description of the design, the installation and the commissioning of the sensing system. It also includes the qualification for the nuclear environment of the sensing components to be installed inside the vessel. In the fourth chapter, apart from the PSL oscillation measurements, results of calculations and numerical simulations are shown. The fifth chapter contains the comparison of these results and a detailed interpretation of the measurements. A lifetime estimation method of the PSL is developed and the operational limits of the internal coils are identified.

2 Experimental environment and theory

2.1 The ASDEX Upgrade device (AUG)

ASDEX Upgrade (AUG) is a large experiment aimed to investigate the physics basis of nuclear fusion. It is the successor to ASDEX (**A**xially **S**ymmetric **D**ivertor **Ex**periment), which was successfully operated in the 1980's, and which has delivered important results in the field of tokamak fusion research. These include milestones such as pioneering the axially symmetric divertor configuration [8] and the discovery of a high energy confinement regime named H-mode [9]. Despite its abstinence from radioactive tritium fuel, AUG has been designed to operate at fusion power plant relevant plasma conditions. This implies, among other objectives, the generation of magnetic confinement with a poloidal divertor configuration by coils which are located mainly outside of the toroidal field magnet (TF) system [10, 11]. This means that neither the TF coils nor the poloidal field coils (PF) need internal electrical joints, because neither have to be split during assembly. Figure 3 shows an artist's impression and a cross-sectional cut of the machine, giving an idea of the overall geometry. Exploiting the magnetic field configuration calls for approaching the

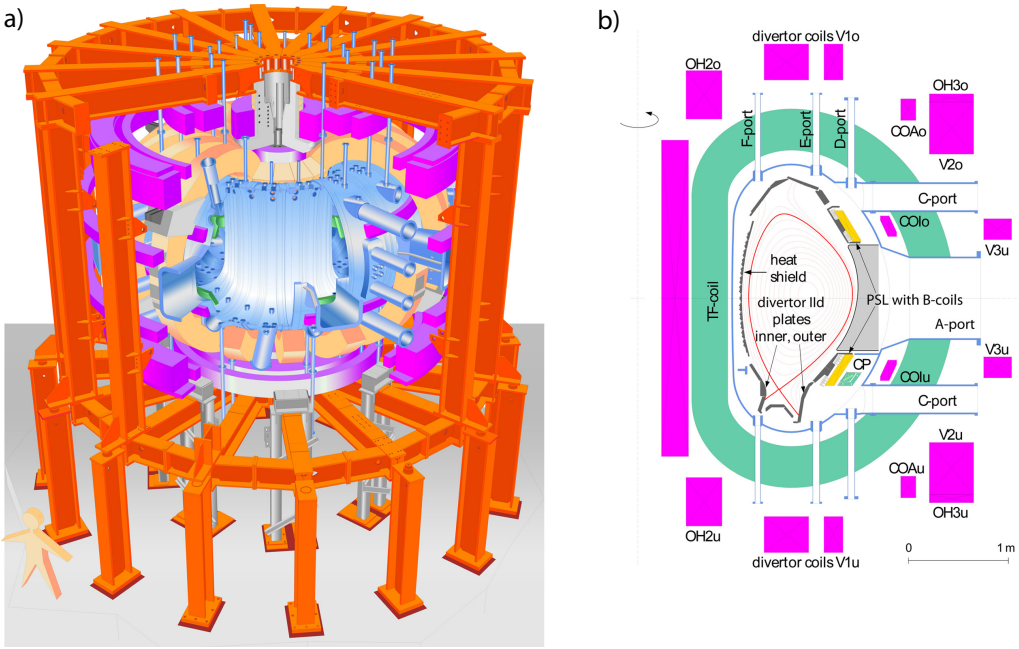

Figure 3: Perspective view (a) and poloidal cross section (b) of ASDEX Upgrade

plasma boundary as near as possible to the inner leg of the TF-magnet. Thanks to the D-shape of these coils, the mechanical stress is constant along the coil legs, efficiently using the material strength. This form provides enough space for the vacuum vessel to study single null (sketched in fig. 3b) and double null plasma configurations and to accommodate plasma diagnostics[10] hardware inside the vessel.

The position of the plasma column needs to be stabilised in vertical and horizontal direction. An elongated plasma is particularly unstable in the direction of its elongation, as outlined in section 1.2. The *ideal* time constant of vertical instability

[10]Measurement systems at fusion devices are called (plasma) diagnostics.

is the time needed for a small perturbation to grow by the factor of e (Euler's number). It is determined by the plasma mass and the external forces due to the vertical field coils, without considering induction in passive components. In the present case, the ideal time constant amounts to several microseconds only [12], far too small for active stabilisation by a position control system, at least with tolerable technical effort and energy efficiency. Electric conductors close to the plasma help slow its movements, because the induced eddy currents, according to Lenz's law, oppose its motion. The closer these conducting structures are located, the more pronounced is the associated damping, due to increased inductive coupling. Owing to the spaciousness of the vacuum vessel of AUG, the time constant would be of the order of the ideal case mentioned above, if no further measures were taken [12]. Therefore, the vertical stabilisation system is based on passive and active components: The so-called **P**assive **S**tabilizing **L**oop (PSL, fig. 3b), which will be described in detail in section 2.1.2, damps plasma movements, increasing the vertical instability time constant to the order of tens of milliseconds [13]. The active, inner control coils (COIo, COIu, fig. 3b) located between vessel and TF coils are feedback controlled and realize the position control on longer time scales. A detailed description of the plasma control in AUG, including the position control system can be found in [14]. Some general technical data of AUG are given in table 1. The numerous machine

General parameters	
overall height	9 m
overall diameter	10 m
total weight	800 t
height vacuum vessel	2.4 m
vacuum vessel volume	32 m^3
first wall material	tungsten coated carbon
vacuum vessel mass	52 t

Operating parameters	
plasma major radius	1.65 m
plasma minor radius	0.8 m (vertical)/ 0.5 m (horizontal)
plasma volume	14 m^3
plasma current I_p	$<$ 1.6 MA (single null)
max. toroidal field strength	$<$ 4 T
max. $B_t * I_p$	4.5 MA*T
total heating power	33 MW
energy supply capacity	2.6 GJ
pulse length	$<$ 10 s

Table 1: Specifications of ASDEX Upgrade

performance limits given here are the outcome of engineering constraints and do not represent those set by plasma physics. They arise from mechanical stressing, thermal heat capacities of components and energy and power limitations of the energy supply of the experiment [15]. Which constraints are performance limiting depends on the experimental scenario. For example, the B_t-limit of 4 T results from the

centering forces on the TF coils and the maximal allowed stresses to avoid internal delamination.

AUG has started operation in 1990 and has been modified repeatedly, mostly regarding in-vessel-components, plasma heating and diagnostics. In addition, the plasma shaping capabilities have been improved by adding independent power supplies for the OH2 coils (see figure 3b for designations of vertical coils).

2.1.1 Mechanical structure

The AUG machine rests on a steel framework of I-beams (red structure in figure 3a). All poloidal field coils (magenta) except the small inner control coils are directly attached to this structure. The toroidal field magnets (green) are fixed inside a cast iron hull, the so-called turnover structure (not shown), that rests on the bottom platform of the framework. As visible in figure 4a, the vacuum vessel is composed of eight similar octants each of which consists of two segments that are welded together [16]. These sixteen segments, or sectors, are numbered and also serve as an orientation for referencing positions relative to the vessel. The octants are connected with thin metal bellows to provide vacuum tightness and high electrical resistance, which is necessary to allow ohmic plasma heating: If the vessel resistivity was too low, the central transformer coil would induce currents in the vessel instead of the plasma. Owing to the low stiffness of these bellows, forces across the octant gaps are transmitted via shear bolts. Thus, the vacuum vessel forms a self-supporting structure. It is suspended from the turnover structure on eight tension rods of 30 mm

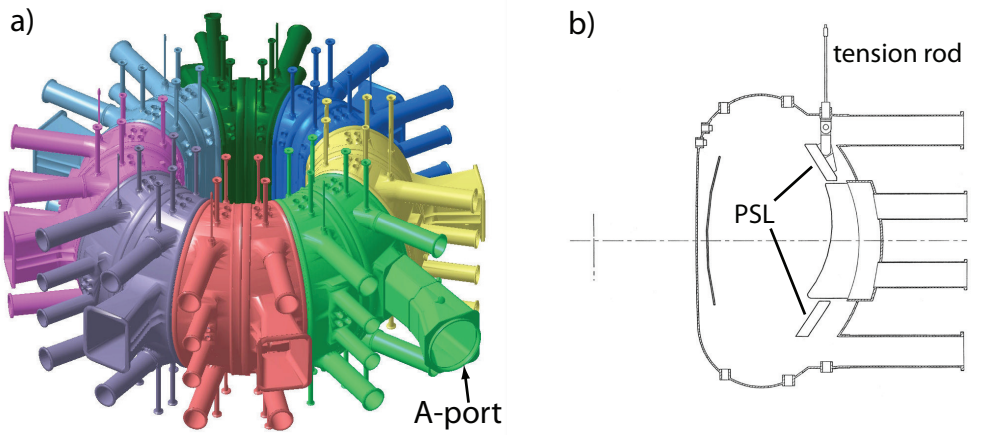

Figure 4: Vacuum vessel with ports: global view (a) and poloidal cross-section (b)

diameter. Via two of its A-ports (fig. 4a), which are the largest access openings, it is radially connected to the external framework. Before operation, conditioning of the vessel and its internal components is carried out by baking at 150℃. The bearings of the two A-ports are designed to permit the corresponding thermal expansion. One of them is equipped with an adjustment mechanism to maintain the vessel's upright and centered position. The tension rods are screwed into vacuum-tight, welded tubular casings at the vessel top and continued inside the vessel to support the PSL, as seen in figure 4b.

2.1.2 The Passive Stabilizing Loop (PSL)

The Passive Stabilising Loop is a large, water-cooled, cage-like structure inside the vacuum vessel. It is composed of two solid horizontal copper rings which are connected by seven toroidally equidistant and insulated stainless steel support bridges and one current-carrying bridge out of copper chrome zirconium (CuCrZr). Detailed information about the used materials is included in the appendix. Figure 5 presents the geometry of the PSL, its specifications are listed in table 2. The ratio of the two principal area moments of inertia I_2/I_1 is about 25 for both PSL rings. Assembling

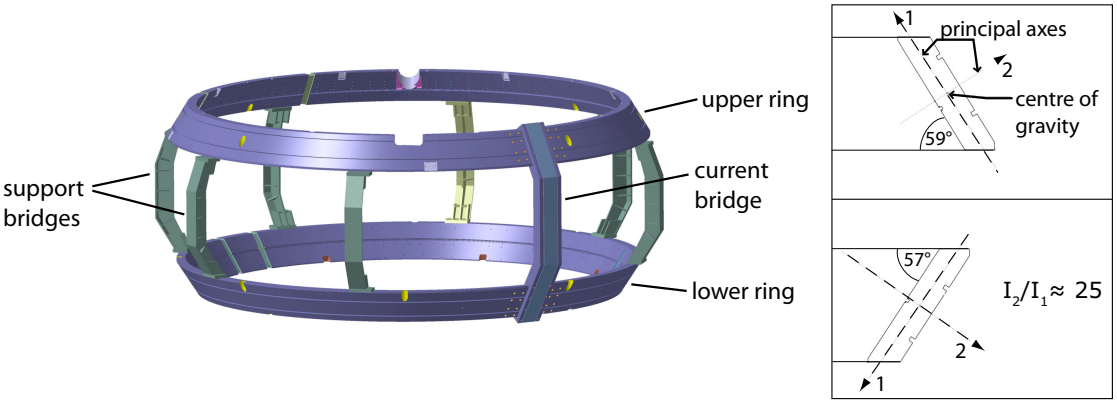

Figure 5: PSL 3D-CAD representation (a) and cross sections (b)

item	value
radius upper ring	1966 to 2233 mm
radius lower ring	1877 to 2158 mm
overall height	1748 mm
total weight	8 t
ring material	copper
current bridge material	CuCrZr
support bridge material	stainless steel

Table 2: PSL main specifications

required that each ring is composed of two joined half-ring elements which have nearly equal size [17, 18]. Figure 6 shows a photograph of one of the PSL halves before its installation in the AUG vessel. Note the current bridge on the right-hand side of the image.

The PSL decelerates plasma movements thanks to its proximity to the plasma and its low electrical resistance. The electric interconnection of the PSL rings is outlined in figure 7. The current bridge has an up-down symmetry and is composed of two insulated coaxial segments. As pointed out by figure 8, the right-hand ends of both rings are bolted to the inner conductor whereas both left-hand ends are attached to the outer conductor of the current bridge. Therefore, currents in the upper and the lower ring always flow in opposite direction, effectively retarding the vertical plasma movement without consuming flux of the central transformer (OH, fig. 3b). As the plasma column starts to move vertically, it is pushed and pulled

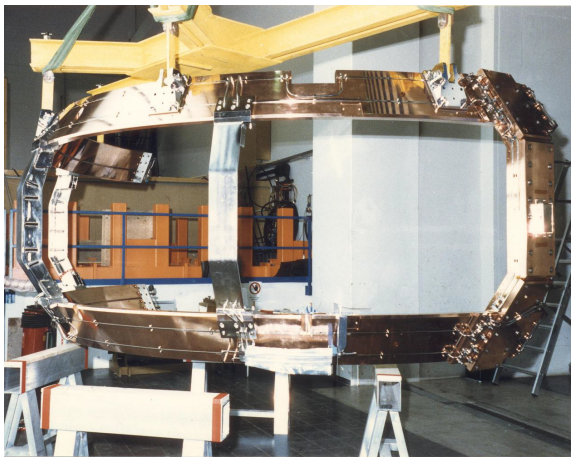

Figure 6: One half of the PSL structure before installation

from both sides towards its initial position. The coaxial design of the current bridge minimises plasma affecting magnetic strayfields and the Lorentz forces on the two conductors compensate to a large extent. During plasma break-down, the full loop voltage drops across the current bridge, implying the risk of arcing. For that reason, two bridging resistors with an effective resistance of 250 $\mu\Omega$ each were mounted on the current bridge which directly connect its two conductors. This compares to a total resistance of 23 $\mu\Omega$ for a complete turn of the PSL (bridge and both rings). Theoretically, the current reversing efficiency of the bridge is weakened by these resistors, but this effect is neglected in the following. The seven support bridges are electrically insulated[11] from the PSL and are designed as a stainless steel welded construction.

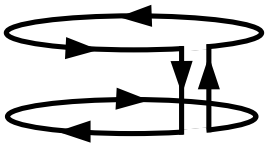

Figure 7: Electric interconnection of the PSL

Like the suspension of the vacuum vessel, the support of the PSL allows unconstrained thermal expansion. The upper PSL ring is suspended on eight hinges and rotation about the vertical axis is blocked by four horizontal tie-rods per ring (not shown). These connect the vacuum vessel and the PSL rings and transmit tangential forces only. The general, cylindrical coordinate system of the ASDEX Upgrade

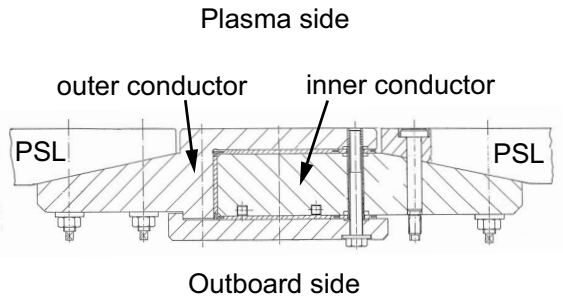

Figure 8: Sectional view of the current bridge at PSL-ring level

[11]The insulation is realised using a foil that is placed between the PSL surface and the attachment brackets of the support bridges. Even though the bolts securing the bridges penetrate the foil, the resulting electrical resistance is very high compared to the rest of the PSL and can be neglected.

machine is defined with a vertical z-axis and using the common plane of sectors one and sixteen of the vacuum vessel as zero for the toroidal angle. See figure 9 for the coordinate system definition and the positions and details of the vertical hinges. In the following and throughout this work, a PSL coordinate system is used, which is rotated about the vertical axis with respect to the machine coordinate system. The zero-point of its toroidal angle lies in the middle of the current bridge, which is more convenient for studying the PSL. Due to the 8 hinges the PSL is overdetermined in the vertical direction. However, the load distribution is monitored individually by strain gauges and homogenized with adjustable bearings. Therefore, the assembly is presumed to be free of prestresses.

The PSL, in particular the upper ring, has a number of geometric irregularities disturbing the toroidal symmetry of its mass and stiffness distribution [18]. The most notable are two opposing notches on the upper ring providing sightlines for plasma boundary diagnostics, the current bridge with different mechanical characteristics compared to the support bridges, and the connection of the PSL half-rings by bolted backplates. Table 3 lists the toroidal position of these items and the PSL bearings.

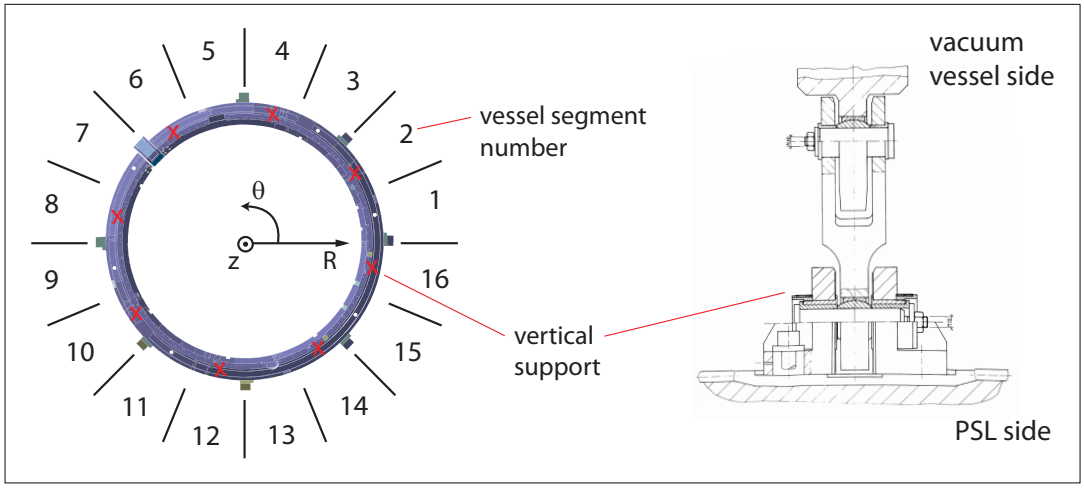

Figure 9: PSL top view (left) and vertical support details (right)

item	N	sector(s)	toroidal position, n ∈ N
vertical hinges	8	even	12.25°+n×45°
toroidal tie-rods	4+4	1,5,9,13	17.75°+n×90°
current bridge	1	6/7	135°
support bridges	7	2/3, 4/5,...	n×45°
notches upper ring	2	5, 13	102.25°, 282.25°
ring connection	1	15	331°

Table 3: Bearings and structural features of the PSL

The PSL is equipped with Rogowski-coils which permit measurement of the electric currents induced in both rings, which is of general importance for plasma stability control, but also useful for the calculation of Lorentz forces later in this work.

The dimensioning of the PSL suspension and the current bridge was governed by worst case plasma disruptions. The maximum plasma currents allowed in limiter, single null (one magnetic stagnation point) and double null configuration due to the above mentioned stress limits on the coils are 2, 1.6 and 1.2 MA respectively. The case of a 1.6 MA single-null plasma disrupting was identified as the most demanding in terms of the involved forces. The vertical and horizontal supports, the two rings, the bridges and different minor parts have been dimensioned for this case. Safety coefficients in terms of maximum allowed stresses and forces, determined by calculations and finite element computations refer to *static loading, exclusively* [19]. Neither structural oscillations nor fatigue phenomena have been taken into account.

2.1.3 The internal coil system

A recent major enhancement of AUG is a set of internal saddle-coils to produce magnetic perturbations in the plasma edge region on the low field side. These small perturbations of the magnetic configuration mitigate the so-called **E**dge **L**ocalized **M**odes (ELMs) [20, 21], even though the involved physics is presently not completely understood. ELMs are cyclic magnetohydrodynamic instabilities at the plasma edge, driven by high pressure gradients and current densities. They expel large bursts of the plasma energy (typically 1-15%) which could erode or even melt divertor and first wall materials in large devices like ITER [22]. This makes them a major concern for Tokamaks of fusion power plant (FPP) size.

The internal coil system is located at the low field side inside the vacuum vessel and consists of toroidal belts at three different poloidal positions. As shown in figure 10, each of these comprises 8 coils. The coils around the A-ports in the midplane, named A-coils, are still in the planning stage. The upper and lower coils, the B-coils, are mounted on the PSL and operational. They consist of five turns of a hollow copper conductor with central water cooling, embedded in resin and contained in a twofold, deep-drawn and laser welded Inconel sheet casing [23].

The B-coils are bolted to the PSL rings. Thus, the forces they experience due to the interaction of coil currents and magnetic fields are transmitted to the PSL. The largest forces are to be expected on the poloidal legs of the coils in normal direction to the PSL surface, as the coil current is directed perpendicular to the toroidal magnetic field there. Assuming a maximum current per coil of 1200 A and a toroidal field strength of 3.5 T, the maximal forces (on the five windings) in the poloidal leg amount to 21 kN per meter, or roughly 5.5 kN per leg of 0.26 m poloidal length. The coils are designed to be operated in alternating current, with peak frequencies of 1.2 kHz for the B-coils and 3 kHz for the A-coils. The accompanying harmonic excitation of their support structure, mainly the PSL rings, is one of the motives for carrying out the present work.

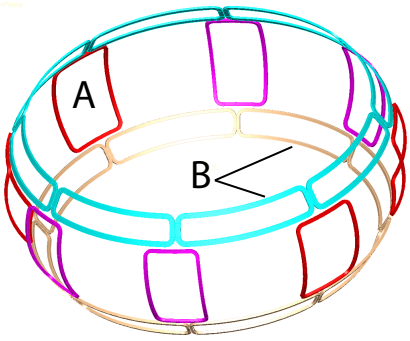

Figure 10: The complete set of 24 internal coils

Further future plans include the installation of copper wall elements between

the PSL rings, the so-called conducting wall for AUG [24], to enable control of the resistive wall mode, a plasma instability constraining advanced high performance plasma scenarios in tokamaks.

The present study is focussed on AUG, but is relevant also for other machines employing internal coils with alternating current and addressing the problem of resonances like DIII-D [25] and COMPASS-D [26] and most importantly ITER, which will also be equipped with internal coils for ELM control [27, 28]. The development, the experimental qualification and application of the optical strain measurement system in a Tokamak environment, which is a major part of this work, is of even greater universality.

2.1.4 Current status of the PSL studies

Prior to this work, the knowledge about the structural properties of the PSL relied mostly on the calculations and specifications from its design and dimensioning phase. The vertical supports of the vacuum vessel are equipped with conventional strain gauges, providing data of vertical vessel movements. The deformations of the PSL had never been measured so far, nor had calculations of its natural frequencies been part of the dimensioning.

In connection with the design of the A-coils, different finite element (FE) analyses were performed to determine their impact on the PSL, in case they were to be mounted on the two rings. This design was abandoned later, but a slightly modified version of the existing FE PSL model was used for the finite element modal analyses described in this work.

2.2 Oscillation theory

2.2.1 The single oscillator

In the theory of oscillations, mechanical models are commonly characterized by their number of degrees of freedom (DOF). The example of a single oscillator with one DOF is used here to introduce the concepts of free vibrations, linear damping and harmonic excitation response that also apply to more sophisticated systems, basically following Thomsen's introduction to oscillations [29]. Figure 11 shows the model of a mass capable of moving horizontally, attached to a spring and a damper element. Assuming linearity of the spring and damper characteristics, the equation

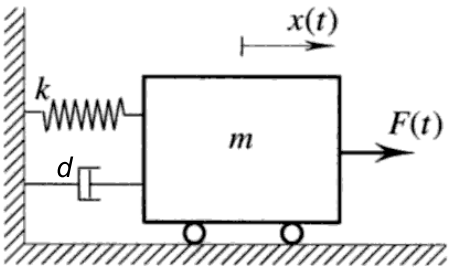

Figure 11: Model of a system with one DOF [29]

of motion can be written applying d'Alembert's principle:

$$m\ddot{x} + d\dot{x} + kx = F(t) \tag{3}$$

The equations of motion of many linear systems can be written in this form. For larger systems with n DOFs, the coefficients m, k and d, characterising the mass and stiffness distribution and the damping, are square matrices of order n. With known initial conditions $x(0)=x_0$ and $\dot{x}(0)=\dot{x}_0$, equation (3) has a unique solution. For undamped and free oscillations, the damping coefficient d and the external force $F(t)$ equal to zero and the solution is found with the ansatz $x(t)=Ae^{\lambda t}$, using the abbreviation $\omega_0=\sqrt{k/m}$.

$$m\ddot{x} + kx = 0 \;\Rightarrow\; (\lambda^2 + \omega_0^2)Ae^{\lambda t} = 0 \;\Rightarrow \lambda_{1/2} = \pm i\omega_0 \tag{4}$$

The general solution reads

$$x(t) = A_1 e^{i\omega_0 t} + A_2 e^{-i\omega_0 t} = B_1 \cos(\omega_0 t) + B_2 \sin(\omega_0 t) = C \sin(\omega_0 t - \varphi), \tag{5}$$

where the coefficients B_i and C are real and the A_i are complex. We see that the motion is a purely harmonic oscillation with amplitude C and phase angle φ, both determined by the initial conditions. As the spring constant k is always positive here, the solution is stable [30], and ω_0 is the natural frequency of the system without damping.

If we now assume a non-zero damping coefficient d, the solution

$$x(t) = Ae^{-\zeta\omega t}\sin(\tilde{\omega}t - \varphi), \quad \text{where } \zeta = \frac{d}{2\sqrt{mk}} \in (0,1) \text{ and } \tilde{\omega} = \omega_0\sqrt{1-\zeta^2} \tag{6}$$

is obtained in a similar way. The natural frequency of the damped oscillation $\tilde{\omega}$ is smaller than in the undamped case; it decreases with growing damping ratio ζ. An oscillatory system is called underdamped ($\zeta < 1$), critically damped ($\zeta = 1$) or overdamped ($\zeta > 1$). Critical damping refers to the smallest damping value where no oscillatory movements occur. Figure 12 shows the solution for initial values of $x(0)=1$ and $\dot{x}(0)=0$ and different values of ζ. Apart from the dimensionless parameter ζ, the so-called logarithmic decrement Λ is of great practical importance [30]. It describes the amplitude ratio of two consecutive cycles of a damped oscillation and is defined as

$$\Lambda = \ln\frac{x_k}{x_{k+1}} = \frac{2\pi\zeta}{\sqrt{1-\zeta^2}}, \tag{7}$$

thus providing the relation between the system's inherent damping and data which is easily accessible by measurements. For real structures, damping at least partially results from material damping. This is an internal energy dissipation mechanism generating heat by visco-elastic or plastic deformations at the crystallite level of the material (in the case of metallic structures).

In the case of harmonic external forcing $F(t)=F_0\sin(\Omega t)$, the solution is the superposition of the homogeneous solution ($F(t)=0$) just described and a particular solution of the form

$$x(t) = H\sin(\Omega t - \phi). \tag{8}$$

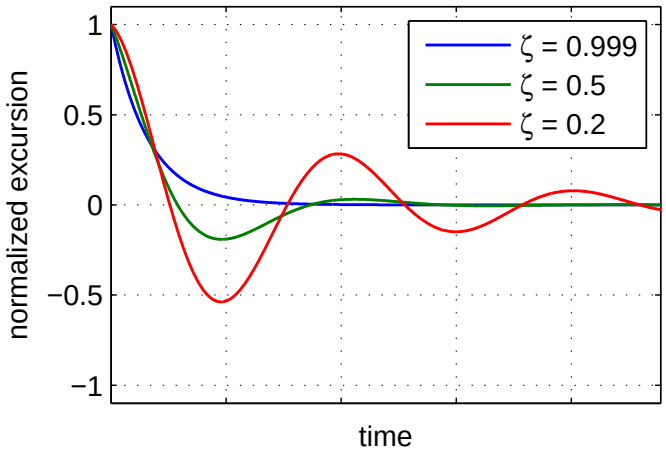

Figure 12: Oscillations with differing damping ratios

It is important to bear in mind that for continuous harmonic external forcing, the eigenoscillation of a system described by the homogeneous solution will disappear completely after a certain time, owing to damping. The system will then oscillate uniquely with the excitation frequency Ω, regardless of its eigenfrequencies. The amplitude and phase angle depend on k, m, d, and the amplitude and frequency of the external forcing F_0 and Ω. A mathematical proof of these dependencies shall not be given here, an exhaustive demonstration can be found for example in the work by Wittenburg [30]. Figure 13 shows a graphical representation of amplitude and phase as a function of the excitation frequency for different damping ratios. When

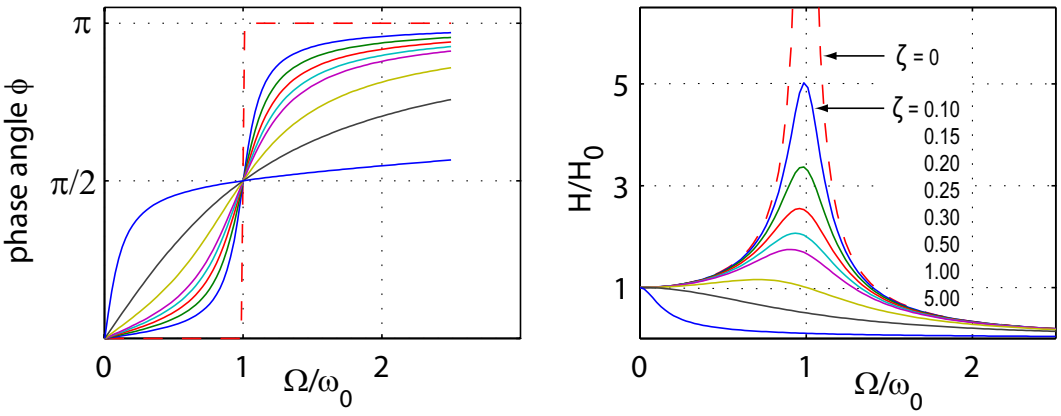

Figure 13: Phase (left) and ratio of amplitude H over static deflection H_0 (right) versus excitation frequency for various damping ratios

the excitation frequency is equal to the eigenfrequency of the oscillator, the phase angle is equal to $\frac{\pi}{2}$. For underdamped systems ($\zeta < 1$), the amplitude exhibits a maximum which is very pronounced for small damping ratios. This is called the resonance case. Note the dependency of the maximum amplitude *and* the peak

width[12] on the damping ratio.

Even for arbitrary forcing, it is possible to calculate the system response using the so-called Duhamel integral, and the solution becomes

$$x(t) = \int_0^t F(\tau) g(t-\tau) \mathrm{d}\tau, \text{ with } g(t) = \frac{1}{m\omega} \frac{e^{-\zeta\omega t}}{\sqrt{1-\zeta^2}} \sin(\tilde{\omega} t). \tag{9}$$

Again, the homogeneous solution must be added in the case of non-zero initial conditions.

Note that the solution for arbitrary forcing is in principle already covered by the harmonic solution. If the forcing function is decomposed into its harmonic constituents, the harmonic responses can be determined separately. The superposition of these yields the desired solution. Even though this requires in general an infinite number of harmonic constituents, it is an appealing option for forcing functions which are primarily of harmonic nature.

2.2.2 Systems with multiple degrees of freedom

If we move on to higher order linear systems with multiple degrees of freedom, the general equations of motion have a similar structure as in the 1 DOF case and read

$$\mathbf{M}\ddot{\mathbf{x}} + \mathbf{D}\dot{\mathbf{x}} + \mathbf{K}\mathbf{x} = \mathbf{f}(t) \tag{10}$$

in matrix notation. $\mathbf{M}$ is the mass matrix, $\mathbf{D}$ is the damping matrix and $\mathbf{K}$ is the stiffness matrix. The vectors $\mathbf{x}$, $\dot{\mathbf{x}}$ and $\ddot{\mathbf{x}}$ represent *generalized* coordinates and their respective time derivatives, whereas $\mathbf{f}$ represents the *generalized* forces. A method often suitable to obtain these equations is to use Lagrange's equations [31]. The oscillatory properties of a multi-DOF system are analogical to those of a single oscillator: In the undamped case without external forcing, the ansatz $\mathbf{x}(t)=\mathbf{A}\cos(\omega t)$ leads to the eigenvalue problem

$$(\mathbf{K} - \omega^2\mathbf{M})\mathbf{A} = \mathbf{0} \rightsquigarrow \ |\mathbf{K} - \omega^2\mathbf{M}| = 0. \tag{11}$$

The determinant yields a characteristic polynomial of degree n in ω_i^2, the ω_i being the *natural frequencies* of the undamped system. Each natural frequency has an associated eigenvector $\mathbf{A}_i$ determined by equation (11), also called the *mode shape* at frequency i. The n components of this eigenvector represent the relative amplitudes of the harmonic oscillations of the n DOF of the system at this frequency. These components can have different sign, but no phase difference (in time) between the oscillators.

2.2.3 Continuous media: Beam and ring

Real, continuous mechanical structures like the PSL of AUG possess in principle an infinite number of degrees of freedom. Many systems can be simplified to multi-DOF lumped systems. However, in the case of certain construction elements, classical

[12]The peak width can be described by the full width at half maximum (FWHM). Here, this corresponds to the width of the frequency interval at half the maximum value of H/H_0.

continuum mechanics offers possibilities to investigate the static and dynamic behaviour. This covers for instance beams, plates, membranes and shells, which have been subject to extensive theoretical investigation since the 18th century. A beam is a rod-like element with straight longitudinal axis, loaded perpendicularly to this axis [32], as shown in figure 14. A prevalent method to determine the equations of

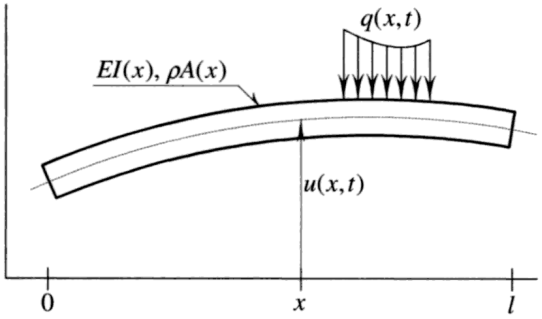

Figure 14: Beam element under distributed load [29]

motion is Hamiltons's principle, which applies to systems with an infinite number of DOFs. A different approach is used here. The force and moment balance of an infinitesimal beam element combined with Hooke's law lead to $M_z = EIu''$ and the equation of motion of the beam [29]:

$$\rho A(x)\ddot{u} + d\dot{u} + [EI(x)u'']'' = q(x,t). \tag{12}$$

The structure of this equation is similar to the cases with one (eq. (3)) and multiple degrees of freedom (eq. (10)). The four terms represent the inertia, damping, spring and external forces, from left to right. The deflection u depends on time and x, the spatial coordinate along the beam's centre axis. Primes denote derivatives with respect to x and dots those with respect to time. The cross-sectional area $A(x)$, the second area moment of inertia $I(x)$ and the external load per unit length $q(x)$ are often variable over the length of the beam. The mass density ρ as well as Young's modulus E are set constant, here. The variable u is the deflection along x, the deflection axis pointing downwards by convention in beam theory. If we now assume a constant cross-section and moment of inertia, we can write the equation of motion of the free, undamped oscillation of the beam as

$$\ddot{u} + \frac{EI}{\rho A}u'''' = 0. \tag{13}$$

The harmonic ansatz separating time and space dependency by Daniel Bernoulli $u(x,t)$=$U(x)(A\cos\omega t + B\sin\omega t)$, first mentioned in a correspondence with Leonhard Euler in the 18th century [33], leads to

$$(-\omega^2 U + \frac{EI}{\rho A}\frac{\partial^4 U}{\partial x^4})\ (A\cos\omega t + B\sin\omega t) = 0, \tag{14}$$

and thus finally to

$$\frac{\partial^4 U}{\partial x^4} - \beta^4 U = 0, \text{ with } \beta^4 = \omega^2\frac{\rho A}{EI} \tag{15}$$

an ordinary differential equation for U [30]. The solution is found inserting $U(x)$=$ae^{\lambda x}$ which leads to

$$\lambda^4 - \beta^4 = 0, \text{ with roots } \lambda_{1/2} = \pm\beta \text{ and } \lambda_{3/4} = \pm i\beta. \tag{16}$$

By superposition, we find the eigenform

$$U(x) = ae^{\beta x} + be^{-\beta x} + ce^{i\beta x} + de^{-i\beta x}, \tag{17}$$

which corresponds to

$$U(x) = a_1 \cosh \beta x + a_2 \sinh \beta x + a_3 \cos \beta x + a_4 \sin \beta x, \tag{18}$$

which is a solution to the eigenvalue problem of equation (15). The coefficients a_i are found by inserting the boundary conditions in equation (18). This results in a system of linear equations for a_i with coefficients that depend on β. Owing to the linear dependence of these equations for $\omega = \omega_k$, one of the a_i is set to a fixed value which allows to determine the other a_i. This leads to the characteristic, transcendental equation of the beam with roots β_k. For each of these β_k, an eigenfrequency ω_k and an eigenform $U_k(x)$ can be found by equations (15) and (18). Insertion into the ansatz yields the modal solutions

$$u_k(x,t) = U_k(x)(A_k \cos \omega_k t + B_k \sin \omega_k t), \tag{19}$$

and by superposition the general solution

$$u(x,t) = \sum_k U_k(x)(A_k \cos \omega_k t + B_k \sin \omega_k t). \tag{20}$$

The coefficients A_k and B_k are determined by the initial deflections $u(t$=$0)$ and the initial velocities $\dot{u}(t = 0)$. Equation (20), the general solution of the equation of motion of the beam, is the linear combination of the infinite number of its eigenmodes. This approach is called modal expansion. It is based upon the orthogonality property of U_k, which can be shown generally for eigenvectors [34]. Note that any multiple of an eigenform U_k is also an eigenform. Thus, the eigenvectors U_k alone do not contain information about real deflection amplitudes and are usually normalised.

In the calculation presented here, the cross-sections of the beam are assumed to remain perpendicular to the neutral axis, thereby neglecting shear deformation. This is known as the Euler-Bernoulli simplification. It holds satisfyingly for thin beams. Beam theory condenses the original three-dimensional problem to a structural model with one independent parameter only, which is in the present case the spatial coordinate x. All points of the beam at the same location in x are treated as a rigid sub-body of the beam [34]. A related approach can be used to describe the dynamic behaviour of other continua like membranes (planar body, normal loads, in-membrane tensile stresses only), plates (planar body, normal loads) and shells (curved surface body, normal and in-plane loads). For any of these, the thickness is considered small compared to the other surface dimensions. Many of their oscillatory properties appear as an extension of the beam by one spatial dimension. A special case of a circular cylindrical shell is the closed ring.

The following is a *very brief* essay about natural vibrations of rings outlining some basic concepts. Readers are directed to the given literature for a deeper insight. The work by Krapf [35] about circular rings on elastic supports as a model for belted tyres derives equations of motion and properties of oscillating rings. This work is recommended as a complement to this section, because some of the approaches used therein differ substantially from those presented here. Soedel [33] gives a concise overview of the historical development of plate and shell analysis. The set of equations developed in 1888 by A.E. Love [36] and therefore known under the euphonic name *Love's equations* describes the motion of shells due to external forcing in the general case, but neglecting shear deformation and rotary inertia. In the case of a ring with constant radius of curvature R (circular ring), and angular coordinate θ as shown in figure 15, Love's equations reduce to

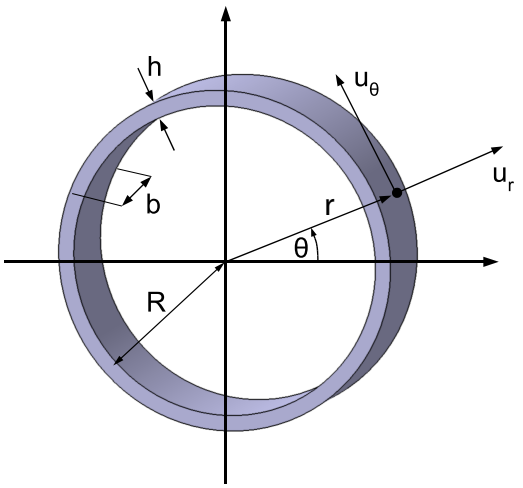

Figure 15: Closed, slender, circular ring

$$\frac{EI}{R^4}\left(\frac{\partial^2 u_\theta}{\partial\theta^2}-\frac{\partial^3 u_r}{\partial\theta^3}\right)+\frac{EA}{R^2}\left(\frac{\partial^2 u_\theta}{\partial\theta^2}+\frac{\partial u_r}{\partial\theta}\right)+q_\theta b=\rho A\frac{\partial^2 u_\theta}{\partial t^2} \tag{21}$$

and

$$\frac{EI}{R^4}\left(\frac{\partial^3 u_\theta}{\partial\theta^3}-\frac{\partial^4 u_r}{\partial\theta^4}\right)-\frac{EA}{R^2}\left(\frac{\partial u_\theta}{\partial\theta}+u_r\right)+q_r b=\rho A\frac{\partial^2 u_r}{\partial t^2}. \tag{22}$$

The external loads are denoted q_θ and q_r, A is the cross-sectional area and EI is the bending stiffness of the ring. For slender rings and in cases where forcing and inertia in the circumferential direction are negligible, equations (21) and (22) can be reduced to a single equation by eliminating u_θ [33]:

$$\frac{EI}{R^4}\left(\frac{\partial^4 u_r}{\partial\theta^4}+2\frac{\partial^2 u_r}{\partial\theta^2}+u_r\right)+\rho A\left(\frac{\partial^2 u_r}{\partial t^2}\right)=q_r b. \tag{23}$$

It describes the radial, in-plane deformation of the ring. In the more general case without this simplification, the natural modes and frequencies of the ring are obtained using equations (21) and (22) with a harmonic ansatz for both the eigenforms and the time dependency:

$$u_{rn}(\theta,t)=U_{rn}(\theta)e^{i\omega_n t}\quad\text{and}\quad u_{\theta n}(\theta,t)=U_{\theta n}(\theta)e^{i\omega_n t}, \tag{24}$$

$$U_{rn}(\theta) = A_n \cos(n\theta) \quad \text{and} \quad U_{\theta n}(\theta) = B_n \sin(n\theta). \tag{25}$$

Note that U_{r0} with mode number n=0 corresponds to a uniform radial excursion along the circumference of the ring (for all values of θ). U_{r1} with n=1 corresponds to a rigid body translation of the ring without any deformation and $U_{\theta 0}$ is the rigid-body rotation. For mode numbers $n \geq 2$, bending occurs. Substituting equations (24) and (25) in equations (21) and (22), we find an even polynomial of the order 4 for the natural frequencies ω_n:

$$\omega_n^4 - K_1\omega_n^2 + K_2 = 0. \tag{26}$$

The constants K_1 and K_2 depend on the mode number n, material constants and the geometry of the ring[13]. For each mode number n, four frequencies $\pm\omega_{n1}$ and $\pm\omega_{n2}$ are found according to

$$\omega_{n1,2}^2 = \frac{K_1}{2} \pm \sqrt{\frac{K_1^2}{4} - K_2} = \frac{K_1}{2}\left(1 \pm \sqrt{1 - \frac{4K_2}{K_1^2}}\right). \tag{27}$$

Figure 16 illustrates the evolution of $\omega_{n1,2}$ over the mode number for a sample set of geometry and material parameters. Usually, $\omega_{n1} << \omega_{n2}$. The ratio of the ampli-

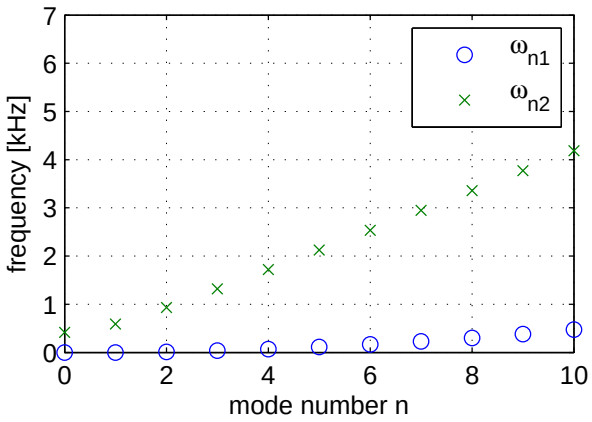

Figure 16: Frequencies $\omega_{n1,2}$ for a sample set of parameters (slender ring)

tudes $A_{n1,2}/B_{n1,2}$ of the formfunctions governing tangential and radial displacement can now be written as a function of the corresponding eigenfrequency $\omega_{n1,2}$.

$$\frac{A_{ni}}{B_{ni}} = \frac{\rho h\omega_{ni}^2 - \left(\frac{n^2}{R^2}\right)\left[\frac{D}{R^2} + K\right]}{\frac{n^2}{R^2}\left[\frac{Dn^2}{R^2} + K\right]} \tag{28}$$

This number describes the radial over the tangential displacement component of a given modal shape. All eigenmodes of an ideal ring have components in θ and r, the ratio of the amplitudes of these components are given by equation (28). Figure 17 depicts the amplitude ratios for the same set of parameters as used for figure 16. It can be shown that for small mode numbers, $\frac{A_{n1}}{B_{n1}} \approx -n$ and $\frac{A_{n2}}{B_{n2}} \approx 1/n$ [33]. Consider for example $n = 2$: At ω_{21}, the absolute radial amplitude is twice as high as the

[13]For the definitions of K, D and $K_{1/2}$, refer to the calculation in chapter 4.1 (p. 52).

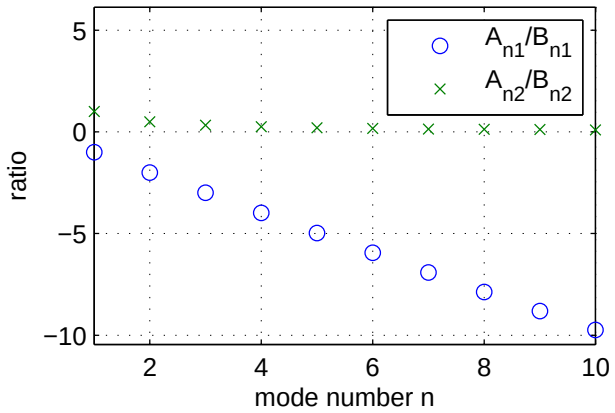

Figure 17: Amplitude ratios of the form functions

tangential amplitude and at ω_{22}, the tangential amplitude is twice as high as the radial amplitude. These ratios grow with increasing mode number, as illustrated in figure 17. This means that *natural oscillations at frequencies ω_{n1} are dominated by radial displacements whereas those at ω_{n2} are dominated by tangential displacements.*

However, this rule does not hold for n=0: The frequency ω_{01} is equal to zero because it represents the undeformed, rigid-body rotation of the ring to which no natural frequency is attributed. The non-zero frequency ω_{02} corresponds to the so-called breathing mode of figure 18a, even though the deflections are purely radial. An analogous inspection of the amplitude relations for n=1 leads to the conclusion that ω_{11} stands for the rigid-body translation of the ring (fig. 19a), whereas ω_{12} is a real natural mode with an approximate ratio of radial to tangential deflection amplitude $\frac{A_{12}}{B_{12}}$ of 1. The tangential deflection leads to one domain under compression and one domain under tension on the circumference of the ring. Due to these reasons, the frequencies ω_{01} and ω_{11} are always equal to zero, because no corresponding natural oscillations exists. This also reflects in the natural frequency calculation in section 4.1.

At a given mode number n, the ideal ring shows the same form characterised by n at the frequency ω_{n1} and again at the frequency ω_{n2}, which is usually higher. The deformation states differ only in the amplitude of the components along r and θ, A_{ni} and B_{ni}. Figures 18 and 19 illustrate modal shapes of the ideal ring with dominating tangential (fig. 18) and radial (fig. 19) deflection. For each frequency $\omega_{n1,2}$, two modal shapes coexist which are spatially orthogonal[14] , i.e. the nodes of one shape lie at the position of the antinodes of the other and vice versa [37]. Their angular orientation is determined by the direction of the forcing, as ideal rings show no preference in this respect. In contrast, real rings show such a preference. Slight deviations from axisymmetry cause what is known as frequency splitting [38, 39, 40]: The two mode shapes lock at a local mass or stiffness irregularity with their nodes and antinodes respectively, thereby determining the angular mode orientation. Two separate frequencies appear whose deviation depends on the magnitude of the irregularity. The modal shapes are distorted, but conserve their orthogonality.

Therefore, like in the case of the beam, natural ring modes are always orthog-

[14]Here, two modal shapes are orthogonal if they satisfy $\int_0^{2\pi}[U_i(\theta)\cdot U_j(\theta)]\,\mathrm{d}\theta = 0$, for $i \neq j$.

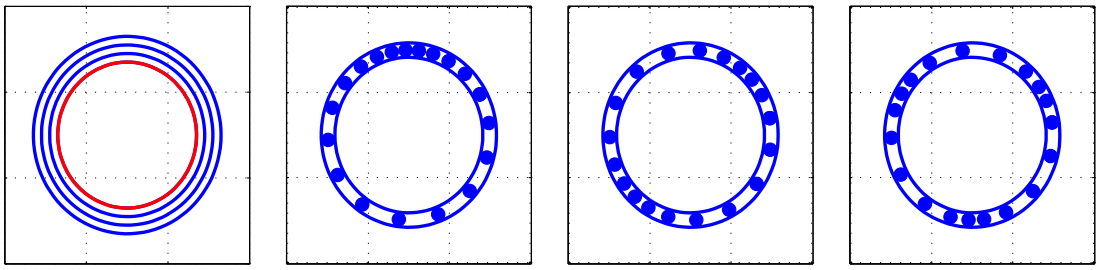

(a) $n_2 = 0$ (breathing mode) (b) $n_2 = 1$ (c) $n_2 = 2$ (d) $n_2 = 3$

Figure 18: Ring mode shapes for $n_2 \in [0, 3]$, mainly tangential excursions, one of two orientations shown

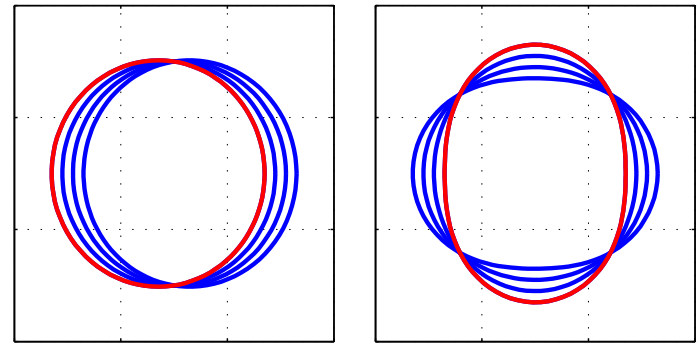

(a) $n_1 = 1$ (rigid body translation) (b) $n_1 = 2$ (elliptical)

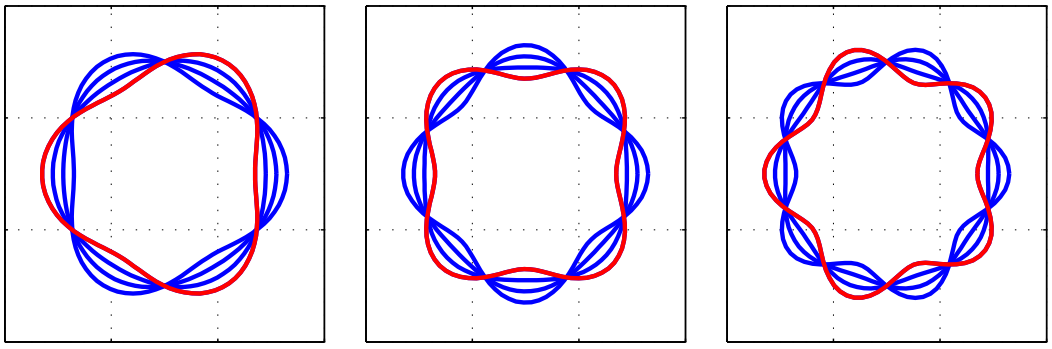

(c) $n_1 = 3$ (triangular) (d) $n_1 = 4$ (quadratic) (e) $n_1 = 5$ (etc.)

Figure 19: Ring mode shapes for $n_1 \in [1, 5]$, mainly radial excursions, one of two orientations shown

onal. Hence, an infinite number of natural modes forms a complete basis of the solution space of the ring's equations of motion (eq. (21)/(22)). *This means that any oscillation, due to any given external forcing can be expressed by a superposition of modal shapes.* Regarding free oscillations (with arbitrary initial conditions), the harmonic ansatz from equation (24) is suitable to describe the evolution in time. Free oscillations can therefore be represented by the superposition of their natural modes in terms of spatial (mode shapes) and temporal (harmonic ansatz functions)

dependency. In practise, an oscillatory system can often be represented with high accuracy using a limited number of its natural modes, e.g. if oscillations at higher frequencies are strongly damped.

The separation ansatz for the deflections u_r and u_θ (eq. (24) and (25)) is composed of functions in the form of standing waves with constant frequency. A different approach using travelling waves instead shall be mentioned briefly, here. The wave formulation of the radial excursion u_{rn} reads

$$u_{rn}(\theta, t) = a\cos(\theta \cdot n - c \cdot t) + b\cos(\theta \cdot n + c \cdot t) \tag{29}$$

in the present case. It consists of two transverse waves of sinusoidal shape travelling with the angular propagation velocity c. The left term with amplitude a is a wave travelling toward higher angles, the right term is a wave with amplitude b propagating in opposite direction. For a=b, this equation yields a standing wave in equivalence to equation (24):

$$u_{rn}(\theta, t) = a\cos(\theta \cdot n - c \cdot t) + a\cos(\theta \cdot n + c \cdot t) = 2a\cos(\theta \cdot n) \cdot \cos(c \cdot t) \tag{30}$$

If the amplitudes a and b are unequal, a travelling wave results, which is not explicitly apparent in the separation ansatz (eq. (24) and (25)) as used before. Nevertheless, the separation ansatz yields a fundamental basis of the solution space, which therefore also includes travelling waves.

It will be shown later how the above described phenomena of linear ring theory apply to the PSL structure with its two solid copper rings.

3 Experimental

For the experimental investigation of the PSL's dynamic behaviour, a suitable sensing system was developed. A tokamak experiment is a demanding environment for in-vessel hardware in terms of electromagnetic interference (EMI), high temperatures, and ionising radiation during operation. The internal components of the vacuum vessel, on the other hand, must not compromise plasma operation by releasing impurities, by generating stray magnetic fields due to their metallic components, by affecting the vacuum conditions in any way, etc.

This chapter describes the physical basics, the qualification, the design, the installation, and the commissioning of the PSL deformation measurement system. It consists of optical strain sensors based on so-called Fibre-Bragg-Gratings (FBGs). They measure the strain in the toroidal direction at various positions on the inner surface of both PSL rings. A fibre-optic sensing technique has been used for the first time inside an experimental fusion device, chosen amongst other things for its insensitivity to EM-fields, a significant advantage over conventional electric measurements. It has been recording data automatically since December 2010 during two consecutive experimental campaigns, and is implemented as a so-called standard diagnostic of ASDEX Upgrade under the name 'OSI' (optical sensing interrogator). Further specifications and detailed information about the structure of the stored data are included in the appendix.

3.1 Fibre-Bragg-Grating sensors

The term optical fibre refers to a flexible waveguide for light, where the transmission of the signal is attained by total internal reflection. When low internal damping is desired, silica glass (SiO_2) is a common base material. The fibres consist of at least two layers, and the signal-carrying fibre core has an index of refraction marginally higher than the one of its cladding. Multimode fibres and mono- or singlemode fibres are distinguished, referring to the electromagnetic modes that develop when light is transmitted [41]. This property is mostly determined by the core diameter and the refractive index deviation of core and coating. The core diameter of monomode fibres is typically several μm and lies in the range of few multiples of the minimal carried wavelength. Higher modes are effectively suppressed. Figure 20 shows a schematic cross-sectional view of a monomode fibre. These fibres offer advantages in

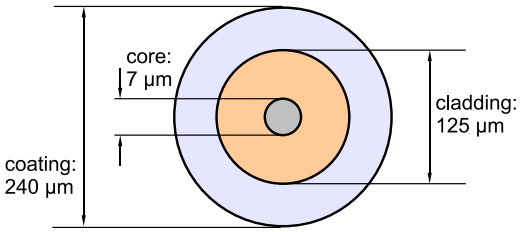

Figure 20: Single mode fibre cross section

long-range applications due to their low damping and minimal transit-time dispersion [42], which is of particular interest in the context of optical sensing. In addition to the two inner layers (core and cladding), industrial fibres usually have one or more

supplementary outer layers for mechanical and environmental protection. Polymeric materials such as polyimides are frequently used for this coating. The fibres used for the PSL deformation measurement are such monomode fibres with a recently developed polyimide coating with a particularly high chemical resistance and mechanical strength.

In recent years, so-called optical Fibre-Bragg-Grating sensors (FBG sensors) have become available [43]. FBGs are reflective Bragg gratings, engraved in the core of an optical fibre during manufacturing. They consist of well-defined domains with a different refractivity compared to the rest of the core. Primarily, gratings with equally-spaced domains of only two alternating refractivities are in use, but a multitude of other variants for different purposes exists [44]. The usual fabrication technique uses silica fibres whose refractivity is made photosensitive by prior doping with germanium atoms. A UV-laser with a reflectometric device is used to inscribe the gratings, which have a typical length of 8-15 mm, into the fibre core. This is done either before the cladding is applied or by removing the cladding at the position of interest and reapplying it afterwards. The latter option has the disadvantage of creating a mechanical weak point. Integrated production processes like the draw tower production are advantageous in this respect, as the production of the fibre and the FBGs, followed by the application of the protective coating are realised in one sequence. As the FBGs are engraved before the coating is applied, no mechanically weak points are generated due to coating removal. The name draw tower originates from the fact that the modular units realising the different steps during manufacture are arranged vertically. The fibre is drawn from the preform, a heated block of glass. FBGs produced using this technique are called draw tower gratings. Such draw tower sensing fibres have been chosen for the present application because of their superior mechanical strength and the possibility of fabricating fibres with numerous gratings (FBG arrays) at defined positions. This allows production of made-to-measure arrays and avoids any excess fibre length in the vacuum vessel.

Figure 21 illustrates the layout of an FBG and its reflective behaviour. When

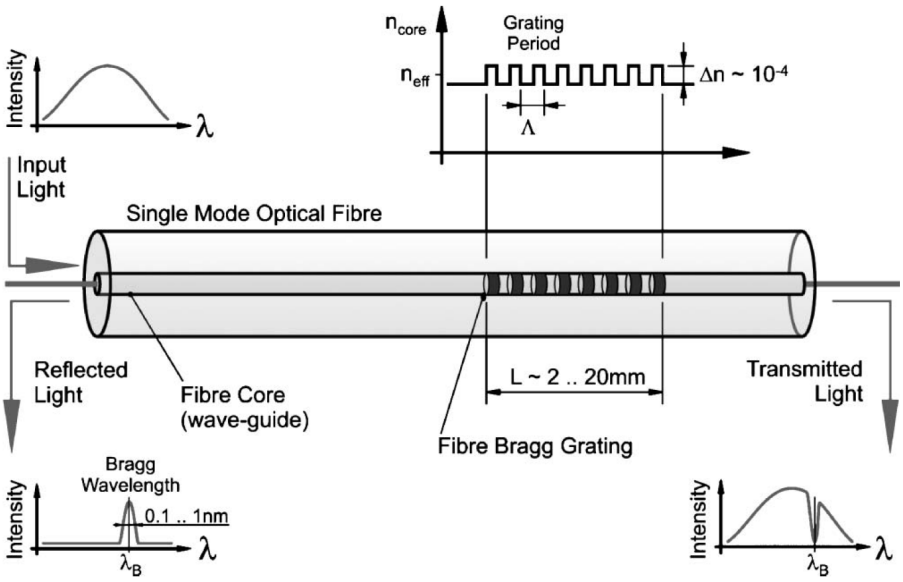

Figure 21: FBG physical working principle [45]

light is sent through it, partial reflection of the signal occurs at every interface of regions with different refractivity. The sensing principle depends on the knowledge of the distance between these regions under defined conditions (during calibration) and the measurement of the reflected signal which contains information about the momentary deformation state. For the aforementioned uniform FBGs, every grating has a characteristic wavelength at which the reflected signal shows an intensity maximum. This wavelength is determined by the known distance between two refractory regions of the undeformed grating (the grating constant Λ). This feature allows the use of several FBGs on a single fibre; a broadband light signal, travelling through a fibre with several FBGs of different grating constant, is partially reflected in such a way that the individual FBGs can be distinguished by the wavelength, or rather the wavelength range, of their reflection. This feature of FBG sensing enormously simplifies cabling. In addition, as the reflection is of interest, the connection of the fibre on one end is sufficient for sensor read-out. Connecting both ends leads to redundancy in the sense that all sensors are still functional even if the fibre is interrupted at one position. The input signal is usually provided by a combined measurement unit which also analyses the reflection and determines the peaks' wavelengths, called FBG interrogator.

The strain of the fibre at the position of the grating determines the reflected wavelength according to equation (31). It formulates the Bragg condition of constructive interference introducing the effective refractivity of the grating n_e. This quantity is the average of the minimum and maximum refractive index of the grating, n_0 and n_1 (see also figure 21). The wavelength of the reflected light λ_B is proportional to the grating constant Λ.

$$\lambda_B = (n_0 + n_1)\ \Lambda = 2n_e\Lambda \tag{31}$$

On one hand, this allows temperature measurements if the grating is attached to a force-free carrier material with known thermal expansion coefficient. On the other hand, mechanical strain can be measured if the grating is bonded to a substrate under deformation. For the latter application, temperature compensation must be provided by separate means to uncouple strain due to thermal expansion and strain due to loading. Equation (31) explicitly provides a wavelength-shift to strain relation, but the refractivities also depend on the temperature and the deformation state of the fibre. Equation (32) accounts for these effects and the relation reads

$$\Delta\lambda = 2n_e\Lambda\left(\left[1 - \frac{n_e^2}{2}[P_{12} - \nu(P_{11} + P_{12})]\right]\epsilon + \left[\alpha + \frac{1}{n_e}\frac{\mathrm{d}n_e}{\mathrm{d}T}\right]\Delta T\right), \tag{32}$$

with piezo coefficients[15] P_{ij} and the Poisson ratio[16] of the material ν [46]. Further influences to consider are the elastic deformation of the bonding and the fibre itself. As these are not easily accessible, industrial FBG-sensors are usually calibrated under defined conditions and average proportionality constants are defined. For

[15]The coefficients P_{ij} describe the relation of material stress and refractivity in the context of photoelastic effects.

[16]Supposing an isotropic material under uniaxial tension/compression, the Poisson ratio is the inverse ratio of transverse to axial strain: $\nu = -d\epsilon_t/d\epsilon_{ax}$

example, the relation of wavelength-shift to strain can be written as

$$\Delta\lambda = F_g \lambda_0 \left(\epsilon + \left[\frac{C_1}{F_g} + \alpha - C_2 \right] \Delta T \right), \tag{33}$$

which is the relation used in this work. λ_0 is the characteristic wavelength of the undeformed FBG and F_g, C_1 and C_2 are calibration[17] constants. Compared to equation (32), the temperature dependence of n_e is approximated by a linear function. Most of the temperature-induced wavelength-shift of an FBG results from the variation of n_e and not from the thermal expansion of the fibre [46]. Therefore, FBG measurements using a relation of the form of eq. (33) are intrinsically erroneous to some extent, particularly when they experience large temperature changes.

For strain measurements, FBGs are either attached directly to the workpiece using adhesives, or embedded under defined conditions into a carrier. A sensor of the second type[18] is shown in figure 22. The carrier can be attached to the substrate

Figure 22: Commercial optical strain sensor with metal carrier

by various means including adhesive bonding, spot welding, soldering and others. The reflection of the grating is related to a distinct strain value so long as the fibre is subject to a positive tensile stress and does not buckle. Therefore, embedding of FBGs into carriers is carried out under a well-known prestress. This ensures that compressive strains working on the sensor tend to decrease this prestress, but do not lead to buckling of the fibre. In the case of the PSL sensors, the fibre is attached to the carriers at two positions only. These attachment points are visible in figure 27 on page 33.

For further information, the review by Kersey et. al. [46] providing an introduction into the physical basics and applications of FBG sensors is strongly recommended.

3.2 The custom sensor arrays for AUG

In this section, the design of the sensor arrays and their installation inside the vacuum vessel of ASDEX Upgrade are described. Section 3.2.1 describes the positioning of the sensors and the specifications of the two sensing fibres. Section 3.2.2 presents pretests investigating the possible impact of the AUG environment on the sensors and vice versa, such as vacuum compatibility. The development of the laser welding process for the dissimilar material combination copper (PSL rings) and stainless steel (sensor carriers) is detailed in section 3.2.3.

[17] Used values (given by the manufacturer): $F_g = 0.89$, $C_1 = 6.156\ \mu\epsilon/K$ and $C_2 = 0.7\ \mu\epsilon/K$.
[18] Micron Optics os3110.

3.2.1 Mechanical design

Positioning the sensors on the PSL structure requires a consideration of the forces acting on it. There are two categories of Lorentz forces on the copper rings of the PSL: Those due to the electric current carried by the PSL and those acting on the internal coils, which are mounted on the PSL. The former loads are almost evenly distributed over the toroidal circumference of the rings, whereas the latter are line loads on the coil legs. All these forces lie exclusively in the R-z-plane (see fig. 9) and have no toroidal (=tangential) component. Therefore, tangential deformation and tangential natural oscillations of the PSL rings as described in section 2.2.3 are not expected. The PSL loading is likely to cause bending deformations of the rings mostly about their first principal axis (see fig. 5), which is the direction of the lowest bending stiffness. The bending about axis 1 can be determined by measuring the surface strain at the intersection of axis 2 and the PSL surface. This is the strategy employed in the present case: All sensors are placed as near as possible to this intersection point. The reasons are twofold: The strain measured at this position depends on the bending about one axis only and not on a bi-axial combination which would be difficult to disentangle; additionally, the ratio of the bending stiffnesses about the two axes is high (ca. 25). High strain values and also high signal-to-noise ratios are therefore expected at this location. On the upper PSL ring, the sensors are mounted exactly at the point where the surface and the first principal axis of the respective cross-section meet. On the lower ring they were displaced upwards by 5 mm, as shown in figure 23, due to the geometric constraint of an existing groove. As the PSL has an eightfold symmetry regarding the supports and

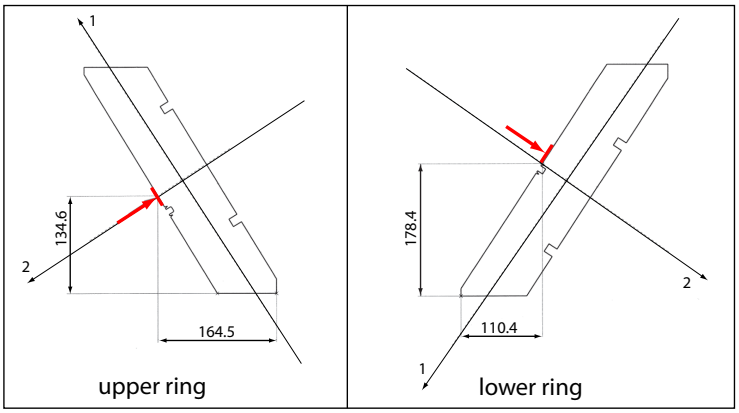

Figure 23: Regular sensor positions on upper and lower PSL ring cross-section

the bridges, the toroidal distribution and the number of sensors was laid out to be able to resolve ringmodes up to the order eight[19]. Therefore, 16 strain sensors are positioned equidistantly on both rings, central with respect to the vessel segments. Thereby, most weak points of the structure are covered, like the two notches on the upper ring, the vertical PSL hinges and various vertical diagnostic bores on both rings. Two additional sensors monitor the deformation of the current bridge, and two opposing temperature sensors per ring allow reliable temperature compensation.

[19] An example of a hypothetical ringmode of order 10, which exceeds the spatial resolution of the system, is given in figure 49 on page 60.

Figure 24 shows the spatial distribution of the sensing system, which consists of 34 strain gauges and 4 temperature sensors on two optical fibres. The angular position

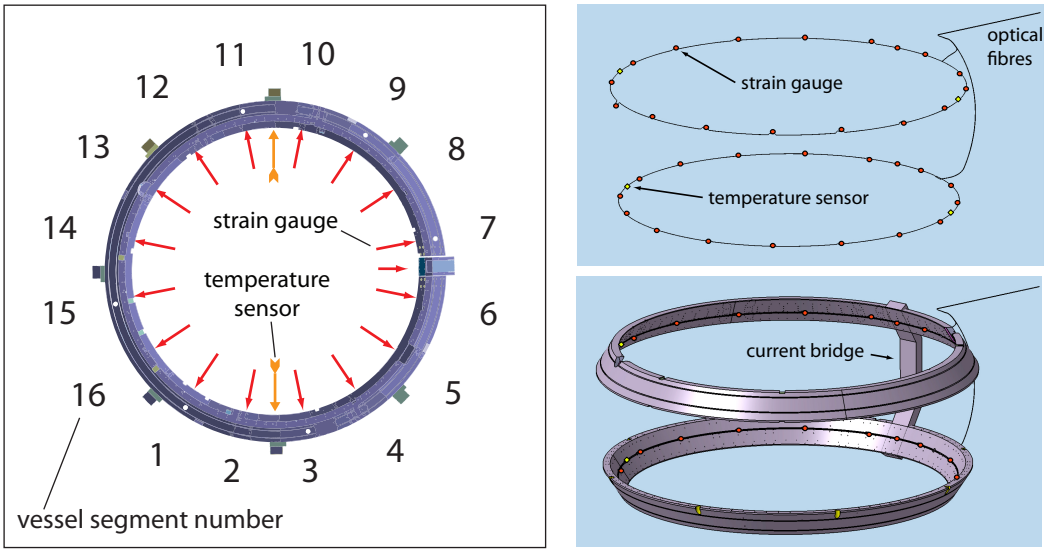

(a) PSL top view (b) isometric views

Figure 24: Spatial distribution of the 38 sensors

(in θ) of the sensors is identical on the upper and the lower ring. A CAD model of the sensor positions and the exact fibre path was developed to define the sensor in-vessel coordinates and to determine the distances between the gratings on the sensing fibres. The fibres could thereby be customised to the geometry of ASDEX Upgrade to avoid excess fibre length inside the vacuum vessel. The necessary machining of wall tiles, under which the fibre is laid, was minimised. Furthermore, less fibre installed in the vessel requires less shielding against plasma radiation.

Most of the fibre was laid into an existing toroidal groove on the PSL, next to the steel pipe of the toroidal voltage measuring loop. The exact toroidal positions of the sensors are included in the appendix. As an example, figure 25 shows the fibre path of a regular and two irregular sensor positions. Underneath every tile

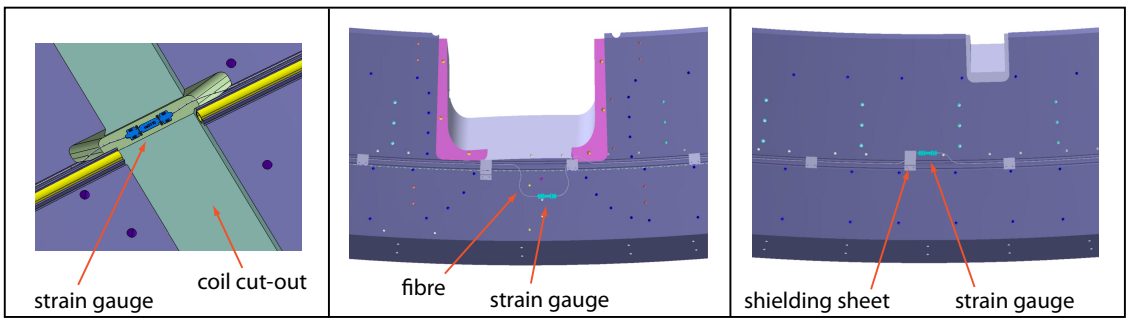

Figure 25: Sensor positions on the PSL: Under Rogowski-coil in segment 15 (left, lower ring), at ring notch in seg. 5 up (middle, upper ring) and at a regular position (right, upper ring)

gap, where a line of sight between the plasma and the fibre is possible, stainless steel sheets of 0.3 mm thickness were spot-welded to the aforementioned steel pipe. The two functions of these sheets are to hold the fibre in place and to shield it from the plasma light.

The boundary conditions for the determination and the arrangement of the centre wavelengths of the FBGs are as follows: The wavelength detection range of FBG interrogators is limited, the unit used in the present case allows detection between 1510 nm and 1590 nm. The individual sensors on one input channel of the unit are identified by their wavelength, i.e. by the small range in which their wavelength varies. This usually means that the centre wavelengths need to be distant enough to assure that no overlap of two neighbouring sensors in terms of wavelength can occur. Therefore, the 80 nm span offered by the interrogator unit is divided into equal wavelength slots for the 17 strain gauges per fibre. Temperature sensors do not need a proper wavelength slot, as their temperature-dependent wavelength drift is synchronous to the one of the strain gauges. In terms of wavelength, they are therefore placed at the common edge of the two slots of neighbouring strain sensors. It is clear that the detection range limits both the number of sensors on one channel as well as the strain range these can detect, as the strain is proportional to the wavelength shift. The maximum strain values of the PSL during AUG operation were not known a priori. The arrangement of the wavelengths on one fibre accounts for this and allows the fibre to be cut in the middle to double all slot sizes while all sensors can still be read out, thanks to the double-sided connection to the interrogator. This is illustrated in figure 26. Slight irregularities arise from wavelength

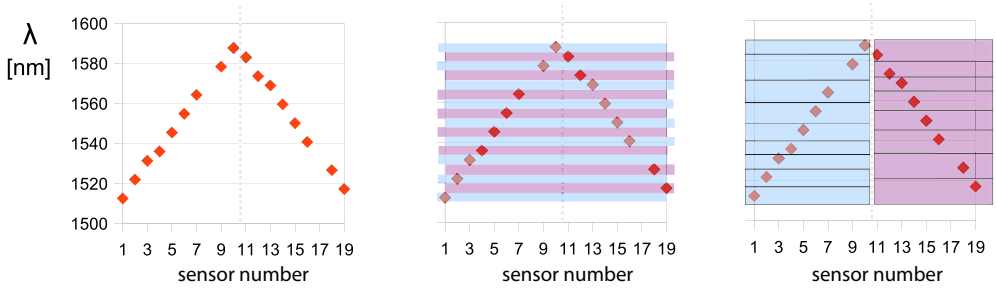

Figure 26: Centre wavelength arrangement on one fibre (left), initial slotwidths (middle) and widened-slot configuration (right, fibre cut between sensors 10 and 11)

deviations due to the grating inscription process. In the initial configuration, the slot size is 4.7 nm, corresponding[20] to ±1,600 $\mu\epsilon$. This means that in this state of the fibre, the maximum tolerable strain is 80% of the technical plasticity limit ($R_{p0.2} \mathrel{\widehat{=}} 0.2\%$ yield). All later measurements showed that the maximum strains are well below these values and cutting the fibre was not necessary.

The custom sensing solution for the PSL deformation measurement includes two monomode optical fibres[21] with 19 FBGs per fibre in defined distances. The installation of 19 separate off-the-shelf sensors instead was discarded firstly due to significantly higher installation efforts. Secondly, connecting these sensors by splicing would create 18 weak points along the fibre in terms of signal damping and

[20] The abbreviation $\mu\epsilon$ is widely used in the field of strain measurement ($1\ \mu\epsilon = 10^{-6}$m/m).
[21] Compliant to industrial standard Corning SMF-28.

mechanical properties. Furthermore, commercial FBG strain sensors are available at certain standard wavelengths only, preventing a custom wavelength design as described before. Two manufacturers were involved in the production of the PSL sensors: One produced the two draw-tower grating arrays according to a detailed specification in terms of the wavelengths and the distances between the gratings. The second supplier embedded these gratings into standard sensor carriers, identical to those utilised for mass production, in order to assure an accurate calibration using standard equipment[22]. Figure 27 shows both sides of a temperature and a strain sensor carrier. As these carriers are made of stainless steel and the PSL rings consist

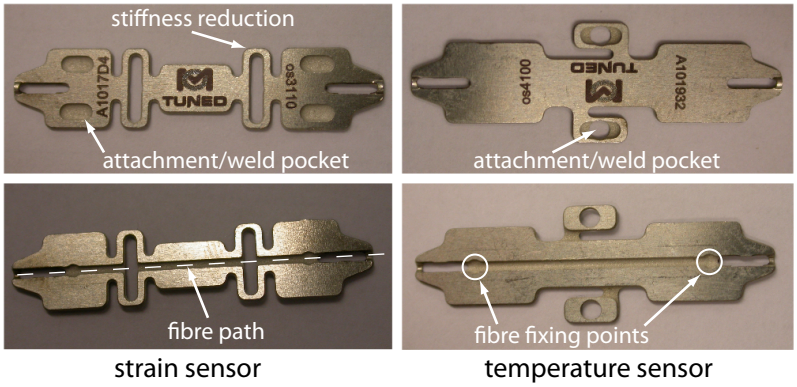

Figure 27: Sample carriers, front (top) and back-side (bottom)

of copper, the weldability of this dissimilar combination was investigated. The steel-copper welding qualification is described in section 3.2.3. Each of the two sensing arrays, consisting of the fibre, 19 steel sensor carriers and connectors on both ends, was installed inside the vacuum vessel as one piece. The main properties of the sensing arrays are given in table 4.

item	value
core and cladding material	SiO_2 (core Ge-doped)
coating	polyimide
upper PSL fibre length	19.7 m
lower PSL fibre length	23.9 m
fibre core diameter	5 μm
fibre outer diameter	ca. 200 μm
minimal bending diameter	17 mm
number of FBGs per fibre	19
carrier thickness	0.79 mm
welding pocket remaining thickness	0.3 mm

Table 4: Main specifications of the two sensing arrays for ASDEX Upgrade

For identification, each sensor is denoted with a code that contains its position on the sensing fibre (from 1 to 19), the position in the vacuum vessel (segment

[22] As no in-situ calibration of the sensors in the mounted state is possible, a reliable initial calibration on an industrial calibration bench is of great importance for the quality of the acquired data.

number 1 to 16), a letter indicating the type of sensor (S for strain, T for temperature) and a reference on which PSL ring they are mounted on (up or low). For instance, 14-1low-S designates the 14$^{\text{th}}$ sensor on the fibre (as seen from the vacuum feedthrough) measuring the strain on the lower PSL ring in the middle of segment 1. In the following, the sensors are referred to using either these denominations or an unambiguous, shortened form like 1low for the aforementioned strain gauge. A detailed overview of the wavelengths and the positions of the sensors and their nomenclature is included in the appendix. This list also accounts for the changes due to the fibre repair procedure described in section 3.3.3.

3.2.2 Compatibility assessment of sensor and environment

Optical fibres and Fibre-Bragg-Gratings are sensitive to electromagnetic irradiation and neutron bombardment. Both lead to a decrease of the fibres transmittance [47, 48]. The fibres installed on AUG can be shielded effectively from UV-radiation but not from fusion neutrons. Neutron bombardment creates point defects in the fibre core that scatter the signal and thereby increase fibre damping. This effect can even be used for measuring radiation at high dose rates [49]. Even small changes in the chemical composition of the fibre or the manufacturing parameters of the FBGs can have a significant impact on the radiation hardness [50, 51]. Contrary to the fibre optics used at AUG in the past, the FBG fibres are doped with germanium atoms in order to increase their photosensitivity which allows the inscription of the gratings with a laser beam. As these fibres are the first of their kind to be used *inside* a fusion experiment, no experience was available and the impact of neutron irradiation needed to be tested prior to installation.

Regarding the complexity of the interaction of FBG-equipped optical fibres with ionising radiation, a pragmatic approach was taken. A sample sensor, identical to those installed later, was stored for 90 discharges[23] at mid-plane level next to the AUG vessel. The expected neutron dose rate at this location is almost as high as at the final position of the sensors. The fibre damping was measured before and after irradiation with the optical sensing interrogator unit used later for measuring the PSL deformation. No damping increase could be detected, i.e. the neutron effect was below the unit's detection limit of 0.1 dB. As the tolerable damping is above 10 dB, the estimated lifetime is at least 9000 discharges. The influence of unclean or misaligned fibre connectors causing damping changes in the range of several dB is far more important than the radiation issues at AUG. The sensors have been operated in the 2010 to 2012 campaigns during more than 2,700 shots and no changes in the damping characteristics were detected.

Another concern was the tolerance of the sensors to the vessel baking temperature of 150°C, as the upper permanent limit specified by the manufacturer is 120°C. A sample sensor was fully operational after three heating cycles at 150°C for 24 hours.

The tokamak concept relies on the toroidal symmetry of the magnetic field configuration. Therefore, stray magnetic fields generated by metallic inserts in the AUG vacuum vessel are an important issue. The error fields are usually evaluated by means of analytic calculations of the error field caused by a metallic sphere in a homogeneous magnetic field. With this method, the error fields of the sensor carriers

[23] From #25800 to #25890 during the 2009 experimental campaign.

were judged to be insignificant due to their small mass.

The vacuum compatibility of the sensing equipment was also assessed in terms of outgassing. Small amounts of halogens or other heavy elements can severely affect plasma operation of AUG, since particles with high charge number in the plasma enhance radiation which leads to the loss of large amounts of the plasma energy. As a first step, all plastic and rubber parts of the sensor arrays were either removed or replaced in the specification. The outer, protective glass-fibre sleeve, drenched with resin, was replaced by a sleeve of pure SiO_2. The elastomeric fibre bend protection at the connectors was replaced by parts made of PEEK[24], a high-temperature polymer and standard material for in-vessel electric insulations. The cladding of the fibres consists of a fluorine-free high-temperature polyimide[25] [52]. The adhesive[26], used in minor quantities to attach the fibre to the carriers and the connectors, meets NASA low outgassing standard ASTM E595. The steel carriers themselves are not critical in this context.

In a second step, the two sensing fibres and the vacuum feedthrough passed an outgassing test, including mass spectroscopy analysis, at 150°C for 24 hours. Following these tests, all components to be installed inside the vacuum vessel were declared qualified. Figure 28 shows one of the sensing fibres before the outgassing test. The two fibres of around 20 m length and with 19 sensors each are very fragile

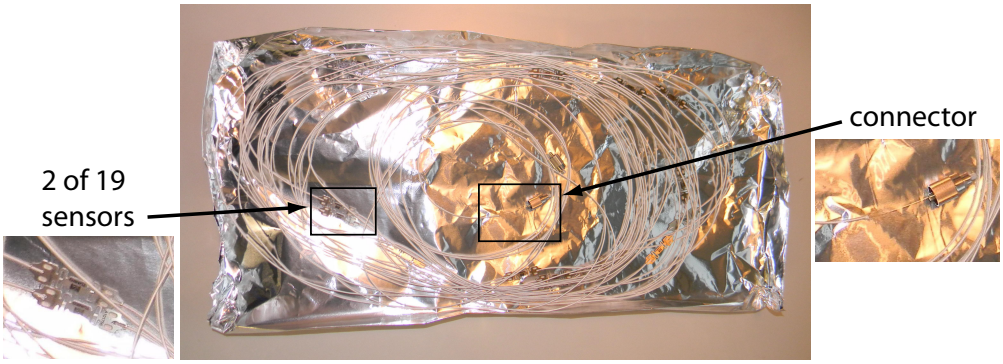

Figure 28: One of two sensing fibres with 19 sensors before the outgassing test

and need to be handled with care. They were spun on reels for transport into the vessel and unwound successively as the sensors were mounted at their final positions on the PSL.

3.2.3 Laser welding process development

The sensor carriers needed to be fixed on the surface of the PSL, which consists of pure copper of type Cu-ETP[27]. The carrier material is an austenitic stainless

[24]Polyether ether ketone (PEEK) is a semicristalline thermoplastic with high mechanical strength up to its glass transition temperature (143°C). It is one of two polymeric materials (besides Vespel, a polyimide) which is approved for in-vessel use, having gone through extensive testing.
[25]ORMOCER®.
[26]Epo-Tek 353ND.
[27]2.0060, formerly E-Cu57, min. 99.9% Cu, not oxygen-free.

steel, grade 302[28]. Owing to the severe dissimilarities of these materials, pulsed laser beam welding was chosen for its high energy density, allowing high cooling rates. This allows the heat affected zone to be tailored to be very localised and to reduce thermal stresses and crack probability. The high precision of this method also minimises the risk of damaging the fibre that passes next to the welding points.

The risks of producing defects during welding of dissimilar metals are significantly higher than with identical materials. One major risk with the present materials is hot cracking (solidification cracking) of the weld due to the different melting temperatures of copper and steel, aggravated by the diffusion of copper to grain boundaries [53]. This phenomenon is more widely known in the context of welding low-quality nickel-based alloys which exhibit high sulphur or phosphor content: As a result of the impurity, a low-melting eutectic point exists. During solidification of the weld bead, a molten pool with the respective (eutectic) chemical composition remains in front of the solidification line or at grain boundaries. This leads to cracking at these positions, as the already solidified domains contract thermally [54]. In the present case of copper-steel welding, the low-melting component is copper.

Even if shielding with an inert gas is provided, formation of pores in the weld may occur due to the high solubility of hydrogen in liquid copper, which in turn leads to a significant reduction of the mechanical strength [55]. The two main operating modes in laser welding are conduction welding and the so-called deep-penetration welding, which was used throughout the pretests and for the sensor installation on the PSL. In this welding mode, the high energy density of the laser beam creates a keyhole, a cavity filled with evaporated metal. Due to the vapour pressure, this keyhole is stable against collapsing due to the pressure of the surrounding liquid metal [56]. In pulsed laser welding, the keyhole is filled with molten metal as soon as the pulse ends. This process can result in pore formation if the filling is not complete. Therefore, porosity also depends on the welding process parameters [57]. This refers mainly to macropores, as opposed to the micropores caused by gases in solution being released.

Another risk lies in the formation of hard intermetallic phases of copper and iron or alloying elements, which is particularly detrimental to the fatigue strength as these provide points of crack initiation [58]. General examples for such phases are Laves phases, Nb_3Sn, FeCr and others. These are stoichiometric compounds with a different metallic bond share than the base material (usually more covalent), resulting in very different mechanical properties, often a high hardness.

The solubility of copper in iron and vice versa at room temperature is low, as shown in the binary phase diagram in figure 29. In agreement to this, published analyses of the chemical composition of copper-stainless steel laser welds have shown that two types of globular phases are encountered in the intermixing zone of the joint [59]. One of these is copper-rich and most likely corresponds to the body-centred cubic (bcc) α-iron, the substitutional solid solution of copper in the iron matrix. The second is its equivalent with copper as base material: a bcc solid solution of small amounts of iron in copper, also referred to as ϵ-phase. Laser test welds of sample sheets of the sensor carrier material on substrates made of Cu-ETP, identical to the

[28] 18% Cr, 8% Ni. Equivalent to X12CrNi 18 8 and 1.4300.

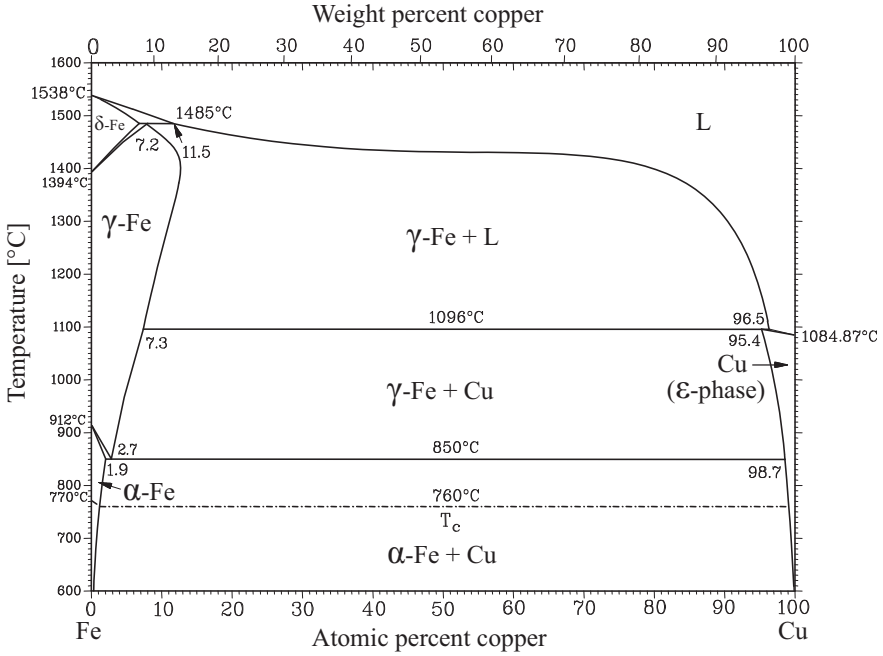

Figure 29: Iron-copper binary phase diagram (from [59], modified)

PSL material, also showed this type of globular domain, which is clearly visible in figure 30, especially on the right micrograph.

According to these considerations, the following issues are considered the main risks in the welding of the sensor carriers to the PSL: Excessive porosity, formation of brittle intermetallic phases, and solidification cracking. A systematic assessment of these issues was conducted, composed of three steps. First, optical and scanning electron microscopic investigations (OM and SEM) were carried out to detect pores in the weld joint. Even though intermetallic phases are likely to be visible on these images, microscopy is not an adequate instrument to confirm their absence. Therefore, the second step consisted of hardness measurements to find peaks of the microhardness in the transition zone between the two materials which would suggest the presence of intermetallics. Finally, two series of tensile tests of test welds were performed to determine appropriate welding parameters and to investigate the importance of hot cracking. Tensile testing alone would not have been sufficient as some of the potential defects, e.g. intermetallic phases, affect particularly the fatigue strength of the joints. All test welds were carried out using either actual sensor carriers supplied by the manufacturer or sample steel[29] sheets of 1 mm thickness with a groove of 0.7 mm depth, i.e. a geometry equivalent to the sensor welding pockets. Prior to welding, all parts were routinely cleaned using propanol and an ultrasonic bath.

Of course, the final goal of these investigations was to find an adequate way of attaching the sensor carriers securely and permanently to the PSL surface. For that reason, the depth of the studies, e.g. in terms of the welding parameter space or the number of hardness measurements was limited in order to keep the total effort on

[29]Made of 1.4301 = X5CrNi18-10/AISI 304/V2A. This steel is comparable to the material of the carriers in terms of chemical composition, weldability and mechanical properties.

a reasonable level. The following process parameters were not varied: All weldings were realised by aiming the laser beam at the groove of the specimen or the welding pockets of the sensor carriers, penetrating the remaining 0.3 mm of stainless steel and melting the copper surface underneath. The beam was misaligned by 5-10° with respect to the direction normal to the steel surface, to avoid deterioration of the welding head optics by direct reflections. The welding pockets of the carriers (see fig. 27) are machined by spark erosion which results in a rough surface and is beneficial for low reflections, i.e. an efficient coupling of the laser power into the material. The laser focus diameter was set to 0.75 mm to make use of the full width of the welding pockets. The laser pulse frequency was between 0.6 and 1 Hz and each weld consists of 6-10 pulses. The welding spot overlap[30] O, resulting from these parameters and the length of the welding pockets, is between 35% and 64%.

Microscopy revealed that the intermixing zone formed in the weld does not exhibit microporosities. Figure 30 shows two examples of such a micrograph of the weld joint. Domains with high content of either copper or steel are clearly visible, consistent with the low solubility of copper in iron and vice versa. The transition

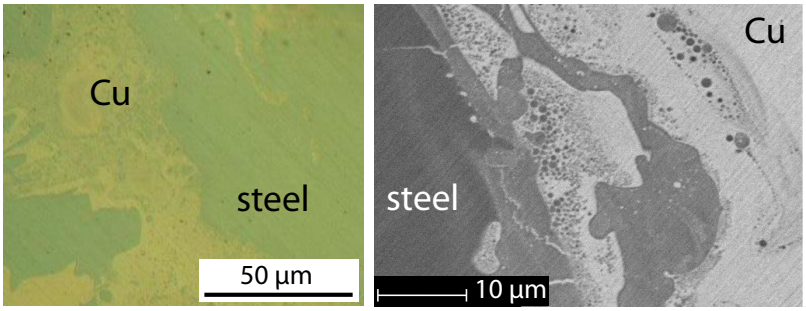

Figure 30: Intermixing zone of two test welds, optical microscopy (OM, left, U=399 V, τ=8 ms, O=70%), scanning electron microscopy (SEM, right, U=365 V, τ=10 ms, O=90%)

zone between the copper and the steel base material has a considerable width where the two materials mix. However, based on contrast differences on the micrographs (optical and SEM), only two distinct phases can be distinguished. These phases are, as stated before, most probably the ϵ-phase and α-iron.

A sample Vickers hardness measurement over the weld, the heat affected zone and the base material was made, since hardness maxima in the weld would be a sign of intermetallics. The utilised specimen represents a worst case in terms of welding parameters, as the beam power was maximised in order to produce the highest thermal loading and as many defects as possible. This caused a very high penetration depth and significant superficial hotcracking. No local hardness peaks are present, as shown in figure 31a. For comparison, figure 31b shows an example of a similar measurement[31] from a work by Mai et al. [55] which exhibits a very pronounced hardness peaking in the weld. Excessive hardness could also result

[30] O: welding spot overlap = 1 - (welding speed / (spot diameter x pulse frequency)). Two spots at the same position corresponds to an overlap of 100%, two spots 'touching' each other tangentially have an overlap of 0%. The percentage corresponds to a length and not to an area ratio.

[31] Medium carbon tool steel with 1.6% Mn, 0.8% Si (respective to weight), butt welded to copper.

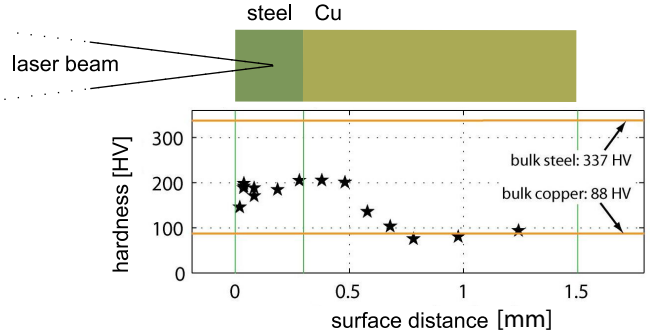

(a) Hardness of a PSL sensor test weld showing no hardness peaking (stainless-steel sample sheet/copper)

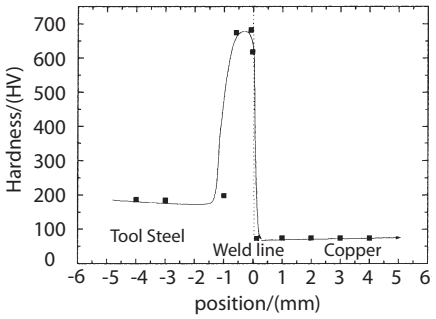

(b) Hardness of a tool-steel/copper laser weld with pronounced hardness peak (pulsed Nd:YAG) [55]

Figure 31: Comparison of the Vickers microhardness of two test welds

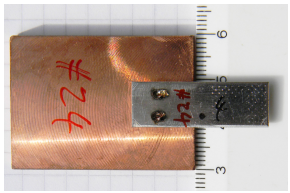

(a) Sample steel sheet specimen for welding parameter determination

(b) Half-carrier specimen for spread assessment using final parameters, tensile force direction shown

Figure 32: Two types of welding specimen used for tensile tests (scales in mm)

from a martensitic transformation due to high cooling rates. However, as the sensor carrier material has an austenitic microstructure, this transformation is not possible. The obvious lack of a hardness maximum in the weld of this high-power welding clearly indicates the absence of intermetallics.

Since the properties of the weld depend essentially on the process parameters, a large number of test weldings was performed at different beam power and pulse length settings. In addition, two separate series of tensile tests were conducted using two different types of welded specimen: Sample steel sheets and spare carriers, cut into halves as shown in figures 32a and (b), respectively. The first series (with specimen of type a) was designed to provide better understanding of the failure mechanism with the aim to define a parameter set for welding the sensors to the PSL. Making use of the results of these tests, pulse length and beam power were optimised for tensile strength and high stiffness. The second series of tensile tests used this parameter set and actual carriers (type b). This allowed to assess the statistical spread of the tensile strength and to determine a safety factor for the weld.

It was found that with the present materials and welding geometry, the laser pulse energy must be chosen in a narrow interval. Below a critical energy limit, the steel surface reflects most of the beam power instead of absorbing it, as the energy is too low to evaporate the surface material [56]. A weld keyhole can only form if material is evaporated, because the presence of metal vapour drastically increases laser absorption. Above a certain energy threshold, excessive surface defects arise.

Both phenomena are easily detected by visual inspection and characteristic welding sounds of the different welding regimes. In this manner, the required pulse energy was determined to be in the interval of 22-39 J. This limits the parameter space which is relevant for this application.

The pulse energy E_p is determined by the pulse length τ and the beam power, which is proportional to the laser flash lamp voltage U. To analyse the effects of the parameters and to find an appropriate working point, voltage and duration were varied in such a way that the pulse energy remained constant. Table 5 shows the covered welding parameter range and the variables that were intentionally set constant.

Parameter	Value
Focus diameter	0.75 mm
Shielding gas (rate)	Argon (6 $\frac{l}{min}$)
Angle of incidence	80-85°
Pulse frequency	0.7 Hz
Flash lamp voltage U	320-400 V
Pulse length τ	6.5-14 ms
Pulse energy E_p	28-38 J
Number of spots/pocket	6-10
Spot overlap O	35%-64%

Table 5: Laser welding parameters of the tensile test welds

It is a general observation that both the deterioration of the steel surface by hot cracks and the penetration depth into the copper substrate grow with increasing voltage. When the voltage, i.e. the beam power, is much too high, the metal vapour-filled keyhole cavity [56] created by the laser pulse does not close before solidification of the welding point and a vertical channel remains. With beam powers below this threshold, it shows that a compromise between insufficient penetration depth and excessive surface cracking (fig. 33) is required.

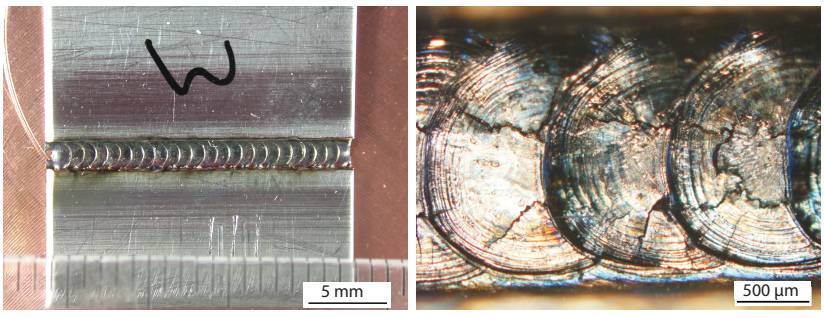

Figure 33: Surface hotcracking of a sample steel sheet on a copper substrate (X5CrNi18-10 on Cu-ETP substrate, U=372 V, τ=10 ms, E_p=39.3 J, O≈50%)

This effect also reflects in the tensile behaviour of the welds as illustrated in fig. 34. There exist two different modes of failure, substantially different in the amount of plastic deformation before reaching the force maximum. The first shows high stiffness at low shear (fig. 34, failure mode A, specimen 10,11,15,17) and low

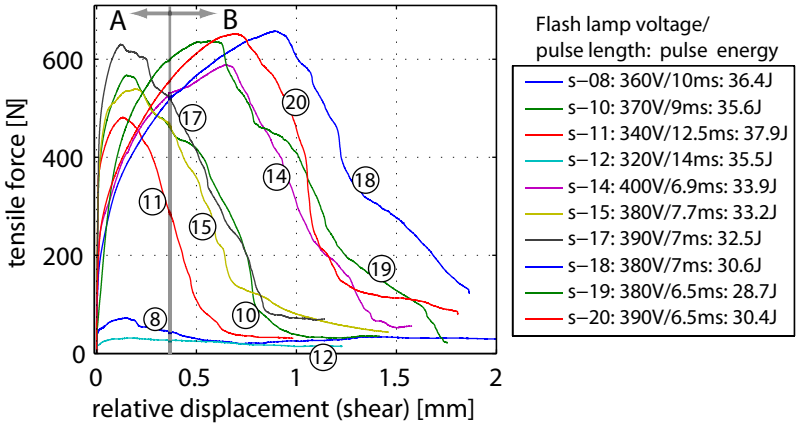

Figure 34: Tensile tests results of weld specimen (sample steel sheets on copper substrates) with different welding parameter sets

overall elongation before the peak force is reached. It corresponds to rupture at the interface of the copper matrix and the intermixing zone. The second exhibits considerable plastic deformation (mode B, specimen 14,18-20), and corresponds to failure of the carrier material (steel). As the voltage increases, the surface deterioration of the carrier increases, as well as the penetration depth into the copper. This means that failure in the carrier material (mode B) becomes more likely than failure in the copper (mode A). Domain A is preferable for welding the sensors because the high initial stiffness is beneficial for measurement precision. Therefore, a parameter set corresponding to mode A of figure 34 was chosen, reliably avoiding excessive hot cracks on the steel surface.

It turned out that the pulse energy settings leading to a particular mode of failure are slightly different for the specimen of type (b) and (a), probably due to small differences of welding pocket geometry and surface roughness. This means that the welding parameters of the tensile tests illustrated in figure 34 cannot be used without modification for welding the sensors. However, parameters for welding a type (b) specimen which reproduce the visual appearance of a weld of type (a) with the desired tensile behaviour are easily found, thanks to the experience gained through the tests. The equivalence of the two welds in terms of their failure mode was confirmed by the second tensile testing series. The parameters determined hereby which were eventually used for welding the specimen of the second series of tensile tests and the sensors on the PSL are: U=330 V, τ=7.5 ms, 7 spots per pocket, pulse frequency 0.7 Hz.

For the second series of tensile tests, 8 spare half-carriers (specimen type b) were welded on solid copper. The mean strength value resulting from these tests was 672 N, and the lowest tensile strength was 564 N. A force-strain dependency test of a sensor carrier yielded a force of 21.4 N at the maximum design strain of the sensors, which is 2,500 $\mu\epsilon$. Hence, the safety factor of the weld joint amounts to 26, and the in-service loads are well below the static force limit. Even though the fatigue properties of the joints are not known, the high safety factor suggests that the loads are most probably even lower than the endurance strength.

3.3 Integration of the sensor system at AUG

This section describes in three parts the installation process of the sensors in the ASDEX Upgrade vacuum vessel, the integration of the sensing hardware in the environment of the AUG data acquisition system and the description of the fibre repair procedure after a breakage occurred on the upper sensing array.

3.3.1 In-vessel mounting procedure

The positions of the sensors were predefined in the same CAD model used to define the sensing arrays. These positions were located in the vacuum vessel with an accuracy of 0.5 mm using a 3D-measurement arm in combination with the template sheet shown in figure 35a. This machined aluminium sheet is designed to accommodate the probe ball of the measurement arm and a sensor simultaneously in order to position the sensor. It also makes use of existing grooves on the PSL front surfaces for a relative positioning. Thereby, the exact toroidal alignment of the grating axis, which is the measurement direction of the sensor, is ensured. It is suitable for both types of optical sensors (strain and temperature) as well as the conventional strain gauges which will be described in section 3.4. All sensors were positioned using this tool. This includes both regular sensor positions on the two rings as well as six exceptional positions, for example those on the current bridge and at the upper rings' notches, as shown in figure 25.

A pulsed Nd:YAG laser welder of a special design, permitting the separation of the welding head from the laser generator, which remained outside the vacuum vessel, was used. The welding head was supplied by a cable harness of 10 m length for remote control, laser transmission and shielding gas supply. It was mounted inside the vessel on a versatile, dedicated holding device, which allowed virtually every point inside the vessel to be reached with the laser beam. Figure 35b illustrates the welding setup.

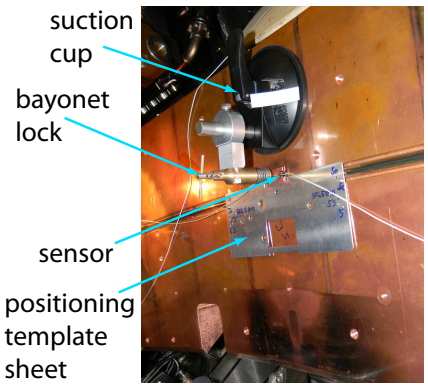

(a) Setup of positioned sensor prior to welding with clamping device and template sheet for positioning

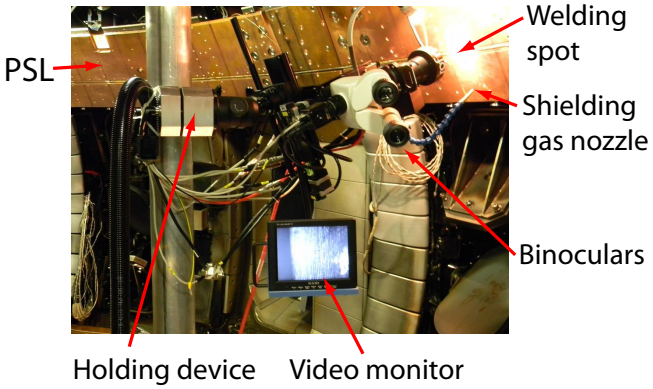

(b) Laser welding head inside the vessel fixed on holding device and connected with the welding machine (outside) by means of the cable harness

Figure 35: Sensor positioning and welding setup in the vacuum vessel

Avoidance of stiffness variations in the sensor welds was required, as they would lead to systematic errors in the measured strains. Such errors would hinder, in

particular, detection and identification of natural bending modes of the PSL rings. Hence, apart from the requirement of simple strength of the weld joints discussed earlier, comparability of the sensor signals requires identical stiffness between all welds. This requires a repeatable weld gap between the sensors and the PSL surface, since the clearance and pressure between the parts to be welded is known to be as important a process parameter for the final weld properties as beam power and pulse length. This importance was also observed during the test weldings. A clamping device was therefore designed to apply a well-defined, constant, normal pressure on the sensor carrier during welding. This tool is equipped with a suction-cup and a spring loaded bayonet-lock mechanism, which in principle[32] allows the welding to be performed by a single person. After positioning a sensor with the measurement arm and the template sheet, the suction-cup was attached to the PSL surface and the bayonet-lock was engaged on top of the sensor carrier. The sensor was thereby locked in position and all sensors experienced the same pressure during welding. A sensor after welding is shown in figure 36.

Figure 36: Result: Strain sensor on upper PSL ring after welding (segment 3)

After completion of all sensor weldings, most of the optical fibre was installed in a toroidal groove on the PSL surface (the upper groove visible in figure 36), held in place by metal sheets also serving as UV-light shielding, as described in section 3.2.1. The internal coils were mounted on the PSL rings on top of the sensors. These are covered and protected by plasma-facing wall tiles made of tungsten-coated carbon. The ends of the optical fibres are fed through the PSL rings making use of two bores of the toroidal voltage measurement loop in segment 6. From the rear of the PSL, they are guided to the upper C-port in segment 6 (Co6) through flexible steel hoses which are electrically insulated by PEEK tubes in order to conserve the separation of PSL and vessel electric potential. On the port vacuum flange the four sensing fibres are plugged onto a vacuum feedthrough which is connected outside to four fibre-optic cables which end in the ASDEX Upgrade control room in control box 28. The optical sensing interrogator, whose specifications are part of the next section, is situated in this cabinet.

[32]Safety regulations require at least two instructed persons with protective equipment for operating a class 4 laser device.

3.3.2 Data acquisition

The sensing interrogator module detects the peak wavelengths of the reflected signals and caches this data. It is network-compatible and implemented in the ASDEX Upgrade data acquisition infrastructure as a standard diagnostic. It provides a web-interface by which current status information can be retrieved from every computer in the same network. The main specifications of the sensing chain and the interrogator module are given in table 6. The data acquisition is started automatically before

item	value
torus feed-through	upper C-Port segment 6
flange diameter	35 mm
flange type	4 optical connections (FC/APC)
interrogator model	sm130
control room cabinet	#28 (top)
permanent IP	130.183.105.114
principle	swept laser, internal peak detection
sampling rate	1 kHz
detection range	1510-1590 nm
trigger	hardware: DV1
aquisition time per discharge	28 s
diagnostic name	OSI (optical sensing interrogator)
peak wavelength signal name	lambda
diagnosis spectra signal name	spectra

Table 6: Specifications of the data acquisition chain

every discharge by an AUG hardware trigger (a low voltage ramp signal) supplied to the interrogator via its trigger input jack on the front panel of the unit. The trigger DV1, used routinely, starts acquisition typically[33] 10.3 s before the plasma discharge is started by ramping the current of the central transformer coil. This early start accounts for potential PSL deformations due to the powering up of the toroidal field, which begins before the plasma discharge itself.

After each discharge the data is retrieved via the local area computer network from the interrogator and stored in the centralised AUG database in so-called shotfiles under the diagnostic name OSI. The diagnostic then flushes its internal buffer and waits for the next trigger. This means that the PSL deformation data is acquired and stored automatically for every discharge of ASDEX Upgrade. In normal operation, no supervision or maintenance is required. An appropriate interrogator unit with the highest sampling rate available (1 kHz) was chosen. There are units which sample at 2 kHz, but those provide a detection wavelength range of only 40 nm instead of 80 nm. This is insufficient for the number of sensors of the present application. Consequently, the shotfiles contain the reflected peak wavelength values of all sensors with a time resolution of 1 ms. The data is stored in an array with 28000 rows representing the time points, where the columns are sorted by ascending peak wavelength, one input channel after the other. These values can be processed

[33] All times quoted are relative to the opening of the OH-switch (plasma start, t=0 s). The machine trigger signals are defined in the shot program and stored for every individual discharge.

to obtain the actual strain values of the PSL. This is done using a computation with the calibration constants of the sensors according to equation (33). As to the temperature dependence of this relation, it was observed that the temperature increases during an experimental day, but no temperature shifts are detected during single shots. Therefore, temperature dependence is neglected on short timescales. The strain is computed using the mean of the first 1000 wavelength values of a discharge as zero-point for a particular shot. These wavelengths correspond to a time interval when the PSL is force-free from -10.3 s to -9.3 s with respect to the start of the plasma discharge.

Figure 37 shows some of the first strain signals obtained from the optical strain measurement of the PSL - the diagnostic OSI. This data was recorded during a technical discharge[34] with no magnetic field and no plasma and therefore allows an assessment of the intrinsic measurement noise. Typical noise values are

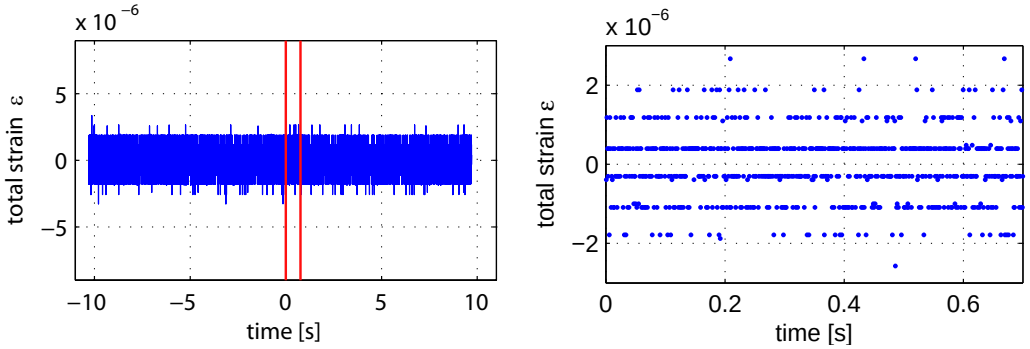

Figure 37: Full time trace (left) and detail (right) of strain sensor 12-15up-S in sector 15 (#25988, no plasma discharge, PSL force-free)

$\pm 3 \cdot 10^{-6}\ \frac{m}{m} = \pm 3\ \mu\epsilon$ of strain. The noise level of the strain depends heavily on the quality of the reflection of the Bragg grating, i.e. the signal to noise ratio of the intensity peak. It also relies on low damping at the fibre connectors which demands absolute cleanliness and good alignment. A close look at the signals reveals that there are two characteristic step sizes of about 0.7 $\mu\epsilon$ and 0.1 $\mu\epsilon$. The noise also shows a characteristic pattern in the frequency space. Figure 38 presents a normalised frequency spectrum of all strain sensor signals from the above discharge. The notation introduced here, plotting the power spectral density of the upper ring's sensors with positive sign and the lower sensors' data with negative sign (=inverted) is frequently used in this work. Systematic differences of the frequency behaviour of the two rings are thereby easily recognisable. There are three sharp peaks at frequencies of 72 Hz, 7.8 Hz and 464 Hz[35]. These do not represent a significant drawback for the measurement of PSL oscillations, as the frequency at which they appear is constant. In most cases, the noise is insignificant compared to the measured signals, and if not, it can easily be subtracted. There is another characteristic, broad noise frequency range between 370 Hz and 410 Hz. As will be shown later,

[34]Experiments (that are intended to be) without plasma are called technical discharges, as opposed to plasma discharges.

[35]These typical noise frequencies originate from the properties of the internal opto-electronic components of the interrogator module.

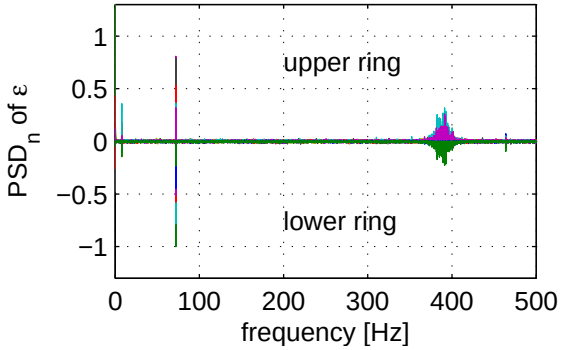

Figure 38: Noise spectrum of all strain sensors (discharge #25988, no plasma)

the PSL oscillation frequency range extends from static deformation up to roughly 150 Hz. Hence, this noise regime is at much higher frequencies than the actual frequency domain of interest. It must, however, be kept in mind that these signals are intrinsic to the diagnostic, in order not to mistake them for real deformations.

3.3.3 In-vessel fibre repair

During the in-vessel installation of the 38 sensors, a breakage of the upper sensing array occurred between segment 5 and 6 due to a mechanical impact. Additionally, the sensing fibre was damaged when an isolating plate at the left-hand side of the current bridge, located underneath the fibre path, was reinstalled. This caused a break of the upper and lower fibres between segment 6 and 7. Thanks to the redundancy feature of the sensing network, these incidents resulted in the loss of only one sensor, which was the upper strain gauge on the current bridge (02-cb6/7up-S). The fibre repair was therefore postponed to the subsequent vessel opening.

During the disruptive discharge #26335, more damage occurred to the upper fibre in segment 5, leading to the loss of all upper sensor signals except the sensor in sector 6. Fortunately, deformation data from more than 300 discharges, a sufficient number for a thorough study of disruptive loadings on the PSL, had already been recorded. It showed later that incorrect fibre laying under the wall tile between the internal coils Bu2 and Bu3 was responsible for the damage. This particular type of wall tile is mounted with a small clearance for thermal expansion and assembly reasons and can therefore move slightly during AUG operation. The sensing fibre was clamped between the steel sheet covering the sensor and the PSL and finally broke due to the load exerted by the wall tile. The self-developed repair procedure described in this section included the correction of the fibre path at this position in order to avoid similar damages in the future. The procedure is highly adapted to the conditions inside AUG, such as the temperature range and the requirement of vacuum compatibility. Furthermore, the properties of the sensors and the fibres was also taken into account, i.e. the lack of excess fibre length and the coating being particularly durable.

The repair of the fibre optics was realised with a portable, battery-powered fusion splicing device[36]. This apparatus is able to connect two open ends of a fibre with an electrical arc discharge, creating only a small additional optical damping. First,

[36]Fujikura 3-axes arc fusion splicer.

the coating is stripped off the fibres and they are trimmed with special equipment to produce a clean cut at each end. The unusual durability of the polyimide coating required the manufacture of special equipment. Pliers with silicone-covered flat nose, as illustrated in figure 39, were manufactured for the safe clamping of the fibre ends

Figure 39: Special pliers for safely gripping fibre during coating removal

when the coating is stripped off. The fibres are inserted into the splicer which means in practise that at least 10-15 cm of fibre have to be available on both sides of the damaged location. As two of the breakages of the sensing fibres were located right next to a sensor, these sensors were dismantled and spare sensors were laser welded at the same locations. The different characteristic wavelengths of these sensors have to be considered in data analysis. A detailed list of all sensors' wavelengths can be found in the appendix. The upper current bridge strain gauge was removed without replacement. The lower array is covered entirely by the internal coils and their substructure, making repair troublesome and further damage improbable. As its single defect does not affect the measurement, it was not repaired.

The splices are weak points in a mechanical sense and were protected with stainless steel tubes, on which the fibre was attached on one end only, in order to avoid tension on the splice due to thermal expansion of the tube. The protective fibre glass sleeve was fixed on both sides of the tube using an adhesive similar to the one already used for embedding the gratings and the connectors. This made a second outgassing test unnecessary. The unavoidable excess fibre length was wound up and stored behind the long legs of the internal coils and their substructure, as shown in figure 40. The adhesive was hardened with a hand-held heat gun; the completion of the curing process is indicated conveniently by the adhesive turning to a reddish colour.

The mean wavelengths of the two newly installed sensors shifted slightly due to the stresses induced by welding. As a consequence, the wavelengths of two of

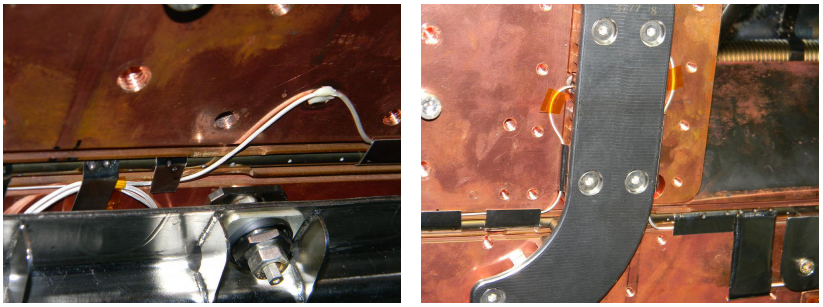

(a) Loop under B-coil toroidal leg (b) Under B-coil substructure

Figure 40: Storage of excess fibre length after repair procedure

the gratings have converged enough to trouble the (hardware) peak detection of the interrogator in some cases. The wavelength ranges of the two sensors still do not overlap, but the measurement unit cannot always detect all the gratings. The result is that some time points possess one additional wavelength datapoint compared to the others. Consequently, the columns in the data array stored in the shotfile are misaligned, because the wavelengths detected on one input channel are sorted strictly in ascending order. This effect is compensated using a modified postprocessing routine which sorts the data depending on input channel number and nominal wavelengths. These nominal values are determined with the secondary operating mode of the interrogator, which is mainly a tool for diagnosing the reflectivity of the gratings and the transmissivity of the fibres. In this mode, all input channels are scanned with low sweep rate and high precision and the intensity as a function of the wavelength is recorded. The peaks of these spectra are then used as the nominal wavelengths. A reliable identification of the sensors is thereby assured. A scan in this mode is performed after every AUG discharge as a routine examination of the sensing hardware.

With the exception of the upper current bridge strain gauge (02-cb6/7up-S), which was removed, the repair procedure restored the availability of all installed sensors.

3.4 Additional sensors for comparison purposes

Several additional sensors for measuring accelerations and strains on AUG were employed in the course of this work apart from the optical PSL strain gauges. First, a piezo-electronic accelerometer was mounted on the upper PSL ring during the hammer testing described in section 4.3.1. Second, a pre-production optical accelerometer[37] sensor was successfully tested for ex-vessel compatibility during AUG operation. This sensor was mounted on the outer flange of the upper C-port in segment 6 for 120 discharges. An example of the data of this sensor is included in figure 74 (p. 90). Third, conventional electrical strain gauges were installed at five locations on the PSL, of which three are directly adjacent to optical sensors, as an alternative measurement for comparison with the OSI data. Unfortunately, these conventional sensors were destroyed shortly after installation, probably by electrical arcs between the rear side of the wall tiles covering them and their electrical connection, which has a different electrical potential than the PSL. As no useful data could be retrieved from these sensors, the following description is kept intentionally brief. It is intended to provide information necessary for a possible repair and operation of these sensors in the future. Table 7 gives an overview of status information of the diagnostic OSI including the availability in terms of shotnumber-range of the optical sensors and the optical acceleration sensor (os7100).

The five electrical strain sensors consist of four strain gauges each, connected in a Wheatstone[38] bridge and bonded to a rectangular copper sheet of 0.5 mm thickness.

[37] Sensor type: Micron Optics os7100, characteristic wavelength λ_B=1539.76 nm, sensitivity: 16 pm/g = 1.63 pm/$\frac{\mathrm{m}}{\mathrm{s}^2}$.

[38] The Wheatstone bridge is an electrical connection scheme for four resistors which allows, amongst other uses, the measurement of small changes of resistance with high precision. In the present case, another beneficial feature of this circuit is the intrinsic temperature compensation.

discharge range	data storage	used trigger	acquisition length	available sensors	channel 1	comment
25985 - 26001	CGV	TS6	20 s	37	01-6up-S	
26002 - 26040	CGV	DV1	28 s	37	01-6up-S	
26041 - 26133	AUGD	DV1	28 s	37	01-6up-S	
26134 - 26257	AUGD	DV1	28 s	37	os7100	
26258 - 26354	AUGD	DV1	28 s	37	01-6up-S	
26355 - 27399	AUGD	DV1	28 s	20	01-6up-S	
27400 - 28700...	AUGD	DV1	28 s	37	01-6up-S	repaired (new λ's)

Table 7: Status of the diagnostic OSI during the first ∼2700 acquisitions

The adhesive is cured at 150°C, which is the reason why the strain gauges cannot be applied directly to the PSL. It is not possible to heat the PSL rings locally due to their high mass and thermal conductivity. The copper sheets were laser welded to the PSL. Figure 41 shows a photograph of such a copper sheet with four strain gauges after welding. The edges of the sheets and the neighbouring PSL areas had

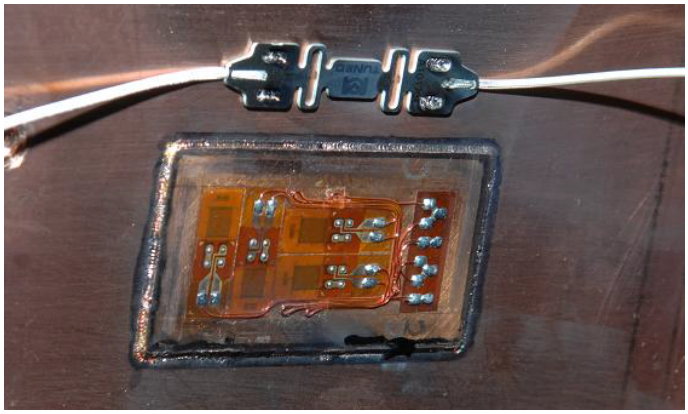

Figure 41: PSL strain sensors in sector 5: Optical sensor (19-5up-S, above), electrical sensor consisting of 4 strain gauges bonded to copper sheet, welded on PSL surface (DMS 3, below)

to be blackened[39] to reduce the reflection of the laser pulses on the smooth copper surfaces. Figure 42 shows a CAD representation of the positions of the electrical strain sensors. The five sensors are toroidally equidistant between the middle of sectors 4 and 6. Consequently, three of them are at the same toroidal angles as the optical sensors 4up, 5up and 6up. Two electrical sensors are placed between segments 4/5 and 5/6. The narrower toroidal spacing of these five sensors compared to the optical system was intended to identify natural ring modes with orders higher than 8, in case these occur during AUG operation. It will be shown in section 4.4.1 that this is not the case. The optical sensors 5up and 7up also visible in figure 42 are those that were replaced during repair of the fibre.

[39]Vacuum compatible, low halogen felt pens of type *edding 8030 NLS* and *8404 aerospace marker* were used for this task. These comply to aerospace standards LN 9051 and British Aerospace ABP 9-3323 Class A, respectively.

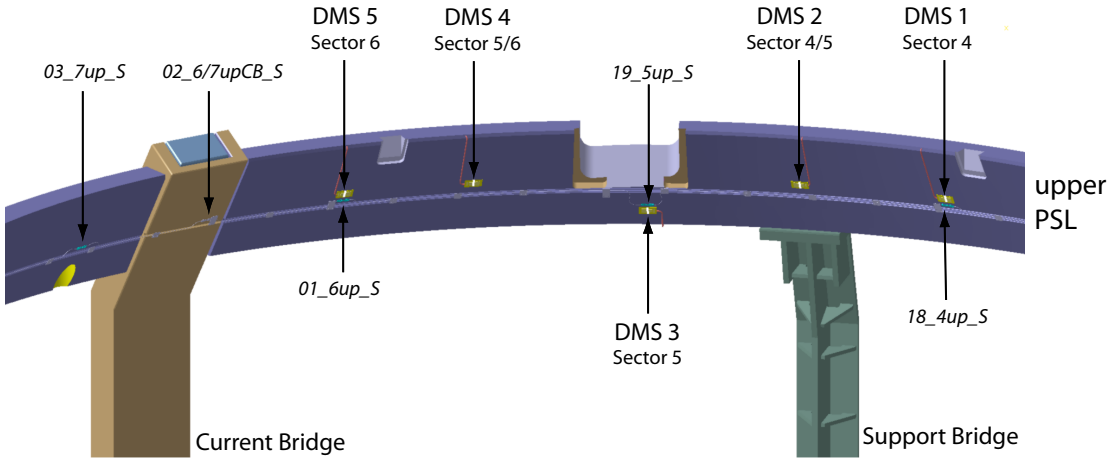

Figure 42: Positions of the conventional strain gauges (DMS) and the optical sensors in sectors 4 to 7

4 Results

In this chapter, results of calculations and experiments are presented and described. Their comparison, interpretation and associated conclusions are the topic of the subsequent chapter.

The deformation of the PSL during plasma disruptions as described in chapter 1.2.2 is naturally of prime interest in this work. Apart from data recorded during disruptions and standard plasma operation of ASDEX Upgrade, structural oscillations of the PSL have also been produced intentionally for different reasons. Two kinds of dedicated experiments have been carried out. First, pretests of the sensing system in different states of machine assembly, thereby changing the mass distribution of the PSL have been conducted. Second, technical discharges using a static toroidal magnetic field and varying the current in the internal coils to apply alternating forces on the PSL have also been carried out. The latter experiments relied heavily on the experience gained from measurements during plasma operation, e.g. as far as tolerable maximal strain values were concerned. The experimental results described at the end of this chapter are divided according to the origin of the PSL loading: Excitation produced on purpose (section 4.3) and measurements during operation (section 4.4). Sections 4.1 and 4.2 briefly present the results of an analytical calculation and a finite element modal analysis of the PSL.

4.1 Analytical approach

With a number of simplifications, the PSL natural frequencies and shapes can be determined in a first approximation based on ideal ring theory. The ball-head type supports of the PSL (fig. 9b) transmit only vertical forces and no bending moments or radial forces, if friction, in particular initial break-away torques in these bearings, is neglected. This is reasonable, considering the length of the hinges, the high mass of the structure and the large expected magnetic loads. The PSL as a whole is thus free to move in the radial direction and for small deflections only vertical constraints apply at the 8 positions of the hinges of the upper ring. The mounting points of the hinges on the vessel side are considered immobile: Possible in-service movements of the vacuum vessel, which might transmit vertical forces to the PSL, are neglected. As the bending stiffness about axis 1 (see fig. 5b) is far smaller than about axis 2, deflections are expected to be directed mainly along axis 2. In addition, forces in the z-direction induce deflections in the R *and* z-direction. The PSL principal axes are rotated by about 30° with respect to the vertical and horizontal directions. A unit displacement in direction 2 therefore has components of 0.5 along z and of 0.87 ($\approx \sqrt{3}/2$) along R.

Assuming small deflections and undeformed cross-sections, the natural frequencies of the ideal ring can be calculated with equation (27) from section 2.2.3. This equation describes the in-plane vibrations of thin rings, and is not readily applicable to the PSL, as its bending deflections are directed partly out of the R, θ-plane. The geometry and orientation of the PSL as shown in figure 43 suggests deflections directed primarily along its second principal axis. Therefore, an equivalent body concept is introduced here: The equivalent body for a PSL ring is an axis-symmetric planar ring with rectangular cross-section. It has the same mass distribution, overall

geometry and bending stiffness, i.e. area moments of inertia, as the corresponding PSL ring. The equivalent body allows the calculation of the natural frequencies and modal shapes of the PSL rings under the assumption of negligible deflections in the first principal direction. This is justified as the bending stiffness is 25 times higher in this direction compared to the second principal direction. The dimensions of the equivalent rings are determined based upon the requirement of identical area moments of inertia. The equivalent ring diameters are set corresponding to the centres

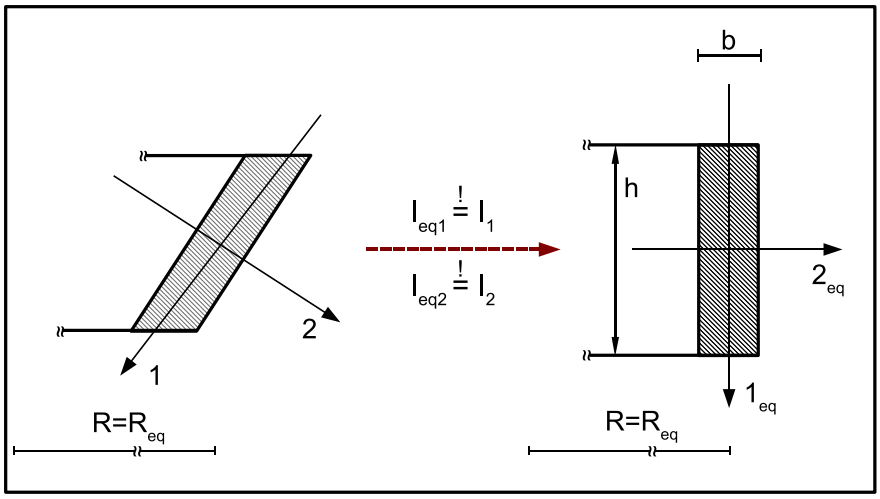

Figure 43: Equivalent PSL geometry for natural frequency calculation

of mass of the PSL rings. The moments of inertia were extracted from the PSL CAD model. Starting with the requirement of equal area moments of inertia

$$I_{eq1,2} \stackrel{!}{=} I_{1,2}, \text{ where } I_{eq1} = \frac{b^3 h}{12} \text{ and } I_{eq2} = \frac{bh^3}{12}. \tag{34}$$

we find the width and height of the equivalent ring with rectangular cross section according to

$$b = 12\frac{I_2}{h^3} = \left(\frac{12I_1}{h}\right)^{\frac{1}{3}} \rightarrow \frac{h^{-\frac{1}{3}}}{h^3} = \frac{(12I_1)^{\frac{1}{3}}}{12I_2} = h^{-\frac{8}{3}} \rightarrow h = \left(\frac{I_2^3}{12I_1}\right)^{\frac{1}{8}}. \tag{35}$$

The parameter set used to calculate the ideal natural frequencies of the two PSL rings is given in table 8. The natural frequencies are determined according to equation (27) from section 2.2.3

$$\omega_{n1,2}^2 = \frac{K_1}{2} \pm \sqrt{\frac{K_1^2}{4} - K_2} = \frac{K_1}{2}\left(1 \pm \sqrt{1 - \frac{4K_2}{K_1^2}}\right), \tag{36}$$

with the mode number dependent parameters

$$K_1 = \frac{n^2+1}{R^2\rho h}\left(\frac{n^2 D}{R^2} + K\right) \text{ and } K_2 = \frac{n^2(n^2-1)^2}{R^6(\rho h)^2} DK, \tag{37}$$

the so-called membrane stiffness

$$K = \frac{Eh}{1-\mu^2} \begin{array}{l} = 1.321 \cdot 10^7 \frac{\text{N}}{\text{mm}} \quad \text{(upper ring)} \\ = 1.316 \cdot 10^7 \frac{\text{N}}{\text{mm}} \quad \text{(lower ring)} \end{array} \tag{38}$$

	upper ring	lower ring	unit
1st moment of inertia I_1	1.48×10^7	1.50×10^7	mm^4
2nd moment of inertia I_2	3.35×10^8	3.45×10^8	mm^4
equivalent diameter R	2101.7	2019.8	mm
equivalent thickness h (horizontal)	78.5	78.2	mm
equivalent width b (vertical)	368	375	mm
mass density	8900	8900	kg/m^3
Young's modulus	1.5×10^5	1.5×10^5	N/mm^2
Poisson's ratio μ	0.33	0.33	1

Table 8: PSL equivalent data for eigenfrequency calculation

and the bending stiffness [33]

$$D = \frac{Eh^3}{12(1-\mu^2)} = 6.79 \cdot 10^9 \text{ Nmm (upper ring)} \quad (39)$$
$$= 6.71 \cdot 10^9 \text{ Nmm (lower ring).}$$

The results of the calculation are presented in table 9. Two important points should be noted here: The non-zero frequencies f_{02} correspond to the (no-bending) breathing mode sketched in figure 18a on page 24. The natural frequencies f_{01}=0 and f_{11}=0 represent the rigid-body rotation and translation of the ring, to which no natural frequency is attributed. Consistently, the calculation yields a frequency equal to zero for these cases. Readers are referred to section 2.2.3 for further details.

	PSL up	PSL low	PSL up	PSL low
n	f_{n1}	f_{n1}	f_{n2}	f_{n2}
0	0,0	0,0	329	343
1	0,0	0,0	466	485
2	9,5	10,3	737	766
3	26,9	29,1	1042	1084
4	51,7	55,7	1358	1413
5	83,5	90,1	1680	1748
6	122,5	132,2	2004	2085
7	168,7	182,0	2330	2424
8	221,9	239,4	2657	2764
9	282,2	304,5	2984	3104
10	349,5	377,2	3312	3445
...				

Table 9: Calculated eigenfrequencies in Hz of the upper and lower PSL ring in deformation dominated by bending ($f_{n1} = \omega_{n1}/2\pi$) and tangential tension/compression ($f_{n2} = \omega_{n2}/2\pi$)

There are 5 resonances (n=2...6) dominated by bending below 150 Hz, as shown in figure 44. The frequencies of the two rings differ by less than 10% in this range, with growing deviation towards higher frequencies. The natural modes with predominant tension/compression occur at much higher frequencies ω_{n2}. As the

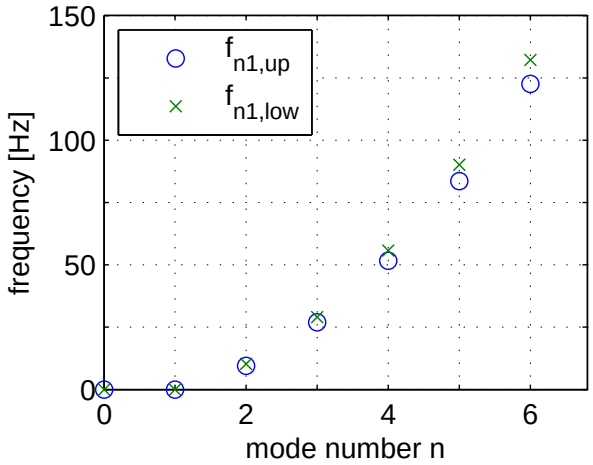

Figure 44: Calculated PSL eigenfrequencies for dominant bending f_{n1} $(= \omega_{n1}/2\pi)$

in-service loads of the PSL lie exclusively in the R, z-plane, these modes are not directly excited, contrary to the bending modes. Therefore, this study focuses on the bending modes.

4.2 Numerically determined natural frequencies and shapes

The finite element method is a computational technique used in many fields of engineering and physics to find approximate solutions to systems of partial differential equations. The underlying concept is the discretisation of continuous media with a finite number of subdomains (elements) followed by the solution of the equations for every element [60]. These equations are often linearised and their nature depends on the type of the simulation. For instance, the dynamic analysis of an oscillating system usually requires solving the equations of motion together with a material law describing the deformation behaviour.

Though finite element (FE) analyses are not a fundamental part of the present work, a brief investigation was made using an existing FE model [61, 62]. Contrary to the ideal ring calculations of the previous chapter, this model includes the coupling of the two rings and the most important geometrical features of the PSL that deviate from toroidal symmetry: The two types of bridges connecting the two rings, the vertical holes and the two notches on the upper ring with reduced cross-section as well as the two connections of the four half-rings opposite the current bridge which possess a solid backing plate. Figure 45 displays a three-dimensional view of the meshed PSL model. The materials of the rings and the support bridges (copper and stainless steel) are accounted for in the simulations in terms of their respective Young's moduli and mass densities. Two modal analyses with different boundary conditions have been conducted. The first does not contain the PSL bearings; the mechanical system is thereby considered as free floating. The second analysis sets the vertical displacement at the 8 positions of the vertical hinges of the upper PSL ring to zero. These two options mark both extreme cases of vertical hinges having zero and infinite stiffness (in z-direction), respectively. They were chosen in order to identify the significance of the hinges for the dynamic behaviour with the least

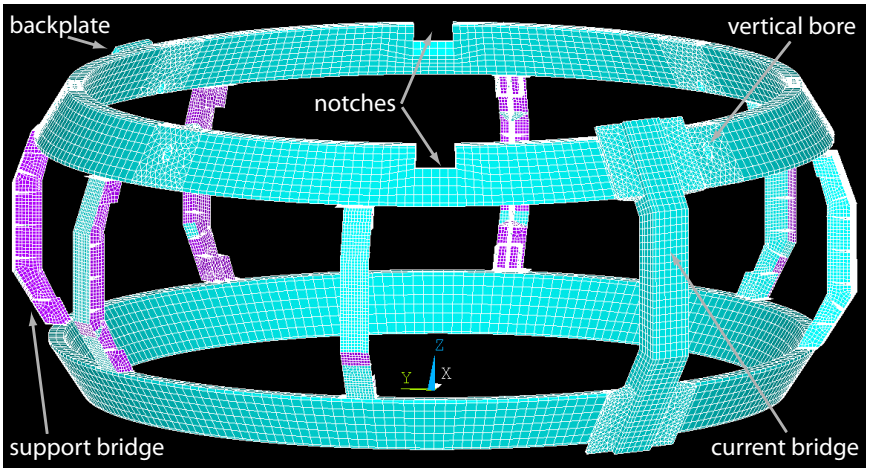

Figure 45: Finite element model of the PSL

possible effort. The properties of the real hinges necessarily lie between the two alternatives and the supports were not studied in more detail.

The modal analyses solve the homogeneous equations of motion. The outputs are *normalised* modal shapes with strain and stress information for every element and mode number, as well as the associated eigenfrequency. Damping is not included. Both cases have been studied for the first 66 eigenmodes, corresponding to frequencies up to 300 Hz.

The accuracy of this calculation is limited by uncertainties concerning the material data, such as the modulus of elasticity, by the considered number of elements (the fineness of the mesh), by the negligence of minor geometric features and due to disregarded effects such as relative movements of bolted parts and non-linearities in general. Naturally, the boundary conditions also have a decisive influence on the results.

Figure 46 shows a selection of modal shapes for different mode numbers in the case of free and fixed vertical hinges. The colour scale represents the total deflection from the undeformed state (normalised to unity). As will be specified in the following, the two modal shapes displayed per row have identical bending mode numbers of the upper and lower PSL ring. The frequency difference results from the modified boundary conditions. Table 10 and figure 47 present all natural frequencies up to 300 Hz for the two extreme bearing configurations. The finite element solver assigns a mode number n_{FE} to the natural oscillations of the whole structure including the bridges, instead of treating the rings separately, as in section 4.1.

In both configurations, some mode shapes can clearly be related to ideal ring bending modes. For example, the first four eigenshapes from the FE-simulation with free hinges (see figure 46, top left) are similar to the elliptical, 2^{nd} ideal ringmode. The upper and the lower PSL either have a phase lag of zero or π, where the latter means that the deflection and velocity values have opposite sign at all times. The first case is referred to as co-going or 'even', the second as counter-going or 'odd'. For both phasings, the FEA predicts two different spatial orientations, which are orthogonal, giving a total of four distinct natural modes with elliptical shape. The top left shape is referred to as 2/2 even, where the numbers stand for the bending mode number of the upper and lower ring according to the analytical analysis, where

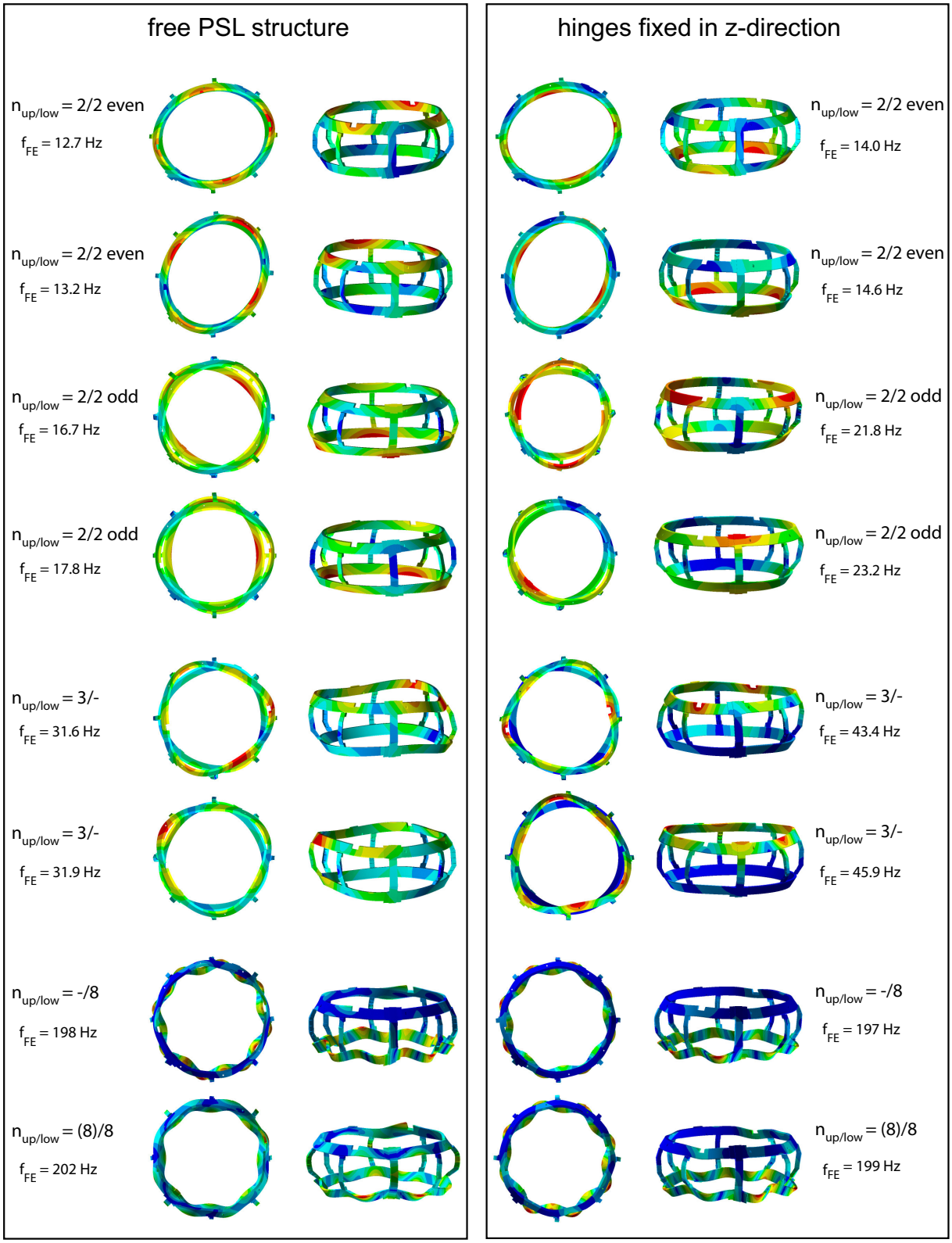

Figure 46: Assorted modal shapes determined by finite element simulation, two different boundary conditions

n_{FE}	f_{free}	f_{fixed}	n_{FE}	f_{free}	f_{fixed}	n_{FE}	f_{free}	f_{fixed}	n_{FE}	f_{free}	f_{fixed}
1	12,7	14,0	18	65,9	68,2	35	138	157	52	238	251
2	13,2	14,6	19	71,1	72,3	36	139	161	53	243	257
3	16,4	20,0	20	71,8	73,7	37	140	166	54	245	269
4	17,8	20,3	21	72,2	83,2	38	145	194	55	247	272
5	21,2	21,8	22	74,9	94,1	39	154	197	56	250	274
6	21,7	23,2	23	76,2	103	40	155	199	57	253	277
7	26,8	34,1	24	77,5	104	41	160	201	58	257	280
8	29,3	34,9	25	77,6	113	42	178	208	59	260	281
9	31,6	39,6	26	82,2	116	43	181	225	60	265	282
10	31,9	43,4	27	84,0	119	44	194	228	61	268	286
11	34,4	45,9	28	84,8	122	45	196	229	62	274	288
12	34,9	50,0	29	103	133	46	198	233	63	276	288
13	42,1	53,3	30	110	134	47	202	238	64	277	290
14	46,7	57,3	31	123	138	48	222	239	65	278	296
15	51,7	59,9	32	125	142	49	222	243	66	279	300
16	53,9	61,1	33	129	148	50	227	246	...		
17	62,9	67,9	34	132	151	51	232	248			

Table 10: PSL natural frequencies (in Hz) from finite elements modal analysis with free and fixed hinges

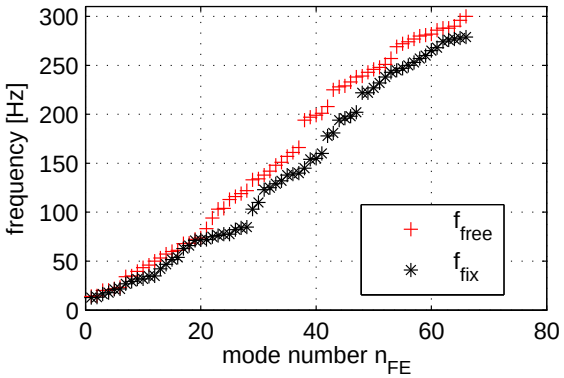

Figure 47: PSL natural frequencies from finite elements modal analysis with free and fixed upper hinges

each ring was considered separately. According to this notation, table 11 presents a classification of the first 20 finite element modal shapes in the free hinges case. The odd configurations appear mostly at higher frequency than the even configurations. The fixed hinges case generally yields higher frequencies than the one with free hinges, as also outlined in figure 47. Mode shapes, where both rings show the same ring mode number are encountered more often in the free-hinges case, and at low frequency. At higher frequency, beginning at approximately 70 Hz, the two rings show different mode numbers or the shape of one or both rings does not correspond to a bending eigenmode at all. The highest ring mode among the first 66 FE mode shapes presented in table 10 and figure 47 is of order eight with 16 nodes and antinodes per ring. The possible ideal ring bending modes in odd and even and

n_{FE}	f_{free}	$n_{up/low}$	phasing
1	12,68	2/2	even
2	13,18	2/2	even
3	16,31	2/2	odd
4	17,67	2/2	odd
5	21,35	1/1	odd
6	21,81	1/1	-
7	26,88	2/2	even
8	29,36	3/3	odd
9	31,37	3/3	-
10	31,84	3/3	odd
11	34,14	3/3	even
12	34,66	3/3	even
13	41,88	3/-	-
14	46,37	4/4	even
15	51,7	4/4	odd
16	53,75	4/4	(odd)
17	62,81	4/4	odd
18	65,64	4/5	-
19	71,05	5/5	even
20	71,61	-/5	-
...			

Table 11: PSL ring mode numbers, natural frequencies and phasing up to order 20 (FE modal analysis with free hinges)

both spatial orientations up to the 8$^{\text{th}}$ order sum up to 4×8=32 modes. Apart from these, intermediate modes ($n_{up} \neq n_{low}$) as well as combined modes, which involve deformation of the whole PSL structure, exist. Both occur more frequently in the upper half of the studied frequency range. They show either different numbers of nodes per ring, a toroidally asymmetric deflection distribution or high torsional deformations of the rings. Towards 300 Hz, the vertical stiffener ribs of the support bridges show their first (torsional) eigenfrequency.

4.3 Deformation measurements after artificial excitation

For the presentation of experimental strain data in the following, a top view representation displaying the shape of the two PSL-rings is frequently used. For small strains, the measured strain values ϵ_s from all 32 regularly positioned optical strain sensors are assumed to be proportional to the (inverse) deflection of the PSL at the sensors' positions. These strains ϵ_s are multiplied with an arbitrary, negative constant $-ct$ for visibility reasons. Using the 32 deflection values $u_s{=}{-}ct \cdot \epsilon_s$, a third-order spline interpolation is calculated for the whole toroidal circumference of both rings. This gives an intuitive, qualitative idea of the momentary shape of the rings and also of the phase of the oscillations at the sensor positions when image sequences of subsequent time points are examined.

In static, linear-elastic bending of a beam, the curvature $w''(s)$ is described by

the relation $M(s)=EIw''(s)$, with the bending moment M, Young's modulus E, the corresponding area moment of inertia I and the geometric coordinate s [63]. Considering the PSL rings as beam elements, and assuming that the ball-head type hinges of the upper PSL are unable to transmit moments (no friction), a continuous bending moment distribution $M(s)$ in the rings can be assumed. Therefore, an adequate interpolation function for $w(s)$ must have a continuous second differential. The cubic spline function satisfies this requirement.

Figure 48b presents an example using numerically generated strain data of an n=3 eigenmode in odd configuration, i.e. with a phase difference of π between the upper and the lower ring. The blue and the green lines represent the upper and

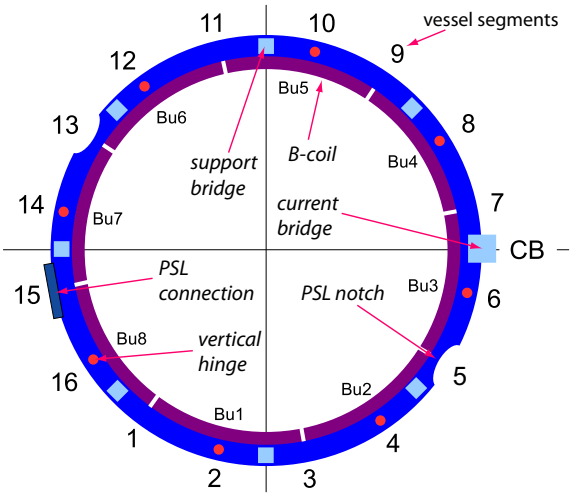

(a) Schematic top view with significant structural features

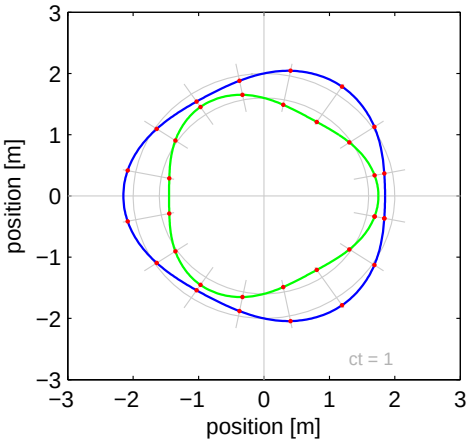

(b) Simplified view of measured strain values of upper (blue) and lower PSL (green)

Figure 48: PSL top view representation example

the lower ring, the size difference of the rings is exaggerated for clarity. The gray lines indicate the undeformed shape, and the sensors' positions are marked with red dots. The magnification factor ct is noted on the bottom right of the figure. Figure 48a shows once more the essential mechanical features of the PSL and their positions. It has the same angular orientation as figure 48b. The current bridge and the connection of the PSL half-rings are almost exactly opposed, lying on the horizontal axis of the plot. The notches with reduced cross-sectional area are located in the 2^{nd} and 4^{th} quadrant.

It should be kept in mind that radial deflections will be accompanied in most cases by axial, out-of-plane displacements that cannot be shown here. In addition, despite the sensors being positioning at the weak points of the structure as reported in section 3.2.1, the real strain maxima are not necessarily located at a sensor position. If the highest values are encountered at an unobserved position, the spline-fit will show smaller strains than the real ones. Finally, the number of sensors per ring does not allow the detection of ringmodes with orders beyond n=8 due to spatial aliasing. This effect is illustrated in figure 49. The dashed magenta line represents the input data of the order n=10 and the blue line is the resultant, erroneous spline fit resembling an n=6 mode. The calculated deflections of the 16 sensor locations

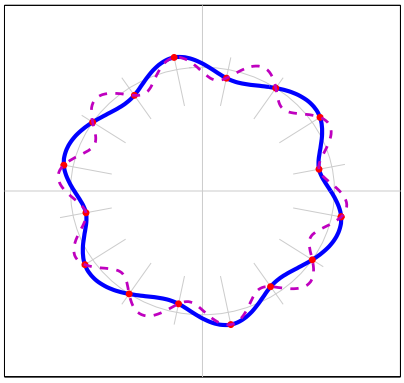

Figure 49: Example of spatial aliasing with numerically generated n=10 data (magenta), false interpretation resembling to n=6 (blue)

are marked by red dots. These points are shared by both lines, of course.

4.3.1 Hammer testing

Immediately after the installation of the sensors, when access to the inside of the vacuum vessel was possible, the sensing system was tested manually to ensure the functioning of all sensors. An impact force on the PSL was applied using a 5 kg plastic-head hammer, and a series of hits was performed either in vertical direction or normal to the inner PSL surface at defined positions. This procedure was repeated later after the fibre repair procedure (section 3.3.3) with all 16 B-coils in place. A final series was conducted with all 16 B-coils and all wall tiles mounted, to investigate potential effects of the additional mass on the response spectrum of the PSL structure. The extra mass on the upper ring amounts to 184 kg in the second series and to 517 kg in the third. The lower ring bears an extra mass of 550 kg in the second and 970 kg in the third series. This mass is nearly uniformly toroidally distributed. The large differences between the two rings' additional loads result from the mass of the solid supportive structure of the lower B-coils, made of stainless steel. For the first series of hammer tests, a high-resolution piezo-electronic acceleration sensor was mounted on the upper PSL in segment 3, measuring the acceleration component in the normal direction with respect to the ring's inner surface, and taking advantage of the absence of EM-interferences. Its technical specifications are included in the appendix. Given the high stiffness of the structure, the acceleration sensor naturally measures strong signals compared to strain measurements on the PSL surface. Unfortunately, this technique is not applicable during operation of ASDEX Upgrade, due to the strong interferences and the environmental factors mentioned earlier in section 3.2.2. For the two latter series of hammer testing, a plastic block serving as a spacer was mounted on the PSL surface to protect the wall tiles and the B-coils. Figure 50 presents the experimental setup of the impact tests with the hammer and the spacer block during the second test series, when all B-coils but no wall tiles were mounted. Table 12 introduces the testing scheme, which remained the same for the three series. To reduce errors, each hit was repeated once.

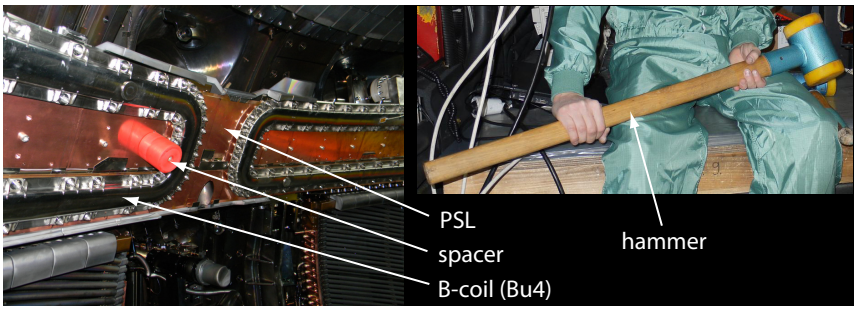

Figure 50: Setup with safety spacer (left) and hammer for manual excitation of the PSL structure (right)

An advantage of these experiments compared to measurements during disruptions is that the point of application and the direction of the loading is well known.

impact no.	sector	impact direction
1,2	3 up	normal on inner PSL surface
3,4	1 up	normal on inner PSL surface
5,6	2 low	normal on inner PSL surface
7,8	13 low	vertically downwards
9,10	11 up	normal on inner PSL surface
11,12	9/10 low	normal on inner PSL surface
13,14	5 low	vertically downwards

Table 12: Common hammer testing scheme of all three series

Figure 51 shows the time trace and the frequency spectrum of the accelerometer signal during impact test #3 of series 1 (impact 1.3). We notice the presence of a

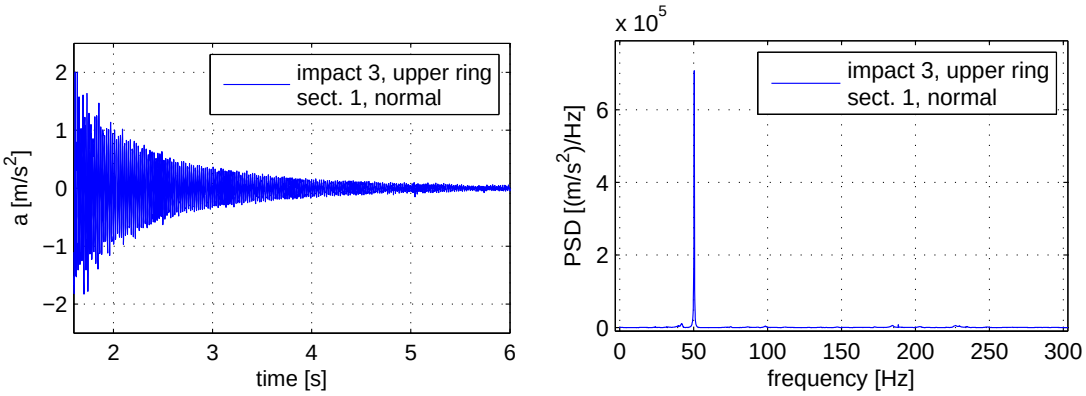

Figure 51: Time trace (left) and frequency spectrum (right) of the accelerometer signal during impact test 1.3

very pronounced peak at 50 Hz. Coincidentally, this is the same frequency at which the public electricity grid is commuted. However, since a battery-powered, portable amplifier and a professional oscilloscope were used for data acquisition, it can be assumed that the peak does not result from an external electric perturbation.

The first test series revealed that all optical sensors were working properly, even though the signal amplitudes and hence their signal-to-noise-ratios were weak due to the limited momentum of the hammer and the high stiffness and mass of the structure. Nevertheless, the system proved sensitive enough to clearly resolve the marginal deformation induced by an average person pulling on one of the PSL rings by hand. Figure 52 shows the strain signals of three of the sensors during hammer hit number 3 of series 1 (denoted by impact 1.3). These signals are the first data recorded with the PSL strain sensors (OSI[40] diagnostic).

Despite the weak excitation leading to a fast decay of the oscillations to noise level, the frequency spectra constructed on the basis of the strain signals show clearly visible, regular patterns. The structure of these patterns depends on the impact location and direction. Figure 53 presents the *normalised* power spectral density[41] (PSD) versus frequency plots for two different impact locations and directions, and for the three examined mass distributions. The signals from the upper PSL ring are plotted above the zero line, those from the lower ring below.

The high number of measurement locations and their spatial distribution allows statements about the momentary deformation of the whole mechanical structure of the PSL. In the present case, we can visualise the travelling bending wave that develops along the PSL after the impact of the hammer. This is demonstrated in figure 54 with several representations over a total time span of 16 ms. The indicated time refers to the start of the acquisition, not the impact time. The bending wave crest introduced at the impact location has travelled over one quarter of the toroidal circumference after 6 ms, and apparently decomposes into a larger number of waveforms thereafter. The two bumps visible at t=1.904 s in the top right image are the positions with reduced cross-section on the upper PSL. The lower ring does not seem to show any distinct reaction until around 16 ms after impact as displayed in the bottom right image. As we see in figure 52, the oscillation continues with non-negligible amplitudes, even after t=1.914 s. The impact force during the hammer experiments is naturally located at one position and the magnitude is not known. The excitation by internal coils does not exhibit these limitations.

4.3.2 Harmonic excitation by internal coils

Experimental layout

Electric currents in the B-coils interact with the external magnetic field, creating Lorentz forces ($j \times B-$forces) which are directed perpendicular to both the current and the B-field. On the one hand, this effect can result in severe loading conditions for the PSL, as the forcing might match structural resonances when the coils are operated with alternating current. On the other hand, it offers an elegant way to induce well-defined, distributed loads onto the coils and thereby onto the PSL on which they are directly mounted. In the course of this work, two series of technical

[40] OSI refers to the sensors' so-called **O**ptical **S**ensing **I**nterrogator. It converts the light signals, caches and transmits the data to the shotfile database.

[41] The power spectral density of a signal describes how the power of the signal is distributed with frequency. It is determined here by calculating the square of the absolute values of the complex Fourier coefficients of the signal.

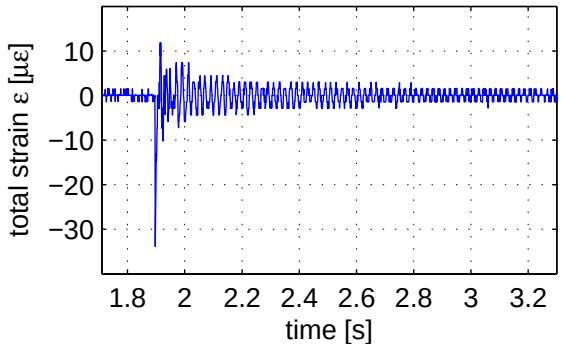

(a) Sensor 1up: upper ring, sector 1

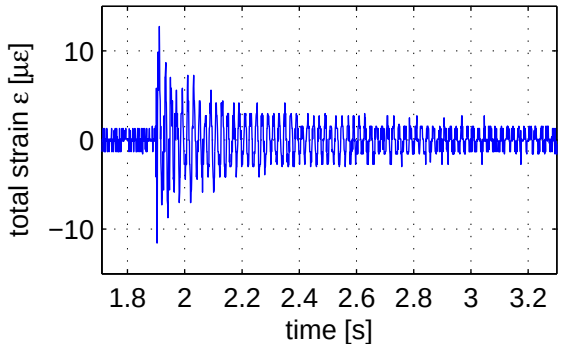

(b) Sensor 5up: upper ring, sector 5

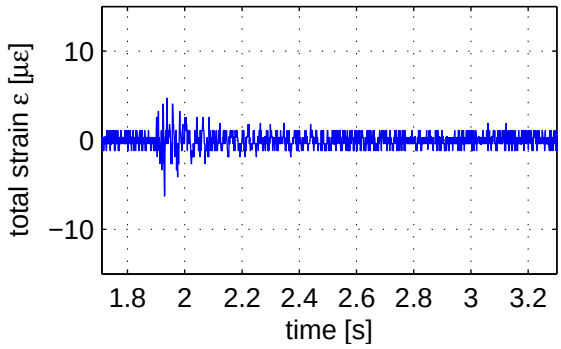

(c) Sensor 1low: lower ring, sector 1

Figure 52: Strain over time during hammer test 1.3 (impact in sector 1, normal)

shots of ASDEX Upgrade using this technique have been carried out in order to investigate the dynamic behaviour of the PSL structure. All of these were conducted at constant toroidal field strength (B_T=-2.4 T) and zero poloidal field, feeding alternating current to one ore more of the B-coils. By reversing the connection to the power supply, any coil can be operated either with a phase difference of 0 or π with respect to the other coils. Thereby, cyclic forces are introduced on the poloidal (short) legs of the actuated coils, as only these lie perpendicular to the toroidal field. Given that the current in two neighbouring coils is of equal amplitude, the forces of

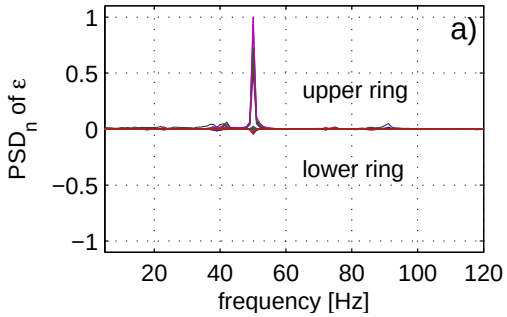

(a) Impact 1.4: Normal hit on upper ring without coils/tiles

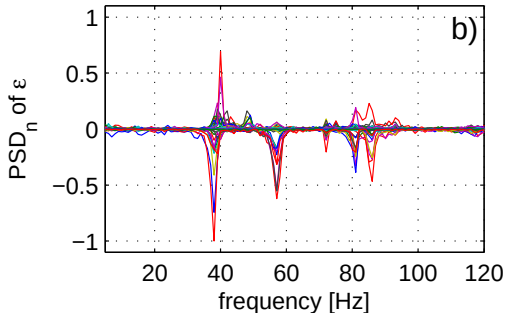

(b) Impact 1.7: Vertical hit on lower ring without coils/tiles on PSL

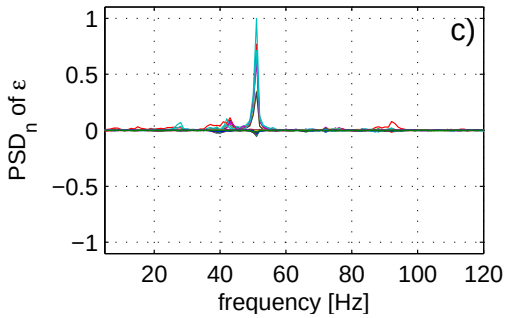

(c) Impact 2.4: Normal hit on upper ring with 16 coils mounted

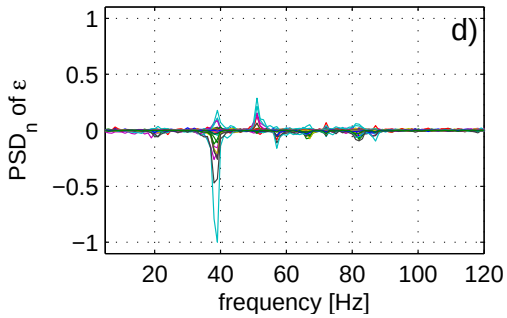

(d) Impact 2.7: Vertical hit on lower ring with 16 coils mounted

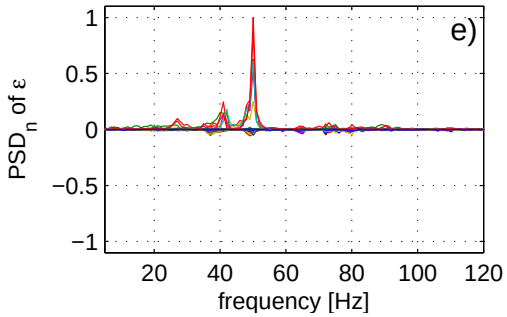

(e) Impact 3.4: Normal hit on upper ring with 16 coils and all tiles

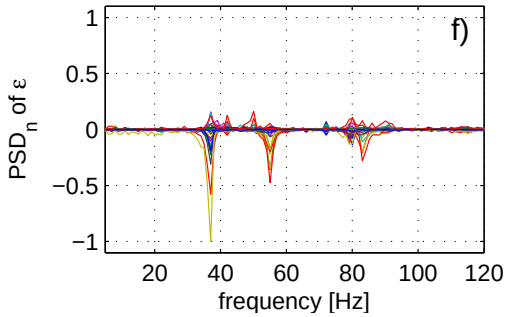

(f) Impact 3.7: Vertical hit on lower ring with 16 coils and all tiles

Figure 53: Hammer testing frequency spectra under different conditions

two adjacent poloidal legs either cancel out, if their currents have the same phase, or add up, if the phase is π. This resultant force is always directed normal to the PSL surface. The connection scheme of the power supply to the B-coils - called the 'recipe' - determines the spatial distribution (application points) and the orientation (polarity) of the forces. Figure 55 shows an example where an n=2 ringmode is excited using an adapted coil recipe. Plus and minus refer to a coil phasing of either zero (+) or π (−). One can imagine the coils with positive polarity having the tendency to turn in one direction (e.g. clockwise), and the others to turn in the opposite direction. Supposing that the points where these forces are applied become antinodes of the resulting oscillation, the only ring modes that can be excited in a straightforward manner with the given set of 8 B-coils per ring are the n=1,2,4 modes, as this setup offers a maximum of 8 positions to introduce forces

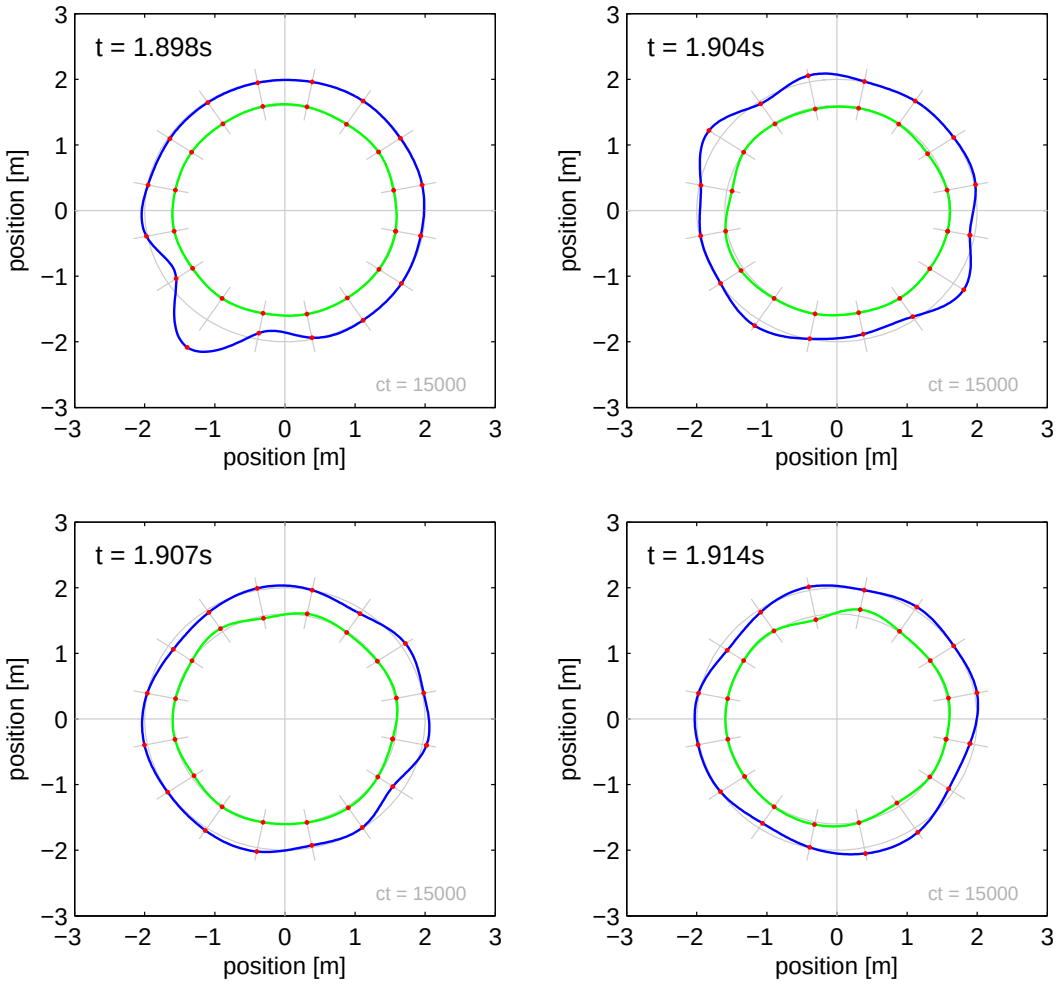

Figure 54: Travelling bending wave after hammer hit on upper ring in sector 1 (impact 1.3, no coils/tiles)

at. See figure 19 on page 24 to recall the corresponding modal shapes. Other forms like the triangular n=3 eigenmode cannot be excited properly, because even with a recipe with six loading positions, thereby supposedly producing six antinodes, these cannot be 60° apart in toroidal angle. Table 13 lists the possible recipes for one

ringmode	coil polarities	spatial variants
$n = 1$	$++++----$	4
$n = 2$	$++--++--$	2
$n = 4$	$+-+-+-+-$	1

Table 13: B-coil recipes for the excitation of bending ringmodes

ring, the mentioned variants refer to a load application rotated toroidally (in θ with respect to figure 9) to obtain a form with different angular orientation. Of course, reversing all signs of one of these does not make another recipe. The n=1 ringmode is a rigid body motion which does not involve bending of the PSL rings, so the PSL deformation diagnostic OSI is unable to measure the associated displacement. This mode is therefore not of interest here. If B-coil recipes with n=1 are ever to

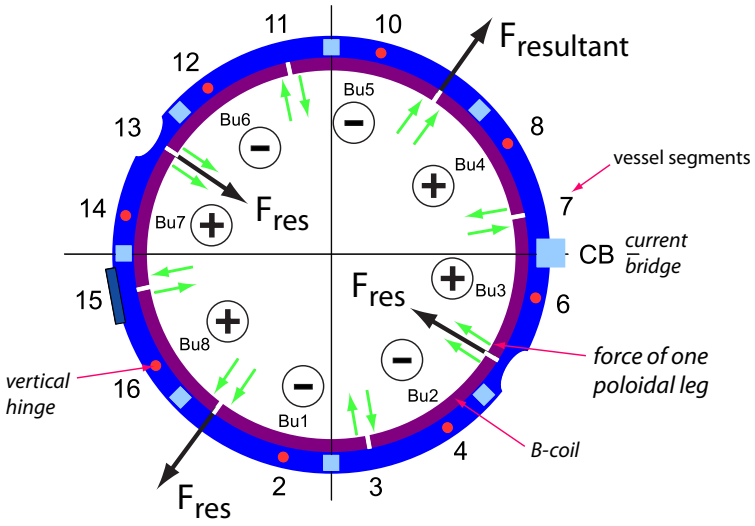

Figure 55: Force application on the PSL with n=2 recipe

be used with high alternating currents in the future, the PSL movements need to be observed by different means. If we now consider both PSL rings, we find two different recipes with n=4 and eight with n=2, differing in the toroidal orientation of the loading. The selection of recipes that were eventually used for the technical shots is presented in table 14. This selection represents the load cases estimated to be the most demanding for the structure. Every recipe is identified by a three-digit

recipe	n	Bu1...8 (upper coils)	Bl1...8 (lower coils)	even/odd
901		+		
905	2	− − + + − − + +	− − + + − − + +	even
906	2	+ + − − + + − −	− − + + − − + +	odd
906b	2	+ − − + + − − +	− + + − − + + −	odd
907	4	+ − + − + − + −	+ − + − + − + −	even
908	4	+ − + − + − + −	− + − + − + − +	odd

Table 14: Used coil recipes

code, those with equal polarity of upper and lower coils are named 'even', those with inversed polarity 'odd'. The recipe outlined in figure 55 is 905. The experimental AC converter is limited to a maximal current of around 120 A in continous operation. This is roughly *one tenth* of the design value of the planned AC power supply system for the internal coils. Nevertheless, every recipe was tested at low current first, and the current was increased only after a brief investigation of the obtained deformation. The applied 120 A create line loads in the order of $F_{max} \leq 5 \cdot B_t I_{coil}$ = 1.4 kN/m. The factor of 5 corresponds to the number of turns of each coil. As the toroidal magnetic field at the coil's position is lower than the nominal value at the magnetic axis, this is a maximum value estimate.

Due to a malfunction of the provisional AC converter, the n=2 tests were performed in voltage-controlled instead of current-controlled mode. This led to a slight current ripple and minor, frequency-dependent deviations of the current amplitude (<13%). Apart from that, the shots were carried out at constant current amplitude.

The frequency was gradually increased over 13 s for the shots with n=4 and over 14 s for the shots with n=2. One shot was performed at constant frequency. The experimental programme is outlined in table 15. In all cases, the coil current followed a sinusoidal waveform. The initial excitation frequency ranges were chosen based

shotnumber	n	up/low phase	recipe	current	frequency
27479			901	50 A	5-150 Hz
27480			901	115 A	5-150 Hz
27481			901	115 A	10-80 Hz
27482			901	115 A	30-60 Hz
27483			901	115 A	40-55 Hz
27484	4	even	907	50 A	40-55 Hz
27485	4	even	907	110 A	40-55 Hz
27486	4	odd	908	110 A	40-55 Hz
27487	4	odd	908	110 A	45-55 Hz
27488	4	odd	908	110 A	45-60 Hz
28021	2	odd	906	60 A	16-24 Hz
28022	2	odd	906	120 A	20 Hz
28023	2	odd	906	120 A	17-23 Hz
28024	2	odd	906	120 A	15-30 Hz
28025	2	even	905	120 A	15-30 Hz
28026	2	odd	906b	120 A	15-30 Hz

Table 15: Parameters of the 16 technical shots

upon a preliminary study of PSL frequency spectra after disruptive excitation and the finite element and analytical results mentioned in sections 4.1 and 4.2. Thereby, the relevant frequency range for every configuration was determined. The frequency window was subsequently narrowed according to the oscillation obtained in every shot, in order to map the structural response at a low sweep rate and with high frequency resolution.

Excitation by one coil

For broadband-excitation of all ringmodes within a given frequency interval, the applied forces should not favour particular modes by their spatial distribution. A point load excites any mode that does not accidentally have a node at the point of application. With the B-coils, generating a point load is not possible. Broadband excitation was therefore realised by application of an electrical current to one coil only (Bu1, according to recipe 901, cf. table 14). This applies a pair of forces to the PSL with a toroidal angular separation of 22.5°. Figure 56 shows time traces of several sensors as well as a frequency spectrum of all sensor signals. The spectrum (d) is based on 1000 data samples from t=4.2±0.5 s, where the excitation frequency rose from 46.3 to 57.4 Hz. The two sensors adjacent to the excited coil (a) show the largest strain amplitudes and are clearly phased by π. Directly opposite, the two

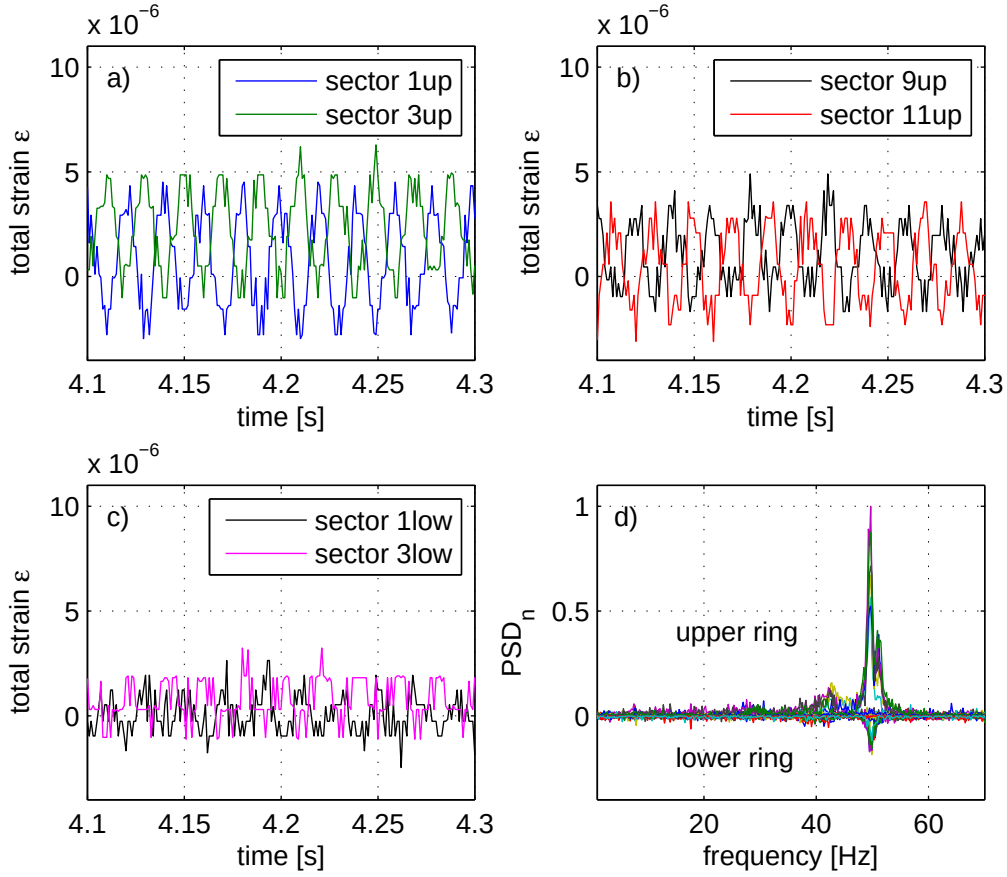

Figure 56: Strain data from discharge #27480, 115 A on Bu1, 5-115 Hz for 13 s. Sensors next to the excited coil (a), on the opposite side of the same PSL-ring (b), at the location of the excited coil on the other ring (c). Frequency spectrum of all signals from t=3.7-4.7s (f_{ex}=46.3-57.4 Hz) (d)

sensors in sector 9 and 11 on the upper ring (b) show a similar behaviour at slightly lower amplitudes. The lower ring also shows inverse phasing of the signals in sectors 1 and 3 (c), even though their signal-to-noise-ratio is smaller, making interpretation difficult. Despite the small load and the forces only being applied to two closely spaced positions on the upper PSL-ring, we see that the oscillation propagates to the whole structure of the PSL, to some extent. This impression is affirmed by the frequency spectrum, which exhibits a significant, sharp peak at approximately 50 Hz for the sensors of both rings. The top-view visualisation in figure 57 reveals that the upper PSL's notches in sectors 5 and 13 seem to participate above average in the overall oscillation. Once more, we see here that the deformation is not spatially localised at the position of force application.

Varying the frequency windows for the different shots while maintaining a constant duration results consequently in higher sweep rates for the larger frequency windows. The frequency-dependent system response is also a function of the sweep rate, if a frequency sweep is applied. For small sweep rates, the response approaches the static frequency response, which is usually of principal interest. In the present case however, it can be noticed that the spectral response of all five shots with recipe 901 is highly comparable. Figure 58 shows the spectra of 3 shots with sweep rates

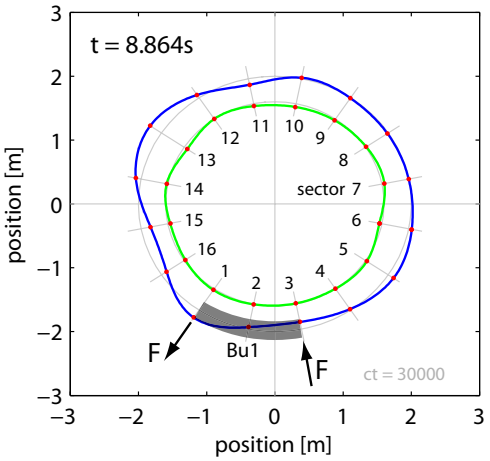

Figure 57: PSL shape during excitation by one coil (shot #27483), point forces in sectors 1 and 3

of 11.2, 5.4 and 2.3 Hz/s (top to bottom). These normalised spectra were calculated from the strain data of the whole excitation period (of 13 s). In the studied

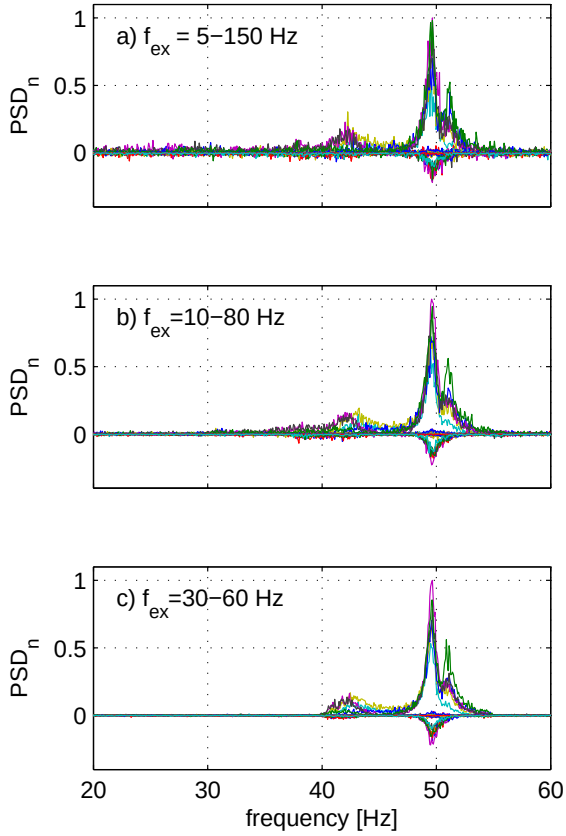

Figure 58: Frequency spectra of shots #27480 to #27482 (top to bottom) with different excitation frequency window, ramped in 13 s (recipe 901: Bu1 only)

range, the appearance of the response spectra is hardly affected by the sweep rate variation. One noticeable difference between the three plots is the reduced noise as the frequency window is narrowed. This is at least partly due to the simple fact

that the excitation frequency stays longer in a range with vivid structural response, leading to more cycles with considerable amplitude. This produces higher peaks in the frequency space and therefore less noise if these signals are normalised. The influence of the sweep rate on the *absolute* strain amplitudes will be investigated at the end of this chapter, where strain amplitudes resulting from different types of loading are compared.

Excitation with all coils: n=2

Out of the 8 different configurations for n=2 excitation with the B-coils, the three that seemed the most important were realised. These configurations were selected as they had the largest measured amplitudes of the n=2 mode after excitation of the PSL by disruptions. These chosen setups are the modes with antinodes at the notches of the upper ring in odd and even layout, and the identical load distribution with odd phasing, only rotated toroidally by 45°, i.e. one coil. The corresponding recipes are 905, 906 and 906b. The maximal strain amplitudes in the n=2 configurations are surprisingly low, only marginally higher compared to the tests with one single coil, considering the additional forces generated by the full set of 16 coils. Figure 59 gives an example of time traces from a discharge supplying 115 A to all coils with an n=2, odd recipe. The frequency was swept from 15 Hz to 30 Hz in 14 s, corresponding to a rise from 23.4 Hz to 23.6 Hz in the plotted time interval. The time traces show the sensor signals at the antinodes of the ringmode in segments 1, 5, 9, and 13. The signals plotted together in graphs (a), (b) and (c) are four segments - or one quadrant - apart, hence the inverse phasing under n=2 excitation. The lower PSL vibrates out of phase with the upper ring, in accordance with the odd coil recipe. The spectrum (d) of the strain data of the whole discharge shows two major resonance peaks, with the lower ring having a lower main resonance frequency in this configuration than the upper one. There is a secondary resonance on the lower ring at around the same frequency as the primary peak of the upper ring.

The response dependency from the loading distribution can be judged by comparing response spectra from shots with different coil recipes. Figure 60 gives a spectral overview of the six n=2 discharges that were realised. The spectra are normalised for better comparability and do not contain information about strain magnitudes. Some of the spectral lines, especially those in plot (c), exhibit a remarkable ripple.

The second shot with constant excitation frequency (b) naturally produced a single peak in the response spectrum. One valuable piece of information contained herein is the absolute response amplitude under static frequency conditions. The parameters of (a) and (c) vary only slightly in terms of the excitation frequency range, but the current and the loads were twice as high in the latter experiment. The peaks of the spectrum of (c) are more pronounced compared to (a). The frequency range was broadened for the following 3 shots. The prior impression of two distinct resonance frequencies of the upper and lower PSL ring is also suggested by plot (d). The maxima are broader here and no sharp peaks appear. The peaks on the high frequency side in the former examples (a) and (c) look sharper compared to case (d). This might be due to the excitation frequency window being too narrow, cutting off the response spectrum of (a) and (c). Contrary to the former examples, spectrum (d) clearly shows diminished amplitudes towards both boundaries of the excitation

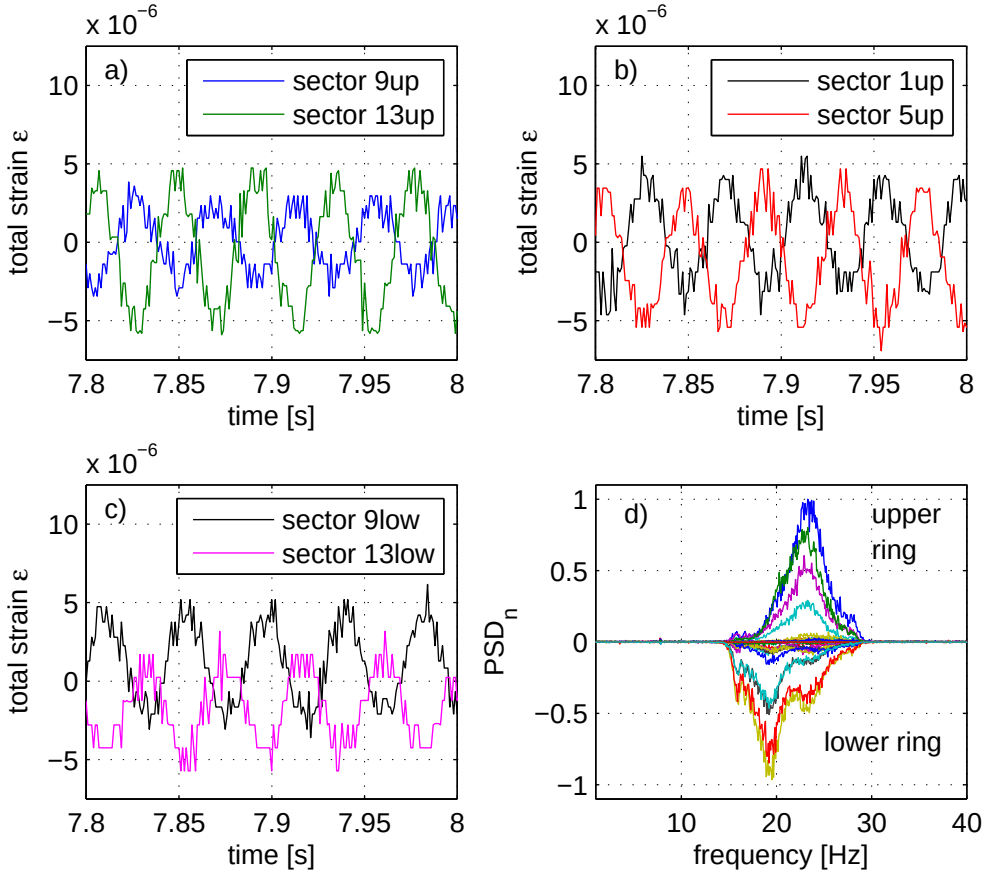

Figure 59: Strain time traces and frequency spectrum, recipe 906, n=2, odd, I_B=110 A, #28024

frequency range. One can therefore assume the whole n=2 resonance domain to be covered by this experiment, i.e. that the excitation frequency range covers all high-amplitude structural responses that can be excited with this coil recipe. For that reason, this parameter set was used as a reference and repeated with two other recipes. The even configuration (e) produces a primary peak of the lower ring sensors, comparable to the previous shots. The upper ring shows practically no response apart from a small peak, or rather a flat bump, at the frequency of the lower ring resonance, or marginally lower. The spectrum of the last shot (f), with the force application turned by one coil and odd phasing, is completely different. Interestingly, one sensor on the lower ring (magenta) shows PSD values that are superior to the others by a factor of 2 or more. This signal belongs to the strain gauge in sector 15, opposite the current bridge, where the PSL half-rings are bolted together with a solid back plate. There is a peak of the lower sensors at the low frequency boundary, so the frequency window may have to be extended to lower frequencies to show all n=2 resonances with this recipe. The upper ring shows only weak reactions to the excitation around 22-28 Hz. The primary peak of the lower ring lies at 23 Hz. With the ordinary n=2, odd recipe (d), *the upper ring* showed a maximum at this frequency.

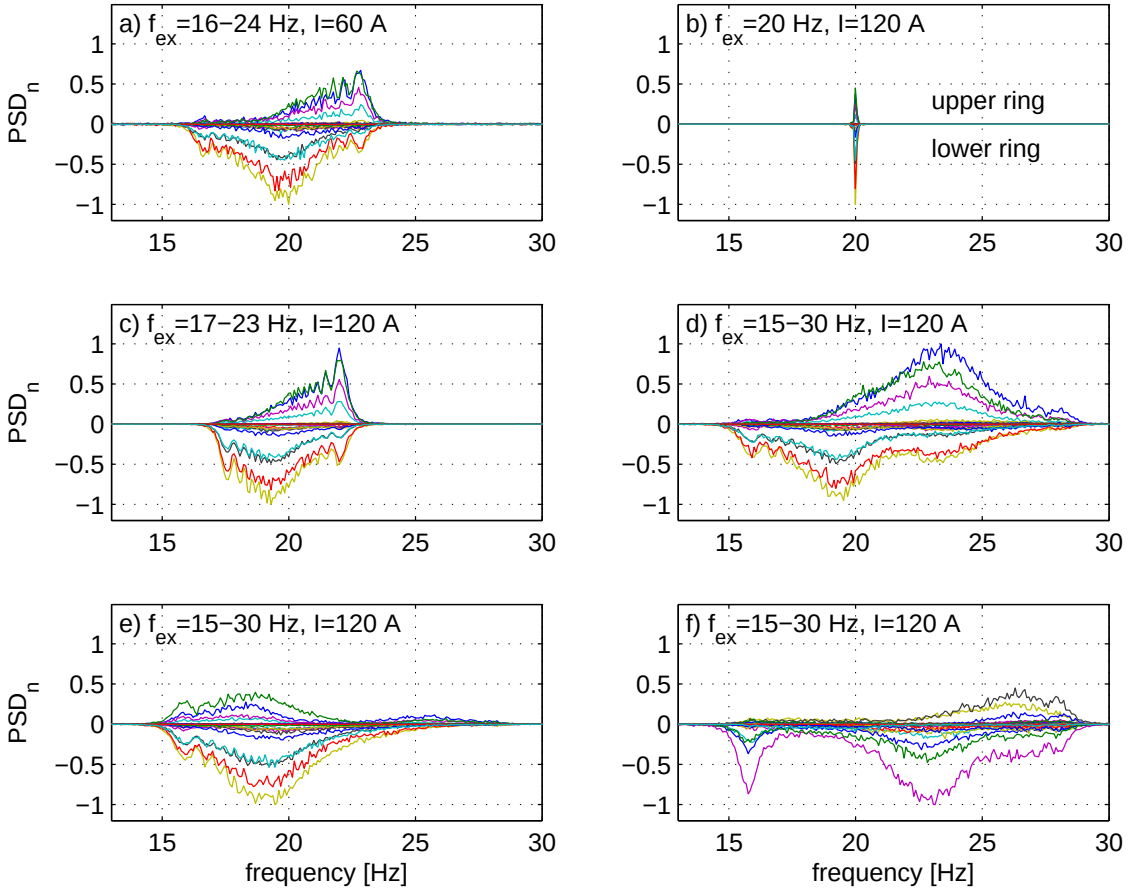

Figure 60: Response spectra of n=2 technical shots. Configuration: Recipe 906 odd (a to d, #28021-24), recipe 905 even (e, #28025), recipe 906b odd & turned by 45° (f, #28026)

Excitation with all coils: n=4

As mentioned before, n=1 deformations of the PSL cannot be detected by the optical strain sensors. Therefore, the n=4 eigenmodes are, apart from the n=2 modes treated just before, the only other configuration of interest that can be excited properly with the 16 B-coils. Contrary to n=2, there is only one possible orientation for recipes exciting n=4 PSL ringmodes. These can be either of even or odd polarity. Five technical discharges were realised, with frequency sweeps in the range of 40 to 60 Hz. Regarding both the higher order of the eigenmode and the stronger damping usually associated with higher frequencies, even lower strain amplitudes than with n=2 were expected. This was not the case at all. The measured maximal strain values were greater than those in n=2 configuration throughout the experimental parameter range. Figure 61 presents an overview comparing the odd and even configurations using the example of shots #27485 and 88. The horizontal axes of time and frequency are aligned such that the excitation frequencies, plotted as a function of time in (e) and (f) correspond to the frequency axis of the response spectra in (g) and (h). The four uppermost plots contain the time traces of the sensors in sectors 12 and 13 on the upper and lower ring. These are two of the presumed locations of

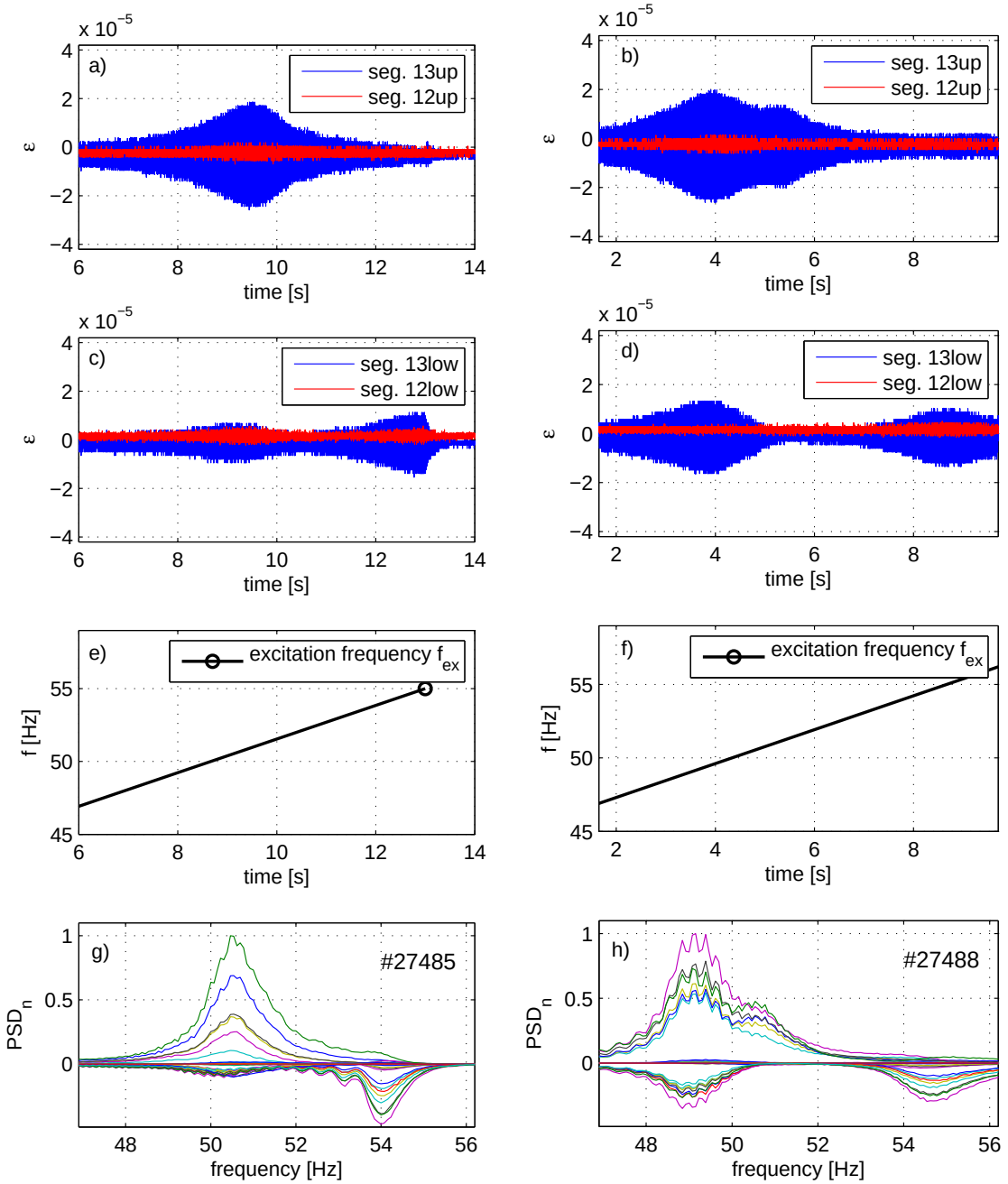

(a) Recipe 907 (even), f_{ex}=40-55 Hz (#27485) (b) Recipe, 908 (odd) f_{ex}=45-60 Hz (#27488)

Figure 61: Overview of two n=4 technical shots, 110 A on all B-coils, even and odd

the nodes (even sectors) and antinodes (odd sectors) of deflection and bending of the PSL, given the forcing on the poloidal coil legs in the middle of the odd sectors. The time traces from segment 12 of both rings indeed suggest the presence of the nodes of the oscillation. For an n=4 mode, having a toroidal separation between two nodes of 45°, the middle of sector 13 and all other odd sectors is therefore likely to be the site of the anti-nodes. The sweep rate was identical for the two shots, but the frequency window was lower by 5 Hz in the left example. The frequency ramp ends at 55 Hz in this case, when the strain signal from the lower ring's sensor in

segment 13 (c) still shows a considerable amplitude. The direct comparison to (d), where the ramp goes up to 60 Hz, suggests that the upper (higher-frequency) part of this resonance peak was cut by the excitation frequency range being too narrow. This motivated shifting the range for shot #27488.

In the even case shown on the left, two resonance frequencies that can clearly be attributed separately to the upper and the lower ring occur. The upper ring's resonance occurs at 50.5 Hz, with very little contribution from the lower ring (see (c) at t=9 s). The lower ring's resonant peak lies at higher frequency, at around 54 Hz, but cannot be located precisely due to the limitation of the excitation frequency range. The maximum strain amplitudes of the upper ring are clearly higher than those of the lower ring.

In the odd configuration, the most remarkable difference is the occurrence of a resonance with substantial oscillations of both rings at 49 Hz, lower than both separate resonance frequencies in the even case. These peaks are also visible here, still being unique to one of the rings, but the upper ring's response at 50.5 Hz is covered to a large extent by the common oscillation (h). There is an apparent undulation in this spectrum, which is hardly observed in the even case (g).

For both configurations, we can state that the frequency spectra (bottom, g/h) do not seem to show their peaks exactly at the frequency where the time traces of the strain signals (top, a/b) exhibit the highest amplitude. Instead, they are slightly shifted in frequency. This means that the system response frequency does not exactly correspond to the instantaneous excitation frequency, probably resulting from and depending on the non-zero sweep rate.

Comparison of all shots with excitation by internal coils

The maximal strain amplitudes measured during the technical discharges depended primarily on the coil current and the recipe, but also on the excitation frequency sweep rate. Figure 62 presents the maximal strain amplitudes out of all strain signals over the whole duration of the discharge in question, without considering the location of the sensor. The amplitude $\Delta\epsilon_{max}$ is the total, peak-to-peak strain stroke. For single-coil excitation and the n=4 recipes, it can generally be stated that the response of the upper ring is much more pronounced, whereas for n=2, the lower ring's response tends to be marginally higher (not shown, consult figures (58), (60) and (61) for details). The error bars represent the steady-state noise of the optical sensors. The first shot of each series (#27497, #27484 and #28021) was realised at reduced current for the sake of machine safety, before switching to maximum current for the rest of the shots. This explains the large difference of the associated strain values. The sweep rate dependency is reflected in the slight rise of the amplitude between shots #27480 and #27483, where the sweep rate was gradually decreased. This relation is addressed specifically in figure 63. It indicates that a further decrease of the sweep rate $\dot{f}$ would have little effect. It must be admitted that the number of datapoints is low while the noise is not. The relation of sweep rate and amplitude is less explicit for the n=2 and n=4 discharge data, where different recipes were used to excite different mode configurations, making the maximal values less comparable.

During both the n=4 and n=2 test series, all 16 B-coils were actuated with virtually the same current. The resulting strains differ by a factor > 5. Surprisingly,

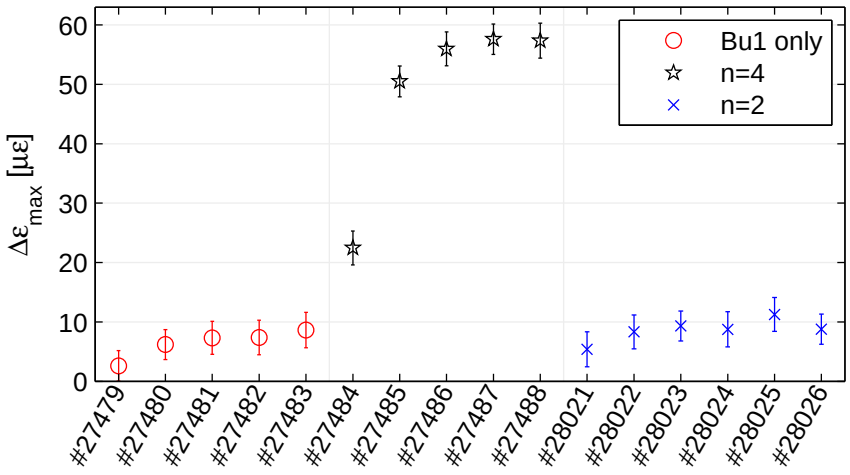

Figure 62: Maximal strain amplitudes of technical shots

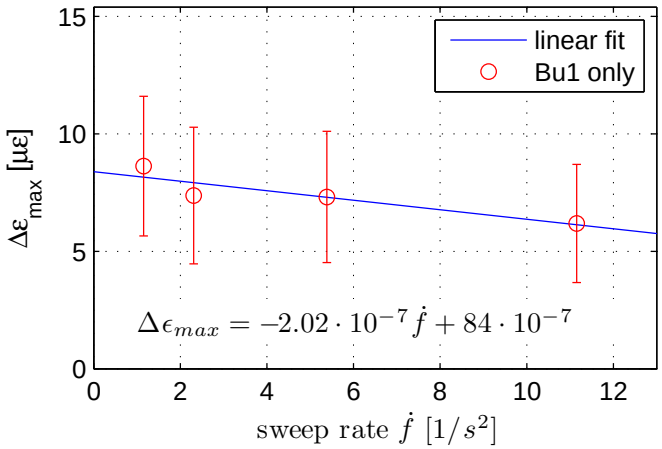

Figure 63: Amplitude over sweep rate of the single-coil tests at 115 A

the amplitudes reached during the n=2 tests exceed only slightly those from the first series, when just one coil was powered (see figure 62).

As for the dependence of the maximum strain amplitude on the B-coil current, only the first two shots of each series allow an assessment. Each of these pairs features not only the same coil recipe at different electric currents, but also identical sweep rates. Figure 64 presents the ratio of strain amplitude to current as a function of the current itself. Thus, the datapoints represent the deformation of the PSL per ampere of current supplied to the B-coils. For comparison purposes, additional horizontal lines through the datapoints are plotted. Constant values of $\Delta\epsilon_{max}/I_B$ over a range of I imply proportionality of strain and current. The measurements at least show agreement, if not confirmation of proportionality, even if the errors in the range of low strain are non-negligible.

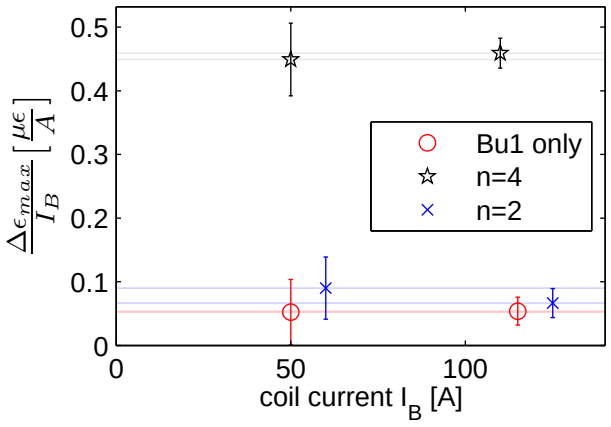

Figure 64: Ratio of strain amplitude to internal coil current as a function of this current (6 shots: #27479-80 (Bu1 only), #27485-86 (n=4), #28021-22 (n=2))

4.4 Deformation measurements during plasma operation

The sources of the forces acting on the PSL structure during plasma operation are diverse. Two fundamentally different categories can be distinguished: The point loads due to the B-coils, which were already discussed in the previous section, and all other in-service loads, distributed along the rings' circumferences, which result from currents induced in the PSL that interact with the poloidal magnetic field. The major toroidal non-uniformity of these loads results from the current bridge. The bridging resistors of the current bridge (see section 2.1.2) do not play an important role in this context by causing loading asymmetries or in any other way. The induced currents are linked to specific working conditions of ASDEX Upgrade and in most cases, lead to characteristic patterns in the PSL deformation.

The most important causes of loadings during operation have been identified and are presented in the following. These are: major plasma disruptions, B-coil operation and the impact of the real-time plasma position control system in combination with movements of or changes in the plasma. The control system reacts to plasma movements first of all and essentially by actuating the inner control coils (COIo/COIu, fig. 3). The effect of the current induced thereby in the PSL is visible, for example, in the presence of ELMs, or when the plasma is cyclically shifted up and down for ELM triggering (called 'wobbling' or 'kicks', see section 4.4.3). With highly elongated plasmas, the structural response tends to be more pronounced. In one documented case, even the currents of the lower vertical field coils led to a considerable, quasi-static deformation of the PSL, while they were ramped down at the end of a plasma discharge. Of course, the overall magnetic flux topology and its time derivative, which together determine the PSL current, result from a multitude of influences. But often, one effect can be identified that dominates the PSL's motion, for instance thanks to the different time behaviour of the loadings. Disruptions can be considered as impulse forces exciting free, structural oscillations while in other cases, the loading itself is highly oscillatory.

The measurements of the PSL deformation for all these load cases, especially from the disruptive excitations of the structure, contain precious information about

its oscillatory properties. Disruptions offer high absolute strain values and hence favourable signal-to-noise ratios, but contrary to the technical shots from section 4.3.2, the direction and magnitude of the applied forces are not known. The second important difference is that the frequency and magnitude of the load cannot be chosen systematically.

To provide an idea of the strains reached during service and the percentage of discharges with high strain magnitudes, the maximal, absolute strains measured during the first 300 shots that were recorded are shown in figure 65. The shotnum-

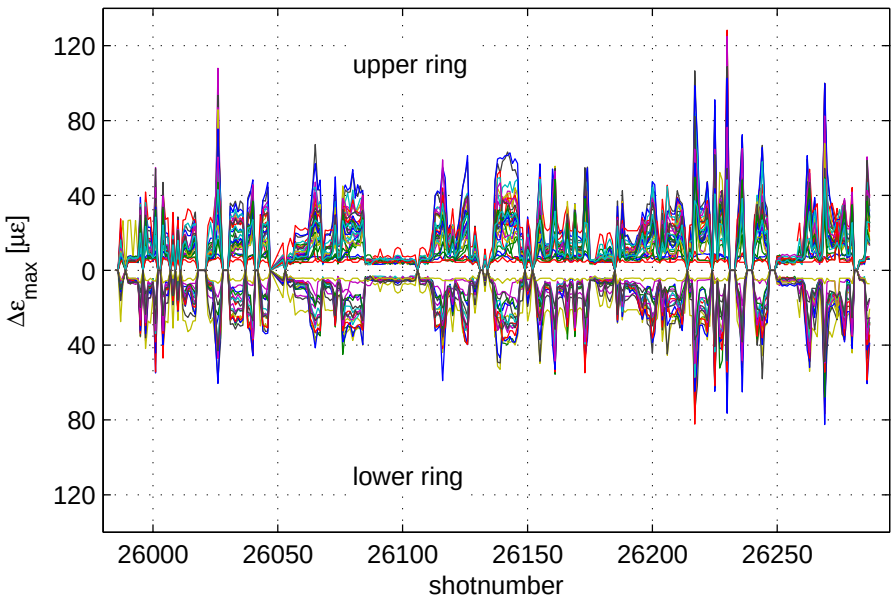

Figure 65: Strain amplitudes of shots #25985 to #26284

bers with zero absolute strains are unsuccessful shots[42] where the diagnostic was not triggered. Shots without plasma in which the diagnostic was triggered, such as the discharges #26250 to #26258, exhibit only stand-still noise (about 6−8 $\mu\epsilon$). The disruptive shots, presented in the next section, clearly show the highest strain values.

4.4.1 Excitation by disruptions

The measurement data of the PSL deformation during plasma disruptions suggests a very high, instantaneous and evenly distributed loading taking place at the time of the plasma current quench, and resulting in a peak of the strain signal of the majority of the sensors. After the plasma has disappeared, a phase of structural, damped oscillations of the PSL which decay during several hundreds of microseconds follows. Such an example is presented in figure 66, which shows experimental data from shot #26026, where a disruption was triggered intentionally by deactivating vertical position control. The strain signals of all PSL sensors, the time trace of the

[42]When a problem arises in an early phase of a discharge, the shot is aborted and no trigger signals are sent to the diagnostics. Consequently, these measurements do not start acquisition and no data is stored for the shot in question.

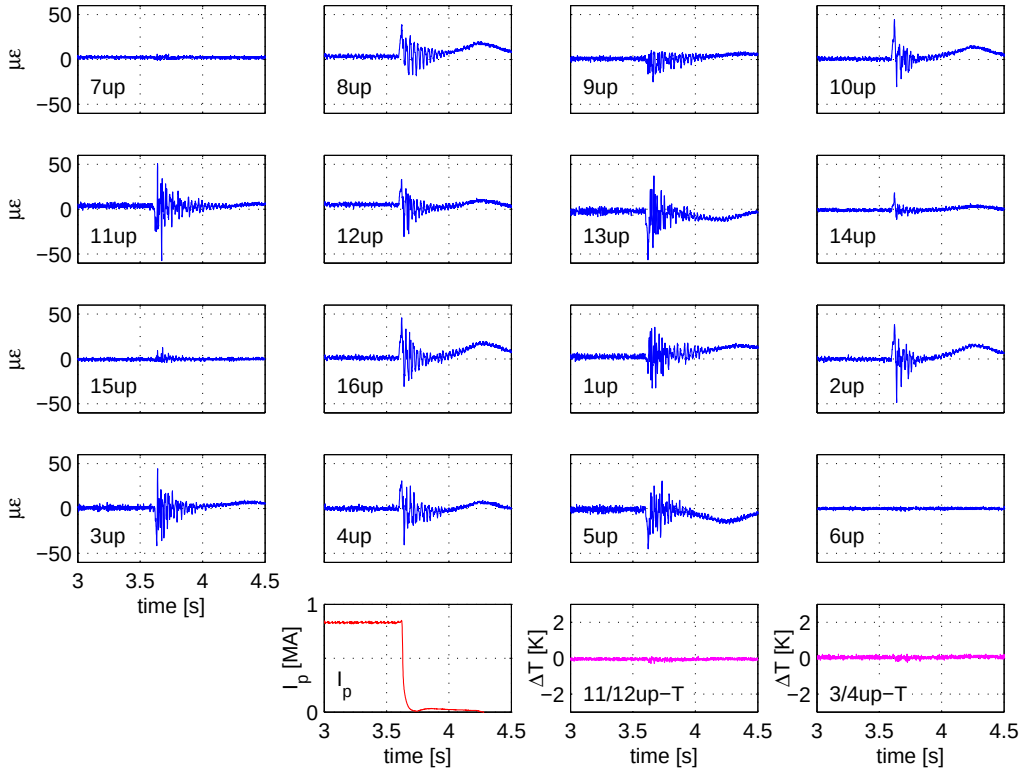

(a) Strain (blue) and temperature (magenta) signals of upper PSL, plasma current (red)

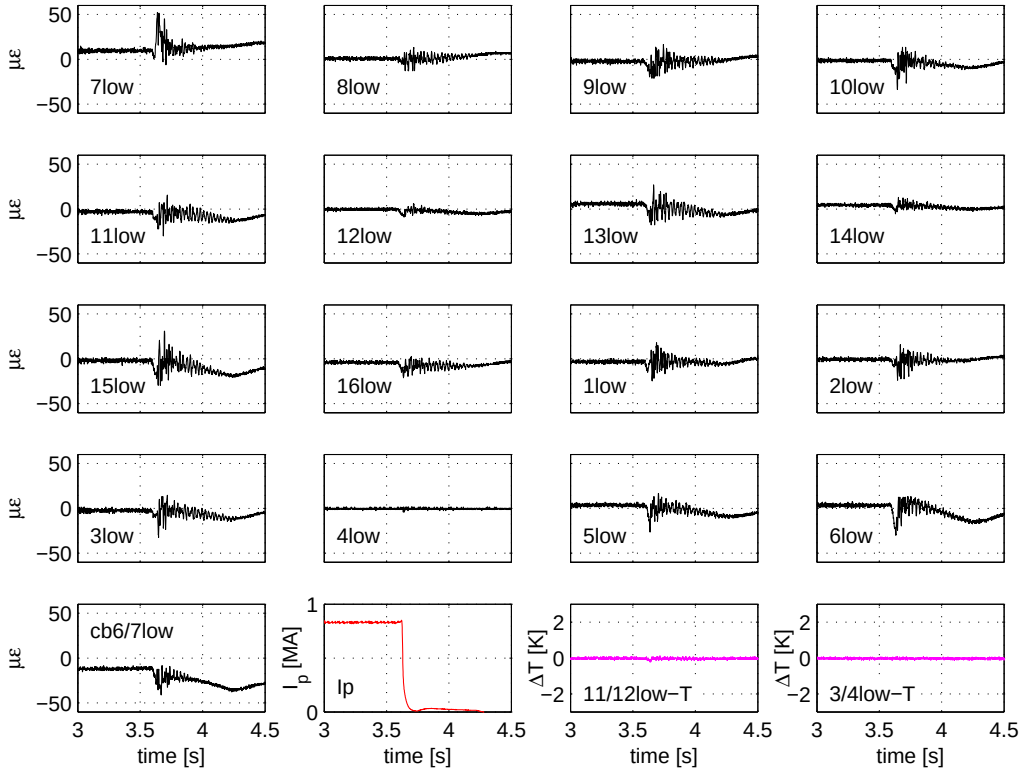

(b) Strain (black) and temperature (magenta) signals of lower PSL, plasma current (red)

Figure 66: PSL related measurements from disruptive shot #26026

plasma current (I_p) and the four temperature monitoring signals are shown. The lower ring is equipped with one sensor more than the upper ring, which is the lower current bridge strain sensor shown on the bottom left. Each row represents one quadrant (4 sectors) of the corresponding PSL ring, starting in sector 7, next to the current bridge, analogous to the top-view representation presented in chapter 4.3 (fig. 48 on p. 59). On average, the peaking is more intense on the upper ring than on the lower one. At several positions on both rings, the response is very weak. The temperature signals confirm the absence of short-timescale shifts, which would necessitate temperature compensation of the strain signals.

Even though all disruptions feature the above mentioned similarities with respect to their mechanical effect on the PSL, they never manifest exactly the same behaviour. Before the current quench, some shots show strong oscillatory bending of the rings and others do not. For different disruptions, the maximal deformation at the time of the current quench is located at different positions and varies strongly in amplitude. The decay of the structural oscillation after the plasma has disappeared sometimes takes considerably more time than in most of the cases. The appearances of the post-disruptive frequency spectra of the strain signals are quite diverse. Some of these qualitative observations are directly connected to the plasma behaviour, e.g. the direction of a vertical displacement event (VDE, cf. chapter 1.2.2), or performance parameters like the plasma current, but few of them can be interpreted intuitively. Therefore, a set of 11 disruptions was selected for a detailed investigation, with a focus on the frequency spectra of the oscillation in the post-disruptive phase. Of the first 350 shots following the start of the OSI diagnostic (#25986 to #26335), 236 were plasma discharges and 67 of these disrupted. Out of these, 23 disruptions caused strain amplitudes above 30 $\mu\epsilon$. The aforementioned 11 discharges were selected due to their dissimilarity in oscillatory behaviour with respect to the criteria mentioned before. The main parameters of these discharges are outlined in table 16. The variable $t_{Ip,quench}$ denotes the point in time of the

shotnumber	I_p [MA]	B_t [T]	$t_{Ip,quench}$ [s]	$\lvert\epsilon\rvert_{max}$ [10^{-6}]	direction
# 26026	0,80	-2,48	3,6	54	up
# 26139	1,00	-2,49	1,57	30	up
# 26217	1,00	-2,49	6,81	53	down
# 26218	1,00	-2,49	5,15	36	up
# 26225	1,00	-2,50	5,79	46	down
# 26230	1,00	-2,49	2,79	64	up
# 26236	1,00	-2,50	4,43	36	up
# 26244	1,00	-2,40	3,03	33	up
# 26269	0,70	-2,49	1,22	50	down
# 26314	1,00	-2,49	1,68	45	down
# 26335	1,20	-2,40	1,34	48	down

Table 16: Discharge parameters of 11 disrupted shots

plasma current quench, when the plasma current decreased below 10% of its initial (set-) value. The rightmost column indicates whether the plasma was moving up- or downwards just before disrupting. This does not mean that each of these discharges was terminated by a vertical displacement event, which was not the case.

The discharges in this selection were conducted at almost identical toroidal field magnitudes. Figure 67 presents the plots of their normalized power spectral density

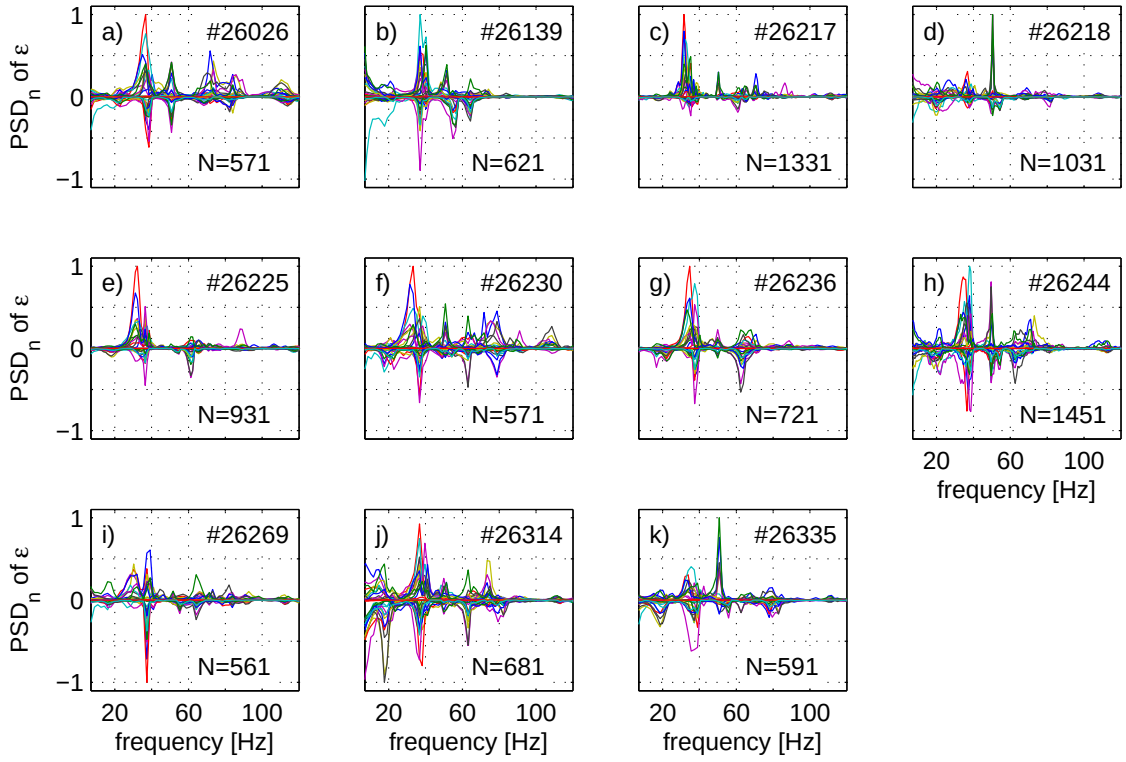

Figure 67: Post-disruptive frequency spectra of the strain signals of 11 disruptions

(PSD) over the frequency of their strain signals. The indicated number of samples N corresponds to the examined time interval in ms (while sampling at 1 kHz), always starting immediately after the current quench. This window length is the time until the structural oscillation is damped to noise level, after which a further frequency analysis would be useless. Each plot is normalised to its maximum PSD for better comparability, accounting for the unknown and potentially strongly varying excitation forces. As before, the lower rings' sensors are plotted below the zero line and those of the upper ring are shown above. The traces of the individual sensors are distinguished by color.

The analysis of these frequency spectra allows a few major remarks. First, both rings show the strongest responses in a frequency range between 30 and 40 Hz. The peaks in this range are broad, spanning over about 10 Hz in some cases. This might be due to the Fourier transformation of the damped oscillation: The decreasing amplitude is represented in the frequency domain by oscillations with slightly different frequencies, the superposition of these corresponds to a damped oscillation, until the amplitude reaches zero, like the beat in acoustics. Nevertheless, in some cases the clear separation of peaks in this range suggests the existance of at least two distinct oscillations on the upper ring (see e,g,h,j). As for the lower ring, the peak is often situated at a slightly higher frequency. Comparing the 11 examples, it appears that these oscillations (30-40 Hz) can occur much more pronounced on one ring than on the other (see c,e in contrast to i,k). Second, both rings exhibit a very distinct, narrow peak at 50 Hz (a,d,h,k). Third, the lower ring shows activity below 20 Hz,

with a recurring local maximum at 18 Hz, whereas the upper ring generally displays less response in this range. Fourth, there are other peaks, like the resonance at 61 Hz, that appear repeatedly at certain frequencies, but these are smaller and show a less explicit pattern than those discussed previously.

The forces on both rings are, except for those caused by B-coil activity, directly related to the electrical current in the PSL, which, in turn, depends on plasma parameters. Figure 68a displays the vertical plasma position and the plasma current for disrupted discharge #26230. Figure 68b presents a strain signal of the upper ring plotted together with the PSL current. The current shows two principal peaks

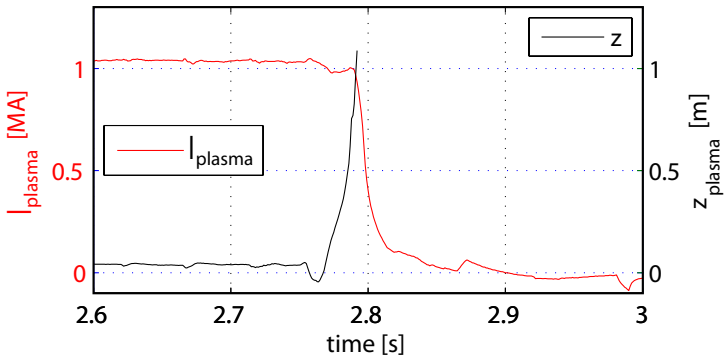

(a) Vertical plasma position and plasma current

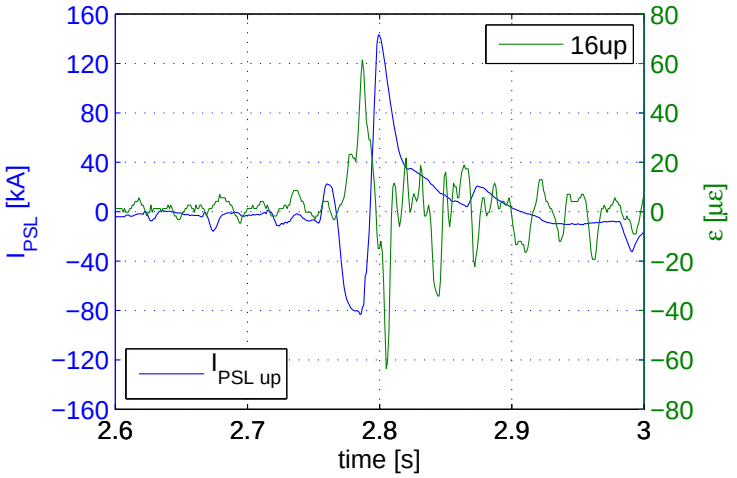

(b) Upper PSL electric current and sector 16 strain signal

Figure 68: Plasma and PSL parameters during a disruption (#26230)

in opposite directions before slowly approaching zero. The strain signal reaches extremal values slightly after these current maxima, and shows a persisting mechanical oscillation while the current fades out. This behaviour of rapid current decay and abiding structural response was observed during the majority of the investigated disruptions and for most sensor signals, although some of the sensor signals had opposite sign.

4.4.2 B-coil induced bending during plasma operation

During plasma operation, the internal coils of ASDEX Upgrade have been operated only in direct current, i.e. below all relevant PSL bending resonance frequencies, up to the present day. The AC supply used for the technical discharges from section 4.3.2 was applied for testing purposes only and is very limited in current. Just like during the technical shots, the B-coils experience line loads at their poloidal legs directed perpendicular to the PSL surface when operated during a plasma discharge. Additionally, forces on the long, toroidal legs arise due to the presence of a poloidal magnetic field[43]. The forces are proportional to the coil current and the magnetic field component perpendicular to this current. This causes the loads (per meter) on the short coil legs to be much larger than those on the long legs, because the poloidal component of the magnetic field is smaller than the toroidal component, usually by a factor of around 5.

The primary differences between B-coil loads during plasma operation compared to the technical discharges is that the overall magnetic field topology is much less steady, mostly due to effects of the plasma current and the plasma position control system. Furthermore, the B-coil currents and hence the loads are static, and dynamic response of the PSL structure can only be observed in some shots as a slight overshoot, when the coils are switched on or off. Resonance effects, therefore, do not play a role in this context. However, the deformation of the PSL rings is not negligible, as the currents are of the order of 1 kA. Figure 69 presents a typical example, where the strain signal has been inverted for simple comparison. The axis limits are set accordingly. The strain sensor in segment 13 on the lower PSL is

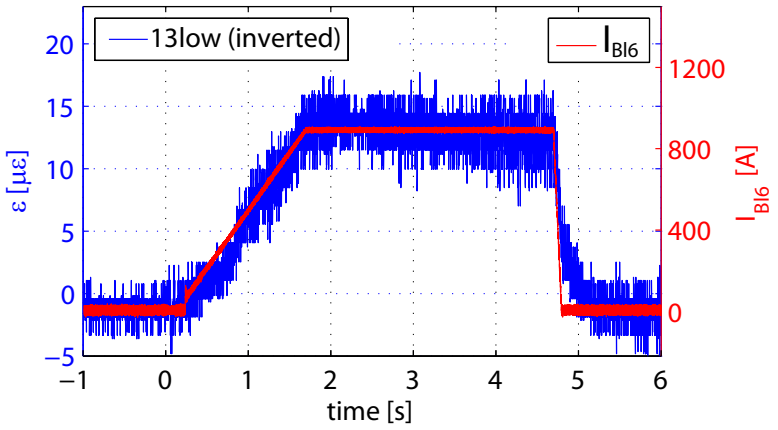

Figure 69: Quasi-static PSL deformation due to DC B-coil operation (#26032)

located at a poloidal leg of coil Bl6, where the point load is applied. We can see a slight reduction in strain magnitude during the flat-top phase of the coil current. This effect might result from a reduction of the toroidal magnetic field strength (B_t) by 10% from 1.7-4.7 s during this discharge.

This kind of deformation pattern can generally be found during discharges with high B-coil currents when a toroidal magnetic field is present. Typical maximal

[43]These loads induce torsional moments in the rings that cannot be detected by the strain sensors.

strain values[44] are in the range of 30±2 $\mu\epsilon$ for the upper ring and of 20±1 $\mu\epsilon$ for the lower ring at coil currents of 915±10 A. The flattop of the strain signal is usually much more disturbed due to the secondary effects discussed in the following.

4.4.3 Control system related deformation

Under plasma operation conditions, the PSL strain signals show a couple of recurring, typical patterns that do not belong to any of the previously discussed categories. These must be related to electrical currents induced in the PSL by a change of the magnetic flux permeating it. The global magnetic configuration of ASDEX Upgrade is determined by a multitude of inputs, some of which have been shown to be crucial for the loading and the deformation of the PSL. These are the plasma's position and current, and the currents in the vertical field coils, especially the inner control coils (CoI). For all coil and coil current designations, see figure 3 on page 8. The plasma position is, like a lot of other plasma parameters, feed-back controlled by the discharge control system (DCS). Therefore, any change in the plasma position and the control coil currents are closely linked. This means that the effects on the PSL due to the magnetic coils that compensate the plasma's movements and the effect of the plasma itself cannot be distinguished by a simple analysis of the strain measurements. This would be beyond the scope of this work and is unnecessary for a force analysis, which can be done based on the PSL current measurements. But identifying the typical PSL loadings and the operation conditions under which these occur allows an assessment of the total operational demands, e.g. in terms of a fatigue load spectrum based upon the PSL load history.

A reasonable distinction of these loading conditions is by frequency of the response of the PSL: Vibrations above 5 Hz are considered as dynamic deformations and those below as quasi-static and independent of the oscillatory properties of the structure. This limit is based on the observed frequency spectra described before. The PSL structure generally shows only very little response below 5 Hz, even when it is excited by loads that may be considered as broadband excitations like the impulse forces of a hammer or a plasma disruption. Thus, 5 Hz is likely to be much lower than the first resonance frequency. The structural response to excitations below this limit consequently follows the time behaviour of the loading.

Figure 70 illustrates an example where quasi-static stresses of the PSL correlate with the vertical field coil currents. This is data from the same discharge portrayed in the disruptions section, focussing on the post-disruptive phase, here. The great similarity of the strain and current signal traces suggests a direct relation. The plots contain, from top to bottom, the vertical field coil currents, PSL and control coil currents and strain sensor signals from the upper PSL ring. The gray vertical lines mark significant time points, the leftmost designating the plasma current quench (t_1=3.6 s) coinciding with the PSL current peaking. The middle and the right one highlight the point of inflexion of I_{V2u} (t_2=4.2 s) and the time when all vertical coil currents have reached zero (t_3=5.7 s) and the PSL current decays according to its intrinsic time constant. The lower graph depicts the strain measurements at the upper ring's 'notches', the positions with minimal cross-section and bending

[44] Data from quiescent, non-disruptive B-coil conditioning discharges #26142-46. B_t=-2.4±0.1 T, I_p=0.8 MA, recipe 211.

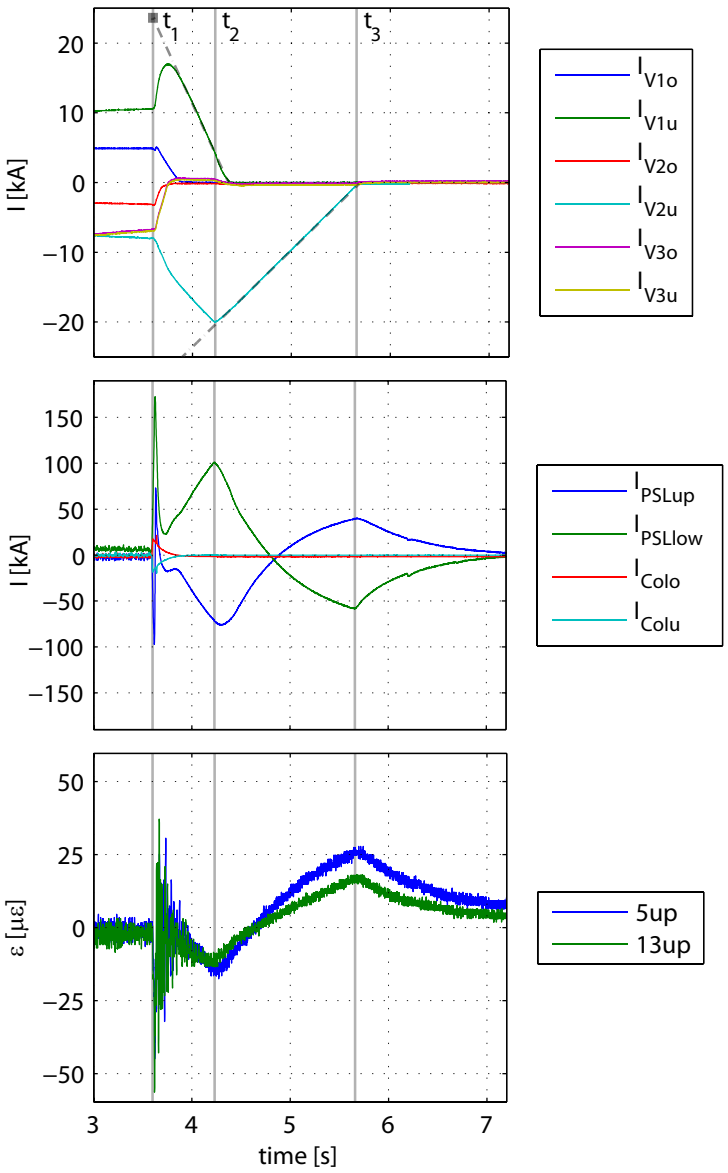

Figure 70: Disruption followed by quasi-static PSL bending due to vertical field coils (#26026)

stiffness. The relation between the PSL current and these strain traces is striking. The disruption produces a single peak of the PSL current and a peak with post-pulse oscillation of the strain signals. The current of the lower vertical field coil number 2 (V_{2u}) shows a significant post-disruptive drift. The (absolute) inductive current in both PSL rings is rising continuously, reaching a climax at t_2, when the slope of I_{V2u} inverses. It then reaches a secondary maximum with opposite sign at t_3, when I_{V2u} has reached zero. After the post-disruptive oscillation of the PSL has ended, the deformation follows roughly the trend shown by its current (I_{PSLon}). At 7.2 s, the PSL currents and the strain signals have attained constant values. The final strain values differ slightly from those prior to the disruption.

In this particular example, a complex interaction between the measured and reference values of the different vertical field coil currents lead to the excessive

post-disruptive activity of lower coils V_{1u} and V_{2u}. Before the position control was disabled, the plasma was given a 'kick' upwards by increasing the reference value of its z-position by roughly 10 cm. Thereby, the reference value of the inner control coil (C_{oI}) currents instantly jumped to around $\pm$20 kA (80% of the design maximum, not shown in figure). The vertical coils V_{1u} and V_{2u} received a similar command in order to allow the inner control coils to reduce their currents while maintaining the same magnetic field configuration and effect on the plasma. This is routinely done, owing to the low flux limit of the C_{oI}-coils. When the plasma touched the wall at 3.63 s and the discharge disrupted, these reference values were not set to zero, but to linear trajectories, starting at their high initial set-values (dashed grey lines). This explains the post-disruptive evolution: Both V_{1u} and V_{2u} ramp down after meeting these target ramps, which took a much longer time for V_{2u} due to its higher inductance.

An example for a typical PSL response of the second category (fast dynamic deformation) is the reaction to the magnetic triggering of ELMs. This method of ELM control, also called 'wobbling' or 'kicks', was first demonstrated in TCV (Tokamak à configuration variable) in 2003 [64] and could be reproduced in AUG one year later [65]. Wobbling is the intentional, typically cyclic shifting of the plasma column in the vertical direction by actuation of the plasma position control coils. If the triggering is successful, the ELM frequency locks to the frequency of the plasma displacement. It was shown that vertical excursions are efficient in this respect, whereas radial excursions are not [66]. The time behaviour of the displacement typically follows a waveform of trapezoidal, triangular or approximated sinusoidal shape. The shift of the plasma and the oscillatory actuation of the magnetic coils are reflected in a characteristic, mechanical oscillation of the PSL. But not only intentional plasma shifts provoke such a reaction of the mechanical structure. Similar effects are observed in discharges without wobbling. Here, the 'natural' oscillations of the plasma column due to its vertical instability and the stabilisation by the control coils are the origin of cyclic induced currents in the PSL rings. Highly elongated plasmas with accordingly lower vertical stability exhibit larger vertical displacements and reach higher velocities. This results in higher inductive PSL currents and hence higher forces. One has to think of the plasma being pulled on violently from above and below, while a small force stabilises it, that can only be modified after a constant time-step. Figure 71 presents the strain signals of one quadrant of the upper PSL ring, from a discharge with magnetic ELM triggering (top, black) and another discharge without (bottom, green). The latter is a high-current, high-elongation shot in the so-called ITER-like configuration. The PSL shows a clear response to the wobbling, which was applied from 5.5 s to 5.8 s. However, the amplitudes reached during the second discharge are much larger, especially in sector 8. The time development of this signal suggests a resonant effect. Figure 72 shows the strain data together with the PSL current, allowing a closer investigation. There is an enhancement of the ripple of the PSL current and a matching strain signal with a slight time offset in the discharge with magnetic ELM triggering (a). The other shot obviously shows a different mechanism (b), as the peak-to-peak amplitude of the current does not change significantly in the displayed time-interval, contrary to the amplitude of the structural response. This might be related to the change in frequency of the PSL current and the associated oscillating Lorentz force on the ring, catching a structural

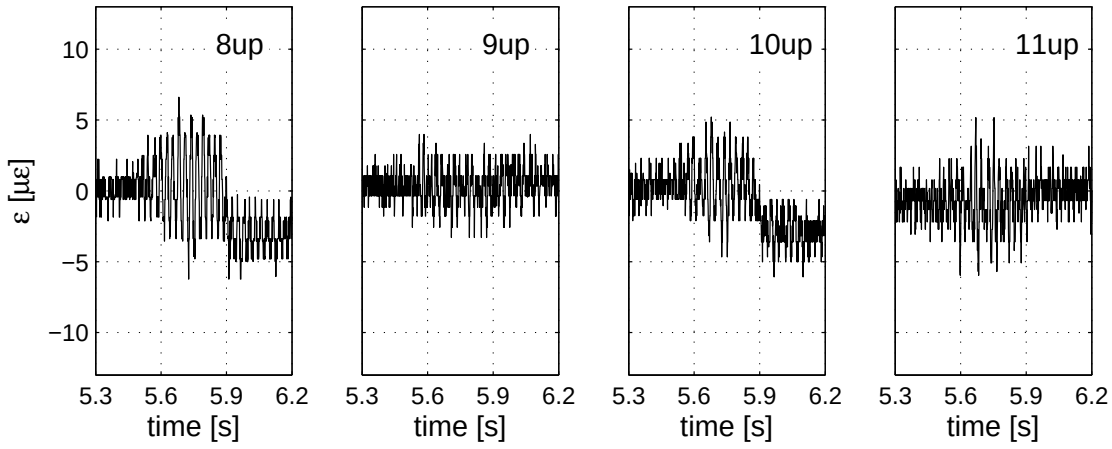

(a) #27910, wobbling from t=5.5-5.8 s, I_p=1 MA, B_t=-2.48 T

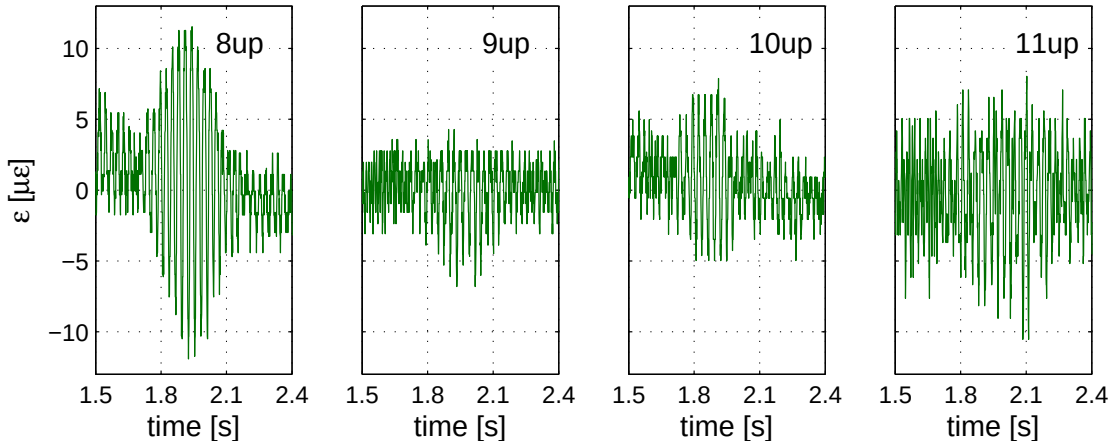

(b) #27916, ITER like configuration, I_p=1.2 MA, B_t=-2.52 T

Figure 71: Comparison of strain data of one quadrant of the upper PSL: Two shots with intentional (a) and unintended relevant vertical plasma shift (b)

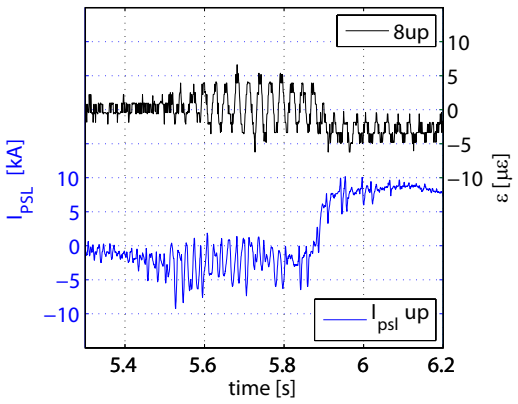

(a) #27910, wobbling from t=5.5-5.8 s, I_p=1 MA, B_t=-2.48 T

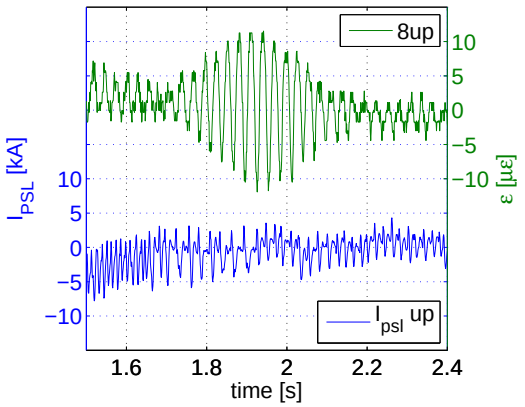

(b) #27916, ITER like configuration, I_p=1.2 MA, B_t=-2.52 T

Figure 72: Comparison of strain signal of sector 8, upper ring and PSL current with (a) and without wobbling (b)

resonance. In any case, this type of oscillating loading condition does not rely on the presence of the B-coils or even wobbling, but can occur in any type of discharge with elongated plasma, i.e. almost every discharge since the start of operation of ASDEX Upgrade. Therefore, a thorough assessment of the fatigue loading of the PSL (or the complete AUG device) covering life-time considerations needs to take this aspect into account.

It is quite obvious that disruptions are causing the most severe loading and deformation of the Passive Stabilising Loop structure. Figure 73 provides an overview of the maximal strain amplitudes, categorised by the state of operation under which they occurred. Out of more than 800 shots from shotnumber #25985 to #26834, the

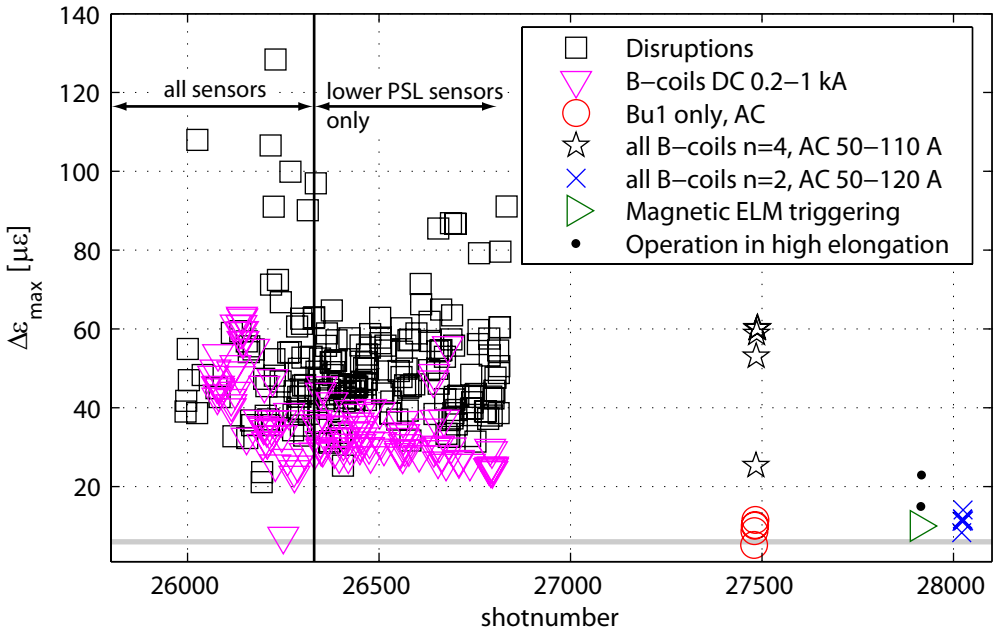

Figure 73: Maximal strain amplitudes under different loading cases

black squares represent the 212 disrupted discharges and the magenta triangles the 123 shots with B-coil currents above 200 A which did not disrupt[45]. For the latter, the plotted maximal strain values represent the superposition of static bending and the in-service oscillation as described just above and in section 4.4.2. All technical shots are included in this picture, whereas only a small selection of examples of wobbling and high elongation discharges have been included. The plotted amplitude is the peak-to-peak maximum, regardless of the location where this maximum was measured. The gray horizontal line at the bottom of the plot illustrates the mean noise of the sensors of 6−8 $\mu\epsilon$. A minority of the disruptions clearly produces the strongest structural response over all, but the bulk is in a range that is also met by some of the non-disruptive shots with B-coils in DC operation. These show

[45]It has to be kept in mind that the upper ring's sensors failed after #26354 (see section 3.3.3) and were not available until the end of this range of shots. All datapoints in figure 73 with shotnumbers above 26354 therefore rely on the lower ring's sensors only. As the upper ring mostly showed slightly higher deformations, this might subsequently result in fractionally lower maximum amplitudes.

strain amplitudes between 20 and 60 $\mu\epsilon$. The technical shots with n=4 provoked notable values with AC currents of 120 A, comparable to the upper limit of those with 1000 A in DC operation and above most disruptive excitations. As already seen before, the technical shots with n=2 and single coil excitation are insignificant in this context. Interestingly, the maximum strains measured during wobbling are exceeded by certain discharges with high elongation.

5 Discussion

This chapter is composed of five sections. The first section provides approaches for the interpretation of the experimental results and a few demonstrative data examples. The second section compares experimental data, especially modal shapes and frequencies, with the analytical and numerical results. In the third section, a discrete model for the representation of the PSL deformation using modal expansion is developed. The aim of this effort is the calculation of modal participation factors out of the measured signals which allow the determination of strains and stresses of the PSL with little computational effort. In the fourth section, the relation of discharge parameters and the PSL oscillation is investigated. First, the forces on the PSL rings are calculated based on the magnetic equilibrium reconstruction and the measured PSL currents. The instantaneous frequencies of these force time traces are compared to the PSL vibration. Second, a brief test is performed to determine if the PSL strain amplitudes of disrupted discharges correlate in a simple way with parameters such as the plasma current and the plasma stored energy. The fifth and final section presents the fatigue damage state of the PSL rings, calculated using actual data from 368 shots and a rainflow counting algorithm. An approximated Wöhler curve (S-N curve) of copper, combined with a linear accumulation model yields the total damage. A similar calculation is carried out using an extrapolation of the maximum strain values to higher B-coil currents. Thus, the operational limits of the coils in view of fatigue failure of the PSL are defined.

5.1 Understanding the experimental results

The following subsections provide background information and examples of side-effects necessary for a proper interpretation of the experimental data. This includes a data example concerning the mechanical coupling of the PSL to the ASDEX Upgrade structure, information about the influence of the vertical hinges and the nature of a disruption on the development of certain PSL modes, and the role of the PSL bridges in view of odd and even oscillation configurations. Finally, an example of a post-disruptive PSL oscillation is used to demonstrate the possibility of its decomposition into separate ringmodes by means of Fourier frequency filtering.

5.1.1 Importance of PSL deformation for the entire AUG machine

The optical acceleration sensor presented in section 3.4 was tested on the outer flange of the upper C-port in sector 6 (outside the vessel, cf. fig. 3 and 4). As the vacuum vessel features an eight-fold symmetry, there are 8 upper and 8 lower C-ports with identical geometry. The sensor measured the vertical component of acceleration between shotnumbers #26134 and #26257. Figure 74 presents the acceleration of the port and PSL strain signals during the disruptive discharge #26217. There is clearly a correlation between the strain of the PSL and the acceleration of the port flange. The amplitude evolutions over time are quite similar, which does not hold for the frequency of the oscillations. This becomes obvious comparing the right-hand plots which show a smaller time interval. The frequencies of the oscillation are most

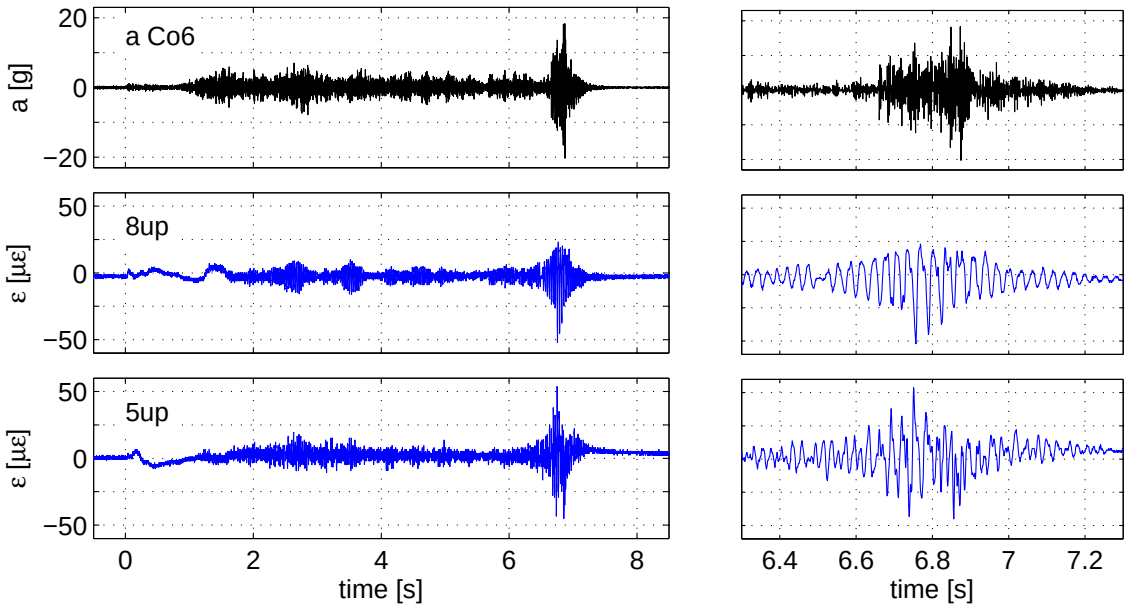

Figure 74: Vertical acceleration of upper C-port sector 6 outer flange (top, black) and upper PSL strain signals sectors 8 and 5 (middle/bottom, blue) resulting from disruption #26217, current quench at t=6.75 s.

likely the result of the different bending natural frequencies of the port[46] and the PSL. In addition, oscillation components with higher frequencies are naturally more pronounced in the acceleration signal because $a \sim \omega^2$. In this example, the maxima of the strain signals appear before those of the acceleration of the port, with a time difference of the order of 10-20 milliseconds. The probable reason for this time lag is that the PSL is directly exposed to the electromagnetic forces of the plasma, while the oscillation of the port is a reaction to displacements and deformations of inner parts of the machine (e.g. abrupt vertical vessel movements or bending of the port-vessel connection) which lie closer to the plasma. This simple example underlines that the PSL deformation is of some generality for the entire AUG device, as it correlates with the deformation at a totally different place of the machine. Regarding the high mass and the strong electromagnetic forces, which act on the PSL, this is not a surprising conclusion. First, loadings on the PSL e.g. due to activity of the B-coils may be transmitted to the surrounding structure via its supports. Second, the forces on the PSL resemble those on the rest of the machine because they often have a common origin, like disruptions that induce mirror-currents in the PSL and the vacuum vessel alike. Either way, the PSL deformation is indicative of the overall structural load, to a certain extent. This makes it interesting for structural investigations of a general kind, as ASDEX Upgrade is not equipped with an excessive number of mechanical sensors. A simple application is for instance the identification of discharges with strong structural response.

[46]The AUG vacuum vessel upper C-ports are basically steel tubes of around 1.25 m length and an inner diameter of 280 mm.

5.1.2 Insignificance of the elliptical natural modes

As stated before in the results chapter, the technical discharges with single-coil excitation were intended to excite broadband oscillations of the PSL system where influences of the load distribution should be minimised. The application of a single point load is not possible with the given setup, as the operation of a single B-coil already introduces two radial forces with different sign. These are applied at a toroidal distance of 45°, the span of the coil. Although this corresponds to the distance of the nodes of an n=4 eigenmode, the excitation of other modes is quite possible, particularly on the lower ring, which moves freely without direct forcing. Figure 75 compares three response spectra of discharges with alternating current supply of the B-coils. Again, the upper PSL ring signals are plotted above zero and those from the lower ring below. Top to bottom, (a) is the one-coil case, (b) an n=2 and (c) an n=4 excitation. Total excitation time and the coil currents differ by less than 10%, details can be found in table 15 on page 67. The vertical axes show absolute power spectral density (PSD) values. The scales in the vertical direction are different for better visibility of the peak shapes. Note the large differences between the maximum PSD values, especially between (b) and (c), where all 16 coils were used.

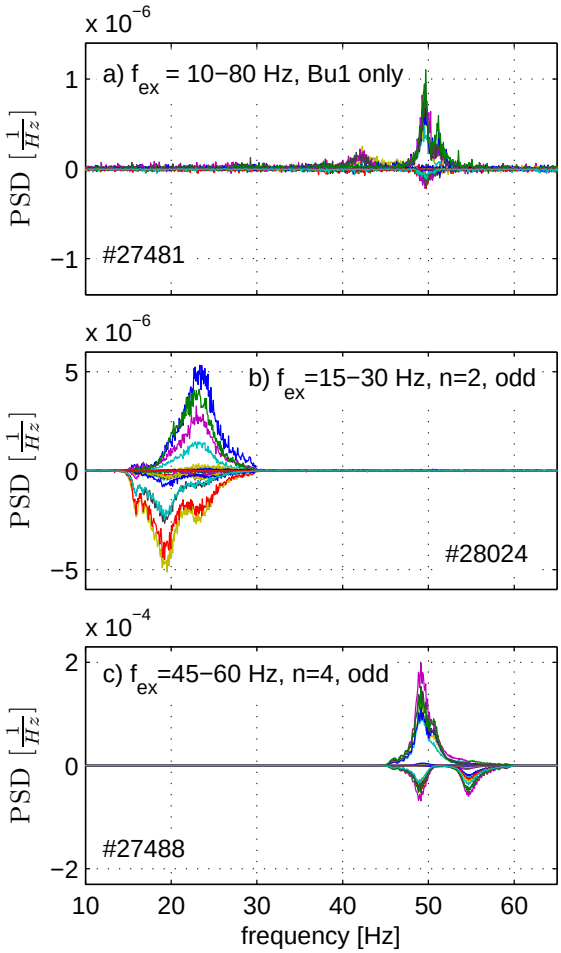

Figure 75: Comparison of spectra with single-coil, n=2 and n=4 excitation

Obviously, the single coil configuration does not excite n=2 modes above the noise threshold. It is possible that there is some minor oscillation around 15-30 Hz in the n=2 range, but it is not visible with this excitation frequency sweep rate (10-80 Hz in 13 s). In contrast to this, the single coil case (a) shows a strong resemblance to the n=4 case (c), with the only difference being that the signal-to-noise ratio is much higher in the latter case. Both spectra show a major peak at 49-50 Hz, with contributions mostly from the upper ring. The lower ring's response is stronger in n=4 (c) than in (a). There is a secondary maximum in (a) at 51-52 Hz that can also be found in (c), but is almost covered by the main peak there. The main differences between the broadband and the n=4 spectrum are a low bump of activity of the upper ring around 40-45 Hz in (a) that is not visible in (c), and a secondary resonance of the lower ring at 55 Hz, that (a) does not exhibit. The first point might just be a result of the high noise in the top spectrum. The second point is probably the n=4 resonance peak of the lower ring alone. It is not surprising that (a) does not exhibit this maximum, as there was no forcing on the lower ring. Here, all response from the lower ring results from the forces transmitted by the PSL bridges. And the movements of the PSL bridges, and hence the transmitted forces are largest when the upper ring is in resonance, which is not the case at 55 Hz.

As already pointed out in the results chapter, the n=2 resonance (b) shows a vastly smaller amplitude than the n=4 resonant oscillation (c). The n=2 resonance peaks are much broader, evidence for strong damping. Interestingly, the two main peaks' shape resembles roughly the n=4 spectrum (c). There are two maxima, whereas at the frequency of the maximum of the upper ring, also a peak on the lower PSL is observed. The smaller peak is almost exclusively a resonance of the lower ring. Contrary to n=4, the lower ring's resonance lies at a lower frequency, here.

The reason for the extreme differences in amplitude of (b) and (c) lies primarily in the constraints set on the upper ring by the vertical supports. These also affect the lower ring which is mechanically coupled to the movements of the upper ring through the PSL bridges. The kinematics of the vertical hinges with two ball-head type bearings allow only radial excursions. As stated before in the mechanical system description (section 2.1.2), bending of the PSL about its first principal axis results in an excursion directed along the second principal axis. The bending stiffness in this direction is lower by a factor of 25 compared to the first principal direction. Therefore, mostly deflections along this axis 2 are expected, as long as the loading does not act solely perpendicular to it. A unit displacement along axis 2 has a vertical (ca. $1/2$) and a radial component (ca. $\sqrt{3}/2$). It is obvious that the upper PSL is constrained vertically at the 8 positions of the hinges, and this has severe consequences for the bending eigenmodes below 150 Hz. The finite element calculations reveal that the modal shapes in this frequency range mainly show displacements along axis 2, resulting in vertical excursions of half the size. There is only one ringmode of the upper PSL that is not affected by the supports, which is the n=4 configuration illustrated in figure 76. The displacement nodes of this modal shape are located at the positions of the hinges. This means that the mode can develop freely. The positions and the number of the hinges are the reason why this particular mode locks in this angular position. Therefore, it has to be considered as the prime concern in the context of B-coil operation with alternating current.

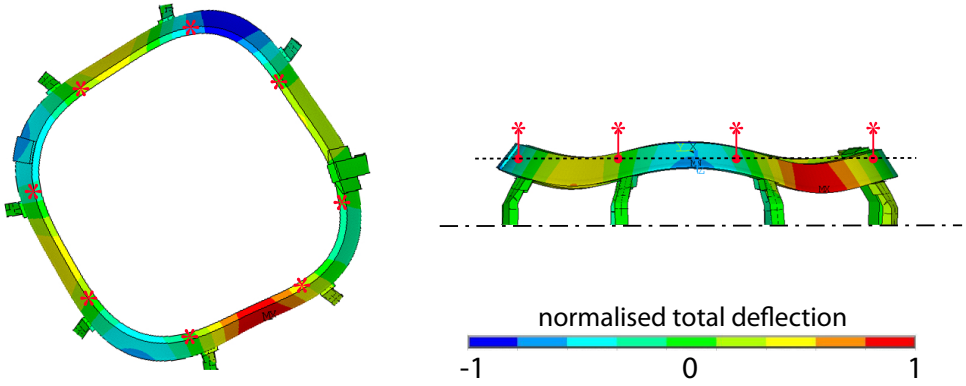

Figure 76: Shape representation of an n=4 ringmode, unaffected by the vertical supports (marked in red), which are nodes of displacement. Top-view (left) and side-view (right)

In contrast to this configuration, the second n=4 natural mode of the upper PSL ring is effectively blocked by the vertical supports. Its shape is spatially orthogonal to the first n=4 mode (fig. 76) which means that its anti-nodes are located at the support positions which avoid vertical movements. In other words, there is only one n=4 mode that develops on the upper ring, and no frequency splitting can occur. This is visible even in the disruptive frequency spectra, as the n=4 spectral peak at 50 Hz is very 'sharp' (narrow in frequency) compared to the other peaks which correspond to other modes. In figure 67 on page 80, especially the graphs a, d, h and k are convincing examples of this effect.

Only n=2 and n=4 ring-modes can be excited properly with the internal coils. For this reason, and because the amplitudes reached with n=2 recipes are insignificant compared to n=4, only excitations of n=4 ringmodes are considered in the following. This applies for instance to the fatigue lifetime estimates in section 5.5.

5.1.3 Favouritism of odd configurations

It has been shown in section 4.3.2 that the maximum strain amplitudes of odd configurations are higher than with even coil recipes. This effect is particularly clear when n=4 excitations are applied. There is a kinematic explanation for this phenomenon. As the PSL rings deform, they perform radial and vertical movements. In odd configurations, this means that the attachment points of the PSL bridges move in such a way as to impose a rotation on the bridges, without stretching or compressing the bridges along the vertical axis. This effect is illustrated in figure 77. In the even case, the bridges show no rotation, but are stretched and compressed vertically, as shown in figure 78. Under identical conditions, the measured strain amplitudes are generally higher in odd configurations by 10-15% compared to the even case. The bridges oppose the motion of the rings in different ways: In tension/compression, the vertical stiffness of the bridges works against the movement of the attachments. The rotation of the bridges leads to bending of their attachment points, which induces a restoring torque on the attachments depending on their bending stiffness. The proportion of these two stiffnesses governs the coupling of the oscillations of the upper and the lower ring. In other words, the question is

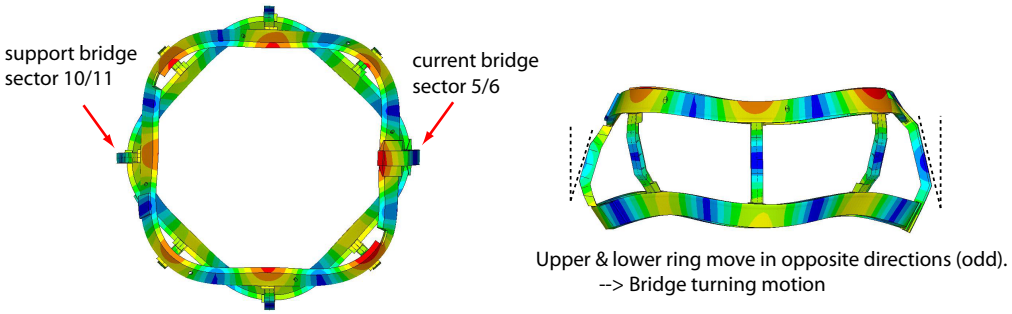

Figure 77: Schematic explanation of the turning motion of the PSL bridges due to odd configurations. Image shows an n=4 odd configuration, top (left) and side view.

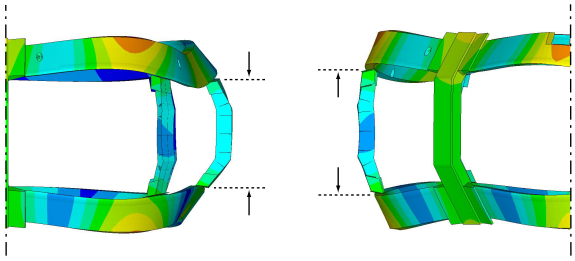

Figure 78: Illustration of an n=4 ringmode in even configuration. Instantaneous compression of support bridge in sector 10/11 (left) and tension of bridge in sector 8/9 (right) due to in-phase deflection of upper and lower ring.

as follows: The main deflection of each of the PSL rings is directed along its 2nd principal axis (cf. figure 5). If an inward translation along axis 2 is imposed on the upper joint of a bridge, will this cause the lower attachment to move inward (high bending stiffness) or rather outward (high lateral stiffness) in order to conserve the length of the bridge?

The actual behaviour gives a clear answer to this question, consistent with intuition. The technical discharges of section 4.3.2, when only one single coil was used, allow a first statement. As shown by figure 56, the forcing at two points on one ring only make the other ring oscillate in antiphase. Hence, the influence of the bending stiffness is smaller than the one of the lateral stiffness, and *the antiphased oscillation of the two rings can be considered as the natural behaviour of the PSL.* Another example is the comparison of odd and even n=4 configurations in figure 79. The spectrum of the even configuration discharge (a) shows two separate peaks, corresponding to the upper and the lower rings' resonances. In the odd configuration (b), the resonance at the frequency B is an oscillation with strong involvement of both rings. The frequency of this combined mode is lower than both resonance frequencies of the separate rings (B compared to A and the lower ring's resonance at 54 Hz). The movements of the rings are coupled by the turning motion of the bridges. Therefore, odd configurations show larger deflections. The low frequency of the combined mode can be thought of as a consequence of the larger total mass that is involved in the oscillation. However, as the coupled oscillation involves only little deformation of the lower ring, the frequency decrease is small (ca. 3%). The current bridge is very stiff compared to the support bridges, which explains the small deflections in sector 6/7 (see fig. 79c and d). The large deflections in sectors 5

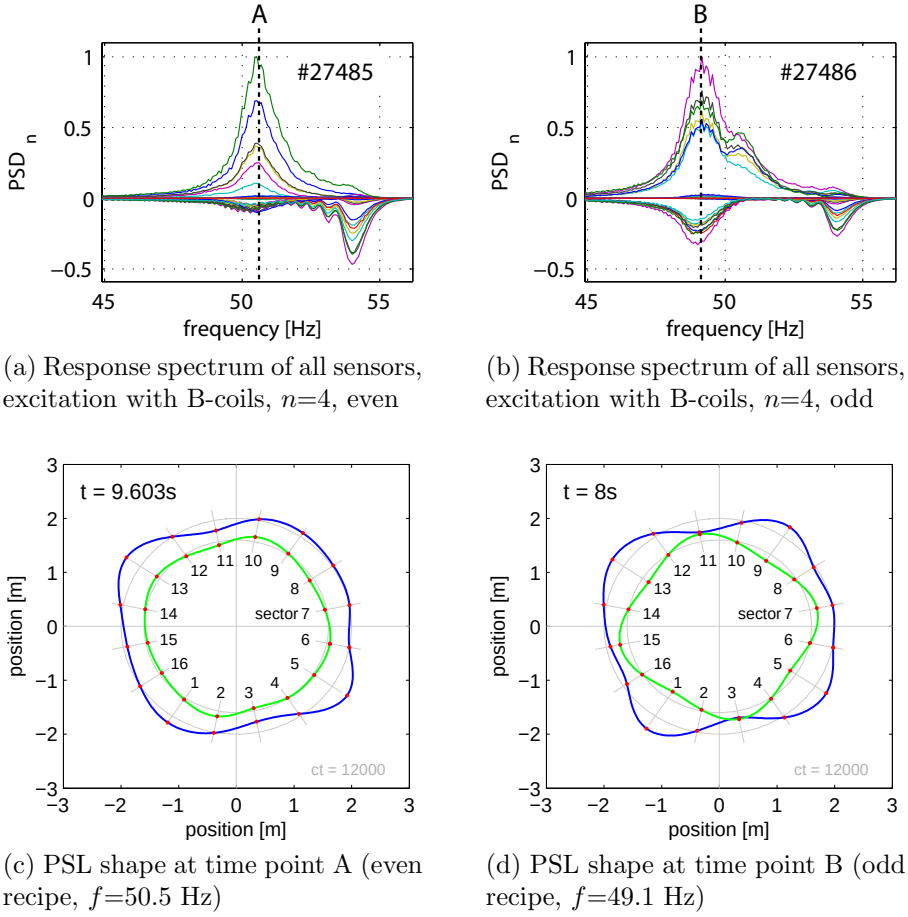

(a) Response spectrum of all sensors, excitation with B-coils, n=4, even

(b) Response spectrum of all sensors, excitation with B-coils, n=4, odd

(c) PSL shape at time point A (even recipe, f=50.5 Hz)

(d) PSL shape at time point B (odd recipe, f=49.1 Hz)

Figure 79: Coupling of the PSL rings in even and odd configuration

and 13 on the upper ring result from the reduced cross sections (diagnostic notches) there. The strong undulation of the spectrum in figure 79b results from the non-zero sweep rate of the excitation frequency. This is a well-known effect during start-up procedures of oscillatory devices [30, 67]. As has been shown before, one of the n=4 ringmodes is not constrained by the vertical supports of the PSL. As odd configurations generally show larger deflections, this n=4 mode in odd configuration[47] has to be considered the most dangerous mode to be excited with the B-coils. For this reason, the strain extrapolation of section 5.5 is based on this setup.

5.1.4 Initial conditions of PSL deformation set by nature of disruption

The great variety in the appearance of post-disruptive frequency spectra (see fig. 67) suggests that the force load on the PSL also varies greatly. There are, however, recurring patterns, which arise in terms of frequency ranges that show higher activity than others. This is due to the excitation of natural modes of the PSL rings and is explored in the following section 5.1.5. The variety in the disruptive spectra is due to different modes that oscillate with different amplitudes, depending on the excitation. In turn, as far as this excitation is concerned, two different types of disruptions have been observed, which are presented here. The first is a uniform

[47] According to recipe 908 (cf. table 14, p. 66).

vertical displacement event of the plasma, which means in the present case that the plasma centre shifts upwards until the edge comes into contact with the wall at some point. The plasma temperature drops, and the plasma current collapses as its resistivity increases. The plasma current and centre position as well as the PSL shape at different times before and after the current quench are shown in figure 80. At t=3.62 s (b), at full plasma current, the plasma centre is moving upwards

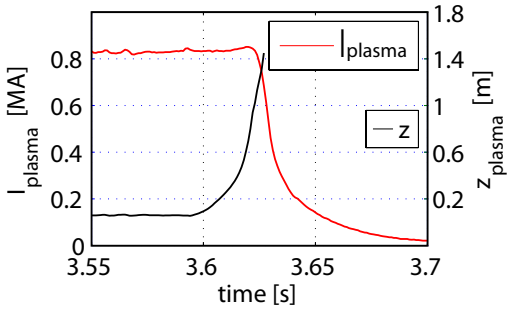

(a) Plasma current and vertical position during vertical displacement event #26026

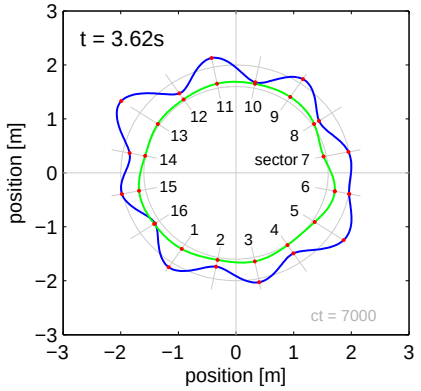

(b) Upper PSL, constrained by vertical supports is deformed to an n=8 shape by plasma moving upwards

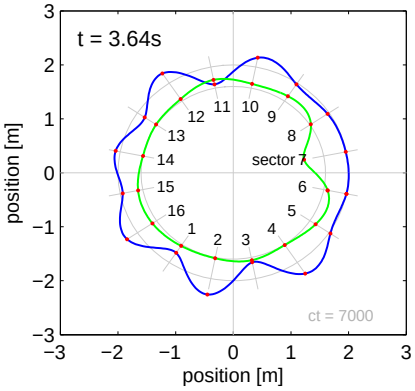

(c) Upper ring swinging back, 20 ms after plasma current quench

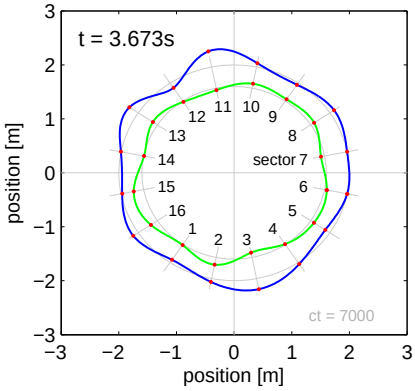

(d) Decomposition of n=8 shape to lower mode numbers, oscillation has spread over lower ring after 53 ms

Figure 80: Example of a uniformly moving vertical displacement event (VDE) leading to an n=8 initial shape of the upper ring (blue) at the time of the current quench

with considerable speed. It thereby repels the upper ring of the PSL which is held by the vertical hinges in the middle of the even-numbered sectors. The distributed line load on the ring leads to deflection antinodes at the hinges' positions and in the middle between them. As a consequence, the ring bends to an n=8 shape, according to the number of supports. As soon as the plasma current decays, the PSL is released, swings back and reaches the inverted n=8 shape after approximately 20 ms (c), although the oscillation has already come to rest in the region of the very stiff current bridge. This modal structure rapidly decomposes into oscillations with lower mode numbers (d), including the whole PSL structure. If the n=8 initial condition was perfectly symmetric, no other oscillations could theoretically occur.

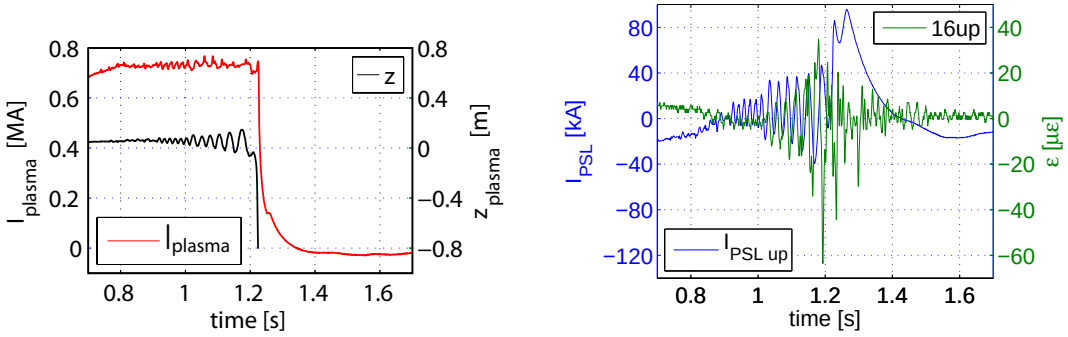

(a) Plasma current and oscillating vertical position prior to disruption

(b) Upper PSL electric current and strain signal in sector 16

Figure 81: Forced excitation of the PSL prior to disruption due to cyclic plasma shift (swinging up), followed by impact load of current quench (#26269)

It is likely, however, that the specific mass and stiffness distribution of the PSL generally do not allow to generate such initial conditions with a uniform line load, only. In this example, the solitary n=8 mode on the upper PSL ring exists for less than 3 oscillation periods. The initial condition probably contains components with lower mode numbers. These experience lower damping compared to n=8, as a result of their lower frequency. Hence, they persist after the n=8 oscillation has ceased. In this context, see also the frequency spectrum of this disruption (fig. 67a on p. 80). An additional possible influence is wavelength dispersion, which leads to lengthening of the wave peaks along the medium (the PSL ring). This mechanism and the aforementioned asymmetries in the initial conditions probably lead to the observed behaviour. The effect of seemingly uniform loading and sudden release is also observed for downwards-oriented plasma displacements (downward VDEs), but this leads to deformation patterns of the lower ring which are less ordered.

The other type of disruptive excitation is illustrated in figure 81, where the plasma performs cyclic vertical movements prior to the current quench. Naturally, this motion also causes an oscillation of the PSL current and the forces on the PSL rings. Therefore, in the present example, the strain signals oscillate with increasing strain amplitude until the plasma current quench occurs. The quench itself generates a sudden rise of the PSL current followed by a decay according to the PSL's resistance and inductance. The effect of the quench is an impulse loading on the PSL, i.e. a broadband excitation. Only in rare cases do the control coils induce significant PSL currents in this phase (cf. section 4.4.3). After the current quench, the PSL structure oscillates freely. A closer look at the frequency spectra presented in figure 82 reveals a number of important features of this type of disruptive discharge (with unintentional, cyclic plasma displacement). The plots show the vertical position of the plasma centre, the PSL electric current and the strain sensor signals. The frequency of the plasma position signal correlates almost perfectly with spectrum of the PSL current, which causes the mechanical excitation in the predisruptive phase. In turn, the forced oscillation before the current quench (b) is obviously strongly related to this excitation. The resulting oscillation between 20 and 30 Hz is carried on even after the quench (c). In this example, mostly the upper ring is involved in the oscillation at this point, which interferes with the natural PSL modes in the

aftermath of the disruption. These modes are either excited by the impact loading at t=1.2 s, or result from the decomposition of the formerly forced oscillations. The frequency peak at 38 Hz in the post-disruptive phase (c) is an n=3 eigenmode of the lower ring. The remnants of the forced vibration at 20-35 Hz do not correspond to a natural ring mode of either of the rings. This judgement is based on a back-transformation of certain Fourier coefficients that correspond to a specific frequency. This method is used in the next section to visualise the natural PSL ring modes that are excited by disruptions.

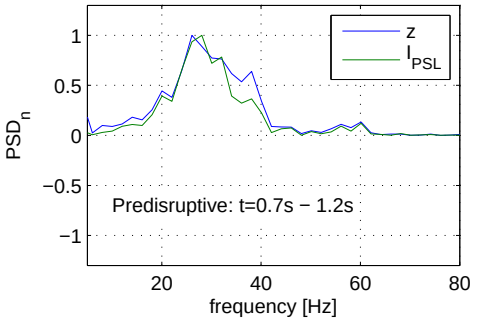

(a) Spectrum of vertical plasma position and PSL current before current quench

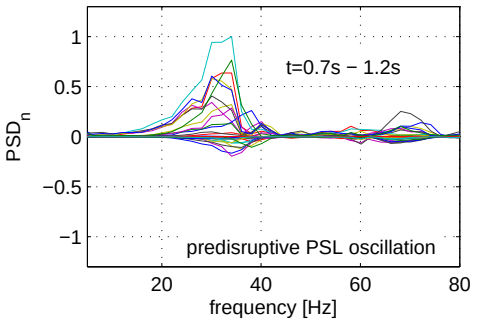

(b) Spectra of PSL sensor signals before current quench (forced oscillation)

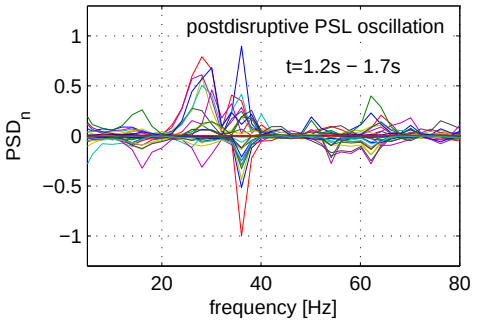

(c) Spectra of PSL sensor signals after current quench (free oscillation)

Figure 82: Normalised frequency spectra of PSL loading (a) and PSL oscillations before (b) and after the current quench (c, all #26269)

5.1.5 Natural ring modes excited by disruptions

The post-disruptive oscillation of the PSL shows recurring frequency peaks, as can be seen by comparing the 11 response spectra of figure 67 on page 80. Characteristic frequency domains lie for instance at approximately 18, 37, 50, 63 and 73[48] Hz. These domains correspond to specific modes of the PSL rings which include either one or both of the PSL rings. Figure 83 presents the most active PSL modes seen in example discharge #26314. The shape representations are constructed by isolating the Fourier coefficients of the highest spectral peaks of the response spectrum (i.e. setting all other coefficients to zero). These correspond to a specific frequency or a frequency range [68], which was then transformed back to real space. The peaks corresponding to b,d,e and f represent coupled oscillations involving both rings, though the deformation of the upper ring tends to be small and slightly asymmetric for the latter two. This is at least partly due to an interaction of the high stiffness of the ring at the position of the current bridge and the nearby vertical hinges. The PSL shows only little deformation in this part of the rings for all measurements. In the even elliptical mode (b), the upper ring is much less involved than the lower one, probably because of the constraints set by the vertical hinges as has been stated before. Mode (d) corresponds exactly to the PSL shape generated by B-coil oper-

[48]The characteristic noise frequency of the optical sensing interrogator at 72 Hz affects all sensors, but has a negligible amplitude compared to the strains measured here and during disruptions in general.

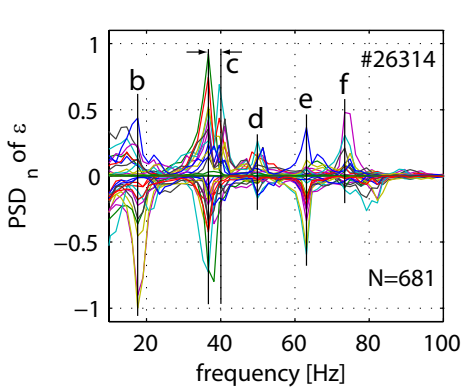

(a) Postdisruptive frequency spectrum

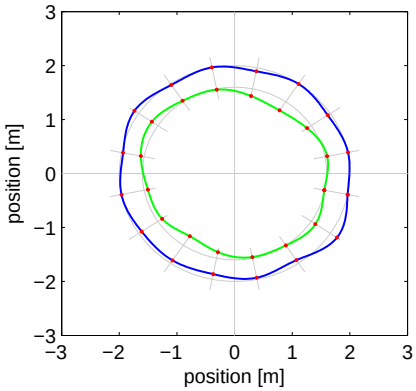

(b) $n_{up/low}$= 2/2 (even, 17.6 Hz)

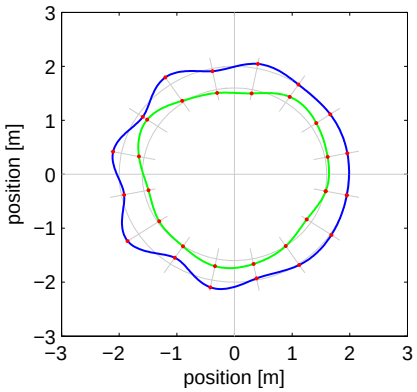

(c) $n_{up/low}$= -/3 (36.7-39.7 Hz)

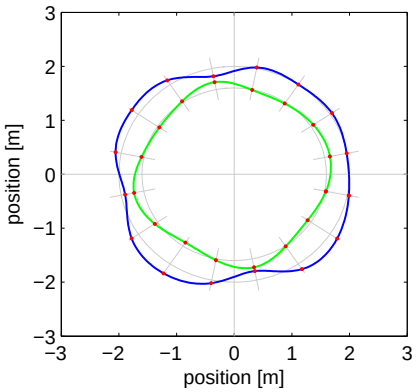

(d) $n_{up/low}$= 4/4 (odd, 49.9 Hz)

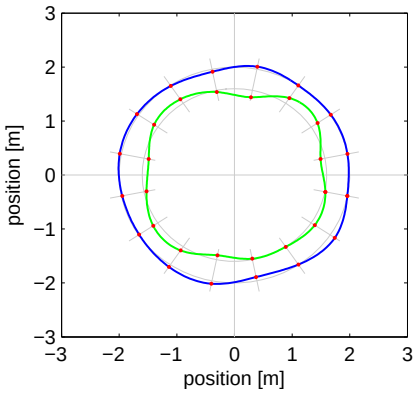

(e) $n_{up/low}$= (4)/4 (63.1 Hz)

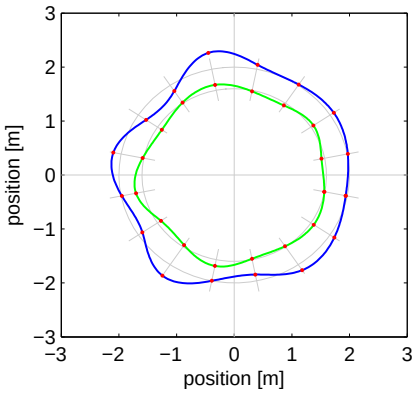

(f) $n_{up/low}$= (5)/5 (73.4 Hz)

Figure 83: Visualisation of PSL ring natural mode oscillations after plasma disruption #26314 by selective back-transformation of single (b,d,e,f) or a few (c) Fourier coefficients to real space

ation with recipe 908 (figure 79d on p. 95). The resonance frequency determined during resonant B-coil operation was 49.1 Hz, whereas the spectral peak here is at 49.9 Hz. The frequency resolution of the shown disruptive spectrum being 1.5 Hz, this discrepancy is within experimental resolution. This mode shows only little involvement in the present discharge, relative to other disruptions, where its spectral peak at roughly 50 Hz is often the second-highest or even the highest maximum.

The mode at 63.1 Hz (e) is spatially orthogonal with respect to case (d). The upper ring is practically at rest, while the n=4 shape develops visibly on the lower ring. Actually, this is the angular mode orientation where the upper ring is effectively blocked by the vertical supports, as outlined in section 5.1.2. The higher frequency of this mode can be explained by thinking of the supports adding stiffness to the system in this particular configuration. The mode in picture (f) has a clear n=5 structure on the lower ring, whereas the oscillation is highly asymmetric on the upper PSL ring. This may be due to the high stiffness around the current bridge and the influences of the hinges. Contrary to the lower ring, the upper one is constrained by the PSL bridges *and* the vertical supports. It is a general observation that the modes excited by disruptions show ideal ring mode shapes on the lower ring, but only seldom on the upper one. Most modal shapes of the PSL as a whole seem to consist of an ideal ring mode on the lower ring, combined with an oscillation of parts of the upper PSL by forcing through the bridges. Therein, the motion of the upper ring appears to be unsystematic. The triangular (n=3) oscillation of the lower ring depicted in graph (c) is such a case. It is accompanied by a seemingly unordered deformation of the upper ring. The oscillations in this frequency range (roughly 30 to 40 Hz) are a matter of particular interest, because this is in general the domain with the highest activity after a disruption, i.e. the most pronounced spectral peaks. These peaks correspond in the vast majority of the observed cases to some triangular mode, be it on the lower or the upper ring or on both. Apparently, these resonances are privileged in some way compared to the lower elliptical (n=2) modes, where lower damping would usually be expected. Even the n=4 shape in the configuration which is unaffected by the PSL hinges (d), and predominant in AC B-coil operation, only rarely shows higher peaks[49]. As mentioned in the preceding section, cyclic vertical plasma movements transmit loads to the PSL and make it oscillate in a forced vibration at the frequency of the plasma shift. If this excitation corresponds to (one of) the n=3 natural frequencies as in the example of figure 81, it is not surprising to find high n=3 activity also in the post-disruptive oscillation. But, as disruptions without significant vertical plasma motion before the quench also exhibit strong n=3 activity, this cannot be the only reason for their dominance.

Another possible explanation for the general dominance of n=3 PSL modes lies in the interaction of the structure with MHD modes inside the plasma. Most disruptions are preceded by magnetohydrodynamic modes, which involve displacements of magnetic surfaces and can lead to the formation of magnetic islands [69]. In the context of mechanical PSL excitations, it is important to note that these instabilities give rise to macroscopic and periodic deformations of the outer plasma shape. In the early phase of such an instability, the magnetic islands rotate around the torus at the rotational velocity of the plasma. As the islands grow, the rotation of the mode slows down and eventually comes to a complete stop. The mode orientates along the direction of the intrinsic (magnetic) error field of the tokamak caused by slight asymmetries of the coils. This process is called mode-locking and occurs immediately before the disruption. The presence of MHD modes prior to disruptions might play an important role for the PSL excitation in two senses: First, the mode rotates at very high frequencies and then slows down. Depending on the time characteris-

[49] As PSL modes with n=3 only cannot be excited with the set of 2×8 internal coils, they were not considered in the context of AC B-coil operation.

tics of this deceleration, the MHD mode might excite certain PSL modes more than others. Second, the distortion of the plasma may cause spatial force distributions which favour certain PSL bending modes, in this case (AUG) those with n=3. Consequently, the n=3 ringmode dominance should not be observed in the absence of a locked mode. For this reason, a set of six disruptions without MHD mode locking, intentionally triggered by turning off vertical position control, was analysed. The frequency spectra of the associated post-disruptive oscillations are shown in figure 84. Compared to the 11 disruptive oscillations presented earlier (cf. fig. 67, p. 80),

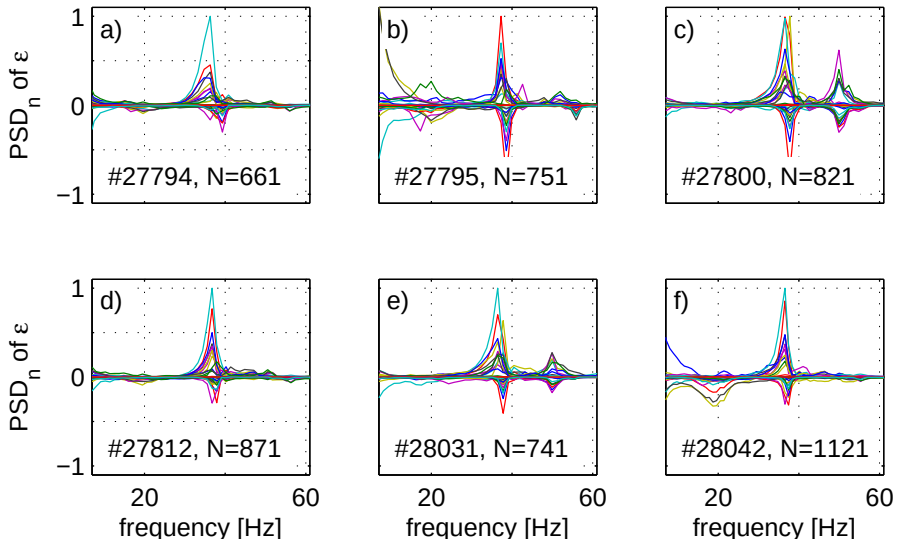

Figure 84: Strain signal spectra of 6 disruptions without locked MHD mode, axisymmetric plasma displacement only.

the only obvious difference is that the peaks are slightly narrower. But also in this case, the largest contribution to the total deformation comes from n=3 oscillations. This disqualifies locked MHD modes as the reason for the dominance of triangular modes.

Another possible explanation is that the typical initial PSL deformation before the current quench, shown in figure 80b, might have significant n=3 components which are not visible to the naked eye. They may persist when the higher modes with higher frequencies are already entirely attenuated. The n=2 modes are generally disadvantaged due to the distribution of the PSL hinges, as stated before. The *spatial* Fourier spectrum shown in figure 85 presents the shares of the first eight (ideal) ringmodes which constitute the initial PSL deformation. This calculation is based on the spline-fit approximation of the measured strains. All amplitudes above the order eight are zero due to the spatial resolution of the sensor network. The odd modes have negligible amplitudes. As expected, the n=8 shape is dominant, but also n=2 and n=4 exhibit remarkable amplitudes. For clarification, figure 86 shows the original shape and the four largest components. Hence, the typical PSL initial shape during disruptions is not a valid explanation for the dominance of triangular modes. This phenomenon apparently also does not originate from specific forcing, as outlined before.

It was shown earlier that one of the quadratic (n=4) modes is privileged as its

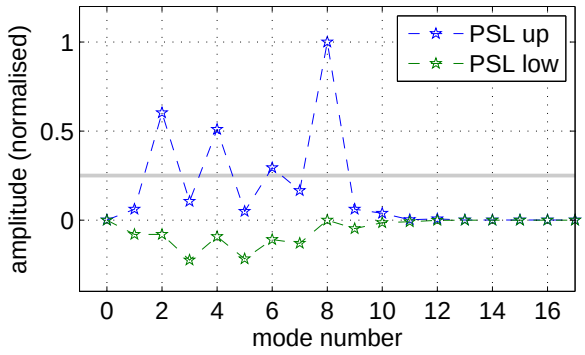

Figure 85: Spatial Fourier spectrum of the typical initial deformation of the PSL during disruptions (cf. section 5.1.4, fig. 80b); plot shows normalised deflection *amplitudes* (no PSD values; modes with amplitude above grey line included in fig. 86b).

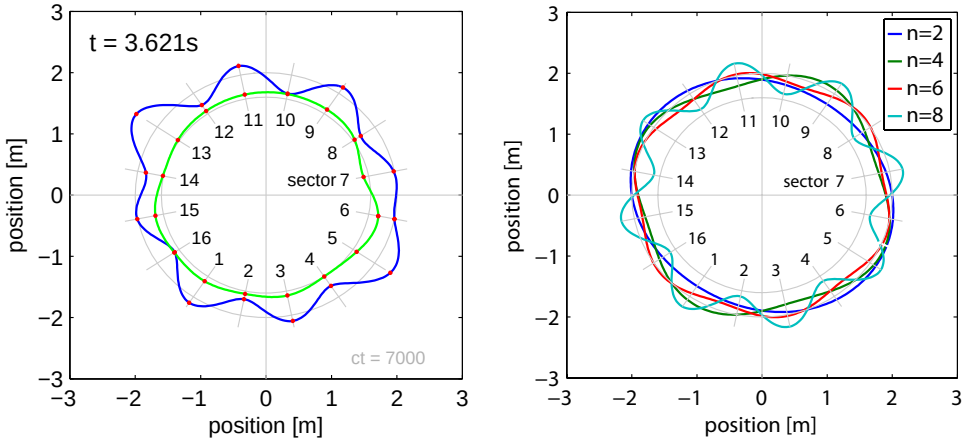

(a) Initial PSL shape

(b) The four strongest spatial modes of the upper ring

Figure 86: Upper PSL initial deformation prior to current quench of disruption #26026 and decomposition by spatial Fourier transformation

nodes of deflection lie at the hinges where the upper ring is constrained in the vertical direction. This mode is, therefore, not influenced by the hinges, and develops freely. Other modes with higher mode numbers theoretically also have this property, for example at n=8. Of course, there is no such angular orientation for n=3 modes. As far as the lower PSL ring, which frequently shows strong oscillations with n=3, is concerned, the boundary conditions are determined by the bridges supporting it. These also have an eightfold symmetry. Any potential preference for a particular mode number or orientation that does not originate from the excitation must result from these bearings. To explain the dominance of the n=3 modes, the theoretical relation of the ring mode number and the resulting deflection at the position of the hinges or the bridges is analysed. The modal shapes are assumed to be harmonic functions according to section 2.2.3. The radial[50] deflections of the rings are

[50] As done before in section 4.1 for analytically calculating the PSL natural frequencies, this 'radial' deflection has to be understood as being directed along the direction of the smallest bending stiffness of the PSL rings.

described by

$$U_{rn}(\theta) = A_n \cos(n(\theta - \xi)) = A_n \cos(n\theta - \eta). \tag{40}$$

Compared to the ideal ring formulation of this equation in chapter 2, the additional parameters η and ξ ($\eta = n\xi$) introduced here describe the angular orientation of the mode with respect to the supports. A value of $\xi = \pi$ corresponds to a rotation of the mode by 180° about the vertical axis in real space. A value of $\eta = \pi$ represents a displacement of the mode by half of its wavelength. For simplicity, the amplitude A_n is set to unity for all mode numbers n in the following theoretical considerations. The eight equidistant positions of the hinges on the upper ring (or the bridges on the lower one) are described by

$$\theta_j = \frac{\pi}{4} \cdot j, \text{ with } j = 1, 2, ..., 8. \tag{41}$$

The hinges *and* the bridges are attached at 16 points to the upper ring. For this ring, the bridges are not taken into account because they are considered much less stiff than the vertical hinges and therefore insignificant for the upper ring's modal preferences. For the lower ring, only the bridges have to be considered. The *average* deflection at the hinges' positions S_n serves as an indication for the mutual interaction of the modal shapes and the hinges. The theoretical absolute values are averaged according to

$$S_n = \frac{1}{8} \sum_{j=1}^{8} |\cos(n(\theta_j - \xi))| = \frac{1}{8} \sum_{j=1}^{8} |\cos(n\theta_j - \eta)|. \tag{42}$$

Figure 87 shows the average deflection as a function of the angular orientation of the mode expressed in radians in real space (ξ, left) and in mode-relative wavelengths (η, right). A value of S_n=1 corresponds to a mode with deflection antinodes at

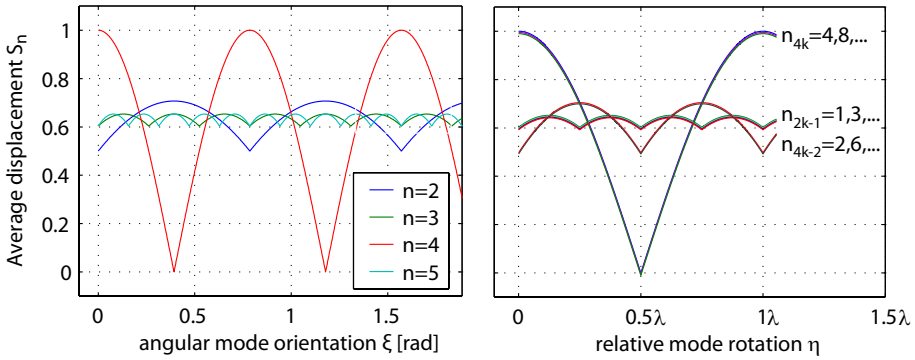

Figure 87: Calculated sum of maximal deflections at 8 equidistant points of a PSL ring (normalised). The sum is plotted as a function of the actual spatial angle (left) and of the rotation in modal wavelengths (right).

all 8 hinges (upper ring) or at all bridges (lower ring). The left graph shows, for instance, that the n=4 mode (in red) is unaffected by the hinges at an orientation of $\xi = \pi/8$, where $S_4 = 0$, and is highly affected at $\xi = 0$, where $S_4 = 1$. The values of the n=3 modes and all higher odd mode numbers are situated in a narrow band of $S_3 \in (0.6, 0.66)$. The same holds for the n=2 mode in a larger interval of

$S_2 \in (0.5, 0.7)$. As illustrated on the right-hand side, three groups of ring modes share the same behaviour, those with mode numbers $n_{k1} = 2k - 1$, $n_{k2} = 4k - 2$ and $n_{k3} = 4k$ (with positive integers k).

The conclusion is that there is no distinct spatial orientation which would be very preferable for n=3 modes, unlike e.g. for n=4 modes and all modes of the same group. As a consequence these modes exhibit a certain 'versatility' in the sense that whatever the direction of a loading, they are constrained to the same, medium extent by the supports. An explanation for the high activity of n=3 modes in general is, therefore, that they represent a good compromise in terms of a low mode number associated to a low natural frequency (low damping), and this versatility in terms of the direction of excitation. Even though low activity of the n=2 modes on the lower ring is not explained, there is another point which fits in: The n=4 modes have been observed to be dominant during several disruptions (see fig. 67), which could be a sign for the loading having been directed in a favourable direction (for n=4) in these cases. Of course, these approaches to explain the dominance of the triangular eigenmodes are no definite proof.

5.1.6 Analytical evaluation of maximal in-service deflections

Based on the maximum strain values for different load cases of the PSL presented in chapter 4.4.3, the maximum deflections of the rings are evaluated. When its strain distribution is known, the deflection of a beam can be calculated according to linear theory. In a similar way, the deflection of the two PSL rings with respect to the undeformed state can be determined based on the pointwise strain measurements, if the following simplifications are applied. The bending around the second principal axis, which is not measured by the optical sensors, is neglected. The toroidal strain distribution is approximated using specific form-functions. Furthermore, Euler-Bernoulli simplifications are adopted, which imply that plane cross sections of the rings that are normal to the neutral axis are assumed to retain planarity and normality also in the deformed state.

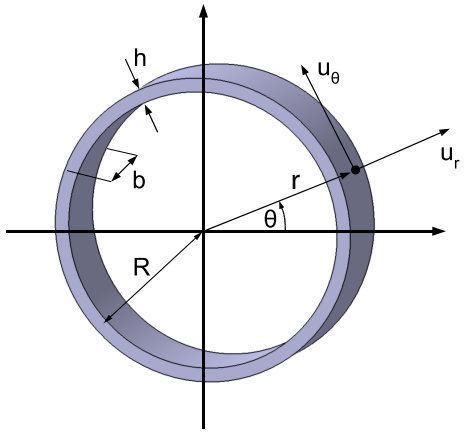

Figure 88: Ring parameter definition

All strain sensors measure the dominant bending component around the first principal axis (cf. figure 5). Following the ansatz in chapter 2.2.3 to calculate the modal shapes, harmonic form-functions are used here to describe the strain distribution. The used coordinate system and parameters are illustrated in figure 88. The strain in toroidal direction on a toroidal circle through the regular sensor positions is thus described by

$$\epsilon(n, \theta) = \epsilon_0 \cos(n \cdot \theta). \tag{43}$$

The neutral fibre, illustrated in figure 89, always has the same length. It is described by

$$\rho d\alpha = R d\theta \quad (d\bar{s}_0 = ds_0) \tag{44}$$

in the deformed and undeformed state, respectively. The general expression of toroidal strain is

$$\epsilon = \frac{d\bar{s} - ds}{ds}, \tag{45}$$

in accordance with the definition of the infinitesimal ring element in figure 89. For

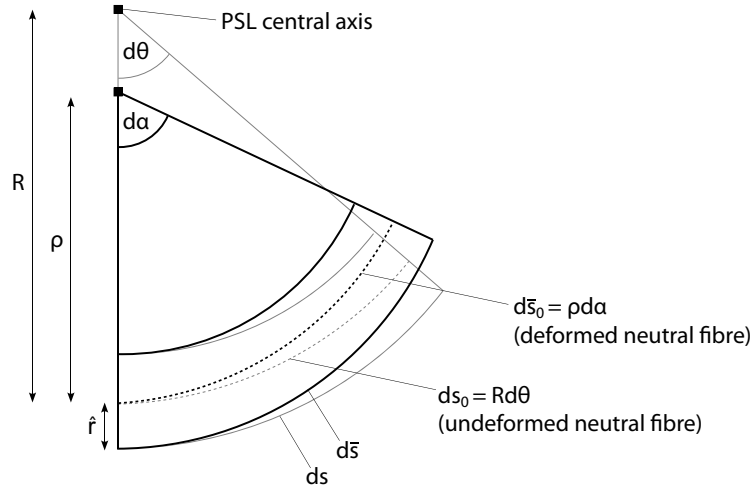

Figure 89: Deformed and undeformed infinitesimal ring element

the deformed and undeformed element we write

$$d\bar{s} = (\rho + \hat{r})d\alpha \quad \text{(deformed)} \tag{46}$$

$$ds = (R + \hat{r})d\theta \quad \text{(undeformed)} \tag{47}$$

$$= (R + \hat{r})\frac{\rho}{R}d\alpha. \tag{48}$$

This yields

$$\epsilon(\theta) = \frac{(\rho + \hat{r}) - (R + \hat{r})\frac{\rho}{R}}{(R + \hat{r})\frac{\rho}{R}} \tag{49}$$

$$= \frac{R\rho + R\hat{r} - R\rho - \hat{r}\rho}{R\rho + \hat{r}\rho} \tag{50}$$

$$= \frac{\hat{r}}{\rho}\frac{R - \rho}{R + \hat{r}} \tag{51}$$

$$\approx \frac{\hat{r}}{\rho}(1 - \frac{\rho}{R})(1 - \frac{\hat{r}}{R}) \qquad (1^{\text{st}} \text{ order Taylor polynomial}) \tag{52}$$

$$\approx \frac{\hat{r}}{\rho}(1 - \frac{\rho}{R}) \qquad (\hat{r} << \rho,\ R) \tag{53}$$

$$= \frac{\hat{r}}{\rho} - \frac{\hat{r}}{R} \tag{54}$$

$$\rightarrow \frac{1}{\rho} = \frac{\epsilon(\theta)}{\hat{r}} + \frac{1}{R}. \tag{55}$$

With the general expression of curvature in polar coordinates [70]

$$\frac{1}{\rho} = \chi = \frac{r^2 + 2r'^2 - rr''}{(r^2 + r'^2)^{3/2}} \tag{56}$$

and the radius of the neutral fibre, expressed as the sum of the undeformed radius and the radial deflection

$$r(\theta) = R + u_r(\theta), \tag{57}$$

we find

$$\begin{aligned}
\chi &= \frac{(R+u_r)^2 + 2u_r'^2 - (R+u_r)u_r''}{[(R+u_r)^2 + u_r'^2]^{3/2}} && (58)\\
&= \frac{1}{R}\frac{(1+\frac{u_r}{R})^2 + 2(\frac{u_r'}{R})^2 - (1+\frac{u_r}{R})\frac{u_r''}{R}}{[(1+\frac{u_r}{R})^2 + (\frac{u_r'}{R})^2]^{3/2}} && (59)\\
&\approx \frac{1}{R}\frac{1+2\frac{u_r}{R} - \frac{u_r''}{R}}{[1+2\frac{u_r}{R}]^{3/2}} && (60)\\
&\approx \frac{1}{R}\frac{1+2\frac{u_r}{R} - \frac{u_r''}{R}}{[1+6\frac{u_r}{R}]^{1/2}} && (61)\\
&\approx \frac{1}{R}(1+2\frac{u_r}{R} - \frac{u_r''}{R})(1-3\frac{u_r}{R}) && (62)\\
&\approx \frac{1}{R}(1-\frac{u_r}{R} - \frac{u_r''}{R}), && (63)
\end{aligned}$$

where primes denote the derivative with respect to θ. Apart from Taylor series expansions, the approximations applied above consist in neglecting higher-order terms ($u_r, u_r', u_r'' << R, \rho$). Combining equations (55) and (63) yields

$$\frac{\epsilon(\theta)}{\hat{r}} + \frac{1}{R} = \frac{1}{R} - \frac{u_r(\theta)}{R^2} - \frac{u_r''(\theta)}{R^2}. \tag{64}$$

Hence,

$$u_r''(\theta) + u_r(\theta) = -\frac{R^2}{\hat{r}}\epsilon(\theta), \text{ where } \epsilon(\theta) = \epsilon_0\cos(n\theta). \tag{65}$$

According to the type of the right-hand side of this equation, we choose the solution ansatz

$$u_r(\theta) = A\cos(n\theta) \tag{66}$$

and obtain

$$-n^2 A\cos(n\theta) + A\cos(n\theta) = -\frac{R^2}{\hat{r}}\epsilon_0\cos(n\theta) \rightarrow -n^2 A + A = -\frac{R^2}{\hat{r}}\epsilon_0. \tag{67}$$

Therefore, the radial deflection amplitude and the deflection can be expressed as

$$A = \frac{\frac{R^2}{\hat{r}}\epsilon_0}{n^2-1} \rightarrow u_r(\theta) = \frac{1}{n^2-1}\cdot\frac{R^2}{\hat{r}}\epsilon_0\cdot\cos(n\theta). \tag{68}$$

In analogy to the equivalent model for analytical frequency calculation introduced in section 4.1, the radial direction corresponds to the second principal bending axis of the PSL rings. The PSL radius R is 2.1 m, and its thickness h=$2\hat{r}$ is 0.07 m. The discharges with the highest strain values are the technical discharges with n=4 (ϵ_0=30 $\mu\epsilon$), and disruptive shots, where n=3 dominates (ϵ_0=65 $\mu\epsilon$). In the first case, the calculated deflection at an oscillation antinode is $u_{r,max}$=0.25 mm. For a hard disruption, the calculation yields $u_{r,max}$=1.02 mm.

Hence, the PSL deflection amplitudes during operation are of the order of one millimeter. The PSL rings have a clearance of at least 10 mm in radial direction for reasons of electric potential separation. Collisions of the PSL and the vessel or other in-vessel structures are therefore not to be expected. They could occur only at B-coil currents in the range of 4 kA and above. It will be shown later that this would result in forces far above the static strength limits of both the PSL rings and the coil attachments.

5.2 Comparison of experimental data with calculations and simulations

The analytical and finite element calculations described in the results chapter assign natural frequencies to ideal ring modes and to resonant oscillations of the whole PSL structure, respectively. The experimental data of resonant PSL oscillations excited either by disruptions or by using the B-coils allow the measurement of the frequencies at which these occur. For excitations with the B-coils, the modal shape is the PSL shape at the resonant frequency. It is visualised as a 'snap-shot' in one of its extremal deflection states. For disruptive excitations where a number of different modes always occur, the modal shape of interest is isolated. This is done by setting all coefficients of the Fourier transform outside the frequency domain of interest to zero. The resulting reduced matrix of coefficents is transformed back to real space and the PSL shape is displayed using these data. For the frequency comparison, only the FE free-hinges case is used here, where more ideal ring modes can be identified among the modal shapes than with fixed hinges. In general, the frequencies with fixed hinges are slightly higher (ca. 10-20%), but show a similar dependency on the mode number (cf. fig. 47). In simple words, the frequency difference is most probably resulting from the increased stiffness of the complete system caused by the extra boundary condition.

Table 17 presents the finite element natural frequencies with free hinges $f_{FE,free}$. In the cases where ideal ring mode numbers $n_{up/low}$ can be assigned to the FE modes, these are indicated separately for the two rings. The n=1 ideal ringmodes are included in the FE solution, but can neither be calculated theoretically nor measured with the PSL sensors, since they involve no deformation of the rings. The phasing describes the up/down configuration of the mode, i.e. if both rings are co- (even) or counter-oscillating (odd). Contrary to the FE frequencies and the frequencies measured after plasma disruptions f_{disr}, those measured during the technical discharges f_{tech} and those that are theoretically calculated are determined separately for the upper and the lower ring. The theoretical values are the same for even and odd phasing, as they do not account for the coupling of the rings. The values of f_{disr} are indicated as intervals, because every mode except n=4 shows considerable frequency spreading in different disruptive discharges. This is due to damping effects and mode splitting caused by mass and stiffness irregularities of the rings.

The frequencies of $n_{FE,free}$=14/15 disclose the unique feature of the quadratic modes again: The frequency interval of f_{disr} has a width of 1 Hz only as a result of the interaction of this specific shape with the PSL supports. This phenomenon has been discussed in detail in section 5.1.2. The agreement of the frequencies in

$n_{FE,free}$	$n_{up/low}$	phasing	$f_{FE,free}$	$f_{th,up/low}$	$f_{tech,up/low}$	f_{disr}
1	2/2	even	12,68	9,5/10,3	23/19,5	15-20
2	2/2	even	13,18	9,5/10,3	-	15-20
3	2/2	odd	16,31	9,5/10,3	(18)/19	15-20
4	2/2	odd	17,67	9,5/10,3	-	15-20
5	1/1	odd	21,35	-	-	-
6	1/1	-	21,81	-	-	-
7	2/2	even	26,88	9,5/10,3	-	15-20
8	3/3	odd	29,36	26,9/29,1	-	36-40
9	3/3	-	31,37	26,9/29,1	-	-
10	3/3	odd	31,84	26,9/29,1	-	36-40
11	3/3	even	34,14	26,9/29,1	-	36-40
12	3/3	even	34,66	26,9/29,1	-	36-40
13	3/-	-	41,88	26,9/-	-	-
14	4/4	even	46,37	51,7/55,7	50,5/54	49-50
15	4/4	odd	51,7	51,7/55,7	49,1/(54)	49-50
16	4/4	(odd)	53,75	51,7/55,7	-	49-50
17	4/4	odd	62,81	51,7/55,7	-	-
18	4/4	-	65,64	51,7/55,7	-	-
19	5/5	even	71,05	83,5/90,1	-	73,5
20	-	-	71,61	-	-	-
(...)						
46	-/8	-	198	-/239	-	-

Table 17: Comparison of natural frequencies of the PSL (in Hz) determined by FEM (f_{FE}), analytical calculations (f_{th}), from measurements during technical discharges (f_{tech}) and plasma operation (f_{disr}); PSL rings considered separately where applicable

the odd configuration ($n_{FE,free}$=15) is very good. The lower ring's resonance at 54 Hz is not represented in f_{disr}, because it is much less pronounced than the upper rings resonance (see fig. 79, p. 95). The theoretically determined values f_{th} are lower than the other frequencies at low mode number (e.g. n=2) and higher at high mode numbers (n=5). For the n=2 ringmodes, both measured frequencies are surprisingly high compared to the calculated values. As mentioned before, there is a strong interaction of these modes with the PSL supports which might explain this mismatch. Apart from that, the angular orientation of the modes also plays a decisive role for the frequency, and the specific forcing with the B-coils might, therefore, lead to the high values of f_{tech}. The frequencies f_{disr}, however, compared to all possible FE modes in the n=2 range, show good agreement. The same is true in the case of n=3. Due to the large frequency spread of the n=3 modes, it is necessary to compare modes with identical angular orientation. Such an example is presented in figure 90. This measurement is taken from a discharge for which only the sensors on the lower PSL ring were online. The angular orientation (toroidal angle θ) of both representations is the same. The frequencies of the modes differ by less than the frequency resolution of the measured frequency of 1.3 Hz. Both shapes are obviously very similar. Most such comparisons of experimental n=3 data

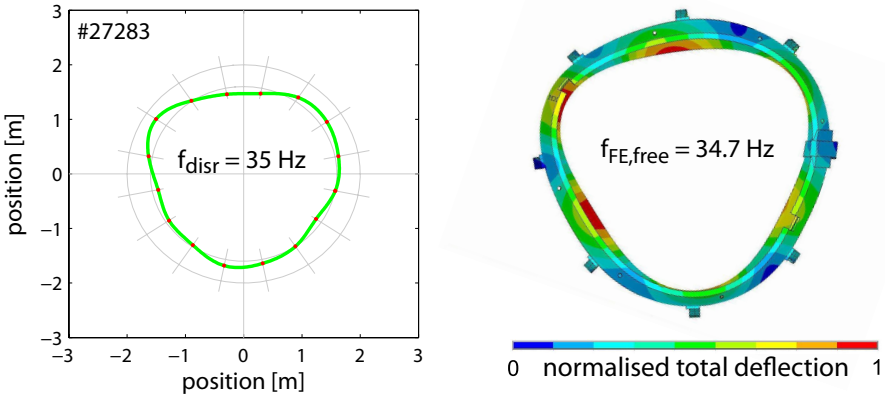

Figure 90: Triangular (n=3) PSL ringmodes: Fourier back-transformation of dominant spectral peak, only lower ring data available (left) and FE modal shape (right, free hinges case); angular orientation identical

and the finite element results show similar agreement. A second example is given in figure 91, which shows the shape of an n=4 mode in odd configuration, excited at the resonance frequency by the B-coils. The shapes and frequencies are in good

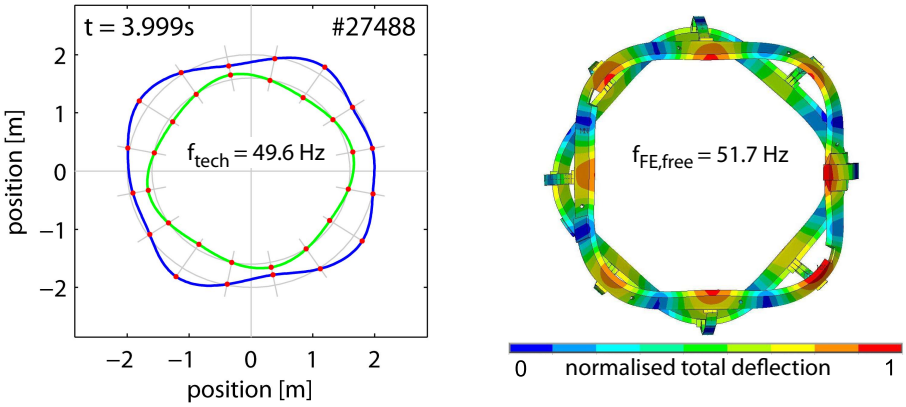

Figure 91: Quadratic (n=4) PSL ringmodes in odd configuration: Experiment (left, resonant excitation during #27488) and FE modal shape (right, free hinges case)

agreement. The angular orientation of the shapes is not perfectly the same. The mode excited by the coils (left) is spatially locked by the specific forcing. But, due to the relative positions of the PSL hinges and the B-coils (and thereby the positions of the coils' point loads), this is also a natural PSL mode. It is identical to the shape of the disruptive n=4 mode in figure 83d on page 99, which is freely oscillating at 49.9 Hz.

A final remark shall be made comparing the above results with the hammer tests. At the example[51] of impact 1.3, the hammer testing series can be interpreted in the following way: The impact induces two transverse bending deformation waves into the PSL which travel around the ring in both directions. These meet at the

[51] Normal impact between two vertical hinges positions in sector 1 of upper ring, no internal coils or wall tiles mounted (see section 4.3.1).

opposite side of the ring (see figure 54 on p. 65), where, under ideal conditions, they would interfere and reproduce the initial deformation of the hammer impact. This is not observed in reality because of wavelength dispersion, damping effects and probably also the influence of the PSL bearings. The shapes of the initial, two single pulses significantly change over time and interfere with each other after having completed half a turn. This leads to an oscillation of the whole structure at the 50 Hz (n=4) natural frequency before the motion is completely attenuated. Concerning the different hammer testing series, there is no visible frequency decrease due to the additional mass of the coils and wall tiles. However, the measured frequency complies to the other load cases.

The experimental results from disruptive and technical discharges are generally in good agreement[52] with the finite element modal analysis. This applies both to frequencies and modal shapes. Having a numerical model on hand to supply the modal shapes and frequencies, which have proven to correspond to the experimental data to a high extent, opens up an attractive option: Building a simplified, yet accurate discrete model for the PSL structure using a superposition of its modal shapes. This is the subject of the next section.

5.3 Discretised mechanical model

An advanced application of the strain sensor data is the representation of the deformation state of the whole PSL structure during plasma operation on the basis of these 32 values per time point. The ultimate goal is to calculate the displacements, strains and stresses in real-time, to avoid critical operational states that could lead to material collisions, plastic deformation or fatigue failure. Purely finite element based methods modelling the ensemble of the mechanical structure (i.e. PSL rings, supports and bridges) are unsuitable here, due to their computational complexity. However, faster models can include components simulated by FEM if these are minor or if the finite element solution is obtained beforehand. The latter approach is used here. The concept relies on structural modelling through superposition of modal shapes which are the eigenvectors of the homogeneous equations of motion. This method is known as modal expansion. The modal shapes[53] are extracted from the finite element calculation, and the associated modal participation factors and phase information are determined using experimental data. The modal participation factors or modal amplitudes are a measure of the amplitude of a mode. The aforementioned phase is in time, not in space, because the modal shapes already contain a defined spatial orientation. The modal amplitudes can be used to superimpose modal shapes of strain, stress or deflection likewise. By using modal shapes from finite element modal analyses as done in the present case, it is possible to calculate the respective values for every finite element by simple multiplications and summations of pre-calculated matrices (the modal shapes). The elegance of the modal expansion method lies in its potentially high performance and the computational simplicity. In practise, the number of modes is often limited to a significant basis by which the system behaviour is represented with satisfactory precision.

[52] This good agreement is also the reason why the finite element analysis was not refined any further (e.g. with more realistic PSL bearings).

[53] See fig. 46 on p. 56 to recall the principal appearance of some of the FE modal shapes used here.

The reduced oscillation model developed in the following can be called discrete for two reasons: First, the approximation routine for the modal amplitudes evaluates the strain measurements at 32 discrete sensor positions, offering a theoretical spatial resolution of up to n=8 ring modes. Second, the number of modes included in the model is limited to 66. This is in practise a restriction to frequencies below a certain limit. The frequency spectra obtained from disruptive excitations presented in chapter 4.4.1 suggest a maximum frequency of 250 Hz to be a justified value, because this limit was never exceeded by any measured signal.

To find the participation factors in the present case, we focus on the toroidal strain component, which is the quantity actually measured by the strain sensors. Following the considerations of chapter 2.2.3 concerning orthogonality of natural modes, the deformation state of the PSL can be represented by the superposition of its modal shapes. The weighted sum of the mode shapes (of toroidal strain) at a given position $\vec{x}$ of the PSL is described by

$$\epsilon_\theta(\vec{x},t) = \sum_{n=1}^{\infty} E_n(\vec{x}) A_n(t) \sin(\omega_n t - \varphi_n(t)). \tag{69}$$

In words, the toroidal strain value ϵ_θ at the time t and the position $\vec{x}$ of the PSL is equal to the weighted sum of *all* modal shapes. The functions describing the time behaviour are harmonics with phase φ_n and angular frequency ω_n. The modal shape E_n describes the spatial distribution of strain, whereas the modal participation factor A_n is the mode amplitude (the 'activity' of the mode). By allowing time-dependent amplitudes $A_n(t)$, non-stationary oscillations like damped vibrations can be represented. As only the toroidal strain is of interest in the following, we abbreviate $\epsilon_\theta := \epsilon$. Two discretisations are introduced: The infinite number of theoretical eigenmodes, i.e. mode numbers n, is limited to N modes, and the continuous body of the PSL is discretised to S points of interest, which are the sensor positions. The modal superposition transforms to

$$\epsilon_s(t) = \sum_{n=1}^{N} E_{sn} A_n(t) \sin(\omega_n t - \varphi_n(t)), \quad s = 1, ..., S. \tag{70}$$

The time evolution of the strain at just one position, e.g. $s = 1$ for the first sensor reads

$$\epsilon_1(t) = E_{11} A_1(t) \sin(\omega_1 t - \varphi_1(t)) + ... + E_{1N} A_N(t) \sin(\omega_N t - \varphi_N(t)). \tag{71}$$

The sine function is transformed to obtain a solvable set of equations with linearity in the coefficients

$$\begin{aligned} A_n(t) \sin(\omega_n t - \varphi_n(t)) &= A_n(t)[\cos(\varphi_n(t)) \sin(\omega_n t) - \sin(\varphi_n(t)) \cos(\omega_n t)] & (72)\\ &= a_n(t) \sin(\omega_n t) + a_{N+n}(t) \cos(\omega_n t). & (73) \end{aligned}$$

The coefficients are set to

$$a_n(t) := A_n(t) \cos(\varphi_n(t)) \quad \text{and} \quad a_{N+n}(t) := -A_n(t) \sin(\varphi_n(t)). \tag{74}$$

Rewriting equation (70) in matrix notation yields

$$\begin{pmatrix} \epsilon_1(t) \\ \epsilon_2(t) \\ \vdots \\ \epsilon_S(t) \end{pmatrix} = \begin{pmatrix} E_{11} & \cdots & E_{1N} & E_{11} & \cdots & E_{1N} \\ E_{21} & \cdots & E_{2N} & E_{21} & \cdots & E_{2N} \\ \vdots & \ddots & \vdots & \vdots & \ddots & \vdots \\ E_{S1} & \cdots & E_{SN} & E_{S1} & \cdots & E_{SN} \end{pmatrix} * \begin{pmatrix} \sin(\omega_1 t) & 0 & \cdots & 0 \\ 0 & \sin(\omega_2 t) & \cdots & 0 \\ \vdots & 0 & \ddots & \vdots \\ 0 & \vdots & \cdots & \sin(\omega_N t) \\ \cos(\omega_1 t) & 0 & \cdots & 0 \\ 0 & \cos(\omega_2 t) & \cdots & 0 \\ \vdots & \vdots & \ddots & \vdots \\ 0 & 0 & \cdots & \cos(\omega_N t) \end{pmatrix} * \begin{pmatrix} a_1(t) \\ a_2(t) \\ \vdots \\ a_N(t) \\ a_{N+1}(t) \\ \vdots \\ a_{2N}(t) \end{pmatrix}, \quad (75)$$

which is the same as

$$\vec{\epsilon}\,(t) = \mathbf{E}\ \mathbf{F}(t)\,\vec{a}(t) \quad \text{or} \quad \vec{\epsilon}\,(t)^{(S\times 1)} = \mathbf{E}^{(S\times 2N)}\ \mathbf{F}(t)^{(2N\times 2N)}\ \vec{a}(t)^{\,(2N\times 1)}. \quad (76)$$

The vector $\vec{a}(t)$ designates the (time-dependent) modal amplitudes, and the matrix of functions $\mathbf{F}$ contains the time dependency of the strain functions. Consider now a single time point t_0. Assume the natural frequencies ω_n as well as the matrix of eigenvectors $\mathbf{E}$, which describes the spatial distribution of all modes, is known. With S measured strain values, we obtain a system of S linear equations to determine the $2N$ unknown coefficients a_n and a_{N+n}. Taking further time points into account and supposing the modal amplitudes to be approximately constant on short timescales, the number of equations increases to $(S \cdot T)$. This set of equations can be solved rigorously for $S \cdot T = 2N$. However, such a solution is probably unstable in the sense that measurements from consecutive time points yield significantly different amplitudes. In that case, the strain input data may be reproduced exactly by the modal amplitudes, but these have no physical meaning. Measurement noise further compromises the said stability of this transformation. Therefore, it is reasonable to provide more data and to find an approximated solution to the resulting overdetermined system. This is applied in the following: The number of measurements $S \cdot T$ is greater than the number of modal amplitudes a_n to be determined.

All modal shapes in the range of n=1−66 are considered. This covers natural frequencies up to 250 Hz and therefore represents a sufficient basis to model the experimental strain data, which exhibits only frequencies below 150 Hz in the vast majority of cases. The matrix of eigenvectors $\mathbf{E}$ is obtained from the finite element simulation (cf. section 4.2). This is done by evaluating the strain solution of the modal analysis at the positions of the sensors for every mode number. As the sensors are not placed on nodes or centrally with respect to the elements of the FE model, the strain values are interpolated linearly from the solutions of their neighbouring elements. Only the strain component in the direction of measurement of the sensors (toroidal) are of interest. Thereby, 66 normalised eigenvectors with 32 elements, which represent the 32 regularly spaced sensor positions are extracted from the

numerical solution. This procedure was performed for the two cases of fixed and free vertical hinges, yielding two slightly different matrices of eigenvectors. It has been shown that both lead to comparable solutions in terms of the modal amplitudes A_n, as will be presented later. The natural frequencies ω_n are also adopted from the two different finite element simulations. The matrix of functions $\mathbf{F}$ and the experimental strain data $\vec{\epsilon}$ being known, the modal amplitudes A_n and phases φ_n can be calculated according to equations (74) and (77). This operation consists of finding the approximated solution of the *overdetermined* system

$$\vec{\epsilon}\,(t) = \mathbf{E}\ \mathbf{F}(t)\,\vec{a}(t) \quad \rightarrow \vec{a}(t) = [\mathbf{E}\cdot\mathbf{F}(t)]^T\cdot\vec{\epsilon}\,(t), \tag{77}$$

which is solved with a least-squares routine[54]. In order to judge the accuracy of the amplitudes $\vec{a}$, they can easily be transformed back to obtain strain data by insertion into equation (77). The difference between this backtransformation and the original sensor signals $\vec{\epsilon}$ represents the error of the modal expansion.

The requirement of over-determination is met if data of at least five[55] consecutive time points is considered. In the case of a major plasma disruption, one would expect to find large amplitudes in the beginning, which fade quickly. The solutions that are found using a low number of time points (5-10) have been shown to be unstable in the sense that they vary very quickly and seemingly in an unordered manner. The algorithm can be adjusted in some way by wisely choosing the length of the considered *time interval* which is used to calculate the modal amplitudes of *one time point*. This means that more data is available to determine the same number of unknowns. With growing time interval, the set of equations thereby becomes more and more 'constrained' and *amplitude* variations over time are smoothed. A set of 30 time points, i.e. data of 30 ms, has been shown to be a good compromise between stability of the solution and the necessity of a finite length in order to allow the amplitudes to vary (e.g. due to damping). This window size has been used throughout the calculations presented in the following. Compared to the experimental data, 30 ms correspond to about one full oscillation cycle at an n=3 (triangular) PSL natural frequency and to 1.5 cycles at n=4. Therefore, the averaging effect of the finite time window is acceptable, because for such low cycle numbers, amplitude variations are very probably negligible. A solution for every time step of 1 ms is found by applying the calculation method to a time interval spanning from 15 ms before to 15 ms after the time point of interest, analogous to a moving average filter. However, while such a filter generally flattens peak values, the present method allows, in principle, to represent peaks (of strain) accurately, because the time behaviour of the model, described by the harmonic functions of the matrix $\mathbf{F}$, varies over time. Only variations of modal amplitude are smoothed, not the strain time traces that are represented by the model. One could say that the time window, which is used for the amplitude approximation, contains the strain signal history just before and after the moment of interest.

As a proof of concept of the approximation method (eq. (77)), a test-run was performed, which used actual measured data to determine the eigenvectors. If the calculation routine is correct, the backtransform, i.e. the superposition of the these

[54]This routine is incorporated in the so-called backslash operator (the \-operator) in MATLAB
[55]$S\cdot T = 32\cdot 5$=160 equations for $2N = 132$ unknowns a_n.

eigenvectors **E** using the amplitudes and phases $\vec{a}$ given by the model, should exactly reproduce the original data $\vec{\epsilon}$. This allows the assessment of the properties of the approximation independently of potentially erroneous eigenvectors (modal shapes) determined by finite element calculations. In a Fourier spectrum of strain data, these measured eigenvectors are given by the amplitudes of the spectral peaks at one frequency. Strictly speaking, the term eigenvector is only justified in the context of free oscillations. However, the following example shows a technical discharge where free, natural n=4 oscillations, previously detected after disruptions, were reproduced using the B-coils. Therefore, this designation is adequate. In any case, the fact that the used data represents a forced oscillation does not have an influence on this test as a demonstration of the approximation routine. Figure 92a illustrates the calculation procedure. The model is considerably simplified by defining an arbitrary

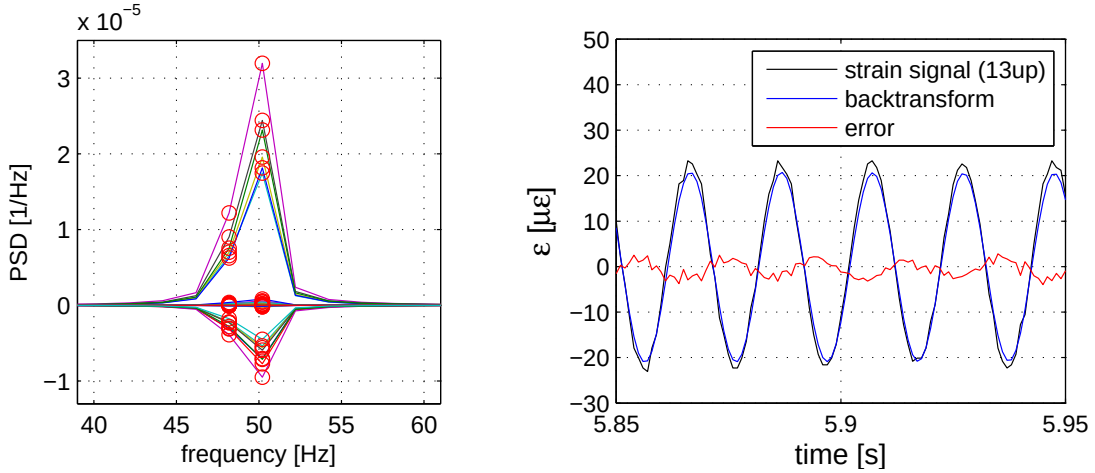

(a) Response spectrum at excitation frequency with values considered for eigenvectors marked by circles

(b) Strain signal of sensor 13up and its backtransformation by the discrete model

Figure 92: PSL response spectrum and time traces of technical discharge #27487 (forced excitation with B-coils, n=4, odd) using the eigenvectors and natural frequencies reconstructed from the measurement (t=5.59 s − 6.09 s)

lower acceptance limit: Frequencies, at which *all* PSD values are below 30% of the absolute maximum amplitude of the whole spectrum are neglected. This allows the restriction of the number of eigenvectors in the present case to two, those at 49 and 50 Hz. The frequencies are adopted from the measurement as well. The components of the two eigenvectors are identical to the spectral values at these frequencies, which are marked by red circles. Here, the power spectral densities (PSD) are shown, the actual single amplitudes that constitute the eigenvectors are the roots of these values. For the following calculation, the eigenvectors are normalised.

The accuracy of the model is high, as shown in figure 92b, where the back-transformation, based on two eigenvectors only, is compared with the original signal. The 31 back-transformations of the other sensor signals show similar agreement. With the measured eigenvectors and oscillation frequencies, the numerical method is apparently working correctly.

This model should not be mistaken as a simple reduction of complexity by frequency filtering. The eigenvectors contain spatial information. The amplitude ratios

of all sensors are thereby determined. Hence, the model is much more specific than a frequency filter. The goal of the present modal expansion is to calculate modal amplitudes A_n which can be used to superpose modal shapes extracted from finite element modal analyses. This would allow to obtain information of the PSL deformation with high spatial resolution. The above example demonstrates the successful operation of the calculation routine (with measured eigenvectors), but the modal amplitudes obtained thereby have no practical importance. This is why this method is used exclusively with eigenvectors extracted from FEM in the following.

Figures 93a and 93c show the time evolutions of the modal amplitudes A_n from the modal expansion routine using the finite element eigenvectors in the free and fixed hinges case. It was applied to a technical discharge with resonant n=4 PSL

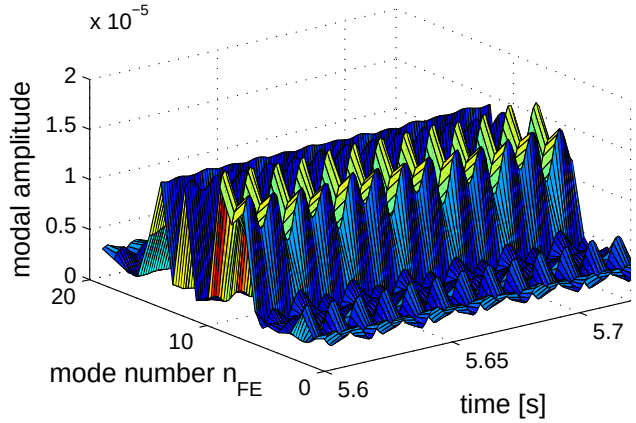

(a) Modal amplitudes $A_n(t)$ (free hinges)

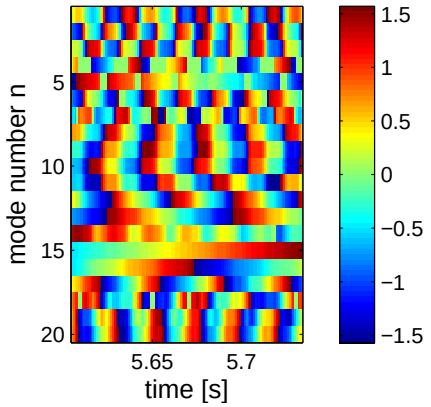

(b) Modal phases $\varphi_n(t)$ (free hinges)

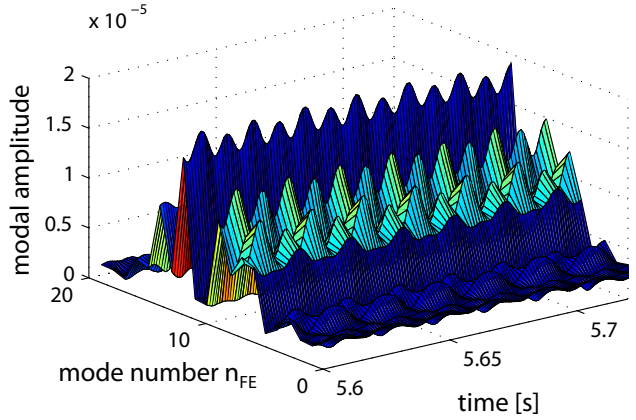

(c) Modal amplitudes $A_n(t)$ (fixed hinges)

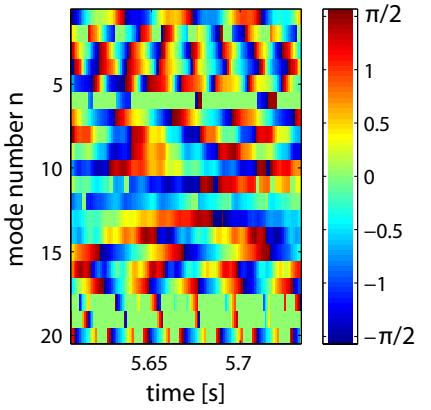

(d) Modal phases $\varphi_n(t)$ (fixed hinges)

Figure 93: Amplitude and phase evolutions of technical discharge #27487 (forced excitation with B-coils, n=4, odd) using the FE eigenvectors and natural frequencies of the free (a,b) and fixed hinges case (c,d); phases associated to amplitudes below significance threshold of 10% of maximum amplitude set to zero (green)

excitation with the B-coils. At mode numbers above 20, only minor amplitudes are found, which are not shown in the graph. In the two different cases (free and fixed hinges), different modes exhibit the largest amplitudes. In both cases, there is a systematic oscillation in time of these modal amplitudes which cannot be explained

intuitively. A close look at the corresponding phases shown in figure 93b and 93d reveals that most phases are either monotonously decreasing or increasing over time. This leads to periodic variations in the phase contour plot because the phase is only defined on the interval from $-\pi/2$ to $\pi/2$. This effect represents a correction of the natural frequencies by the approximation routine. Suppose a modal phase with linear time behaviour according to $\varphi_n(t) = c \cdot t$. This means that according to eq. (70), the argument of the modal oscillation $\omega_n t - \varphi_n(t)$ becomes $\omega_n t - c \cdot t = (\omega_n - c) \cdot t$. The term $\omega_n - c$ is the corrected natural frequency. Generally, this modification of the natural frequencies of the model is not surprising, as an oscillatory system under harmonic forcing vibrates solely at the excitation frequency. When the corrected frequencies are calculated and included in the model, the oscillation of the modal amplitudes vanishes. This effect is shown in figure 94, where the natural frequencies of the seven modes with the highest amplitudes have been corrected. This image shows results using the FE eigenvectors of the free hinges case. This

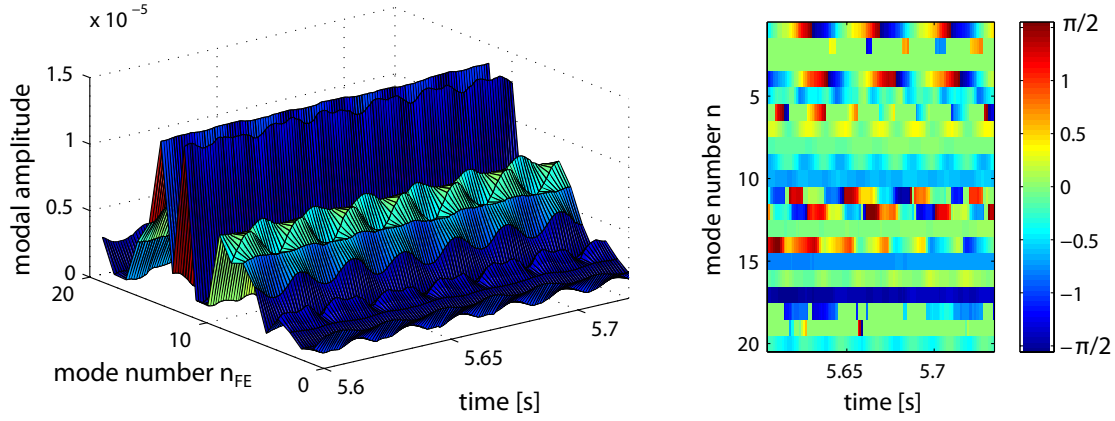

(a) Modal amplitudes $A_n(t)$ (b) Modal phases $\varphi_n(t)$

Figure 94: Amplitude and phase evolutions of technical discharge #27487 (forced excitation with B-coils, n=4, odd) using the FE eigenvectors (free hinges case) and partly adjusted frequencies; phases associated to amplitudes below significance limit of 10% of maximum amplitude set to zero (green)

configuration is used exclusively in the following, because of its good agreement with the experimental data in terms of modal shapes and frequencies demonstrated in chapter 5.2. There is a strong interdependence between the natural frequencies set in the model and the results in terms of the dominant modal amplitudes and their phases. Therefore, after correction was performed for the strongest mode, the routine was rerun and the next correction was carried out based on the newly obtained modal phases. For example, the frequency of the mode with n_{FE}=15 underwent correction and the corresponding amplitude shows no oscillating behaviour. The frequencies ω_9 and ω_{14} have not yet been changed and their corresponding modal amplitudes do oscillate distinctly. This means that the results of the discrete PSL model (the A_n) are stabilised when correct frequencies are used. With incorrect frequencies, the 'real' frequencies of the measured strain signals $\vec{\epsilon}$ are reproduced by oscillating amplitudes A_n. The dominant modes in this example represent the PSL shapes to be expected: The two modes with n_{FE}=13 and 15 are in fact both

n=4, odd ringmodes with slightly different angular orientation. It is notable that the backtransformations of both models are accurate reproductions of the original input signals (not shown). This is even more surprising as the models of figure 93 have obvious deficiencies concerning the natural frequencies and also because the different sets of eigenvectors (free and fixed hinges) have no effect on the accuracy, either.

This suggests that the model should be further constrained by setting the phases φ_n to constant values instead of allowing time-dependent phases for every mode. The phases are determined for a single time point with an interval size of 30 ms, as before. The modal amplitudes of the whole time window of interest are then calculated using these phase values by inserting them in the matrix of functions $\mathbf{F}$. The number of degrees of freedom of the model is thereby halved. A sample result of such a transformation is presented in figure 95, using the same corrected frequencies as in the previous example, fixed phases and a time interval that is four times longer. Grid lines are suppressed for better visibility. The model allows negative values for

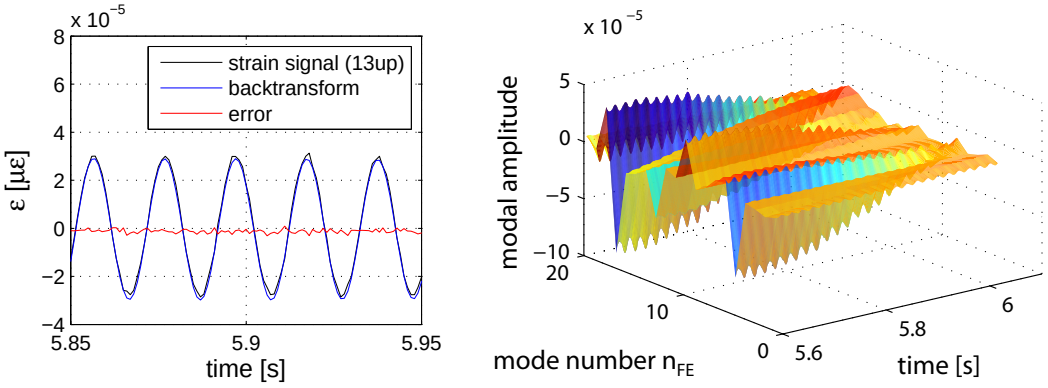

(a) Comparison of sensor signal and backtransformation

(b) Modal amplitudes $A_n(t)$

Figure 95: Strain time trace and modal amplitudes with fixed modal phases of technical discharge #27487 (forced excitation with B-coils, n=4, odd) using the FE eigenvectors (free hinges case)

the modal amplitudes. The precision of the reproduction as demonstrated in figure 95a is high. Again, there is a fast oscillation of the modal amplitudes, and an additional slower time dependency. The second effect might result from the slow sweep of the excitation frequency of about 0.5 Hz in the time interval shown. This also explains the width of the spectral peak of the PSL response in figure 92a as opposed to the sharp peak in the case of constant frequency excitation (see fig. 60b, p. 72). Towards the end of the time interval, all modal amplitudes decrease significantly. This is surprising because the PSL oscillation does not change notably in this short time. Again, this could be an effect of the swept excitation frequency. In any case, large parts of the modal oscillations must compensate each other, because their superposition (fig. 95a) is an oscillation with constant amplitude. Additionally, several of the modal amplitudes are considerably higher than the amplitude of this backtransformation. These observations remain ambiguous and, thereby, naturally reduce the confidence in the model, when it is utilised with forced oscillations.

The application of the model to the short, free oscillations following a disruption is its main prospective function. Such an example is illustrated in figure 96. As high

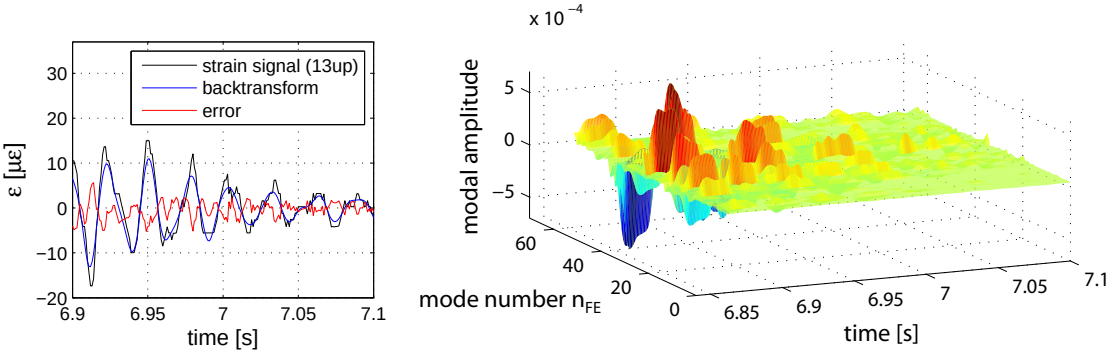

(a) Strain signal of sensor 13up and its backtransformation

(b) Modal amplitudes $A_n(t)$ of all 66 considered modes

Figure 96: Time traces and modal amplitudes of the disruptive discharge #26217, model with fixed modal phases and FE eigenvectors (free hinges case)

activity is observed also for mode numbers above 20, the right graph illustrates the amplitudes of all 66 modes, here. Compared to forced oscillations at almost constant frequency, the much less ordered PSL vibration resulting from a plasma disruption calls for higher robustness of the model. As shown in figure 96a, the accuracy of the back-transformation, i.e. the accuracy of the modal amplitudes, is much smaller in this case. This also limits the precision of the strains, stresses or deflections to be calculated using the present modal amplitudes as weight factors for linear combinations of modal shapes of the full PSL FE model. Therefore, this model is not developed further for approximating disruptive oscillations. The PSL fatigue damage assessment in chapter 5.5.1 is based on a different approach of analytical mechanics and a number of conservative simplifications.

However, under certain conditions, the simple case of a forced PSL oscillation can be represented accurately with the discrete model. This is of particular interest, because it allows to study components like the support bridges, that are otherwise not accessible by mere analysis of the optical sensor data. In the following, the discrete model is applied to the harmonic, n=4 PSL excitation using the B-coils as done before, but utilising a very short time interval for the transformation, which covers two full periods only. The formerly observed unstable behaviour of the modal amplitudes is partly due to the excitation frequency shift which is unimportant on such a short timescale. It has been shown that the absolute modal amplitudes are sensitive to the chosen frequency. The excitation frequency at a given time point is known. However, there is a delay between the PSL system frequency (the system response) and the swept excitation frequency. Figure 97b shows the modal amplitudes of the time interval marked in figure 97a, where a frequency of 50.4 Hz was used. A parameter study with eight different frequencies[56] showed that the smallest modal amplitudes are encountered with this frequency. A frequency mismatch probably leads to higher modal amplitudes where different modes mutually annihilate. Therefore, the *minimum* of the sum of all modal amplitudes can be considered to

[56] f_{test}=49.7, 50.0, 50.2, 50.4, 50.6, 50.8, 51.0 and 51.2 Hz.

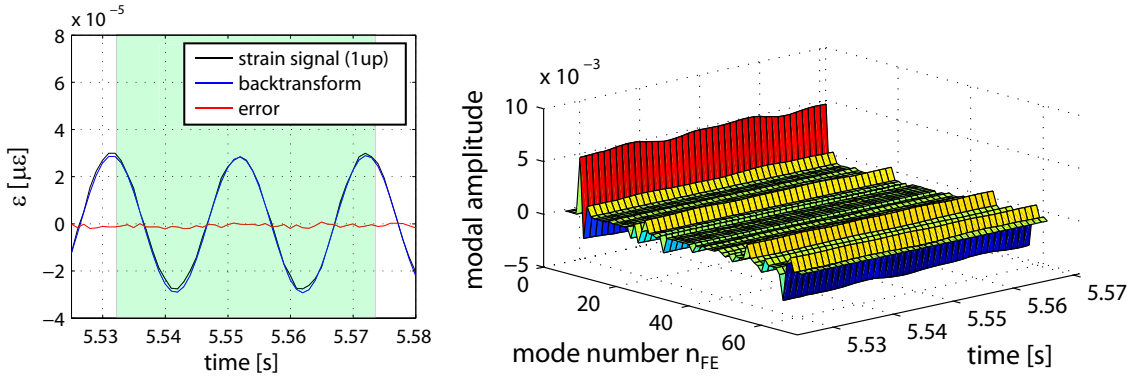

(a) Strain signal, backtransformation and error; time range marked in green used for projection

(b) Modal amplitudes $A_n(t)$ of all 66 considered modes

Figure 97: Time traces and modal amplitudes of an excerpt of technical discharge #27487 (n=4, odd, 110 A); FE model with free hinges, fixed modal phases and $\omega_n = 2\pi f_{ex}$.

indicate the 'true' frequency. Another decorrelating influence are the modal phases φ_n, fixed at the beginning of the time interval of interest, which lead to errors in the calculation of the modal amplitudes of long time intervals. Figure 95 gives an impression of this effect over 600 ms. By analysing shorter intervals and adapting the frequency as said, stable modal amplitudes as depicted in figure 97b are obtained.

According to equation (69), these values are used for a superposition of the first 66 modal shapes of deflection ($E_{u,n}$) extracted from the FE modal analysis:

$$\vec{u}(\vec{x},t) = \sum_{n=1}^{66} E_{u,n}(\vec{x}) A_n \sin(\omega_n t - \varphi_n). \tag{78}$$

The full model has 40265 elements and includes the PSL bridges. The modal shapes $E_{u,n}$ are eigenforms containing the three independent components of deflection for every element. The modal shapes of stress ($E_{\sigma,n}$) and strain (E_n) can be exported as well from the FE modal analysis. This enables to evaluate the deformation state of the PSL in terms of stress, strain and deflection. It will be shown later that the critical point of the PSL in terms of static strength and fatigue is a milled portion on the upper ring in sector 5 (see fig. 107, p. 133). As this is a geometric detail and not included in the global PSL FE model, the modal superposition is not used for stress modeling, here. As an example for the superposition method, figure 98 presents the calculated deflection of the element which exhibits the largest excursion from the undeformed state. The position in question is in the middle of the support bridge between sector 1 and 16 (θ=0°). The maximum deflection is 2.3 mm, which implies that the deflection amplitudes of all other elements of the whole model are inferior to this value. The deflection is almost purely radial. This example demonstrates the potential of this method: The deformation of the bridge can be evaluated by using strain data from a completely different part of the oscillating PSL structure. Unfortunately, verification by another measurement or different means is not possible at present.

In principle, it is also possible to calculate the sum of the external forces on

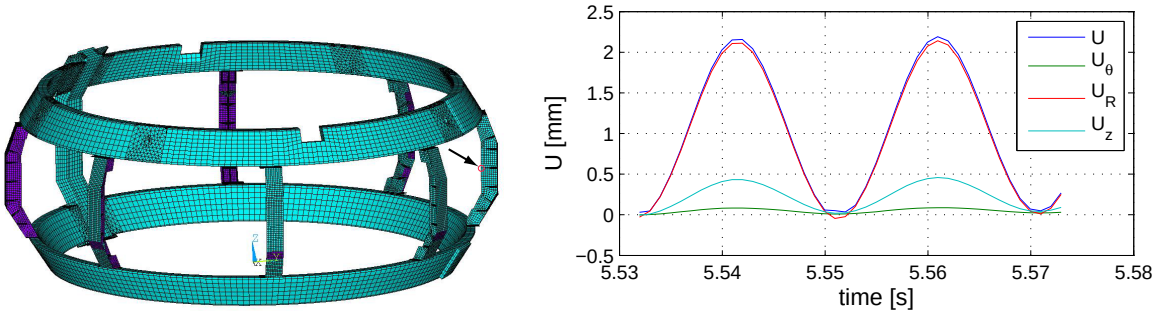

(a) Location of most deflected FE element on support bridge (sector 1/16) of full PSL model

(b) Time traces of the three excursion components and the total deflection

Figure 98: PSL element with maximum total deflection according to superposition of FE modal shapes (#27487, n=4, odd, I_B=110 A)

the PSL by adding up the acceleration of every element multiplied by its mass. The deflections of the upper ring at the positions of the vertical hinges can also be determined. The sum of the vertical forces on the hinges is the sum of the calculated external forces in the vertical direction. The deformation of each hinge is equal to the calculated PSL deflection at the respective position. Hence, these considerations would allow to evaluate the stiffness of the hinges. Of course, it is necessary to either assume the upper parts of the PSL hinges (the vessel) to be at rest, or to measure or calculate their movement. Like other attractive applications of the discretised model, this implies extensive further analyses or an extension of the sensing hardware. This is only justified if the modal amplitude approximation can be applied to all load cases.

The feasibility of a modal expansion model of the PSL was demonstrated in principle. This model yields satisfactory results in some, but not all cases. For an application to every discharge, possibly even in real-time, modifications of the model or a completely different approach would be necessary. Possible modifications of the model include the determination of the eigenvectors with an FE model with more realistic supports with finite stiffness. Another promising approach is, for instance, to include the amplitude decrease due to damping in the theoretical ansatz, similar to the Laplace transformation, instead of allowing the modal amplitudes to vary in time.

The so-called singular value decomposition (SVD) is widely used for the decomposition of data that possesses a certain structure in time and space (or two independent dimensions whatsoever), thereby gaining knowledge about the structure of the underlying system. At first glance, the working principle of SVD and the present simplified model are quite similar: Decomposition of the input signals in eigenvectors in time and space, where the eigenvectors fulfil the requirement of orthogonality. The substantial difference of the present model lies in the restriction of the time behaviour to harmonic functions at specified frequencies. This is necessary to allow the PSL deformation to be represented by the superposition of its modal shapes, because these shapes are obtained by finite element simulations using a harmonic ansatz. As the temporal eigenvectors obtained by SVD are only

in special, rare cases simple harmonic functions, SVD is unsuitable for the present application in this respect. Nevertheless, joined strain data of 17 major plasma disruptions was decomposed using SVD. The goal of this test was to find out if the spatial eigenvectors, determined by this strictly mathematical routine without using any mechanical assumptions, resembled to the measured eigenvectors or those determined by FEM. This is not the case. The SVD spatial eigenvectors seem to have no physical meaning except for one of them, which is similar to the typical PSL n=8 shape prior to a disruption (cf. fig. 80). The singular values, a measure for the 'activity' of the separate eigenvectors are *slowly* decreasing (as order increases), which is a sign that many different eigenvectors contribute to the total strain. The second half of the singular values (order 17-32 of 32) have a cumulated value of more than one fifth of all singular values. This corresponds to a significant contribution to the total strain. Even if this contribution is neglected and only the first half of the eigenvectors (spatial and temporal) is considered, the number of eigenvectors is 16. The number of eigenvectors determined by simple frequency filtering (see e.g. fig. 83) is much smaller. This could be a sign for different modes oscillating at almost similar frequencies which the SVD is able to distinguish due to their spatial orientation while they resemble to one single mode in a Fourier spectrum. This is apparently not the case, because the Fourier backtransformations presented in chapter 5.1.5 suggest that every spectral peak corresponds to one mode shape only. In summary, the SVD does not seem to be appropriate to simplify the PSL strain data in any way.

5.4 Relation of discharge parameters and PSL deformation

In this section, the forces on the PSL and possible dependencies between the maximal deformation and operational parameters of ASDEX Upgrade are explored. The first part presents a numerical method to calculate the forces on the PSL during non-disruptive plasma discharges. This tool provides force data for both PSL rings in the radial and vertical directions. The complex interaction of plasma position, control coil and PSL current and PSL deformation is briefly presented.

The force calculation routine cannot be used to investigate disruptive loads. Therefore, the second part of this chapter contains a very simple, empirical scaling of the maximum strain amplitudes during disruptions to reveal possible correlations.

5.4.1 PSL loading calculation for equilibrium processes

Apart from other tasks, the so-called discharge control system (DCS) realises the permanent control of the plasma position. In simple terms, one can think of the control system possessing a transfer function that connects input information concerning the plasma position and output variables like the set-values for the currents of the control coils COI. Its cycle time, i.e. the time between two consecutive control actions of the DCS, is 1-2 ms (as of 2012). The position of elongated plasmas is always unstable in the direction of elongation. Therefore, the dynamic characteristics of the DCS itself are likely to govern decisively the undulation of the control coil currents. In addition to the effect of the plasma itself, the control coils induce currents in the PSL. The superposition of both currents determines the Lorentz forces

on the PSL. These are calculated in the following using a self-developed numerical routine[57] with magnetic equilibrium data. Data examples of results are given. It is clear that any major modification of the DCS, such as changes of the cycle time, would have an immediate impact on the operational loads of the PSL, especially in terms of the frequency spectra of these loads and potential structural resonances.

The said forces are homogeneously distributed line-loads on the PSL rings, the sole exception being the current bridge, where the PSL is likely to be force-free. As the current bridge spans over a small toroidal angle only, this influence is neglected in the following. The mechanical loading results from the interaction of the electric current in the PSL, for which a measurement is available (through Rogowski coils on both rings), and the poloidal magnetic field. The magnetic topology inside the ASDEX Upgrade vessel is reconstructed for every discharge by a so-called equilibrium solver code. The results are solutions to the magneto-hydrodynamic equilibrium equation[58] in toroidal formulation. They are stored in shotfiles like diagnostic data, as a matrix of values on a spatial grid. These equilibria describe the surfaces of constant magnetic flux as a function of time. Different time resolutions are available, the highest one used here being 1 ms. Knowing the poloidal flux at a given time point, the radial and vertical magnetic field components are calculated according to

$$B_R = -\frac{1}{2\pi R}\frac{\partial \psi}{\partial z} \text{ and } B_z = \frac{1}{2\pi R}\frac{\partial \psi}{\partial R} \text{ [3].} \tag{79}$$

The PSL current flows strictly in the toroidal direction, i.e. perpendicular to the poloidal magnetic field component $\vec{B}_p = \vec{B}_R + \vec{B}_z$. With respect to the AUG coordinate system, the vertical and radial forces per PSL unit length (1 m) F_z and F_R are computed via

$$F_z = -B_R \cdot I_{PSL} \text{ and } F_R = B_z \cdot I_{PSL}. \tag{80}$$

Unfortunately, disruptive loadings cannot be assessed using this technique, because disruptions are non-equilibrium processes and the corresponding equilibria cannot be constructed. Nevertheless, most other load cases like wobbling or vertical plasma oscillations in highly elongated scenarios can be studied in detail. The numerical calculation consists of interpolating the flux values to a finer grid, adapted to the PSL geometry. Cubic spline functions are used for this approximation, which is performed once along z and once along R. The fineness of the grid containing the PSL cross-section is variable, it was set to 30 by 30 cells as a compromise of accuracy and computing time, also because increasing the grid further virtually showed no effect on the results. The single values of B_R and B_z at every grid point are multiplied with the instantaneous PSL current, yielding single forces at the grid points. Summing up all those that lie inside the PSL cross-section and taking the average value gives the net force. This is the average force that acts on one meter of the PSL conductor. The PSL current is assumed to be homogeneously distributed over the cross-section, skin effects are not considered. This probably does not change the results significantly, as the instantaneous B-field does not show strong gradients inside the PSL. Figure 99 shows the field of the Lorentz force inside the upper PSL

[57] This program was realised in the MATLAB environment.
[58] The Grad-Shafranov equation.

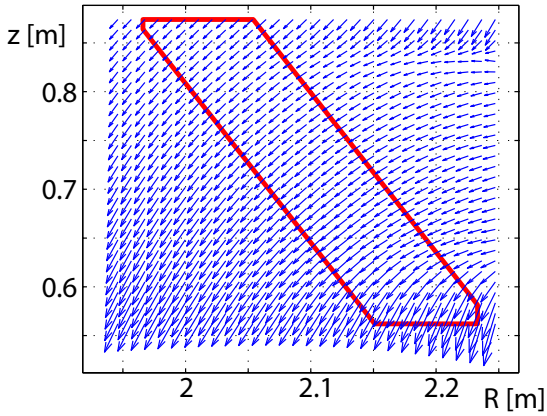

Figure 99: The output of the numerical calculation: Force field on the PSL cross sections (shown here is the upper ring, #28942, t=2 s).

ring[59] during the I_p-flattop phase of a stable plasma discharge. As these values are calculated based on the fast equilibrium and the PSL current measurement, which both have a time resolution of at least 1 ms, time traces of the PSL radial and vertical forces can be constructed at the same sampling rate. For a comparison with the PSL deformation measurement by the optical sensors, the force components in the direction of the principal axes of the PSL (cf. fig. 5) are of interest. In the following, the force vectors in R and z are, therefore, projected on the corresponding axes of the upper and lower PSL ring, respectively. Figure 100 presents a typical case of an H-mode plasma discharge with the presence of ELMs.

During the ELM, plasma particles are expelled and the plasma stored energy decreases. The plasma current usually also diminishes. Since the external magnetic configuration remains unchanged, the major plasma radius reduces, as a consequence of the energy loss. The plasma movement is compensated by the position control system. The sudden rise of the plasma current probably results from the reduced plasma inductance due to the changed geometry and the reaction of the plasma current control system to the initial current loss by steepening the ramp of the central transformer (OH-coil). This causes the plasma current signal to show recurring peaks at almost constant frequency. The vertical plasma position has a comparable behaviour with inverted sign. Both signals are input variables of the discharge control system (DCS) which reacts to the plasma shift. This reaction consists in actuating the inner control coils COI. The PSL current obviously depends on the actions of the control coil situated nearby, with a certain time lag. Finally, the force on the PSL and the PSL current signal show a direct (anti-) correlation. Therefore, the spectra of the excitation and the PSL system response should show similar patterns. Figure 101 presents spectra of the excitation force (F_2) and the PSL response (OSI data), evaluated based on 4 s of a plasma discharge. For the purpose of comparison, the cumulated spectrum of the 11 normalised disruptions from section 4.4.1, that is the average of their power spectral densities, is plotted at the bottom. It represents all PSL modes excited by a hard plasma disruption.

[59]The forces outside the PSL cross section, where no toroidal current flows are zero. The arrows shown there result from the rectangular area of interest of the calculation routine for $B_{R,z}$.

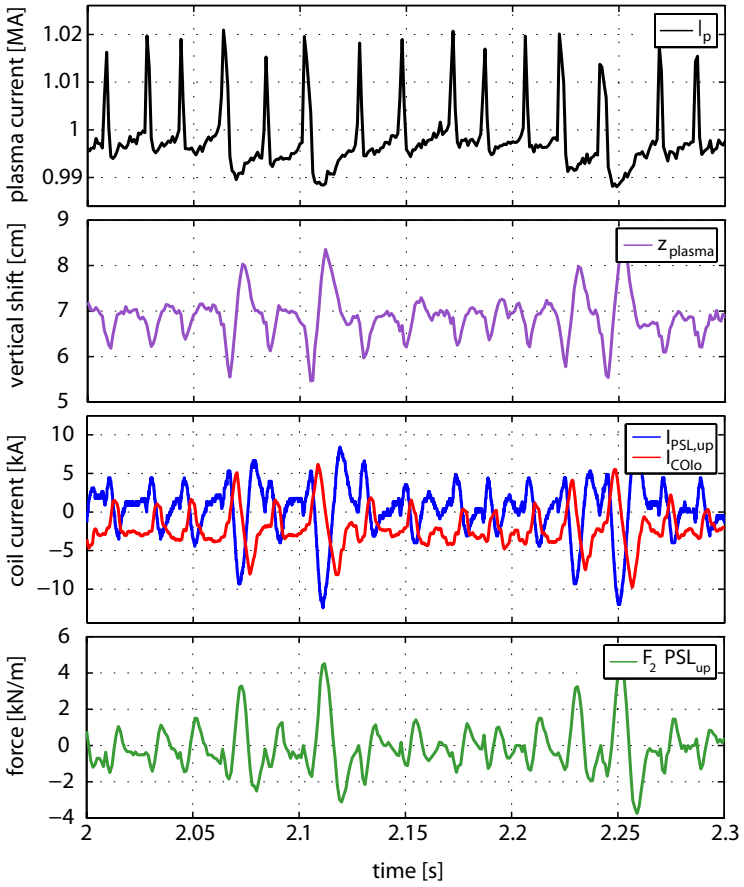

Figure 100: Time traces of vertical plasma position z, plasma current I_p, upper control coil (I_{COIo}) and PSL (I_{PSL}) currents and resulting force (F_2, homogeneous line load) on the upper PSL ring (ELMy H-mode #26217)

The frequency resolution of this spectrum is much lower than in plot (a), due to the post-disruptive oscillation being comparably short. The marked frequency ranges accentuate the domains of the n=3 (34-39 Hz) and the n=4 (46-52 Hz) ring modes. Surprisingly, the PSL current causes a broad-band excitation (b), which does not correspond at all to the mechanical response (a) measured during these 4 s. The PSL vibration (a) caused by the vertical plasma displacement does, however, fit nicely in the n=3 frequency interval. Similar to the disruptions, where the excitation could at least partly be considered as an impulse loading, the n=3 modes also seem to play a predominant role, here. Apart from the reasons for favouring the n=3 modes mentioned in section 5.1.5, a different look at the excitation frequency may help to understand the effects shown here. The amplitude of the PSL response to periodic variations of the PSL current has been shown to change on short timescales, as is visible e.g. in figure 72b. Here, the strain amplitude increases significantly over 8 oscillation cycles (ca. 300 ms), caused by a sudden variation of the frequency of the current (the excitation). The Fourier spectra of strain data have a systematic frequency resolution of $1000/N$ (in Hz), where N is the number of time-points. For this reason, the fast changes in frequency were resolved with an alternative method, called Empirical Mode Decomposition (EMD) or Hilbert-Huang Transform (HHT) [71], that supplies *instantaneous frequency* data. This technique uses two spline

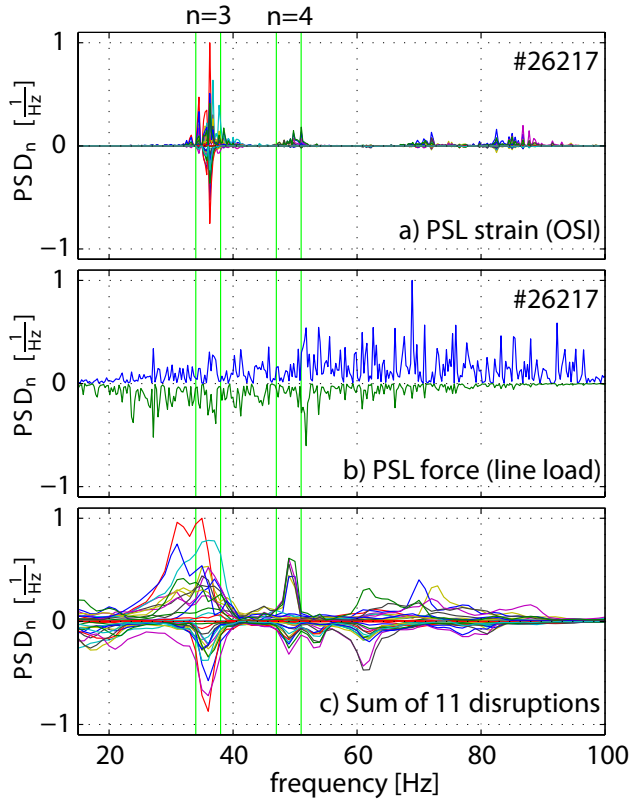

Figure 101: Normalised spectra of PSL deformation (a) and PSL line load (b, both #26217, t=0.816-4.814 s). Cumulated PSL deformation spectrum (OSI) of 11 disruptions for comparison (c). Frequency slots mark n=3 and n=4 ring mode domains.

functions to construct an envelope to the data, of which one coincides with the maxima and the other one with the minima of the original signal. The mean value of the two splines is called the first intrinsic mode function and is subtracted from the signal. The same procedure is applied to the residue yielding the second intrinsic mode function. This process is terminated either when a predefined criterion is met, or when the residual function is monotonic, i.e. having no extrema. The instantaneous frequency of the intrinsic mode functions is found using the Hilbert transform. This means that for every point in time, one frequency value per mode function, characterised by an amplitude, is obtained. A brief overview of different spectral analysis methods and more information on EMD can be found in the extensive report by Huang [71]. Implementations of EMD for different computing environments including MATLAB and IDL are freely available.

Figure 102 presents a time trace of the force on the upper PSL ring in the direction of its lowest bending stiffness (along principal axis 2), computed on the basis of magnetic equilibria and the measured PSL current. This example is taken from the same plasma discharge as before, and the displayed load is distributed homogeneously over the upper ring. Graph (b) is the output of the EMD, where the marker size represents the modal amplitude. The green lines indicate the general frequency domain of the dominating, triangular PSL modes. Red rectangles highlight the time windows with significant excitation in the n=3 ringmode domain from 34 to 39 Hz. The response of the PSL is represented in the bottom graph by the strain time trace

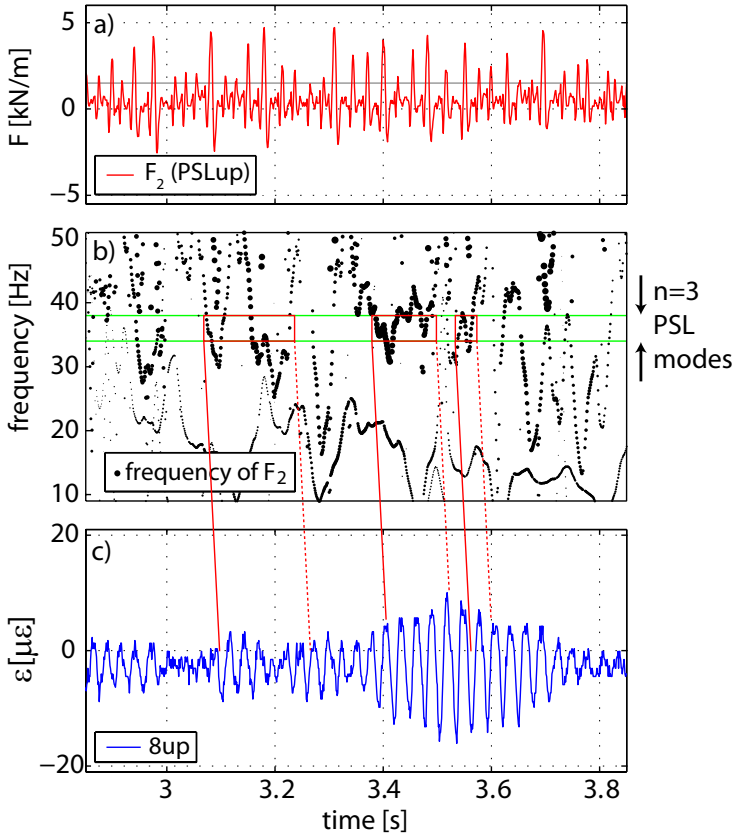

Figure 102: Calculated excitation force (line load) on upper PSL time trace (a) and EMD-determined frequency distribution (b). PSL response represented by strain signal of sector 8, upper ring (c), all data from #26217

from segment 8 on the upper ring (c). As soon as the excitation frequency is in the n=3 range, the PSL 'catches' this loading and the strain amplitude increases considerably. The straight red lines mark the intervals of n=3 excitation as well as the onset (solid line) and the end (dashed) of the strain amplitude increase. The time shift between excitation and onset of the oscillation shown by these lines is about 30 ms. This corresponds approximately to one full cycle of an n=3 natural oscillation. The lines have, as a time indicator, mostly qualitative character. Nevertheless, it can be concluded that the PSL deformation during such plasma discharges, with considerable shifts of the vertical plasma position, is governed by excitations in a narrow frequency band, which lead to n=3 PSL oscillations. The force calculation based upon magnetic equilibria and the measured PSL current is a universal tool which can be applied in every case where equilibria are available. This is not the case for disruptions, which are the subject of the following section.

5.4.2 Correlation of plasma parameters and disruption intensity

When the magnetic equilibrium reconstruction is not available, the method of force calculation of the preceding section is not applicable. As plasma disruptions are non-equilibrium processes and lead to strong oscillations of the PSL, a different method to quantitatively estimate the PSL loading is desirable. In this section, the maximum

strain amplitudes - as a measure of PSL response and thereby mechanical disruption intensity - are plotted against different candidate parameters to identify potential simple correlations. Figure 103 shows plots of the maximum strain amplitudes $\Delta\epsilon_{max}$ of the upper (values>0) and the lower (values<0) PSL ring versus the plasma current I_p, the plasma kinetic energy W_{MHD}, the product of plasma current and toroidal field strength $I_p \cdot B_t$ and the time when the current quench occurred. The last graph (e) shows the maximum strain amplitude plotted versus the maximum force on the 8 vertical tension rods of the vacuum vessel. These hinges are located in the even sectors and support the entire vacuum vessel and its inner components including the PSL (compare fig. 4). Their tension is routinely measured[60] using conventional strain gauges. A disruption mitigation system, based on massive gas injection upon detection of an upcoming major disruption, is used for discharges with plasma currents superior to 800 kA. Consequently, the PSL deformation above this threshold is expected to be smaller than extrapolations of values below 0.8 MA. It must be said that there is no clear correlation between the strain amplitudes and

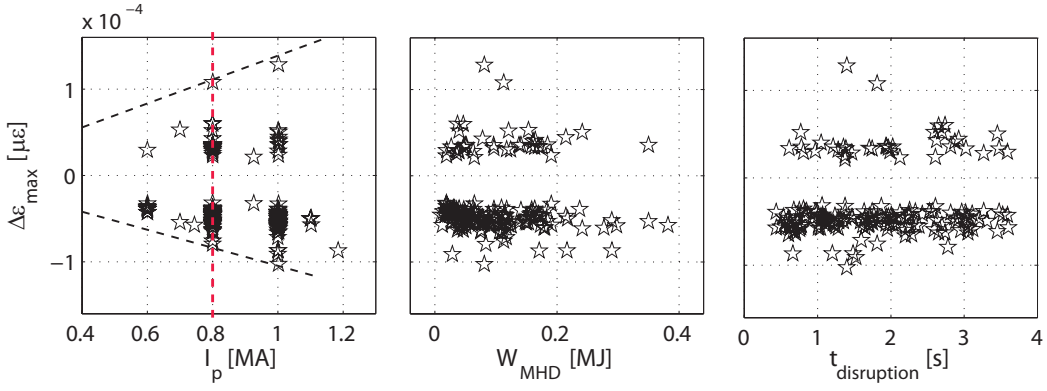

(a) Strain amplitude vs. plasma current

(b) Strain amplitude vs. plasma kinetic energy

(c) Strain amplitude vs. time of current quench

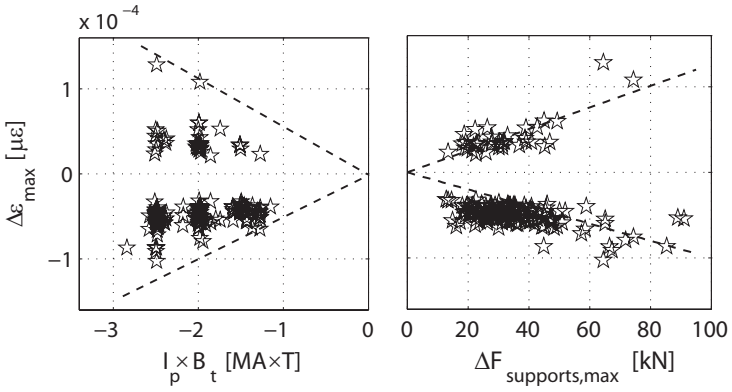

(d) Strain amplitude vs. plasma current multiplied by toroidal field strength

(e) Strain amplitude vs. maximum vacuum vessel vertical support force

Figure 103: Data base of maximum PSL strain values measured during disruptions

any of the chosen parameters. The plot versus I_p (a) suggests that there is an upper limit of the strain amplitude which increases with rising plasma current, illustrated by the dashed line. The analysis of early disruptions gave rise to the suspicion that

[60]Diagnostic KWN, signals V33 to V40.

discharges disrupting in an early stage are harmless. This idea is disproved by plot (c). Even disruptions that occurred at around t=0.5 s are in the bulk concerning their mechanical effect. In plot (d), a straight line through the origin builds an envelope for $\Delta\epsilon_{max}$ according to the idea that $I_p \cdot B_t$ is a measure for the highest electromagnetic loads that *may* arise during a disruption. The linear fit of the vessel support forces (e) accounts for a presumed statistical correlation. The vessel and the PSL form an oscillating structure, hence their relative movements are only indirectly coupled via elastic elements. Therefore, peak PSL strains and support forces are not limited by one another. Altogether, the aforementioned theses (illustrated by the dashed lines in (a,d,e)) agree fairly well with the data. With this number of data points, the present, very inexpensive correlation approach does not allow further deductions.

5.5 Consequential PSL dimensioning considerations

Considering the new loading condition of the PSL structure due to the internal coils and the potentially accumulated damage in view of its 21 years of operation up to the present day, obvious risks are fatigue failures of the PSL bridges, the vertical supports or the rings themselves. The original PSL design and dimensioning relied on a worst case disruption scenario, applying assumptions for plasma current, magnetic field strength and plasma displacement to calculate static loads on the PSL rings. Fatigue and resonance effects were not part of the evaluation. The following presents a fatigue investigation of the PSL rings, which permits direct usage of the signals of the optical sensors. The stresses of other PSL components and their joints are not directly accessible, but may be calculated using a modal expansion method as proposed in section 5.3. In the next section, an estimation method for the fatigue damage of the PSL[61] applying a counting algorithm on the measured strain data is developed. The subsequent section 5.5.2 presents the application of this method to an extrapolation of the strains during AC B-coil operation.

5.5.1 Actual PSL fatigue damage status

As outlined in section 4.4, there are multiple sources of forces on the PSL structure. Most of these are transient or oscillatory, but only excitation using the B-coils can be considered as producing purely cyclic deformation. An assessment of the fatigue condition of the PSL has, therefore, to be based on the quasi-stochastic strain time traces. Generally, special counting methods are used in order to obtain absolute fatigue damage values. These reduce the strain time traces to a so-called load collective which permits lifetime estimates. In the present case, an existing algorithm [72, 73], employing the so-called rainflow counting method [74] was used[62]. This method is a two-parameter counting technique. The parameters are the mean value and amplitude, which are calculated for every strain cycle. In other words, this algorithm counts full stress-strain hysteresis cycles, which has the physical back-

[61] These calculations were carried out under the assumption of a defect-free PSL material without cavities or cracks after installation.

[62] The used toolbox is publicly accessible and contains a set of functions to be used with the numerical computing environment MATLAB.

ground that the energy absorbed by the material is proportional to the area of the hysteresis (the integral over $\sigma \mathrm{d}\epsilon$). This energy corresponds to a certain amount of fatigue damage. The first step of the rainflow counting method consists of reducing an oscillatory signal to its extremal values, as the time intervals between these are unimportant. The oscillation frequency is not accounted for in the calculation, which is justified as long as amplitude and frequency do not attain values which would cause the material temperature to increase significantly. In the present case, the strain values of the order of 100 $\mu\epsilon$, which the PSL structure experiences during discharges of less than 10 s duration, are unlikely to have a relevant thermal effect.

Figure 104 illustrates the workflow of the rainflow counting. The raw strain signal

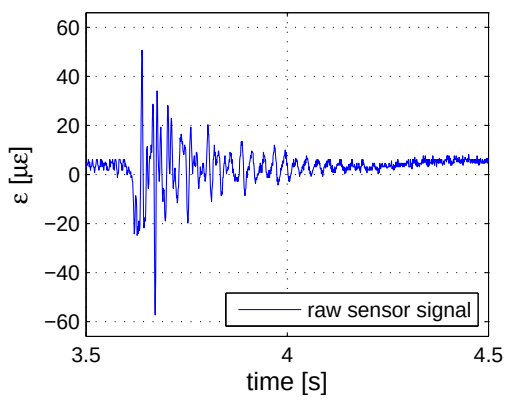

(a) Raw strain signal (sensor 7up)

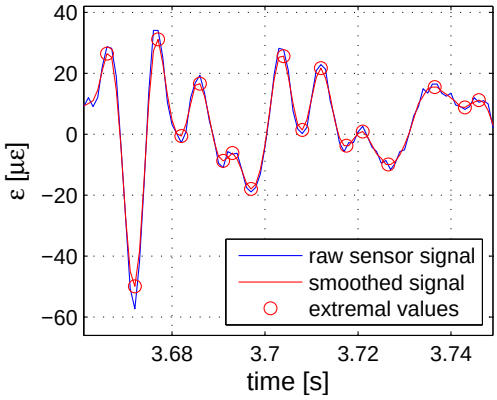

(b) Smoothed signal and identified peaks

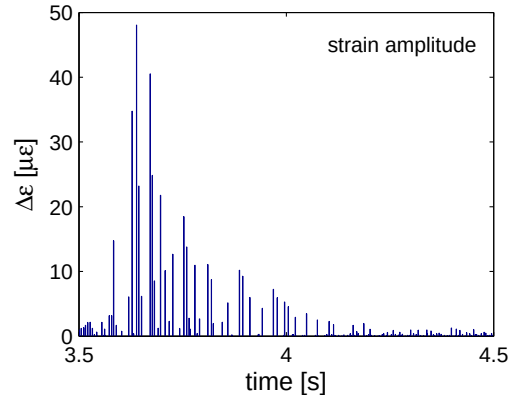

(c) Strain amplitudes computed with rainflow algorithm

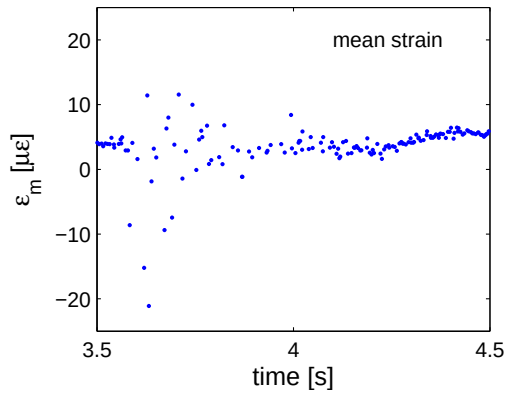

(d) Mean strain values computed with rainflow algorithm

Figure 104: Workflow of the fatigue damage calculation (data from #26026)

(fig. 104a) is smoothed with a moving average filter and the extremal values are identified (fig. 104b). The span of the filter, i.e. the averaged number of data points is three and a compromise to reduce the number of peaks due to measurement noise without too much flattening of the peaks. This would distort the damage calculation towards higher lifetimes. The output of the counting algorithm are the strain amplitudes, the mean strain values for every time point, and the corresponding number of cycles which is either 0.5 or 1. One has to think of the routine counting tensile and compressive half-cycles which are then matched. Typically, a small

number of half-cycles are left over without match. This results in a value of 0.5 of the associated number of cycles[63]. The amplitudes and mean values corresponding to the raw signal are displayed in figures 104c and d.

The number of cycles to failure of a material which is subject to purely cyclic load (with mean stress zero) is typically illustrated in the so-called Wöhler curve. This diagram shows the cyclic stress amplitude versus the number of cycles to failure on a logarithmic scale and is therefore also known as *S-N* curve. As statistical spread is large in fatigue, *S-N* curves are defined for a value of failure probability, usually 50% [75]. The experimental effort to determine these curves is very high and as a consequence, they are not available for every material. For Cu-ETP, the material of the PSL rings, the German Copper Institute provides *S-N* curves only for copper strips of 0.8 mm thickness and different amounts of prior cold working [76, 77]. These are obviously simplified and were constructed by using single data points from an earlier publication [78]. The fatigue data of copper in different geometries and stages of cold working given in this work allows the construction of an approximated *S-N* curve for the material of the PSL rings. Table 18 presents the used data. The suffix *F30* of the PSL material denotes cold-working (*F*) of the

Material	Cu-ETP [78]	Cu-ETP F30 (PSL rings)
Dimensions	Rod (⌀16 mm)	Beam (ca. 350×80 mm)
Prior cold working	30%	n.a.
Tensile strength R_m	304 MPa	300 MPa
Fatigue strength σ_{Nf} ($N_f = 10^8$ cycles)	113 MPa	n.a.

Table 18: Material data from literature of two virtually similar copper grades

half-finished product until a tensile strength of 300 MPa (*30*×10) is reached. As the tensile strengths of both materials are practically identical, it is likely that they also experienced the same amount of prior cold working. Therefore, the mechanical properties are accepted as being similar, and the fatigue strength of 113 MPa at 10^8 cycles is adopted for the PSL material. Based upon this data, the simplified *S-N* curve shown in figure 105 is constructed. The relation between cyclic stress

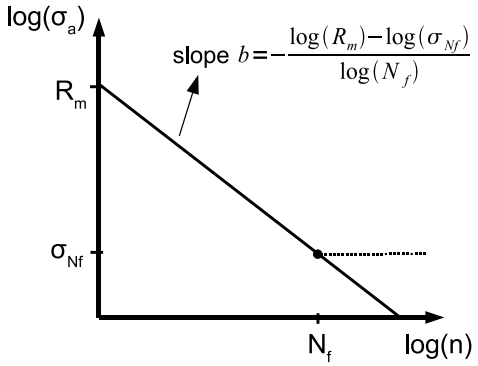

Figure 105: Approximated *S-N* curve (Wöhler curve) based on R_m, σ_{Nf}, N_f [78]

[63] Another consequence of this matching is that the time assigned to the amplitude and mean values is the average of the time-points at which the two half cycles occur.

amplitude σ_a and the number of cycles to failure n is described by the so-called Basquin-equation [79, 80]:

$$n = \left(\frac{\sigma_a}{R_m}\right)^{1/b}, \text{where } b = -\frac{\log(R_m) - \log(\sigma_{Nf})}{\log(N_f)} \approx -0.053. \tag{81}$$

In a double-logarithmic chart like figure 105, this relation obviously corresponds to a straight line. The Basquin equation is a simple and widely used approximation for the *S-N* curve of materials for which more detailed fatigue data is not available. Copper crystallises in a face-centred cubic (fcc) structure, like austenitic steel. This microstructure is generally known not to possess an endurance strength, a stress (or strain) amplitude limit below which the material can withstand an infinite number of cycles. This property is a result of the high number of glide planes of the fcc structure, as opposed, for instance, to ferritic steels, which are of body-centred cubic microstructure. This means that even oscillations with very small amplitudes eventually lead to failure after a high number of cycles. The horizontal dashed line in figure 105 represents the endurance strength, as it can be found, for example, in [77], despite the fcc structure of the material. For the aforementioned reasons, the *S-N* curve is supposed to exhibit no endurance strength, which means that the solid, straight line (fig. 105) connecting the two known data points is adopted as fatigue strength of the PSL material. This represents a conservative approximation. For a given stress amplitude σ_a, the corresponding number of cycles to failure n can be determined by equation (81).

The output of the rainflow counting are pairs of mean strain and strain amplitude. Supposing purely linear-elastic material behaviour, these are converted to pairs of mean stress and stress amplitude according to Hooke's law:

$$\sigma = \epsilon \cdot E. \tag{82}$$

The *S-N* curve of figure 105 is defined for pure cyclic stress without mean stress. Therefore, an equivalent, purely cyclic stress amplitude[64] $\Delta\sigma_{eq}$ $(= 2\sigma_a)$ needs to be determined and inserted in equation (81) to find the corresponding fatigue lifetime. A common concept to do this is the stress transformation as reported in [81], which assumes the linear dependence expressed in figure 106 and equation (83). The equivalent stress amplitude corresponds to the experimentally measured value pairs of amplitude $\Delta\sigma_{exp}$ and mean stress $\sigma_{m,exp}$ supplied by the rainflow algorithm in terms of fatigue damage, or expected lifetime, which means exactly the same. The approximated Smith diagram as shown in figure 106 is generated using the known tensile strength and the rainflow output. It represents a justified and conservative approximation as long as the strains are well below the plastic limit, which is given in the present case. The equivalent stress amplitude is determined according to the intercept theorem:

$$\frac{R_m - \Delta\sigma_{m,exp}}{R_m} = \frac{\Delta\sigma_{eq}}{\Delta\sigma_{exp}} \;\rightarrow\; 2\sigma_a = \Delta\sigma_{eq} = \Delta\sigma_{exp} \cdot (1 - \frac{\Delta\sigma_{m,exp}}{R_m}). \tag{83}$$

The toroidal positions of the strain sensors on the PSL were chosen such that the most stressed points are covered. Only bending about the first principal axis is

[64]The symbol Δ is used to designate peak-to-peak values (as in $\Delta\sigma_{eq}$), whereas σ_a is a 'real' oscillation amplitude.

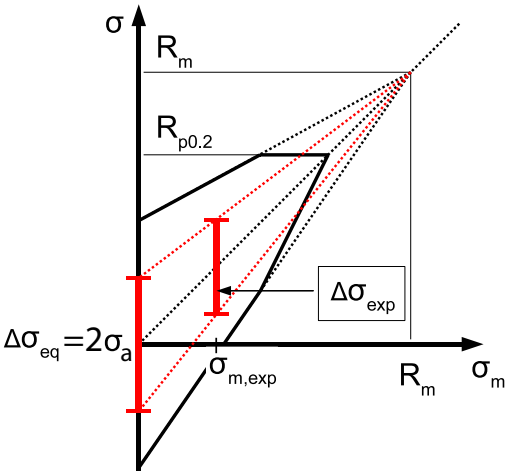

Figure 106: Smith diagram for calculation of equivalent, purely alternating stress amplitude $\Delta\sigma_{eq}$ corresponding to experimentally measured stress amplitude $\Delta\sigma_{exp}$ under mean stress $\sigma_{m,exp}$ (identical lifetime estimate)

measured (see section 3.2.1). However, the high ratio of the principal area moments of inertia $I_2/I_1 \approx 25$ suggest that bending about the second axis can be neglected. This justifies the use of the sensor signals for estimating the fatigue lifetime of the two rings. Under the assumption of uniaxial bending about the first principal axis, consider the PSL cross-sections at the toroidal positions of the sensors. The strain in the toroidal direction due to bending depends linearly on the distance between axis 1 and the position of interest. There are four geometrically different cases to be distinguished, which are illustrated in figure 107. The actual strain value at the most stressed position is determined by multiplying the strain measured by the sensor with the distance between axis 1 and the point with the largest distance to it, divided by the sensor's distance to axis 1. For example, the strain at point A of the regular sensor position on the upper ring (fig. 107a) is

$$\epsilon_A = \frac{44.5\text{mm}}{39.1\text{mm}} \cdot \epsilon_{sensor} \approx 1.14 \cdot \epsilon_{sensor}. \tag{84}$$

The strains at the points D, E and F are determined in a similar way using the conversion factors 1.16, 1.133 and 1.03 respectively.

The milled portion in segment 5 of the upper PSL ring as shown in figure 107e has a sharp edge[65] and represents a location of stress concentration. It is taken into account for the strain calculation with a stress concentration factor of 3. This value is chosen following the stress concentration factors of rectangularly shaped grooves for circlips on shafts [82, 83], and has to be considered as a rough and very conservative number in the present case. The concept of notch sensitivity, which is material and geometry dependent and would probably mitigate the effect of the sharp corner, is not applied here. This also represents worst-case assumption concerning the fatigue lifetime. Consequently, the notch in segment 5 of the upper

[65]This cutout has been machined with a square end milling cutter, the axis of rotation being normal to the inner PSL surface. The radius of curvature of the sharp corner indicated on the image results from the tool geometry and is below 0.1 mm.

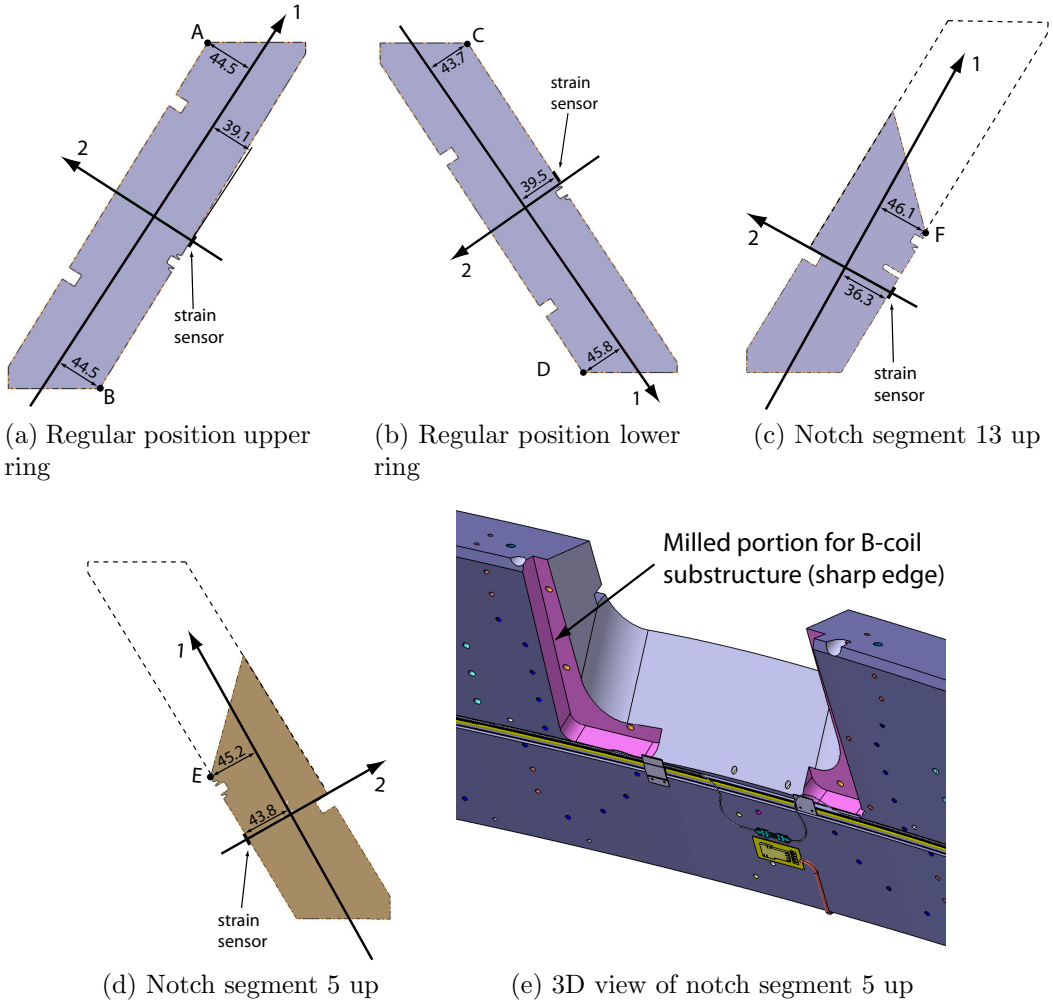

(a) Regular position upper ring

(b) Regular position lower ring

(c) Notch segment 13 up

(d) Notch segment 5 up

(e) 3D view of notch segment 5 up

Figure 107: The four different PSL cross-sections for the fatigue damage calculation (principal axes of inertia and points with largest distance to axis 1 shown)

PSL ring becomes the critical point of the whole structure. The stress concentration factor has a non-linear effect on the fatigue lifetime. The sensor 13up shows similar strain amplitudes as 5up, but the corresponding lifetime is calculated without the said factor of 3. Comparing the calculated lifetimes at these two positions allows to judge the impact of the stress concentration factor. Depending on the actual fatigue load on the PSL in the future, a more precise determination of the stress concentration e.g. by finite element methods to refine the lifetime prediction might be advisable.

The experimental strain measurements of every ASDEX Upgrade discharge consist of a strain time trace for every sensor position. Having the above described tools at hand, these traces can be converted into discrete values of the fatigue damage caused by the oscillations at the respective toroidal positions. This is done following six steps:

1. Calculating the strains of the most stressed positions of the respective PSL ring cross-section out of the strain values measured by the optical sensors. Four different cross-sections have to be distinguished (fig. 107).

2. Application of a rainflow algorithm to calculate first the extrema of the strain time traces and second the number of cycles and their corresponding absolute strain amplitude and mean strains (fig. 104).

3. Conversion from strains to stresses supposing proportional elasticity ($\sigma = \epsilon E$)

4. Determination of the equivalent stress amplitude $\Delta\sigma_{eq}$ without mean stress (pure cycling) according to the Smith diagram (fig. 106 and eq. (83)). This stress value corresponds to the data pair of mean stress *and* stress amplitude resulting from step 2 in terms of fatigue lifetime and damage.

5. Calculation of the fatigue limit n_i (number of cycles to failure) of this stress amplitude according to the approximated *S-N* curve of the PSL material (fig. 105). The inverse of n_i is the fatigue damage D_i of one full hysteresis cycle.

6. Summation of the damage shares of all cycles using a linear damage accumulation according to a Palmgren-Miner law (see e.g. [84]) yields the total damage.

The linear damage accumulation was carried out for a representative set of N=368 AUG discharges[66]. The total damage D_t is the damage sum of all cycles of every one of these discharges and can be written as:

$$D_t = \sum_N D_i = \sum_N \sum_{cycles} \frac{1}{n_i}. \tag{85}$$

This sum is calculated separately for each of the 32 regularly spaced optical sensors. The average damage per discharge is obtained by simply dividing the damage sum D_t by the number of shots N=368. Inversion of this value yields the lifetime of the PSL rings at the respective positions, in other words the expected number of discharges the PSL can withstand. Figure 108 shows this lifetime estimate expressed in discharges that was obtained by linear accumulation. The calculated lifetimes are, even for the most stressed position of the PSL rings, the notch in segment 5 on the upper ring, incredibly high. According to the calculation, the number of discharges that this particular part of the upper ring is able to withstand before fatigue failure occurs is $\underline{7 \cdot 10^{23}}$. This corresponds roughly to $5 \cdot 10^{20}$ years of operation of ASDEX Upgrade. Of course, the last 21 years have to be subtracted from this number. Nevertheless, it can be stated that the copper rings of the PSL are to be considered as undamaged in terms of fatigue. In fact, it should be doubted if the damage model used here is appropriate for such high cycle numbers (due to the small stresses) and if the lifetimes are not simply to be considered as infinite. This is certainly an important message of the present work. Naturally, the next question to ask is how the resonant excitation of the PSL by AC operation of the B-coils fits in this picture.

5.5.2 Operational limits of the internal coils in view of PSL fatigue

As the fatigue loading of the upper PSL in segment 5 dominates the lifetime prediction, the following considerations focus on this position. The worst-case resonant

[66] From discharge #25987 to #26354 during the 2010/11 experimental campaign.

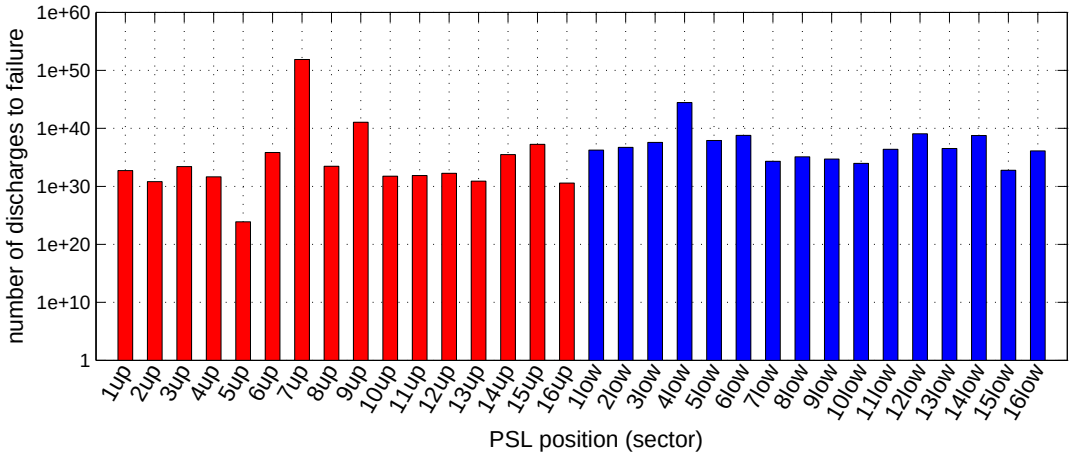

Figure 108: Expected lifetime of the PSL rings at the (toroidal) sensor positions, expressed in AUG discharges. Linear damage accumulation based on 368 shots.

PSL excitation scenario with the largest deformation is during AC B-coil operation in an odd n=4 configuration (recipe 908) around 50 Hz. This was shown in section 4.3. Refer to figure 61 for the associated response spectra of the PSL. This mode 'fits' into the upper hinges in such a way that these do not hinder the deformation, as the nodes of deflection of the mode are located at the hinges. The deformation of the upper and lower ring lead mostly to a rotation of the bridges about a horizontal axis without the need of lengthening them. The relation of the amplitude of the electric current supplied to the B-coils and the strain amplitude was explored in figure 64 and shown to be linear. We find a strain-current ratio of $2.295 \cdot 10^{-7}$/A for the above mode (i.e. 100 A at the resonant frequency yield a strain amplitude of 22.95 $\mu\epsilon$). This is a reliable number as it is based on a high number of cycles during the slow frequency sweep of discharge #27488 instead of a single or a few data points. Hence, the strain of sensor 5up ϵ_{5up} depends on the coil current I_B (in amperes) according to

$$\epsilon_{5up} = 2.295 \cdot 10^{-7} \frac{1}{\mathrm{A}} \cdot I_B. \tag{86}$$

The highest strain in the respective cross-section is given by

$$\epsilon_a = 1.03 \cdot 3 \cdot \epsilon_{5up} = 1.03 \cdot 3 \cdot 2.295 \cdot 10^{-7} \frac{1}{\mathrm{A}} \cdot I_B = 7.1 \cdot 10^{-7} \frac{1}{\mathrm{A}} \cdot I_B, \tag{87}$$

taking the geometry and the effect of the sharp corner into account like before. With Hooke's law and the approximated S-N curve of equation (81), we find the number of cycles to failure N_f as a function of the B-coil current amplitude.

$$\sigma = \epsilon \cdot E \text{ and } N_f(\sigma_a) = \left(\frac{\sigma_a}{R_m}\right)^{1/b} \rightarrow \; N_f(I_B) = \left(\frac{E \cdot 7.1 \cdot 10^{-7} \frac{1}{\mathrm{A}} \cdot I_B}{R_m}\right)^{1/b} \tag{88}$$

Of course, the frequency of the power supply of the B-coils is assumed to be the PSL resonance frequency of 49 Hz. The effect of the mean stress/strain does not have to be considered, as the oscillation is purely cyclic around the zero level. Figure

109 illustrates the two dependencies governing the fatigue life of the PSL under this particular loading: The stress as a function of the current and the fatigue life as a function of this stress. The lifetime on the top right, expressed in numbers of AUG

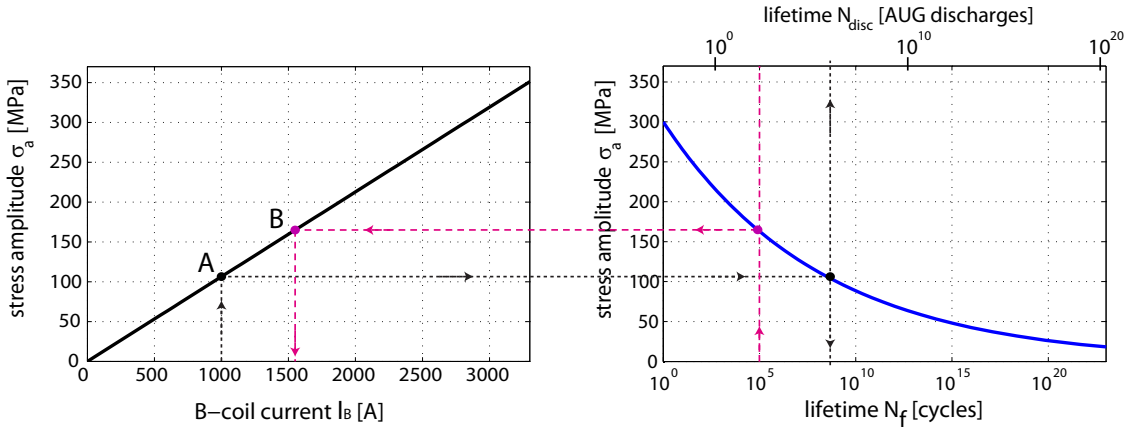

Figure 109: Linear extrapolation of the stress amplitude associated to AC B-coil operation (recipe 908, odd, B_t=−2.4 T) and fatigue lifetime at the upper PSL ring in segment 5.

discharges supposes constant-frequency shots of 500 full load cycles. This number results from the typical length of a plasma discharge of around 10 seconds[67] and the PSL n=4 resonance frequency range at 50 Hz. Two cases, denoted A and B are emphasised on the graph, which correspond to the planned maximum current of the B-coils of 1000 A (case A) and to the current leading to a lifetime of 10,000 cycles (case B). Table 19 summarises these examples. According to the calculation,

example	A	B
B_t	-2.4 T	-2.4 T
I_B	1000 A	1530 A
σ_a	106 MPa	163 MPa
N_f [cycles]	$3.35 \cdot 10^8$	10^5
N_{disc} [discharges]	$7.7 \cdot 10^5$	200

Table 19: Examples A and B of figure 109 in numbers: Fatigue lifetime and associated B-coil current and cyclic stress (resonant case, recipe 908 odd).

a current of 1 kA yields a stress amplitude of 106 MPa,[68] at which 770,000 discharges (of 500 cycles each) would lead to failure. At first glance, one could think of the PSL being invulnerable to any sort of operational load, be it from disruptions, or resonant excitation using the internal B-coils. But increasing the B-coil current in the resonant case by 53% to 1530 A brings the stress amplitude to a value where the number of cycles to failure drops to 10,000, due to the strong non-linear dependence of N_f on σ_a. In the worst-case conditions assumed here, this corresponds to 200

[67] This is a hypothetical scenario. Owing to the results of this work, such an oscillation is probably either going to be avoided or aborted after a short time. The scale in discharges of the right figure is for orientation only.

[68] =N/mm^2.

discharges only. This shows that the resonant excitation of the PSL structure is far from being negligible in terms of machine safety. There is another message included in figure 109 worth noticing. At B-coil currents above 2800 A, the stress level in segment 5 can reach the static tensile strength of the material R_m=300 MPa as soon as the oscillation has reached steady state. This would lead to immediate, irreversible damage in the form of cracks or rupture at this point.

A final remark shall be made about the dependency of stress level and toroidal magnetic field strength. During the technical discharges used here as a reference, the field strength had a constant value of B_t=−2.4 T. The j×B-forces that the B-coils exert on the PSL are proportional to B_t. As was shown earlier (fig. 64), the measured maximum strain amplitude depends linearly on the magnitude of these forces, because it is proportional to I_B. Thus, to estimate the fatigue lifetime at a different toroidal field strength, the stress amplitude obtained with the left chart of figure 109 simply has to be multiplied by a factor of $B_t/-2.4$ T.

The design of the B-coils was validated with a safety factor of 2 for a toroidal field strength of −3.1 T and a maximum B-coil current[69] of 1200 A [85]. The line load on the poloidal (short) coil legs then amounts to 17 kN per meter, the most stressed points being the ends of welded stiffener ribs on the coil casing. Operation at higher current is not planned. However, in the case of an unintended current rise the aforementioned static PSL strength limit is already reached at a calculated B-coil current of 2170 A, assuming B_t=−3.1 T. This current is inferior to the theoretical maximum value of 2400 A of the coils, as expressed by their safety factor. In this context, the PSL has therefore to be considered the weak link.

The calculations allow several concluding remarks:

1. Forced fracture (non-fatigue damaging) of the PSL rings due to disruptions can generally be excluded. The highest stresses caused by disruptive loads are at least a factor of 15 lower than the tensile strength of the material R_m.

2. Based on a load collective of 368 discharges, the accumulated fatigue damage D_t of the PSL rings is practically zero ($D_t < 5 \cdot 10^{-20}$, where a value of 1 corresponds to failure). This value and the following considerations refer to the most stressed position of both rings, the upper ring's notch in sector 5.

3. The operation of the internal B-coils with alternating current (and B_t=−2.4 T) has been assessed by extrapolation of the resulting PSL strains under the worst-case assumption of permanent resonance of the n=4 (odd) mode. A coil current of 1 kA yields lifetimes of hundreds of years of AUG operation.

4. Due to the non-linear relation of stress and lifetime, a current amplitude of 1530 A corresponds to a fatigue lifetime of only 10,000 cycles, or roughly 200 shots. In other words, an ambitious experimentalist could ruin the PSL, and with it the ASDEX Upgrade experiment, within a month or less.

Another consequence of the lifetime calculation being very sensitive to the (equivalent) stress amplitude is that small deviations in the stress calculation lead to large

[69] Concerning the maximum current, the B-coil dimensioning distinguishes between operational limit (1 kA) and absolute maximum rating (1.2 kA). See [85] for details.

deviations of the results. It must be noted that the assumptions entering the calculation, e.g. the stress concentration effect of the milled portion in segment 5, are approximations only. Should the B-coils actually be operated in a critical regime according to figure 109 in terms of electric current and at the PSL resonance frequency for extended periods, a refinement of these assumptions is advisable. This could include a finite element simulation to determine the said stress concentration with higher precision.

The fatigue calculation is valid for the PSL rings themselves only. It has been stated before that a direct fatigue assessment of the PSL hinges, the bridges and the mostly bolted connections of the different components is not possible, due to the lack of an appropriate measurement of their deformation. A modal expansion method as suggested in section 5.3 for the calculation of the deformation state of the whole PSL assembly could provide the necessary data without the need for further instrumentation. Whatever the load on the PSL in the future will be, the deformation is documented by the optical strain measurement during every discharge. This data can be used with the rainflow-based method that was established here to count the actual fatigue damage automatically.

In the resonant case and at the planned maximum B-coil current of 1 kA, the extrapolation yields very large deformation values of the PSL rings. Concerning strain amplitudes, it exceeds the strongest measured[70] plasma disruption by a factor of around 4. Even though the rings of the PSL may be able to handle this load regarding fatigue, it represents an exposure of ASDEX Upgrade to oscillations of an unprecedented scale. Unintentional mechanical consequences affecting for example the PSL bridges and hinges, the vacuum vessel hinges, the vessel itself, the experiment's support structure and also diagnostics are likely to occur. A significant vertical oscillation of the PSL rings would also have effects on the plasma stability. Therefore, it is reasonable to extend the diagnostic OSI to real-time capability in order to be able to use the PSL deformation signals as emergency-stop values. With a real-time measurement, active damping of resonant oscillations of the PSL using the B-coils with alternating current of an appropriate phasing would be feasible.

The combinations of recipes and frequencies with the strongest structural response, which are important to avoid are outlined in table 20. The odd configuration

recipe	odd/even	frequency	upper ring	lower ring
907	even	50.5 Hz	x	
907	even	54.0 Hz		x
908	odd	49 Hz	x	x
908	odd	54.5 Hz		x

Table 20: PSL resonance configurations in n=4 (separate and combined modes)

shows a combined mode at 49 Hz involving significant oscillation of both the lower and the upper ring. This setup shows the largest deformation and is therefore the basis of the above lifetime estimation.

To cope with high deformations, measures involving structural modifications of the PSL like the application of mechanical damping elements or modified supports

[70] By the optical PSL strain measurement (OSI).

are also an option. However, these extensive alternatives are momentarily unnecessary if appropriate measures with respect to the control of the coils are taken. In any case, the increase of the B-coil current should be accompanied by careful observation of the PSL response with the optical deformation sensors. The PSL is vital for the operation of ASDEX Upgrade and it cannot be replaced without completely disassembling the machine. Substantial damage of the PSL could mean a total loss of the experiment.

6 Summary and outlook

This work had two main tasks. The first was the development, commissioning, installation and operation of an optical strain measurement system inside a fusion device with magnetic confinement. The structural components of such a device are constantly subject to high electromagnetic forces leading to deformations. This part is of general importance, because this kind of measurement has not been used inside the vacuum vessel of fusion experiments before, despite its many benefits. Through the successful application of this technology at ASDEX Upgrade (AUG), it was qualified for this environment in multiple ways, including vacuum compatibility and resistance to neutron irradiation. The second task is specifically related to AUG. It consisted in the detailed analysis of the strain data in order to identify and evaluate resonant oscillations of the Passive Stabilising Loop (PSL), on which the sensors are mounted. The set of 16 internal coils, recently installed on the PSL, can exert magnetic forces on its structure which partly motivated the present work. The ultimate goal was an assessment of the operational safety of the PSL in view of disruptive loads and loads due to the internal coils. It was shown that the PSL deflection during operation is in the millimeter range and collisions can be excluded, as long as the operational parameters of AUG do not change dramatically. The PSL deformation due to resonant excitation with the B-coils was extrapolated and operational limits of the coils regarding spontaneous and long-term fatigue failure of the structure were defined.

Fibre Bragg grating sensors were used to measure the strain at the inner surfaces of the PSL. The sensor network was highly customised to AUG in terms of the sensor middle-wavelengths and the CAD-defined dimensions of the two sensing arrays. Thereby, excess fibre length in the vessel was avoided. All components to be installed inside the vacuum vessel were successfully pretested for their vacuum compatibility at 150°C. By mass spectroscopy, it was proven that no gases which could potentially compromise plasma operation were released.

The sensor carriers are made of stainless steel whereas the PSL consists of copper. The melting temperatures of these materials and other of their properties are highly dissimilar, and the solubility of one material in the other is very low. Therefore, a welding process with adapted parameters was developed to assure secure attachment of the sensors using laser beam welding, which was chosen for its high precision and energy density. Microscopy and hardness measurements of test welds revealed the absence of pores and fatigue strength relevant intermetallics. With tensile tests, it was proven that two distinct modes of failure of the joints exist, characterised by failure either on the copper or on the steel side. These modes occur depending on the welding parameters. Laser pulse energies above a certain threshold tend to lead to failure in the steel material. The initial stiffness (at low loads) of the joints in a sensing application is important for measurement precision. As the stiffness of the joints which tend to fail in the copper matrix is higher, welding parameters were tailored accordingly. A final tensile test series using these parameters allowed the calculation of a (static) safety factor of 26 for the produced welds.

The installation of the sensors on the PSL was realised using a laser welder standing outside the torus, and a laser welding head on a dedicated holding device inside. The head was connected to the welder via a cable harness for remote control,

shielding gas supply and laser pulse transmission. A self-developed, suction-cup equipped device was used to assure a constant normal pressure on the sensors to be welded. Their positions were predefined by CAD and located on site with high accuracy using a 3D measurement arm.

The first test of the sensing system, using a 5 kg hammer to excite the PSL was successful and proved the sensors to be fully operational at 1 kHz, as expected. The sensitivity of the measurement proved to be high enough to observe the peak caused by the hammer impact as it was travelling around the PSL ring. The sensing system was implemented as a standard diagnostic at AUG under the name OSI, automatically collecting data during every discharge without the need of maintenance. After a fibre breakage due to inaccurate fibre laying had occurred, a repair procedure, including the development of special tools, was engineered and successfully applied.

The PSL oscillations are categorised as originating from plasma disruptions, B-coil activity as well as plasma movements associated with control coil actions (control system related forces). Major plasma disruptions clearly lead to the largest loads and deformations. The measured maximum strain values at the sensor positions was 130 $\mu\epsilon$, i.e. a factor of 30 below the technical plasticity limit. The current quench of a disruption, which typically has a length of several ms, leads to a peak current in the PSL rings, which interacts with the poloidal magnetic field. Often, the quench is preceded by a vertical displacement event of the plasma which causes an initial, sudden rise in the PSL current that may have a sign opposite to the one due to the current quench. This summarizes the excitation of the PSL by disruptions, which determines the initial conditions of the following free PSL oscillation, when the plasma current has ceased. Triangular (n=3) ringmodes are dominant compared to other orders. This can be explained by the constraints set by the vertical supports on the upper ring. The elliptic (n=2) modes are effectively suppressed, which is also the case when they are explicitly excited with the B-coils by using a dedicated coil recipe. Triangular modes with n=3, the next mode number, also have low frequencies and thus low damping. The interaction with the supports is only moderate, and is almost independent of the direction of the forcing. Their obvious dominance probably results from this advantageous compromise.

The next order of natural PSL oscillations, the quadratic (n=4) modes, are only in rare cases the most active modes after disruptive excitation. However, they may excel the triangular modes in some cases, because for one specific angular orientation, they are not at all affected by the hinges. Accordingly, they are only excited when the forcing has a specific direction. The fact that one spatial orientation is highly favoured is confirmed by the sharp n=4 peak at 50 Hz in the disruptive spectra, showing that no mode splitting occurs.

The n=4 excitation using the B-coils leads exactly to the mode orientation which is favoured. It shows that the largest strain amplitudes occur in odd configuration. The support bridges are stretched and compressed in even cases and perform a turning motion in odd configurations. The latter is not hindering, but leads to a dynamic coupling of both rings' oscillation, which appears at a lower frequency than the one of the separate rings. Therefore, the odd quadratic modes imply the highest strains (up to 60 $\mu\epsilon$) and deformations and are considered to be the most dangerous configuration for operation of the B-coils with alternating current.

The disruptive spectra show recurring patterns which can be attributed in many cases to ideal ring modes by transforming back a specific frequency or a small frequency domain from the Fourier spectrum of the sensor data. These shapes show good agreement with the finite element (FE) modal shapes and frequencies. Furthermore, the shapes and frequencies produced with resonant forcing by the B-coils correspond exactly to those found in the aftermath of disruptions *and* to the FE solution. This motivated the development of a discretised PSL model based on modal expansion of the FE results. This model approximates numerically the modal participation factors of experimentally measured PSL oscillations. It has shown itself to be capable of representing uniform oscillations like those with resonant B-coil excitation, but fails to reproduce disruptive oscillations accurately.

The last category of PSL forces are due to the control coils. Depending on the elongation, the vertical position of a plasma is inherently unstable which can lead to oscillations around the equilibrium position due to the finite cycle-time of the control system in combination with the control coils. These oscillations can lead to large PSL deformations, compared to those due to the deliberate cyclic plasma shift at constant frequencies during magnetic ELM triggering ('wobbling'). Typical maximum strain amplitudes are in the range of 25 $\mu\epsilon$. With a numerical routine using magnetic equilibria and the measured PSL currents, the forces on the PSL rings were calculated. An empirical mode decomposition of the time traces of these forces allows to identify instantaneous frequencies. These suggest a causality between the force frequency being in a n=3 PSL ringmode domain (34-39 Hz) and rising amplitudes of the mechanical oscillation. This kind of plasma oscillation has also been observed prior to disruptions. In these cases, the amplitude of the plasma shift grows until the disruption occurs. Before the current quench, the PSL performs a forced oscillation at the plasma shift frequency which persists until after the disruption, when it superimposes with the 'real' disruptive oscillation.

The strain at critical points of the PSL rings was calculated and their hypothetical fatigue lifetime was estimated with a conservative approach. The fatigue damage was calculated based on a load collective of 368 AUG discharges, using a rainflow counting algorithm and linear damage accumulation. The actual PSL damage state after more than 20 years of operation was estimated to be completely negligible. This applies to the PSL rings only, not to its bridges or the hinges. For assessing the fatigue lifetime for operation of the B-coils in alternating current, the results of the technical discharges were extrapolated assuming linearity. The proportionality constant between strain amplitude and B-coil current at resonant frequency in the worst case scenario (n=4, odd) is $2.295 \cdot 10^{-7}$ per ampere. In other words, a B-coil current of 285 A at 49 Hz would lead to a PSL deformation equivalent to the strongest disruption in the database. The number of cycles to failure with the maximum design current of the coils of 1 kA amounts to $3.3{\cdot}10^8$ cycles, corresponding to $7.7{\cdot}10^5$ AUG discharges. Owing to the non-linear relation of stress amplitude and fatigue lifetime, a coil current (amplitude) of 1530 A leads to a dramatically decreased lifetime of 10,000 cycles, or 200 shots. Static failure occurs at a calculated current of 2800 A.

It was shown that the oscillations of the PSL strongly affect other parts of the AUG machine, or are at least symptomatic for the overall load. Even though the

lifetime at 1 kA is satisfyingly high, it has therefore to be noted that alternating B-coil operation at currents higher than 285 A push the PSL oscillatory system into regions with higher deformation than ever before. This might result in severe consequences for other subsystems (e.g. diagnostics) due to the associated vibrations and transmitted forces. For these reasons, the enhancement of the diagnostic OSI to real-time capability and possibly also its integration into the control system to provide an emergency stop signal is strongly recommended. A further option is to use the B-coils for active damping of resonant oscillations of the PSL. Naturally, any current increase should be carried out gradually and accompanied by monitoring of the PSL deformation with the optical strain sensors.

Future efforts should address explicitly the loads on the PSL bridges and the vertical supports. Additional (optical) sensors at appropriate positions are a feasible option. As an alternative, the discretised mechanical model could be developed further, using corrected modal shapes for the reconstruction. These can be determined with a finite element analysis with more realistic boundary conditions, i.e. support stiffnesses. Knowing the modal participation factors of measured PSL oscillations, the deflections, strains and stresses of the finite PSL elements could be calculated.

The weak points of the PSL rings are principally known. Polishing of these surfaces, if accessible, and regular inspection might be an option for early detection of signs of fatigue damage like surface cracks or extrusions due to persistent slip-bands.

The continuously growing strain database provides countless possibilities for exploitation. Examples are the statistical analysis of the strength of disruptions and their asymmetry and correlations with plasma parameters, the determination of the PSL material damping as input for FE calculations, the investigation of interactions of oscillations of the PSL and the vacuum vessel and others.

7 APPENDIX

The main technical specifications of the piezo-electronic acceleration sensor (see section 4.3.1) and the optical acceleration sensor (see section 5.1.1) are summarised in table 21.

item		
manufacturer	PCB	Micron Optics
model	J320C33	os7100
serial number	7516	pre-series
bias level	8.6 V	-
sensitivity	99.7 $\frac{\mathrm{mV}}{g} = 10.17 \frac{\mathrm{mV}}{\mathrm{m/s^2}}$	16 $\frac{\mathrm{pm}}{g}$
used amplifier	PCB 480E09 (battery operated)	-
amplifier gain	100	-
position	Sec. 3, on upper PSL inner surface	Port Co6, outer flange
measurement direction	normal to surface	vertical
data acquisition	Yokogawa DL 708	sm130-700 (1 kHz)
range of shots	-	#26134−#26257

Table 21: Technical data of both used acceleration sensors

Table 22 presents the materials of the PSL rings and bridges.

item	material	reference
PSL rings	Cu-ETP = 2.0060 = E-Cu57 (F30)	DIN 1787 and 40500
Support bridges	X2CrNi 18 10 = 1.4311	DIN EN 10028-7
Current bridge	CuCrZr, probably 2.1293	DIN 17666

Table 22: Materials of the PSL main components

Table 23 contains the exact coordinates of all optical strain sensors in toroidal and Cartesian coordinates. Table 24 presents the sensor names and centre wavelengths of the Bragg gratings. The wavelengths in the as-received condition do not correspond exactly to the specification (design values) and tend to shift slightly as a result of welding stresses during installation. The after-conditioning measurement of the upper array was carried out when it was still at 150°C, which is why the λ values are shifted towards higher values and 19-5up-S is not visible. The letters S, T and cb in the sensor name designate sensors for strain, temperature and the sensors positioned on the current bridge.

The data of the OSI diagnostic is stored - as defined in the shotfile header - in an array of 28000 rows (depending on the acquisition length) and 100 columns. Usually, the peak wavelength of each sensor is saved in one column (exceptions see p. 48). With less than 100 sensors connected, the remaining columns contain zeros. Strains are calculated from the acquired wavelengths using equation (33) with the calibration constants given on page 29. The MATLAB functions mostly used in the course of this work for data visualisation and analysis are cited in table 25. Type

sensor name	X [mm]	Y [mm]	Z [mm]	R [mm]	θ [°]
01-6up-S	-1149.22	1719.93	696.61	2068.54	124.75
02-cb6/7up-S	-1456.96	1466.69	696.61	2067.34	135.81
03-7up-S	-1719.93	1149.22	696.61	2068.54	147.25
04-8up-S	-2028.8	403.55	696.61	2068.54	169.75
05-9up-S	-2028.8	-403.55	696.61	2068.54	192.25
06-10up-S	-1719.93	-1149.22	696.61	2068.54	214.75
07-11up-S	-1149.22	-1719.93	696.61	2068.54	237.25
08-11/12up-T	-821.52	-1898.41	696.61	2068.54	247.6
09-12up-S	-403.55	-2028.8	696.61	2068.54	259.75
10-13up-S	411.5	-2068.73	630.15	2109.26	282.25
11-14up-S	1149.22	-1719.93	696.61	2068.54	304.75
12-15up-S	1719.93	-1149.22	696.61	2068.54	327.25
13-16up-S	2028.8	-403.55	696.61	2068.54	349.75
14-1up-S	2028.8	403.55	696.61	2068.54	12.25
15-2up-S	1719.93	1149.22	696.61	2068.54	34.75
16-3up-S	1149.22	1719.93	696.61	2068.54	57.25
17-3/4up-T	821.52	1898.41	696.61	2068.54	67.6
18-4up-S	403.55	2028.8	696.61	2068.54	79.75
19-5up-S	-411.19	2067.19	632.7	2107.69	102.25
01-6low-S	-1105.97	1655.2	-690.6	1990.69	124.75
02-cb6/7low-S	-1399.58	1412.25	-690.6	1988.29	135.81
03-7low-S	-1655.2	1105.97	-690.6	1990.69	147.25
04-8low-S	-1952.44	388.36	-690.6	1990.69	169.75
05-9low-S	-1952.44	-388.36	-690.6	1990.69	192.25
06-10low-S	-1655.2	-1105.97	-690.6	1990.69	214.75
07-11low-S	-1105.97	-1655.2	-690.6	1990.69	237.25
08-11/12low-T	-790.6	-1826.96	-690.6	1990.69	247.6
09-12low-S	-388.36	-1952.44	-690.6	1990.69	259.75
10-13low-S	388.36	-1952.44	-690.6	1990.69	282.25
11-14low-S	1105.97	-1655.2	-690.6	1990.69	304.75
12-15low-S	1664.29	-1112.05	-697.77	2001.63	327.25
13-16low-S	1952.44	-388.36	-690.6	1990.69	349.75
14-1low-S	1952.44	388.36	-690.6	1990.69	12.25
15-2low-S	1655.2	1105.97	-690.6	1990.69	34.75
16-3low-S	1105.97	1655.2	-690.6	1990.69	57.25
17-3/4low-T	790.6	1826.96	-690.6	1990.69	67.6
18-4low-S	388.36	1952.44	-690.6	1990.69	79.75
19-5low-S	-388.36	1952.44	-690.6	1990.69	102.25

Table 23: Positions of all optical sensors in Cartesian and toroidal coordinates

on-fibre order	vessel sector	toroidal angle	sensor name	λ design value	λ after conditioning	λ after installation	λ after repair (final)
1	6	124.75	01-6up-S	1512.4	1515.1	1512.69	1512.69
2	6/7	135.81	02-cb6/7up-S	1521.8	1520.3	*not visible*	*demounted*
3	7	147.25	03-7up-S	1531.2	1524.3	1531.61	**1544.002**
4	8	169.75	04-8up-S	1535.9	1530.4	1537.99	1537.99
5	9	192.25	05-9up-S	1545.3	1533.7	1545.39	1545.39
6	10	214.75	06-10up-S	1554.7	1535.9	1555.98	1555.98
7	11	237.25	07-11up-S	1564.1	1539.6	1564.82	1564.82
8	11/12	247.6	08-11/12up-T	1571.2	1544.4	1571.46	1571.46
9	12	259.75	09-12up-S	1578.2	1549	1578.4	1578.4
10	13	282.25	10-13up-S	1587.6	1553.7	1587.68	1587.68
11	14	304.75	11-14up-S	1582.9	1558.3	1582.86	1582.86
12	15	327.25	12-15up-S	1573.5	1562	1573.55	1573.55
13	16	349.75	13-16up-S	1568.8	1567.2	1570.44	1570.44
14	1	12.25	14-1up-S	1559.4	1572.9	1560.21	1560.21
15	2	34.75	15-2up-S	1550	1573.8	1550.52	1550.52
16	3	57.25	16-3up-S	1540.6	1576	1541.09	1541.09
17	3/4	67.6	17-3/4up-T	1533.5	1580.7	1535.39	1535.39
18	4	79.75	18-4up-S	1526.5	1585.2	1527.55	1527.55
19	5	102.25	19-5up-S	1517.1	*not visible*	1518.15	**1563.487**
1	6	124.75	01-6low-S	1512.4	1512.5	1512.61	1512.61
2	6/7	135.81	02-cb6/7low-S	1521.8	1517.3	1522.84	1522.84
3	7	147.25	03-7low-S	1531.2	1522.9	1531.79	1531.79
4	8	169.75	04-8low-S	1535.9	1526.7	1536.27	1536.27
5	9	192.25	05-9low-S	1545.3	1531.7	1546.39	1546.39
6	10	214.75	06-10low-S	1554.7	1533.7	1555.64	1555.64
7	11	237.25	07-11low-S	1564.1	1536.1	1564.12	1564.12
8	11/12	247.6	08-11/12low-T	1571.2	1543.5	1571.73	1571.73
9	12	259.75	09-12low-S	1578.2	1546.4	1578.04	1578.04
10	13	282.25	10-13low-S	1587.6	1550.3	1588.41	1588.41
11	14	304.75	11-14low-S	1582.9	1555.6	1582.89	1582.89
12	15	327.25	12-15low-S	1573.5	1559.7	1574.04	1574.04
13	16	349.75	13-16low-S	1568.8	1564.2	1569.9	1569.9
14	1	12.25	14-1low-S	1559.4	1569.9	1559.8	1559.8
15	2	34.75	15-2low-S	1550	1571.7	1550.56	1550.56
16	3	57.25	16-3low-S	1540.6	1573.7	1543.42	1543.42
17	3/4	67.6	17-3/4low-T	1533.5	1578.1	1533.77	1533.77
18	4	79.75	18-4low-S	1526.5	1583.6	1526.79	1526.79
19	5	102.25	19-5low-S	1517.1	1588.6	1517.27	1517.27

Table 24: Sensor positions on both sensing fibres and their characteristic wavelengths (in nm)

name	description
1. parameters.dat	contains λs, calibration, etc. for use with executables (x_)
2. x_get_osi_data.m	retrieves strain data by calling routines 3-6
3. x_get_raw_lambdas.m	load raw lambda values from shotfile
4. x_organize_lambdas.m	reorganizes columns of raw OSI lambdas by comparison with 'peak number/channel' obtained from 'spectra'.
5. x_sort_sensor_lambdas.m	sort array of lambda values according to sensor attribution defined by parameters.dat
6. x_compute_strains.m	compute strains according to calibration values (1.)
7. x_find_spectral_peaks.m	gives back 4 vectors with the peak values measured at the 4 sm130 channels (extracted from 'spectra'); (used in 4. to allow definite sensor identification)
8. x_extract.m	extract strain data like 1., for a defined time interval only
9. x_overview_up.m	show time traces of all sensors on upper ring
10. x_overview_low.m	show time traces of all sensors on lower ring
11. math_PSL.m	visualise top-view PSL deformation as video
12. math_PSL_fft.m	visualise top-view PSL deformation of strain input data (e.g. Fourier-filtered) as video
13. PSL_F.m	calculate PSL Lorentz force based on equilibrium and I_{PSL}

Table 25: MATLAB scripts for analysis and visualisation of OSI data

help filename at the MATLAB command prompt for a description of the script and its input and output variables.

Bibliography

[1] W.D. Loveland, D.J. Morrissey, and G.T. Seaborg. *Modern Nuclear Chemistry*. Wiley-Interscience, 2006.

[2] W. Demtröder. *Experimentalphysik 4: Kern-, Teilchen- und Astrophysik*. Springer-Lehrbuch. Springer, 2009.

[3] J. Wesson. *Tokamaks*. The International Series of Monographs on Physics. Oxford University Press, USA, 2004.

[4] H.-W. Bartels, H.-S. Bosch, R. Brakel, M. Drevlak, H.-J. Hartfuss, R. Kleiber, A. Könies, K. Krieger, H. Lesch, E. Poli, M. Roth, B. D. Scott, W. Suttrop, and H. Zohm. *IPP Summer University for Plasma Physics*. Lecture notes. Max-Planck-Institute for Plasma Physics, 2009.

[5] G. McCracken and P. Stott. *Fusion: The Energy of the Universe*. Complementary Science. Elsevier Science, 2005.

[6] N. A. Uckan. Special issue on ASDEX Upgrade. *Fusion science and technology*, 44(3):III–III, 2003.

[7] F. C. Schuller. Disruptions in tokamaks. *Plasma Physics and Controlled Fusion*, 37(11A):A135, 1995.

[8] W. Engelhardt, G. Becker, K. Behringer, D. Campbell, and A. Eberhagen. Divertor efficiency in ASDEX. *Journal of Nuclear Materials*, 111:337–342, 1982.

[9] F. Wagner, G. Becker, K. Behringer, D. Campbell, and A. Eberhagen. Regime of improved confinement and high-beta in neutral-beam-heated divertor discharges of the ASDEX tokamak. *Physical Review Letters*, 49(19):1408–1412, 1982.

[10] W. Köppendorfer. ASDEX Upgrade - a Tokamak experiment with a reactor-compatible poloidal divertor. *Proceedings of the 10th Symposium on Fusion Technology*, 1:187–192, 1983.

[11] ASDEX Upgrade Design Team and Tokamak Theory Group. Definition of a tokamak experiment with a reactor compatible poloidal divertor. *IPP report 1/197*, 1:38–45, 1982.

[12] M. Blaumoser. Technical concept of the ASDEX Upgrade device. *Proceedings of the 10th Symposium on Fusion Engineering*, 3:1814–1819, 1983.

[13] O. Gruber. Physics background of the ASDEX Upgrade project. *Journal of nuclear materials*, 121:407–411, 1984.

[14] V. Mertens, G. Raupp, and W. Treutterer. Plasma control in ASDEX Upgrade. *Fusion Science and Technology*, 44(3):593–604, 2003.

[15] M. Blaumoser. Engineering aspects of ASDEX Upgrade. *Proceedings of the 12th Symposium on Fusion Engineering*, 2:1469–1472, 1987.

[16] ASDEX Upgrade Design Team. Vacuum vessel dimensioning. In *ASDEX Upgrade collective document archive*. IPP, 1982-1999.

[17] ASDEX Upgrade Team. PSL system description and overview. In *ASDEX Upgrade technical ringbook*. IPP, 1983-1993.

[18] ASDEX Upgrade Design Team. PSL manufacturing drawings (1GF0685-87). In *ASDEX Upgrade collective document archive*. IPP, 1986.

[19] W. Köppendorfer. Structural dimensioning of the PSL. In *ASDEX Upgrade collective document archive*. IPP, 1993.

[20] W. Suttrop, T. Eich, J.C. Fuchs, S. Guenter, and A. Janzer. First observation of edge localized modes mitigation with resonant and nonresonant magnetic perturbations in ASDEX Upgrade. *Physical review letters*, 106(22), 2011.

[21] W. Suttrop, L. Barrera, A. Herrmann, R.M. McDermott, and T. Eich. Studies of edge localized mode mitigation with new active in-vessel saddle coils in ASDEX Upgrade. *Plasma Physics and Controlled Fusion*, 53(12), 2011.

[22] G. Federici, A. Loarte, and G. Strohmayer. Assessment of erosion of the ITER divertor targets during type-I ELMs. *Plasma Physics and Controlled Fusion*, 45(9):1523–1547, 2003.

[23] T. Vierle, B. Streibl, M. Rott, U. Seidel, A. Herrmann, O. Neubauer, and W. Suttrop. Design and stress analysis of in-vessel saddle coils for MHD control in ASDEX Upgrade. *Fusion Engineering and Design*, 84(711):1928 – 1932, 2009. Proceedings of the 25th Symposium on Fusion Technology.

[24] W. Suttrop. In-vessel saddle coils for MHD control in ASDEX Upgrade. *Fusion Engineering and Design*, 84(2):290–294, 2009.

[25] T.E. Evans. Suppression of large edge localized modes with edge resonant magnetic fields in high confinement DIII-D plasmas. *Nuclear Fusion*, 45(7):595, 2005.

[26] P. Cahyna, M. Becoulet, R. Panek, V. Fuchs, E. Nardon, and L. Krlin. Resonant magnetic perturbations and edge ergodization on the COMPASS tokamak. *Plasma Physics Reports*, 34:746–749, 2008.

[27] R.J. Hawryluk, D.J. Campbell, G. Janeschitz, P.R. Thomas, R. Albanese, R. Ambrosino, C. Bachmann, L. Baylor, M. Becoulet, and I. Benfatto. Principal physics developments evaluated in the ITER design review. *Nuclear Fusion*, 49(6):065012, 2009.

[28] M. Becoulet. Numerical study of the resonant magnetic perturbations for type-I edge localized modes control in ITER. *Nuclear Fusion*, 48(2):24–27, 2008.

[29] J.J. Thomsen. *Vibrations and stability: Advanced theory, analysis, and tools*. Springer complexity. Springer, 2003.

[30] J. Wittenburg. *Schwingungslehre*. Springer-Lehrbuch. Springer, 1996.

[31] H. Goldstein. *Classical mechanics*. Addison-Wesley series in physics. Addison-Wesley Pub. Co., 1980.

[32] D. Gross, W. Hauger, and P. Wriggers. *Technische Mechanik 4: Hydromechanik, Elemente der Höheren Mechanik, Numerische Methoden*. Springer-Lehrbuch. Springer Verlag, 2012.

[33] W. Soedel. *Vibrations of shells and plates*. Mechanical engineering. Marcel Dekker, 1993.

[34] J. Wauer. *Kontinuumsschwingungen: Vom einfachen Strukturmodell zum komplexen Mehrfeldsystem*. Vieweg + Teubner, 2008.

[35] K.G. Krapf. *Der elastisch gebettete Kreisring als Modell für den Gürtelreifen*. Fortschritt-Berichte der VDI-Zeitschriften. Reihe 11. VDI-Verlag, 1981.

[36] A.E.H. Love. The small free vibrations and deformation of a thin elastic shell. *Philosophical Transactions of the Royal Society of London. A*, 179:491–546, 1888.

[37] S.A. Tobias. *Vibrations of Elastic Bodies of Revolution Containing Imperfections: A Theory of Imperfection*. University of Edinburgh, 1950.

[38] H. Park. A study on the mode pair of a slightly asymmetric circular ring with multiple deviations. *Journal of sound and vibration*, 310(1):366–380, 2008.

[39] C. Fox. A simple theory for the analysis and correction of frequency splitting in slightly imperfect rings. *Journal of sound and vibration*, 142(2):227–243, 1990.

[40] D. Allaei. Natural frequencies and modes of rings that deviate from perfect axisymmetry. *Journal of sound and vibration*, 111(1):9–27, 1986.

[41] J.D. Jackson. *Classical Electrodynamics*. Wiley, 1999.

[42] D. Chattopadhyay. *Electronics (Fundamentals And Applications)*. New Age International (P) Limited, 2006.

[43] Y.J. Rao. Recent progress in applications of in-fibre bragg grating sensors. *Optics and Lasers in Engineering*, 31(4):297–324, 1999.

[44] J. Canning. Fibre gratings and devices for sensors and lasers. *Laser & Photonics Reviews*, 2(4):275–289, 2008.

[45] J. Roths and P. Kratzer. Intercomparison of optical FBG-based strain sensors and resistive strain gages. *tm - Technisches Messen*, 75(12):647–654, 2008.

[46] A.D. Kersey et al. Fiber grating sensors. *Journal of Lightwave Technology*, 15:1442–1463, 1997.

[47] E.J. Friebele, C.G. Askins, M.E. Gingerich, and K.J. Long. Optical fiber waveguides in radiation environments, II. *Nuclear Instruments and Methods in Physics Research Section B: Beam Interactions with Materials and Atoms*, 1(2-3):355–369, 1984.

[48] T. Wijnands, L.K. De Jonge, J. Kuhnhenn, S.K. Hoeffgen, and U. Weinand. Optical absorption in commercial single mode optical fibers in a high energy physics radiation field. *Nuclear Science, IEEE Transactions on*, 55(4):2216–2222, 2008.

[49] K. Krebber. Fibre bragg gratings as high dose radiation sensors? *Measurement science and technology*, 17(5):1095, 2006.

[50] H. Henschel, S.K. Hoeffgen, K. Krebber, J. Kuhnhenn, and U. Weinand. Influence of fiber composition and grating fabrication on the radiation sensitivity of fiber bragg gratings. *Nuclear Science, IEEE Transactions on*, 55(4):2235–2242, aug. 2008.

[51] H. Henschel, S.K. Hoeffgen, J. Kuhnhenn, and U. Weinand. Influence of manufacturing parameters and temperature on the radiation sensitivity of fiber bragg gratings. *Nuclear Science, IEEE Transactions on*, 57(4):2029–2034, aug. 2010.

[52] K. Rose. Fraunhofer Institut fuer Silicatforschung (ISC), Wuerzburg, Germany. Private communication, 2009-06-26.

[53] Z. Sun and J. Ion. Laser welding of dissimilar metal combinations. *Journal of Materials Science*, 30:4205–4214, 1995.

[54] W. Bergmann. *Werkstofftechnik*. Number Bd. 2 in Werkstofftechnik. Hanser, 2001.

[55] T.A. Mai and A.C. Spowage. Characterisation of dissimilar joints in laser welding of steel-kovar, copper-steel and copper-aluminium. *Materials Science and Engineering: A*, 374(12):224–233, 2004.

[56] C.T. Dawes. *Laser Welding: A Practical Guide*. Woodhead Publishing, 1992.

[57] T.Y. Kuo and S.L. Jeng. Porosity reduction in NdYAG laser welding of stainless steel and inconel alloy by using a pulsed wave. *Journal of physics. D, Applied physics*, 38(5):722, 2005.

[58] A. Mathieu, R. Shabadi, A. Deschamps, M. Suery, S. Matte, D. Grevey, and E. Cicala. Dissimilar material joining using laser (aluminum to steel using zinc-based filler wire). *Optics and Laser Technology*, 39(3):652–661, 2007.

[59] C. Yao, B. Xu, X. Zhang, J. Huang, J. Fu, and Y. Wu. Interface microstructure and mechanical properties of laser welding copper-steel dissimilar joint. *Optics and Lasers in Engineering*, 47(78):807–814, 2009.

[60] E. Madenci and I. Guven. *The Finite Element Method and applications in engineering using ANSYS*. Springer, 2006.

[61] I. Zammuto. Modal and harmonic analyses on the AUG structures + coil supports. In *ASDEX Upgrade internal report*. IPP, 2009.

[62] I. Zammuto. Development of 4 straps antenna for ASDEX Upgrade. In *ASDEX Upgrade seminar*. IPP, 2008-07-18.

[63] W. Schnell, D. Gross, W. Hauger, J. Schröder, and W. Wall. *Technische Mechanik 2: Elastostatik*. Springer-Lehrbuch. Springer Verlag, 1995.

[64] A.W. Degeling, Y.R. Martin, J.B. Lister, X. Llobet, and P.E. Bak. ELM dynamics in TCV H-modes. In *Plasma physics*, volume 669 of *AIP conference proceedings*, pages 223–227. American Institute of Physics, New York, 2003.

[65] P.T. Lang, A.W. Degeling, J.B. Lister, Y.R. Martin, and P.J. McCarthy. Frequency control of type-I ELMs by magnetic triggering in ASDEX Upgrade. *Plasma Physics and Controlled Fusion*, 46(11):L31–L39, 2004.

[66] P.T. Lang, O. Gruber, V. Mertens, R. Neu, and F. Ryter. Impact of fast vertical and radial plasma movement on type-I ELMs in ASDEX Upgrade. *Czechoslovak Journal of Physics*, 56(12):1329–1337, 2006.

[67] R. Markert. An- und Auslaufvorgänge einfacher Schwinger im Kriechgrenzfall D=1. *Forschung im Ingenieurwesen A*, 48:11–14, 1982.

[68] C. Gasquet and P. Witomski. *Fourier Analysis and Applications: Filtering, Numerical Computation, Wavelets*. Texts in Applied Mathematics. Springer, 1999.

[69] G. Bateman. *MHD instabilities*. MIT Press, 1978.

[70] W. Brauch, H.J. Dreyer, W. Haacke, and W. Gentzsch. *Mathematik für Ingenieure*. Lehrbuch Mathematik. Vieweg+Teubner Verlag, 2006.

[71] N. E. Huang, Z. Shen, S. R. Long, M. C. Wu, H. H. Shih, Q. Zheng, N. C. Yen, C. C. Tung, and H. H. Liu. The empirical mode decomposition and the hilbert spectrum for nonlinear and non-stationary time series analysis. *Proceedings of the Royal Society of London. Series A: Mathematical, Physical and Engineering Sciences*, 454(1971):903–995, March 1998.

[72] ASTM E 1049-85 (Reapproved 1997). Standard practices for cycle counting in fatigue analysis. Technical report, Philadelphia, 1999.

[73] Adam Niesony. Determination of fragments of multiaxial service loading strongly influencing the fatigue of machine components. *Mechanical Systems and Signal Processing*, 23(8):2712 – 2721, 2009.

[74] M. Matsuichi and T. Endo. Fatigue of metals subjected to varying stress. *Japan Society of Mechanical Engineers*, 1968.

[75] H. Gudehus. *Leitfaden für eine Betriebsfestigkeitsrechnung: Empfehlungen zur Lebensdauerabschätzung von Maschinenbauteilen*. Stahleisen GmbH, 1999.

[76] A. Parsi. Deutsches Kupferinstitut, Duesseldorf, Germany. Private communication, 2012-08-31.

[77] Deutsches Kupferinstitut. Copper Data Sheet No. A1, Cu-ETP. 1968.

[78] A. Butts. *Copper: the science and technology of the metal, its alloys and compounds*. American Chemical Society. Monographs series. Reinhold, 1954.

[79] E. Macherauch and H.W. Zoch. *Praktikum in Werkstoffkunde: 91 ausführliche Versuche aus wichtigen Gebieten der Werkstofftechnik*. Studium Technik. Vieweg+Teubner Verlag, 2011.

[80] S. Koczyk. Betriebsfestigkeit und Berechnung der Lebensdauer mit einer allgemeineren Darstellung der Wöhlerlinie. *Technische Mechanik*, 15(1):59–68, 1995.

[81] J. Schijve. *Fatigue of Structures and Materials*. Springer, 2009.

[82] H. Haberhauer and F. Bodenstein. *Maschinenelemente: Gestaltung, Berechnung, Anwendung*. Springer-Lehrbuch. Springer, 2011.

[83] G. Köhler and B. Künne. *Maschinenteile 2*. Teubner, 2004.

[84] F. Ellyin. *Fatigue Damage, Crack Growth and Life Prediction*. Springer, 1996.

[85] *Application for Preferential Support for active in-vessel coils and conducting wall for MHD stabilisation in ASDEX Upgrade (Stage 1) - Addendum to Phase II proposal*. Max-Planck-Institut für Plasmaphysik, Forschungszentrum Jülich, Consorzio RFX Padova, Royal Institute of Technology KTH, 2008.

List of Figures

List of Tables